

AD-A133 530

OPTICAL PROPERTIES OF NATURAL MINERALS AND OTHER
MATERIALS IN THE 350-500. (U) MISSOURI UNIV-KANSAS CITY
DEPT OF PHYSICS M R QUERRY AUG 83 ARO-16512.2-G5

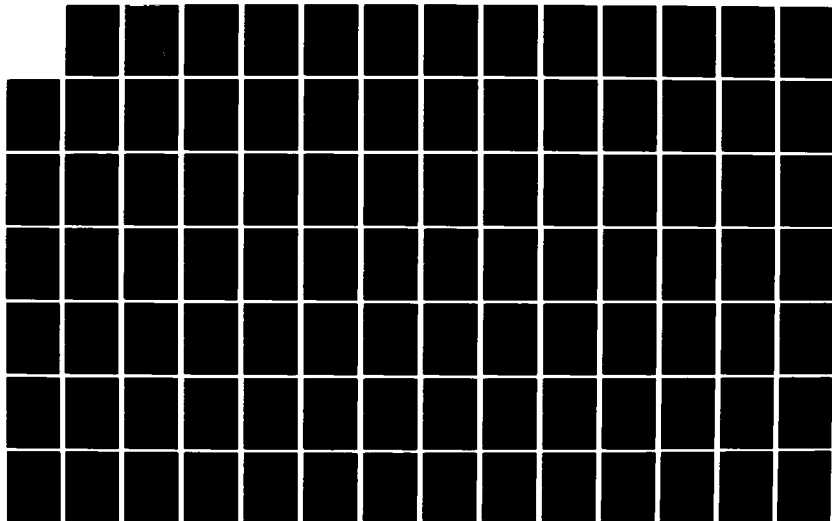
1/4

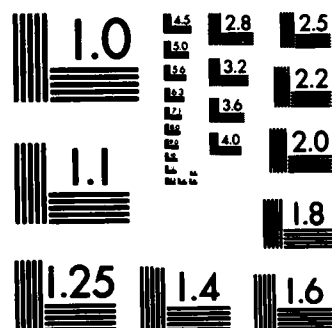
UNCLASSIFIED

DAAG29-79-C-0131

F/G 8/7

NL





MICROCOPY RESOLUTION TEST CHART
NATIONAL BUREAU OF STANDARDS-1963-A

AD-A133 530

ARO 16512.2-GS

(1.7)

OPTICAL PROPERTIES OF NATURAL MINERALS AND
OTHER MATERIALS IN THE 350-50,000 CM^{-1} SPECTRAL
REGION

FINAL REPORT

MARVIN R. QUERRY, Ph.D.

AUGUST 1983

U.S. ARMY RESEARCH OFFICE
CONTRACT NUMBER DAAG-29-79-C0131

DEPARTMENT OF PHYSICS
UNIVERSITY OF MISSOURI-KANSAS CITY

APPROVED FOR PUBLIC RELEASE;
DISTRIBUTION UNLIMITED.

DTIC
S OCT 14 1983
A

THE FINDINGS OF THIS REPORT ARE NOT TO BE
CONSTRUED AS AN OFFICIAL DEPARTMENT OF
THE ARMY POSITION, UNLESS SO DESIGNATED
BY OTHER AUTHORIZED DOCUMENTS.

DTIC FILE COPY

Unclassified

SECURITY CLASSIFICATION OF THIS PAGE (When Data Entered)

REPORT DOCUMENTATION PAGE		READ INSTRUCTIONS BEFORE COMPLETING FORM
1. REPORT NUMBER	2. GOVT ACCESSION NO.	3. RECIPIENT'S CATALOG NUMBER
	ADA 133 530	
4. TITLE (and Subtitle)		5. TYPE OF REPORT & PERIOD COVERED
Optical Properties of Natural Minerals and other Materials in the 350-50,000 cm^{-1} Spectral Region.		FINAL REPORT 15 July 1979 - 31 Dec. 1982
		6. PERFORMING ORG. REPORT NUMBER
7. AUTHOR(s)		8. CONTRACT OR GRANT NUMBER(s)
Marvin R. Query		DAAG-29-79-C-0131
9. PERFORMING ORGANIZATION NAME AND ADDRESS		10. PROGRAM ELEMENT, PROJECT, TASK AREA & WORK UNIT NUMBERS
Department of Physics University of Missouri-Kansas City Kansas City, Mo. 64110		
11. CONTROLLING OFFICE NAME AND ADDRESS		12. REPORT DATE
U. S. Army Research Office Post Office Box 12211 Research Triangle Park, NC 27709		August 1983
		13. NUMBER OF PAGES
14. MONITORING AGENCY NAME & ADDRESS (if different from Controlling Office)		15. SECURITY CLASS. (of this report)
		Unclassified
		15a. DECLASSIFICATION/DOWNGRADING SCHEDULE
16. DISTRIBUTION STATEMENT (of this Report)		
Approved for public release; distribution unlimited.		
17. DISTRIBUTION STATEMENT (of the abstract entered in Block 20, if different from Report)		
NA		
18. SUPPLEMENTARY NOTES		
The view, opinions, and/or findings contained in this report are those of the author(s) and should not be construed as an official Department of the Army position, policy, or decision, unless so designated by other documentation		
19. KEY WORDS (Continue on reverse side if necessary and identify by block number)		
Natural Minerals, Aqueous Solutions, Reflectance, Optical Constants, Refractive Indices, Infrared, Visible, Ultraviolet		
20. ABSTRACT (Continue on reverse side if necessary and identify by block number)		
<p>→ Reflectance spectra were measured in the UV, VIS, and/or IR for several natural minerals and for several aqueous solutions of ZnCl_2 and H_3PO_4. Complex refractive indices were determined for most of these materials by applying Kramers-Kronig methods to the reflectance spectra. Powders of some of the natural minerals were pressed in to pellets in order to obtain the reflectance spectra. Gypsum was studied in the crystalline form, the powder-pellet form, and by transmittance spectra through KBr pellets containing minute quantities</p>		

→ of gypsum. A method was developed for obtaining complex refractive indices from reflectance spectra of the pellets and transmittance spectra of the powder/KBr pellet. The best specularly reflecting pellets were formed from powders of smaller particle size and with forces of from 14 to 16 tons on the 13 mm dia circular face of the pellet.

The complex refractive indices of water were also updated by applying Kramers-Kronig methods to a new composite k spectrum in order to determine the n spectrum.



ABSTRACT

Reflectance spectra were measured in the UV, VIS, and/or IR for several natural minerals and for several aqueous solutions of ZnCl_2 and H_3PO_4 . Complex refractive indices were determined for most of these materials by applying Kramers-Kronig methods to the reflectance spectra. Powders of some of the natural minerals were pressed in to pellets in order to obtain the reflectance spectra. Gypsum was studied in the crystalline form, the powder-pellet form, and by transmittance spectra through KBr pellets containing minute quantities of gypsum. A method was developed for obtaining complex refractive indices from reflectance spectra of the pellets and transmittance spectra of the powder/KBr pellet. The best specularly reflecting pellets were formed from powders of smaller particle size and with forces of from 14 to 16 tons on the 13 mm dia. circular face of the pellet.

The complex refractive indices of water were also updated by applying Kramers-Kronig methods to a new composite k spectrum in order to determine the n spectrum.

TABLE OF CONTENTS

Title Page	i
Form DD 1473	ii
Abstract	iv
Table of Contents.....	v
List of Illustrations.....	vii
List of Tables.....	xx
 I. Statement of Problem.....	 1
II. Summary of Most Important Results.....	1
III. Publications.....	5
IV. Personnel Employed on the Project.....	6
V. Report of Research.....	7
A. Experimental Methods.....	7
1. Methods for Acquiring Reflectance Spectra of Aqueous Solutions.....	7
2. Methods for Acquiring Reflectance Spectra of Crystals.....	10
3. Methods for Acquiring Reflectance Spectra of Pellets.....	12
4. Methods for Acquiring Reflectance Spectra of Diesel Fuel.....	13
B. Theoretical Methods.....	14
C. Uncertainties in $N(\nu)$	16
D. Gypsum Crystals and Powder.....	19
E. Crystalline Samples.....	93
1. Rutile O-Ray.....	93

2.	Calcite.....	97
3.	Biotite.....	104
4.	Phlogopite.....	114
5.	Muscovite.....	121
F.	Powder/Pellet Samples.....	131
1.	Gypsum.....	135
2.	Pyrolusite.....	153
3.	Alabama Limonite.....	162
4.	Kaolin.....	166
5.	Illite.....	170
6.	Colemanite.....	174
7.	Kernite.....	178
8.	Wavellite.....	182
9.	Montmorillonite.....	186
10.	Vermiculite.....	190
11.	Chalcedony.....	191
G.	Diesel Fuel.....	191
H.	ZnCl ₂ /H ₂ O Solutions and H ₃ PO ₄ /H ₂ O Solutions.....	197
J.	Complex Refractive Indices of Water.....	216
VI.	References.....	363

LIST OF ILLUSTRATIONS

Figure A1.	A block diagram of the reflectometer-spectropho- tometer and data acquisition system for measuring the reflectance of the aqueous solutions.....	8
Optical Properties of Gypsum		
Figure 1.	Real part of the complex dielectric function for the 8T gypsum pellet.....	23
Figure 2.	Real part of the composite dielectric function; $\alpha=0.40$, $\beta=0.21$, $\gamma=0.39$	24
Figure 3.	Imaginary part of the complex dielectric function for the 8T gypsum pellet.....	25
Figure 4.	Imaginary part of the composite dielectric function; $\alpha=0.40$, $\beta=0.21$, $\gamma=0.39$	26
Infrared Optical Properties of Gypsum		
Figure 1.	Crystallographic axes of gypsum.....	40
Figure 2.	Optical directions and crystallographic axes of gypsum.....	43
Figure 3.	Relative reflectance of gypsum - X direction.....	51
Figure 4.	Relative reflectance of gypsum - Y direction.....	52
Figure 5.	Relative reflectance of gypsum - Z direction.....	53
Figure 6.	Relative reflectance of gypsum - powder.....	54
Figure 7.	Index of refraction of gypsum - X direction.....	60
Figure 8.	Index of refraction of gypsum - Y direction.....	61
Figure 9.	Index of refraction of gypsum - Z direction.....	62

Figure 10.	Index of refraction of gypsum - powder.....	63
Figure 11.	Extinction coefficient of gypsum - X direction.....	64
Figure 12.	Extinction coefficient of gypsum - Y direction.....	65
Figure 13.	Extinction coefficient of gypsum - Z direction.....	66
Figure 14.	Extinction coefficient of gypsum - powder.....	67
Figure 15.	Real dielectric function of gypsum - X direction.....	69
Figure 16.	Real dielectric function of gypsum - Y direction.....	70
Figure 17.	Real dielectric function of gypsum - Z direction.....	71
Figure 18.	Real dielectric function of gypsum - powder.....	72
Figure 19.	Imaginary dielectric function of gypsum - X direction.....	73
Figure 20.	Imaginary dielectric function of gypsum - Y direction.....	74
Figure 21.	Imaginary dielectric function of gypsum - Z direction.....	75
Figure 22.	Imaginary dielectric function of gypsum - powder.....	76
Figure 23.	Real composite dielectric function of gypsum.....	84
Figure 24.	Real dielectric function of gypsum - powder.....	85
Figure 25.	Imaginary composite dielectric function of gypsum.....	86
Figure 26.	Imaginary dielectric function of gypsum - powder.....	87
Rutile		
Figure E1-1.	Reflectance spectrum of rutile (O-ray) in the 180-4,000 cm^{-1} wave number region.....	94
Figure E1-2.	Index of refraction n of rutile (O-ray) in the 180-4,000 cm^{-1} wave-number region.....	95

Figure E1-3.	Extinction coefficient k of rutile (O-ray)	
	in the $180\text{--}4,000\text{ cm}^{-1}$ wave-number region.....	96
Calcite		
Figure E2-1.	Reflectance spectrum of calcite (O-ray)	
	in the $180\text{--}4,000\text{ cm}^{-1}$ wave-number region.....	98
Figure E2-2.	Index of refraction n of calcite (O-ray)	
	in the $180\text{--}4,000\text{ cm}^{-1}$ wave-number region.....	99
Figure E2-3.	Extinction coefficient k of calcite (O-ray)	
	in the $180\text{--}4,000\text{ cm}^{-1}$ wave-number region.....	100
Figure E2-4.	Reflectance spectrum of calcite (E-ray)	
	in the $180\text{--}4,000\text{ cm}^{-1}$ wave number region.....	101
Figure E2-5.	Index of refraction n of calcite (E-ray)	
	in the $180\text{--}4,000\text{ cm}^{-1}$ wave-number region.....	102
Figure E2-6.	Extinction coefficient k of calcite (E-ray)	
	in the $180\text{--}4,000\text{ cm}^{-1}$ wave-number region.....	103
Biotite		
Figure E3-1.	Reflectance spectrum of Biotite a-axis in	
	the $2.5\text{--}33\text{ }\mu\text{m}$ wavelength region.....	105
Figure E3-2.	Index of refraction n of Biotite a-axis in	
	the $2.5\text{--}33\text{ }\mu\text{m}$ wavelength region.....	106
Figure E3-3.	Extinction coefficient k of Biotite a-axis	
	in the $2.5\text{--}33\text{ }\mu\text{m}$ wavelength region.....	107
Figure E3-4.	Reflectance spectrum of Biotite b-axis in	
	the $2.5\text{--}33\text{ }\mu\text{m}$ wavelength region.....	108

Figure E3-5.	Index of refraction of n Biotite b-axis in the 2.5-33 μm wavelength region.....	109
Figure E3-6.	Extinction coefficient k of Biotite b-axis in the 2.5-33 μm wavelength region.....	110
Figure E3-7.	Reflectance spectrum of Biotite c-axis in the 2.5-28 μm wavelength region.....	111
Figure E3-8.	Index of refraction of Biotite c-axis in the 2.5-28 μm wavelength region.....	112
Figure E3-9.	Extinction coefficient k of Biotite c-axis in the 2.5-28 μm wavelength region.....	113
Phlogopite		
Figure E4-1.	Reflectance spectrum of Phlogopite a-axis in the 180-4,000 cm^{-1} wave-number region.....	116
Figure E4-2.	Reflectance spectrum of Phlogopite b-axis in the 180-4,000 cm^{-1} wave-number region.....	117
Figure E4-3.	Reflectance spectrum of Phlogopite c-axis in the 180-4,000 cm^{-1} wave-number region.....	118
Figure E4-4.	Index of refraction n of Phlogopite c-axis in the 180-4,000 cm^{-1} wave-number region.....	119
Figure E4-5.	Extinction coefficient k of Phlogopite c-axis in the 180-4,000 cm^{-1} wave-number region.....	120
Muscovite		
Figure E5-1.	Reflectance spectrum of Muscovite a-axis in the 400-4,000 cm^{-1} wave-number region.....	123

Figure E5-2.	Reflectance spectrum of Muscovite a-axis in the 180-450 cm^{-1} wave-number region.....	124
Figure E5-3.	Reflectance spectrum of Muscovite b-axis in the 400-4,000 cm^{-1} wave-number region.....	125
Figure E5-4.	Reflectance spectrum of Muscovite b-axis in the 180-450 cm^{-1} region.....	126
Figure E5-5.	Reflectance spectrum of Muscovite c-axis in the 400-4,000 cm^{-1} wave-number region.....	127
Figure E5-6.	Reflectance spectrum of Muscovite c-axis in the 180-450 cm^{-1} wave-number region.....	128
Figure E5-7.	Index of refraction n of Muscovite c-axis in the 180-4,000 cm^{-1} wave-number region.....	129
Figure E5-8.	Extinction coefficient k of Muscovite c-axis in the 180-4,000 cm^{-1} wave-number region.....	130
Gypsum		
Figure F1-1.	Reflectance spectra R(8T) and R(14T) of the 8T and 14T gypsum pellets, and ratio reflectance R(8T)/R(14T) in the 180-4,000 cm^{-1} wave-number region.....	136
Figure F1-2.	Index of refraction n of the 14T gypsum pellet in the 180-4,000 cm^{-1} wave-number region.....	138
Figure F1-3.	Extinction coefficient k of the 14T gypsum pellet in the 180-4,000 cm^{-1} wave-number region.....	139
Figure F1-4.	Transmittance spectra of three of the gypsum-powder/KBr pellets in the 300-4,000 cm^{-1} wave-number region.....	140
Figure F1-5.	Absorbance spectra of three of the gypsum-powder/KBr pellets in the 300-4,000 cm^{-1} wave-number region.....	142

- Figure F1-6. Five difference spectra obtained from four absorbance spectra for the gypsum-powder/KBr pellets in the 300-4,000 cm^{-1} wave-number region..... 143
- Figure F1-7. Relative k spectrum for gypsum from the average of three normalized difference spectra of the gypsum-powder/KBr pellets; 300-4,000 cm^{-1} wave-number region..... 146
- Figure F1-8. Relative k spectrum for gypsum from the average of three normalized difference spectra of the gypsum-powder/KBr pellets, expanded ordinate scale; 300-4,000 cm^{-1} wave-number region..... 147
- Figure F1-9. Smoothed fractional standard deviation Dk/k obtained from the three normalized difference spectra; 300-4,000 cm^{-1} wave-number region..... 148
- Figure F1-10. Comparison of k spectra for gypsum obtained from KK analysis (solid line) of the reflectance spectrum of the 8T pellet and from transmittance (dashed line) measurements of the gypsum-powder/KBr pellets, 300-4,000 cm^{-1} region..... 150
- Figure F1-11. Comparison of n spectra for gypsum obtained from KK analysis (solid line) of the reflectance spectrum of the 8T pellet and from application of the fresnel equation (dashed line) to the k spectrum from transmittance measurements and the reflectance spectrum of the pellet; 300-4,000 cm^{-1} region..... 152

Pyrolusite

- Figure F2-1. Reflectance spectrum of the 8T Pyrolusite pellet in 0.2-50 μm wavelength region..... 155
- Figure F2-2. Index of refraction n of the 8T Pyrolusite pellet in the 0.2-50 μm wavelength region..... 156
- Figure F2-3. Extinction coefficient k of the 8T Pyrolusite pellet in the 0.2-50 μm wavelength region..... 157
- Figure F2-4. Reflectance spectra of the 8T and 16T Pyrolusite pellets in the 180-4,000 cm^{-1} wave-number region, (55-2.5 μm)..... 158
- Figure F2-5. Ratio reflectance spectrum $R(8T)/R(16T)$ for Pyrolusite in the 180-4,000 cm^{-1} wave-number region..... 159
- Figure F2-6. Index of refraction n for the 16T Pyrolusite pellet in the 180-4,000 cm^{-1} wave-number region..... 160
- Figure F2-7. Extinction coefficient k for the 16T Pyrolusite pellet in the 180-4,000 cm^{-1} wave-number region..... 161

Limonite

- Figure F3-1. Reflectance spectrum of Alabama Limonite 8T pellet in the 0.2-50 μm wavelength region..... 163
- Figure F3-2. Index of refraction n of the 8T Alabama Limonite pellet in the 0.2-50 μm wavelength region..... 164
- Figure F3-3. Extinction coefficient k of the 8T Alabama Limonite pellet in the 0.2-50 μm wavelength region..... 165

Kaolin

- Figure F4-1. Reflectance spectrum of the 8T Kaolin pellet in the 0.2-50 μm wavelength region..... 167

Figure F4-2.	Index of refraction n of the 8T Kaolin pellet in the 0.2-50 μm wavelength region.....	168
Figure F4-3.	Extinction coefficient k of the 8T Kaolin pellet in the 0.2-50 μm wavelength region.....	169
Illite		
Figure F5-1.	Reflectance spectrum of the 8T Illite pellet in the 0.2-50 μm wavelength region.....	171
Figure F5-2.	Index of refraction n of the 8T Illite pellet in the 0.2-50 μm wavelength region.....	172
Figure F5-3.	Extinction coefficient k of the 8T Illite pellet in the 0.2-50 μm wavelength region.....	173
Colemanite		
Figure F6-1.	Reflectance spectrum of the 8T Colemanite pellet in the 0.2-50 μm wavelength region.....	175
Figure F6-2.	Index of refraction n of the 8T Colemanite pellet in the the 0.2-50 μm wavelength region.....	176
Figure F6-3.	Extinction coefficient k of the 8T Colemanite pellet in the 0.2-50 μm wavelength region.....	177
Kernite		
Figure F7-1.	Reflectance spectrum of the 8T Kernite pellet in the 0.2-50 μm wavelength region.....	179
Figure F7-2.	Index of refraction n of the 8T Kernite pellet in the 0.2-50 μm wavelength region.....	180
Figure F7-3.	Extinction coefficient k of the 8T Kernite pellet in the 0.2-50 μm wavelength region.....	181

Wavellite

- Figure F8-1. Reflectance spectrum of the 8T Wavellite pellet in the 0.2-50 μm wavelength region..... 183
- Figure F8-2. Index of refraction n of the 8T Wavellite pellet in the 0.2-50 μm wavelength region..... 184
- Figure F8-3. Extinction coefficient k of the 8T Wavellite pellet in the 0.2-50 μm Wavellite region..... 185

Montmorillonite

- Figure F9-1. Reflectance spectrum of the 8T Montmorillonite pellet in the 2.5-50 μm wavelength region..... 187
- Figure F9-2. Index of refraction n of the 8T Montmorillonite pellet in the 2.5-50 μm wavelength region..... 188
- Figure F9-3. Extinction coefficient k of the 8T Montmorillonite pellet in the 2.5-50 μm wavelength region..... 189

Chalcedony

- Figure F11-1. Reflectance spectrum of Chalcedony in the 0.2-2.5 μm wave-length region..... 192
- Figure F11-2. Reflectance spectrum Chalcedony in the 180-4,000 cm^{-1} wave-number region (55-2.5 μm)..... 193

Diesel Fuel

- Figure G1. Reflectance spectrum of diesel in the 180-4,000 cm^{-1} wave-number region..... 194
- Figure G2. Index of refraction n of diesel fuel in the 180-4,000 cm^{-1} wave-number region..... 195

Figure	G3. Extinction coefficient k of diesel fuel in the 180-4,000 cm^{-1} wave-number region.....	196
ZnCl ₂ /H ₂ O Solutions		
Figure	H1. Reflectance spectrum of the 20/80% ZnCl ₂ /H ₂ O solution in the 0.2-2.0 μm wavelength region.....	198
Figure	H2. Index of refraction n of the 20/80% ZnCl ₂ /H ₂ O solution in the 0.2-2.0 μm wavelength region.....	199
Figure	H3. Reflectance spectrum of the 30/70% ZnCl ₂ /H ₂ O solution in the 0.2-2.0 μm wavelength region.....	200
Figure	H4. Index of refraction n of the 30/70% ZnCl ₂ /H ₂ O solution in the 0.2-2.0 μm wavelength region.....	201
Figure	H5. Reflectance spectrum of the 40/60% ZnCl ₂ /H ₂ O solution in the 0.2-2.0 μm wavelength region.....	202
Figure	H6. Index of refraction n of the 40/60% ZnCl ₂ /H ₂ O solution in the 0.2-2.0 μm wavelength region.....	203
Figure	H7. Reflectance spectrum of the 50/50% ZnCl ₂ /H ₂ O solution in the 0.2-2.0 μm wavelength region.....	204
Figure	H8. Index of refraction n of the 50/50% ZnCl ₂ /H ₂ O solution in the 0.2-2.0 μm wavelength region.....	205
Figure	H9. Reflectance spectrum of the 65/35% ZnCl ₂ /H ₂ O solution in the 0.2-2.0 μm wavelength region.....	206
Figure	H10. Index of refraction n of the 65/35% ZnCl ₂ /H ₂ O solution in the 0.2-2.0 μm wavelength region.....	207
Figure	H11. Reflectance spectrum of the 75/25% ZnCl ₂ /H ₂ O solution in the 0.2-2.0 μm wavelength region.....	208

Figure H12. Index of refraction of the 75/25% $\text{ZnCl}_2/\text{H}_2\text{O}$ solution in the 0.2-2.0 μm wavelength region.....	209
--	-----

$\text{H}_3\text{PO}_4/\text{H}_2\text{O}$ Solutions

Figure H13. Reflectance spectra of the 05/95, 10/90, and 20/80% $\text{H}_3\text{PO}_4/\text{H}_2\text{O}$ solutions in the 2,500-50,000 cm^{-1} wave-number region.....	210
---	-----

Figure H14. Index of refraction n of the 05/95, 10/90, and 20/80% $\text{H}_3\text{PO}_4/\text{H}_2\text{O}$ solution in the 2,500-50,000 cm^{-1} wave-number region.....	211
--	-----

Figure H15. Reflectance spectra of the 40/60, 50/50, and 65/35% $\text{H}_3\text{PO}_4/\text{H}_2\text{O}$ solutions in the 2,500-50,000 cm^{-1} wave-number region.....	212
---	-----

Figure H16. Index of refraction n of the 40/60, 50/50, and 65/35% $\text{H}_3\text{PO}_4/\text{H}_2\text{O}$ solutions in the 2,500-50,000 cm^{-1} wave-number region.....	213
---	-----

Figure H17. Reflectance spectra of the 75/25 and 85/15% $\text{H}_3\text{PO}_4/\text{H}_2\text{O}$ solutions in the 2,500-50,000 cm^{-1} wave-number region.....	214
---	-----

Figure H18. Index of refraction n of the 75/25 and 85/15% $\text{H}_3\text{PO}_4/\text{H}_2\text{O}$ solutions in the 300-50,000 cm^{-1} wave-number region.....	215
---	-----

The Complex Refractive Index of Water

Figure 1. The absorption spectrum in the region of adjustment...	240
Figure 2. Detail of Figure 1.....	241
Figure 3. The entire absorption spectrum.....	242
Figure 4. The value of the sum rule integral.....	243

Figure	5. An illustration of increased resolution by reducing the range of integration.....	301
Figure	6. The spectrum calculated for the range 0 to 5×10^{-1} cm^{-1}	302
Figure	7. The spectrum calculated for the range 0 to 5×10^0 cm^{-1}	303
Figure	8. The spectrum calculated for the range 0 to $5 \times 10^{+1}$ cm^{-1}	304
Figure	9. The spectrum calculated for the range 0 to 5×10^2 cm^{-1}	305
Figure	10. The spectrum calculated for the range 0 to 5×10^3 cm^{-1}	306
Figure	11. The spectrum calculated for the range 0 to 5×10^4 cm^{-1}	307
Figure	12. The spectrum calculated for the range 0 to 5×10^5 cm^{-1}	308
Figure	13. The spectrum calculated for the range 0 to 5×10^6 cm^{-1}	309
Figure	14. An illustration of inaccuracy as an endpoint is approached.....	310
Figure	15. Fitting low frequency results.....	311
Figure	16. The transition in the region of 0.1 cm^{-1}	312
Figure	17. The transition in the region of 1.0 cm^{-1}	313
Figure	18. The transition in the region of 10 cm^{-1}	314
Figure	19. The transition in the region of 100 cm^{-1}	315

Figure	20. The transition in the region of $1,000\text{ cm}^{-1}$	316
Figure	21. The transition in the region of $10,000\text{ cm}^{-1}$	317
Figure	22. The transition in the region of $100,000\text{ cm}^{-1}$	318
Figure	23. The final spectrum from 0 to 10^{-1} cm^{-1}	349
Figure	24. The final spectrum from 0 to 10^0 cm^{-1}	350
Figure	25. The final spectrum from 0 to 10^1 cm^{-1}	351
Figure	26. The final spectrum from 0 to 10^2 cm^{-1}	352
Figure	27. The final spectrum from 0 to 10^3 cm^{-1}	353
Figure	28. The final spectrum from 0 to 10^4 cm^{-1}	354
Figure	29. The final spectrum from 0 to 10^5 cm^{-1}	355
Figure	30. The final spectrum from 0 to 10^6 cm^{-1}	356

LIST OF TABLES

Table I.	Materials for which reflectance spectra and or complex refractive indices were obtained during this contract.....	2
Table II.	Mineral specimens used for these investigations.....	3
Table III.	Chemical composition of minerals.....	4
Table IV.	Uncertainties in N from uncertainty in values of R, θ , and ϕ	18
Table V.	Data for natural minerals pressed into pellets.....	132

I. Statement of Research Problem

Research conducted during the term of this contract was measurement of reflectance spectra $R(\nu)$ in the uv, visible, and/or infrared for selected liquids and solids; computational analysis of the measured spectra to obtain spectral values of the complex refractive indices $N(\nu) = n(\nu) + ik(\nu)$ of those materials, and further analysis of the spectra in terms of fundamental intra- and inter-molecular vibrational modes.

II. Summary of Most Important Results

The most significant accomplishments of this project were determination of spectral values of $N(\nu)$ of natural and man made aerosol/obscurant materials and providing these values of $N(\nu)$ to scientists at the Aberdeen Proving Ground, Md. We determined and sent to the Aberdeen Proving Ground values of $N(\nu)$ for the materials listed in Tables I-III. Tabulations of these values of $N(\nu)$ can be obtained from Aerosol/Obscuration Sciences, DRDAR-CLB-PS, Aberdeen Proving Ground, Md. 21010.

Current knowledge of the manner in which electromagnetic radiation propagates through aerosol clouds is based primarily on Mie-scattering computations. Such computations are possible only when there is prior knowledge of $N(\nu)$ for the aerosol. The values of $N(\nu)$ obtained during the term of this contract are now used for Mie-scattering computations by scientists at several U.S. Army Laboratories and by many DOD contractors.

TABLE I. Materials for which reflectance spectra $R(\nu)$ and complex refractive indices $N(\nu)$ were obtained during the term of contract DAAG-29-79-C-0131.

Material	Form	$R(\nu)$ Spectral Region	$N(\nu)$ Spectral Region
Gypsum X	Crystal (010)	0.2 - 55 μm	2.5 - 52 μm
Gypsum Y	Crystal	0.2 - 55	2.5 - 52
Gypsum Z	Crystal (010)	0.2 - 55	2.5 - 52
Biotite A	Crystal (010)	2.5 - 55	2.5 - 33
Biotite B	Crystal (100)	2.5 - 55	2.5 - 33
Biotite C	Crystal (010)	2.5 - 55	2.5 - 28
Rutile O	Crystal	2.5 - 55	2.5 - 55
Philogopite A	Crystal (001)	2.5 - 55	-
Philogopite B	Crystal (001)	2.5 - 55	-
Philogopite C	Crystal (100)	0.25 - 55	2.5 - 25
Muscovite A	Crystal (001)	2.5 - 55	-
Muscovite B	Crystal (001)	2.5 - 55	-
Muscovite C	Crystal (010)	2.5 - 55	2.5 - 25
Calcite O	Crystal	2.5 - 55	2.5 - 54
Calcite E	Crystal	2.5 - 55	-
Gypsum	Pellet 8T	0.2 - 55	2.5 - 52
Montmorillonite	Pellet 8T	2.5 - 55	2.5 - 55
Ga. Limonite	Pellet 8T	0.2 - 55	-
Al. Limonite	Pellet 8T	0.2 - 55	0.2 - 54
Kaolin	Pellet 8T	0.2 - 55	0.25 - 54
Illite	Pellet 8T	0.2 - 55	0.20 - 54
Colemanite	Pellet 8T	0.2 - 55	0.21 - 43.8
Pyrolusite	Pellet 8T	0.2 - 55	0.2 - 54
Kernite	Pellet 8T	0.2 - 55	0.32 - 54
Cn. Vermiculite	Pellet 3T	2.5 - 55	-
Id. Vermiculite	Pellet 3T	2.5 - 55	-
Wavellite	Pellet 8T	0.2 - 55	0.3 - 54
Chalcedony	Solid	0.2 - 55	-
Diesel Fuel	Liquid	2.5 - 55	2.5 - 55
20% ZnC ₂ /H ₂ O	Liquid	0.2 - 2.0	0.2 - 2
30% ZnC ₂ /H ₂ O	Liquid	0.2 - 2.0	0.2 - 2
50% ZnC ₂ /H ₂ O	Liquid	0.2 - 2.0	0.2 - 2
65% ZnC ₂ /H ₂ O	Liquid	0.2 - 2.0	0.2 - 2
75% ZnC ₂ /H ₂ O	Liquid	0.2 - 2.0	0.2 - 2
5% H ₃ PO ₄ /H ₂ O	Liquid	0.2 - 2.0	0.2 - 2
10% H ₃ PO ₄ /H ₂ O	Liquid	0.2 - 2.0	0.2 - 2
20% H ₃ PO ₄ /H ₂ O	Liquid	0.2 - 2.0	0.2 - 2
40% H ₃ PO ₄ /H ₂ O	Liquid	0.2 - 2.0	0.2 - 2
50% H ₃ PO ₄ /H ₂ O	Liquid	0.2 - 2.0	0.2 - 2
65% H ₃ PO ₄ /H ₂ O	Liquid	0.2 - 2.0	0.2 - 2
75% H ₃ PO ₄ /H ₂ O	Liquid	0.2 - 2.0	0.2 - 2
85% H ₃ PO ₄ /H ₂ O	Liquid	0.2 - 2.0	0.2 - 2
Water	Liquid		

TABLE II. Mineral Specimens used during this Investigation

Mineral	Source	Cat. No.
Gypsum	R. Coveney	
Biotite	R. Coveney	
Phlogopite	R. Coveney	
Muscovite	R. Coveney	
Calcite	R. Coveney	
Montmorillonite	*Ward's (Wyoming)	46W 0439 LS
Limonite	Ward's (Alabama)	46W 4684 LS
Kaolin	Ward's (Georgia)	46W 4334 LS
Illite	Ward's (N.Y.)	46W 0319 LS
Colemanite	Ward's (California)	46W 2144 LS
Pyrolusite	Ward's (Brazil)	64W 6424 LS
Kernite	Ward's (California)	46W 4364 LS
Vermiculite	Ward's (CN & Idaho)	46W 0829 LS
Wavellite	Ward's (Arkansas)	46W 8724 LS
Chalcedony	Ward's (California)	46W 0050 LS

*Wards Natural Science Establishment, Inc.

P.O. Box 1712, Rochester, NY 14603

TABLE III. Chemical composition of natural minerals investigated during the period of this project

Mineral	Composition	Structure
Gypsum	$\text{Ca SO}_4 \cdot 2\text{H}_2\text{O}$	Monoclinic
Biotite	$\text{K}(\text{Mg}, \text{Fe}^{2+})_{3-1.5}(\text{Al}, \text{Fe}^{3+})_{0-1}(\text{OH}, \text{F})_2/\text{Al}_{1-1.5}\text{Si}_{3-2.5}\text{O}_{10}$	Monoclinic
Phlogopite	$\text{K Mg}_3 (\text{OH}, \text{F})_2/\text{AlSi}_3\text{O}_{10}$	Monoclinic
Muscovite	$\text{K Al}_2[(\text{OH})_2/\text{AlSi}_3\text{O}_{10}]$	Monoclinic
Calcite	Ca CO_3	Trigonal
Montmorillonite	$\text{Al}_{1.67}\text{Mg}_{0.33}[(\text{OH})_2/\text{Si}_4\text{O}_{10} \text{ Na}_{0.33}(\text{H}_2\text{O})_4]$	Monoclinic
Limonite	$\text{FeO} \cdot \text{OH} \cdot n\text{H}_2\text{O}$	Amorphous
Kaolin	$\text{Al}_4\text{Si}_4\text{O}_{10}(\text{OH})_8$	Triclinic
Illite	hydromuscovite	
Colemanite	$\text{Ca}[\text{B}_3\text{O}_4(\text{OH})_3] \cdot \text{H}_2\text{O}$	Monoclinic
Pyrolusite	MnO_2	Tetragonal
Kernite	$\text{Na}_2[\text{B}_4\text{O}_6(\text{OH})_2] \cdot 3\text{H}_2\text{O}$	Monoclinic
Vermiculite	$(\text{Mg}, \text{Fe}^{3+}, \text{Al})_3[(\text{OH})_2/\text{Al}_{>1}\text{Si}_3\text{O}_{10}] \cdot \text{Mg}_{0.33}(\text{H}_2\text{O})_4$	Monoclinic
Wavelength	$\text{Al}_3[(\text{OH})_3/(\text{PO}_4)_2] \cdot 5\text{H}_2\text{O}$	Orthorombic
Chalcedony	Fibrous Low quartz	

III. Publications

- M. R. Querry, "Complex refractive indices of selected materials in the infrared," Proceedings of the 1979 CSL Scientific Conference on Obscuration and Aerosol Research," Dec 1980, pp. 363-374.
- M. R. Querry, "Complex refractive indices of selected materials in the infrared," Proceedings of the 1980 CSL Scientific Conference on Obscuration and Aerosol Research," In Press, Proceedings have not been released.
- M. R. Querry, "Complex refractive indices of Liquids & Powders," Proceedings of the 1981 CSL Scientific Conference on Obscuration and Aerosol Research, In Press, Proceedings have not been released.
- M. R. Querry & R. L. Strecker, "Optical Properties of Gypsum," Proceedings of The 1982 CSL Scientific Conference on Obscuration and Aerosol Research, In Press, Proceedings have not been released.
- D. J. Segelstein, "The Complex refractive index of Water," M.S. Thesis, University of Missouri-K.C., 1981, 167 pages.
- R. L. Strecker, "Infrared optical properties of gypsum," M.S. Thesis, University of Missouri-K.C., 1982, 83 pages.

IV. Personnel Employed on the Project

Name	Position	Degrees Received
Marvin R. Querry, Ph.D.	Principal Investigator	None
Raymond Coveney, Jr., Ph.D.	Mineralogist	None
Terrence Heese, B.S.	Research Assistant	None
Thomas Hogan, B.S.	Grad. Research Assistant	M.S.
David Segelstein, B.S.	Grad. Research Assistant	M.S.
Richard Strecker, B.S.	Grad. Research Assistant	M.S.
Jan Ben,	Undergraduate Assistant	None

V. Report of Research

A. Experimental Methods

One purpose of the research conducted during the term of DAAG-29-79-C-0131 was to measure the reflectance spectra of selected liquids, crystals, and powdered materials which were pressed into pellets. In this section we present the methods for measuring reflectance spectra.

1. Methods for Acquiring Reflectance Spectra of Aqueous Solutions

Reflectance spectra of aqueous solutions of ZnCl_2 and H_3PO_4 were measured in the 0.2 - 2 μm wavelength region. This constituted an extension of our previous investigations of the reflectance spectra of those solutions in the infrared region.

A block diagram of the reflectometer and data acquisition system used to measure the reflectance spectra of the aqueous solutions is shown in Fig. A1. Radiant flux from a light source G was chopped at C and was then focussed by an f/5 optical system, consisting of plane mirror M_1 and spherical mirror M_2 on the surface of the sample S. The angle of incidence θ was 6.2 degrees for the central ray from M_2 incident on the surface S. Radiant flux reflected from S was imaged by an identical optical system (M_3 and M_4) on the entrance slit of a Perkin-Elmer Ebert double-pass grating monochromator. The entrance slits were manually adjusted to assure spectral resolution $\nu/\Delta\nu$ of 100 or better. After passage through the monochromator, the radiant flux was optically filtered to remove higher diffraction orders,

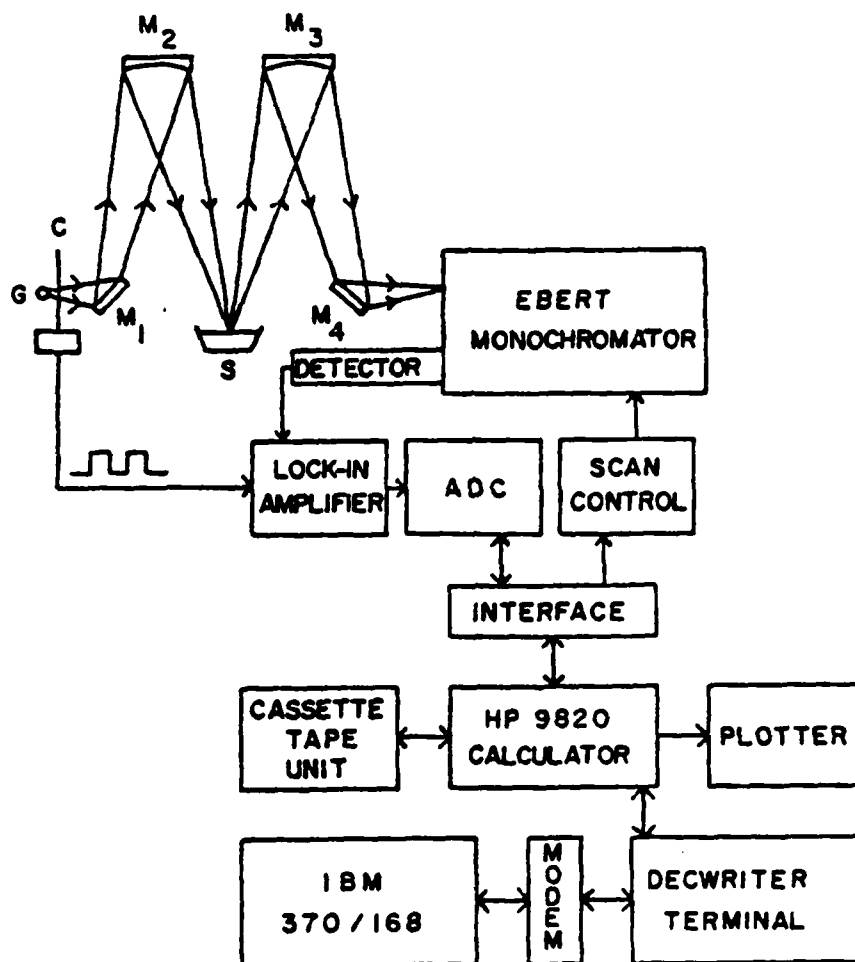


Figure 1. A block diagram of the reflectometer-spectrophotometer and data acquisition system.

and was then focussed on either a InSb or photomultiplier detector. The signal from the detector was synchronously processed by a Princeton Applied Research (PAR) model 124 lock-in amplifier. The analog output signal from the Model 124 was applied to the input of a PAR model 260 analog-to-digital converter (ADC) which both digitized the signal and inserted an index corresponding to the spectral position of the monochromator.

In order to facilitate data acquisition and analysis the system described above was interfaced to a Hewlett-Packard (HP) Model 9820A programmable calculator equipped with an HP 9862A plotter and an HP11223A magnetic cassette tape unit. This entire system was then interfaced through a decwriter LA-36 terminal to either an Amdahl 470 or VAX 11/780 computer which was used for the subsequent Kramers-Kronig analysis of the reflectance data.

During this investigation of the liquids we measured relative specular reflectance $R(v) = R_s(v)/R_w(v)$, where s denotes the sample and w denotes the water standard. Prior to use the water standard was purified, deionized, and filtered through a 0.2 μm Millipore filter. Aqueous solutions were prepared using purified water and reagent grade chemicals. The aqueous solutions and purified water were placed in separate petri dishes which served as sample holders. Each dish was filled to precisely the same level as determined by use of a cathetometer. The levels of all samples were monitored

routinely during data collection and purified water was added to the samples as needed to compensate for evaporation. Each sample was also stirred thoroughly at the beginning of a spectral scan to assure isotropic homogeneity. Data were acquired at 200 equally spaced wavelength positions in each of the wavelength regions 0.2-0.3, 0.3-0.4, 0.4-0.6, 0.6-0.8, 0.8-1.0, 1.0-1.5, and 1.5-2 μm .

All spectra were obtained with the samples at about 27°C. The reflectance spectra $R(\nu)$ were converted from wavelength to wave number and then plotted either by the HP9862A, a Tektronix graphics terminal, or by a calcomp plotter. The standard deviations, based on three independent measurements, were generally $\pm 0.03 R(\nu)$.

2. Methods for Acquiring Reflectance Spectra of Crystals.

Reflectance spectra for optically uniaxial crystalline Calcite and Rutile, and for optically biaxial crystalline Gypsum, Biotite, Phlogopite, and Muscovite were obtained during the term of this contract.

A Perkin-Elmer Model 580 B dual beam infrared spectrophotometer with a common beam wire grid polarizer and a Perkin-Elmer combination 3x beam condenser and specular reflectance accessory were used to obtain the reflectance spectra in the 180-4,000 cm^{-1} (55-2.5 μm) spectral region. The common beam wire grid polarizer was on a KBr substrate and thus was used only in the 400-4,000 cm^{-1} region. This type of polarizer

characteristically passes about 5% of the undesired polarization component so a second wire grid (KBr) polarizer was mounted in the sample beam for measurements in the $400\text{--}4,000\text{ cm}^{-1}$ region. A single wire grid polarizer on a polyethylene substrate was mounted in the sample beam for measurements in the $180\text{--}400\text{ cm}^{-1}$ region. The reflectance accessory provided a convergent beam incident on the sample with the central ray incident at 6.5° and the total included angle of the convergent beam was approximately 10° . All spectra were acquired with the spectrophotometer operating in the transmission mode.

The procedure was to acquire a minimum of three scans each for an aluminum reference mirror, the crystalline sample, and the zero with the sample beam blocked by a shutter. The spectra were digitized at 1 cm^{-1} intervals and stored on floppy discs. The three scans each for the reference mirror, sample, and zero were averaged. The averaged zero was subtracted from the averaged reference mirror and sample spectra and the ratio of the resultant sample spectrum to the resultant reference mirror spectrum provided the reflectance of the sample relative to the reflectance of the mirror. The relative reflectance spectrum was then multiplied by the reflectance of the reference mirror to obtain the absolute reflectance spectrum of the sample. The fractional uncertainty in the absolute reflectance was about $0.025 R(\nu)$.

The crystalline samples were oriented so that all measurements were made for the electric vector of the incident

radiant flux perpendicular to the plane of incidence and parallel to the desired optical direction of the crystal. This required rotating the crystals rather than the polarizers.

The Perkin-Elmer E-system spectrophotometer and data acquisition system described in Section VA1 (see Fig. A1) was used in the $4,000\text{--}40,000\text{ cm}^{-1}$ ($2.5\text{--}0.25\text{ }\mu\text{m}$) region to acquire the reflectance spectra of the crystalline samples. However, the Perkin-Elmer combined 3x beam condenser and specular reflectance accessory, also used with the PE-580B, was installed just prior to the entrance slit of the E-system monochromator, and the sample S denoted in Fig. A1 was replaced by a first surface aluminum mirror. Additionally, a calcite polarizer was placed between the exit slit of the monochromator and the detector. The procedures for acquiring the initial spectra for the reference mirror, the sample, and the zero, and for obtaining the absolute reflectance of the sample were similar to those used with the PE-580B. Initial spectra were acquired at 200 equally spaced wavelength positions in each of the wavelength regions 0.2-0.3, 0.3-0.4, 0.4-0.6, 0.6-0.8, 0.8-1.0, 1.0-1.5, 1.5-2.0, 2.0-3.0 μm . The calcite polarizer cuts off at about 0.25 μm .

3. Methods for Acquiring Reflectance Spectra for Pellets

Many natural mineral materials occur in nature only as powder materials or in forms that prevent one from preparing bulk crystalline samples suitable for specular reflectance measurements. The clay minerals are examples of such

materials. In order to obtain reflectance spectra of such materials they were reduced to powder by grinding and the powder was then formed into a 13 mm diameter pellet by loading the powder in a die between polished stainless steel rams and pressing the powder with a hydraulic press. Materials for which pellets were prepared were Gypsum, Montmorillonite, Ga. Limonite, Al. Limonite, Kaolin, Illite, Colemanite, Pyrolusite, Kernite, Cn. Vermiculite, Id. Vermiculite and Wavellite. The procedure for obtaining the initial spectra and absolute reflectance spectra of the pellets was similar to those for the crystalline samples except the polarizers were not used when obtaining reflectance spectra of the pellets.

4. Methods for Acquiring Reflectance Spectra of Diesel Fuel

The PE-580B spectrophotometer and a Barnes reflectance accessory modified for use with liquids was used to acquire spectra in the 180-4,000 cm^{-1} region for Diesel Fuel. The reflectance of the Diesel Fuel was measured relative to a first surface Aluminum mirror. A cathetometer was used to insure that the surface of the reference mirror and the Diesel Fuel were the same when each was separately placed in the reflectance unit. The modified reflectance unit is housed in a small plexiglas box. The box was equipped with entrance and exit windows of KBr in the 400-4,000 cm^{-1} region and of polyethylene in the 180-400 cm^{-1} region. The plexiglas box was separately and continually purged with dry CO_2 -free air to eliminate absorption spectra of diesel-fuel vapor.

The procedures for acquiring the initial reference mirror, Diesel Fuel, and zero spectra and the absolute reflectance spectrum of the Diesel Fuel were similar to those described in Section VA2.

B. Theoretical Methods

The reflectance spectra $R(\nu)$ were analyzed by use of causal Fourier transform dispersion relations and algorithms based on the Fresnel reflectivity equations to obtain $N(\nu)$ the complex refractive index. The Fourier transform dispersion relations are equivalent to Kramers-Kronig methods but require much less computer time when digital fast Fourier transforms are used rather than the numerical integration techniques required for conventional Kramers-Kronig methods.

If one measures $R(\nu)$ for a material over a broad spectral region then the modulus $\rho(\nu)$ of the complex reflectivity $\rho(\nu)\exp[i\phi(\nu)]$ is the square root of $R(\nu)$. The dispersion relation provides a means for computing the phase shift spectrum $\phi(\nu)$ by use of the $\rho(\nu)$ spectrum. The dispersion relation is

$$\phi(\omega_0) = \frac{1}{2\pi} \left\{ \int_{-\infty}^0 K(t) e^{i\omega_0 t} dt - \int_0^{\infty} K(t) e^{i\omega_0 t} dt \right\}, \quad (1)$$

where

$$K(t) = \int_{-\infty}^{+\infty} \text{Ln}[\rho(\omega)] e^{-i\omega t} d\omega. \quad (2)$$

The angular frequency ω is $2\pi\nu c$ where ν is wave number in units of cm^{-1} and c is the speed of light in vacuum.

In theory $\rho(\omega) = \rho(-\omega)$ must be known throughout the region $-\infty < \omega < \infty$. In practical situations measurements of $\rho(\omega)$ can only be made over some finite spectral region $\omega_1 \leq \omega \leq \omega_2$. One must therefore extend $\rho(\omega)$ into the regions $0 \leq \omega_1$ and $\omega_2 < \omega < \infty$ to make ultimate use of the dispersion relation. In these investigations we assigned $\rho(\omega) = \rho(\omega_1)$ in the region $0 \leq \omega < \omega_1$, and $\rho(\omega) = \rho(\omega_2)$ in the region $\omega_2 < \omega < \infty$. Our experience shows that in most cases such assignments of $\rho(\omega)$ introduces error in $\phi(\omega_0)$ predominantly in spectral regions nearer the end points ω_1 and ω_2 of the measured spectrum.

The Fresnel reflectivity equation for the component of the incident radiant flux linearly polarized with the electric vector perpendicular to the plane of incidence (s-polarization) is

$$\rho_s(\nu) e^{i\phi_s(\nu)} = [Z(\nu) - \cos\theta] / [Z(\nu) + \cos\theta] \quad (3)$$

where

$$Z^2(\nu) = N^2(\nu) - \sin^2\theta \quad (4)$$

$N(\nu) = n(\nu) + ik(\nu)$ is the complex refractive index, and θ is the angle of incidence. Denoting the left-hand side of Eq. (3) as $r_s(\nu)$ and solving Eq. (3) for $Z(\nu)$ one obtains

$$Z(\nu) = \cos\theta [1 + r_s(\nu)]/[1 - r_s(\nu)]. \quad (5)$$

Thus, $N(\nu)$ is determined by applying Eqs. (1) and (2) to $\rho(\nu)$ the square root of $R(\nu)$, compute $Z(\nu)$ by use of Eq. (5), and then compute $N(\nu)$ by use of Eq. (4). This was the procedure used to determine $N(\nu)$ for the materials investigated during the term of this contract.

The complex dielectric function $\epsilon(\nu)$ of the non magnetic materials investigated is given by

$$\begin{aligned} \epsilon(\nu) &= N^2(\nu) \\ &= Z^2(\nu) + \sin^2\theta. \end{aligned} \quad (6)$$

C. Uncertainties in $N(\nu)$

It is important to know what uncertainties in $N(\nu)$ can be expected from uncertainties in the measured reflectance $R(\nu)$, the measured angle of incidence θ , and the phase shift $\phi(\nu)$ determined by use of Eqn. (1). Solving Eqs. (4) and (5) for $N(\nu)$ provides

$$N^2 = \sin^2\theta + \cos^2\theta (1 + r)^2/(1 - r)^2 \quad (7)$$

where subscript s and explicit functional dependence on ν have been suppressed. Differentials of Eqn. (7) provide the means for computing uncertainties in N . We find

$$\frac{\Delta N}{\Delta \theta} = - \frac{4r \sin \theta \cos \theta}{N(1-r)^2}, \quad (8)$$

$$\frac{\Delta N}{(\Delta R/R)} = \frac{r(1+r) \cos^2 \theta}{N(1-r)^3}, \text{ and} \quad (9)$$

$$\frac{\Delta N}{\Delta \phi} = \frac{12r(1+r) \cos^2 \theta}{N(1-r)^3}. \quad (10)$$

Or we could write

$$\Delta N = \frac{r(1+r) \cos^2 \theta}{N(1-r)^3} \left\{ \frac{4(1-r) \tan \theta \Delta \theta}{(1+r)} + \frac{\Delta R}{R} + 12 \Delta \phi \right\} \quad (11)$$

We computed $\Delta N/\Delta \theta$, $\Delta N/(\Delta R/R)$, and $\Delta N/\Delta \phi$ with $\theta = 6.5$ deg. and for n ranging from 1.3 to 1.6 and k ranging from 0.01 to 3.0. Results of these computations are presented in Table IV. Columns 1 and 2 of Table IV are values of $N = n + ik$. Columns 3 and 4 are $\Delta N/\Delta \theta$, columns 5 and 6 are $\Delta N/(\Delta R/R)$, and columns 7 and 8 are $\Delta N/\Delta \phi$. Note that $\Delta N = \Delta n + i \Delta k$. Uncertainties ΔN for a specific set of data would be obtained by appropriately multiplying the entries in Table IV by $\Delta \theta$, $\Delta R/R$, and/or $\Delta \phi$ for that set of data. For example, a typical value for $\Delta R/R$ is 0.025, and all entries in columns 5 and 6 would be multiplied by 0.025 to determine ΔN for this fractional uncertainty in R . As will be seen later in this report, diffuse reflectance from rough pellet surfaces can yield systematic errors in specular reflectance of the order $\Delta R/R = -0.3$ at $4,000 \text{ cm}^{-1}$. Values of $\Delta \theta$ and $\Delta \phi$ used as multiplication factors for columns 3, 4 and 7, 8, respectively, should be in radians. Typical values are $\Delta \theta = 0.01745$ and $\Delta \phi = 0.05236$ corresponding to 1 and 3 degrees, respectively.

TABLE IV. Uncertainties in N for uncertainties in angle $\Delta N/\Delta\theta$,
in reflectance $\Delta N/(\Delta R/R)$, and phase angle $\Delta N/\Delta\phi$.

N		$\Delta N/\Delta\theta$		$\Delta N/(\Delta R/R)$		$\Delta N/\Delta\phi$	
1.300	0.010	-0.060	-0.002	0.173	0.007	-0.013	0.346
1.300	0.030	-0.061	-0.005	0.173	0.020	-0.039	0.345
1.300	0.050	-0.061	-0.009	0.172	0.033	-0.065	0.345
1.300	0.070	-0.061	-0.013	0.172	0.046	-0.091	0.343
1.300	0.090	-0.061	-0.016	0.171	0.059	-0.117	0.342
1.300	0.100	-0.061	-0.018	0.170	0.065	-0.131	0.341
1.300	0.300	-0.065	-0.053	0.150	0.196	-0.392	0.300
1.300	0.500	-0.072	-0.086	0.110	0.327	-0.653	0.219
1.300	0.700	-0.080	-0.116	0.049	0.457	-0.915	0.098
1.300	0.900	-0.089	-0.144	-0.032	0.588	-1.176	0.063
1.300	1.000	-0.093	-0.156	-0.079	0.654	-1.307	0.159
1.300	3.000	-0.134	-0.374	-2.093	1.963	-3.925	4.185
1.400	0.010	-0.078	-0.002	0.241	0.007	-0.014	0.481
1.400	0.030	-0.078	-0.005	0.241	0.021	-0.042	0.481
1.400	0.030	-0.078	-0.009	0.240	0.035	-0.070	0.480
1.400	0.070	-0.078	-0.012	0.240	0.049	-0.098	0.479
1.400	0.090	-0.078	-0.015	0.239	0.063	-0.127	0.477
1.400	0.100	-0.079	-0.017	0.238	0.070	-0.141	0.476
1.400	0.300	-0.082	-0.051	0.218	0.211	-0.422	0.436
1.400	0.500	-0.087	-0.083	0.178	0.352	-0.704	0.355
1.400	0.700	-0.094	-0.112	0.117	0.493	-0.985	0.234
1.400	0.900	-0.102	-0.140	0.036	0.634	-1.267	0.073
1.400	1.000	-0.106	-0.152	-0.012	0.704	-1.408	-0.023
1.400	3.000	-0.145	-0.373	-2.025	2.113	-4.227	-4.049
1.500	0.010	-0.095	-0.002	0.314	0.008	-0.015	0.627
1.500	0.030	-0.095	-0.005	0.313	0.023	-0.045	0.627
1.500	0.050	-0.095	-0.008	0.313	0.038	-0.075	0.626
1.500	0.070	-0.095	-0.012	0.312	0.053	-0.106	0.625
1.500	0.090	-0.095	-0.015	0.312	0.068	-0.136	0.623
1.500	0.100	-0.095	-0.016	0.311	0.075	-0.151	0.622
1.500	0.300	-0.098	-0.049	0.291	0.226	-0.452	0.582
1.500	0.500	-0.103	-0.080	0.251	0.377	-0.754	0.501
1.500	0.700	-0.109	-0.109	0.190	0.528	-1.056	0.380
1.500	0.900	-0.115	-0.136	0.109	0.679	-1.358	0.219
1.500	1.000	-0.118	-0.149	0.061	0.754	-1.509	0.123
1.500	3.000	-0.156	-0.372	-1.952	2.264	-4.529	-3.903
1.600	0.010	-0.111	-0.002	0.392	0.008	-0.016	0.783
1.600	0.030	-0.111	-0.005	0.391	0.024	-0.048	0.783
1.600	0.050	-0.111	-0.008	0.391	0.040	-0.080	0.782
1.600	0.070	-0.111	-0.011	0.391	0.056	-0.113	0.781
1.600	0.090	-0.111	-0.014	0.389	0.072	-0.145	0.779
1.600	0.100	-0.111	-0.016	0.389	0.080	-0.161	0.778
1.600	0.300	-0.114	-0.047	0.369	0.241	-0.483	0.738
1.600	0.500	-0.117	-0.077	0.328	0.402	-0.805	0.657
1.600	0.700	-0.123	-0.106	0.268	0.563	-1.126	0.536
1.600	0.900	-0.128	-0.133	0.187	0.724	-1.449	0.375
1.600	1.000	-0.131	-0.146	0.139	0.805	-1.610	0.279
1.600	3.000	-0.167	-0.371	-0.874	2.415	-4.831	-3.747

D. Gypsum Crystals & Powder

Gypsum is an optically biaxial material that we investigated in crystalline form and pellet form to learn how measurements of reflectance for the pellets compared with measurements of the reflectance for each of the three optical directions X, Y, Z of the crystal. The following two publications provide the preliminary results of those investigations. The first paper is a reprint of an article that appeared in the Proceedings of the 1982 CSL Scientific Conference on Obscuration and Aerosol Research. The second is the M.S. thesis of Mr. Richard Strecker. The thesis presents a more detailed description of the investigations of Gypsum. Only the 8T Gypsum pellet is considered in this Section. Eight tons of force were applied to the 13 mm surface to press the 8T pellet. Additional investigations of Gypsum are presented in Section VF1 of this report.

OPTICAL PROPERTIES OF GYPSUM

M. R. Querry and R. Strecker
Department of Physics
University of Missouri-Kansas City
Kansas City, Missouri 64110

ABSTRACT

Near-normal incidence specular reflectance spectra in the 180-4,000 cm^{-1} spectral region were measured for crystalline Gypsum and for powdered Gypsum that was compressed into a pellet. Complex dielectric functions for the crystal and the pellet were obtained from the reflectance spectra. A composite dielectric function was constructed from the three dielectric functions of the crystal and compared to the dielectric function for the pellet. These investigations were recently extended to the UV-vis-nir (4,000-50,000 cm^{-1}) spectral region.

EXPERIMENTAL METHODS

Gypsum is an optically biaxial (+) crystal with monoclinic prismatic-2/m layered structure and eminent (010) cleavage. The optical directions X,Y,Z are mutually perpendicular with directions X and Z lying in the (010) plane. Two crystalline samples were prepared; one was a (010) cleavage surface, the other was cut perpendicular to (010) and polished. The orientation of the optical directions was determined with light of sodium D wavelengths. A portion of the same crystal was reduced to a powder and was then compressed to form a disc-shaped pellet. The density of the crystal was 2.3 g/cm^3 and was 2.1 g/cm^3 for the pellet.

Near-normal incidence reflectance spectra were measured in the 180-4,000 cm^{-1} spectral region for incident radiant flux linearly polarized parallel to the X,Y, and Z optical directions of the crystal. A similar reflectance spectrum was measured for unpolarized radiant flux incident on the pellet. The spectra were obtained with a Perkin-Elmer 580B Spectrophotometer and specular reflectance accessory.

Spectral values of the complex dielectric functions ϵ_x , ϵ_y , ϵ_z , and ϵ_p were determined from the reflectance spectra by use of Kramers-Kronig (kk) methods.

NORMALIZATION PROCEDURES

The real and imaginary parts of the dielectric-function spectra ϵ_x , ϵ_y , and ϵ_z were normalized according to the following procedure. In the 1,800-2,200 cm^{-1} region where Gypsum has no strong absorption bands, the normalization factors were obtained as simple averages of the ratios

$$R_i = \frac{\text{Re} [\epsilon_p(\nu_i)]}{3} \sum_{k=x}^z 1/\text{Re} [\epsilon_k(\nu_i)] ,$$

$$I_i = \frac{[\text{Im } \epsilon_p(v_i)]}{3} \sum_{k=x}^z 1/\text{Im}[\epsilon_k(v_i)]$$

which were computed at 1 cm^{-1} intervals (401 points). Index k ranges over X, Y, Z ; subscript p denotes pellet; and v denotes wave-number in units of cm^{-1} . The normalization factors were $R = 0.934$ and $I = 0.598$ for the real and imaginary parts, respectively. The normalized dielectric functions $\bar{\epsilon}_x = \text{Re } \epsilon_{xr} + i\epsilon_{xi}$, etc. were then computed throughout the $180\text{--}4,000 \text{ cm}^{-1}$ region.

The normalization factors determined in this region of relatively low absorption show fairly good agreement between $\epsilon_r = n^2 - k^2 = n^2$ for the crystal and the pellet; i.e. $R = 0.938$ is a favorable comparison with 0.913 the ratio of the density of the pellet to that of the crystal. There is poorer agreement, however, between $\epsilon_i = 2nk$ for the pellet and the crystal; i.e. $I = 0.598$ shows the k value for the pellet are about 60% of the k values for the crystal in the $1,800\text{--}2,200 \text{ cm}^{-1}$ region. This is possibly due to multiple reflections by the particles in the pellet.

COMPOSITE DIELECTRIC FUNCTION

A composite dielectric function $\bar{\epsilon}_c$ was constructed from $\bar{\epsilon}_x$, $\bar{\epsilon}_y$, and $\bar{\epsilon}_z$ according to

$$\bar{\epsilon}_c = \alpha \bar{\epsilon}_x + \beta \bar{\epsilon}_y + \gamma \bar{\epsilon}_z,$$

where α, β, γ were adjustable parameters subject to the condition $\alpha + \beta + \gamma = 1$. Parameters α, β, γ were adjusted in 0.05 increments and $\bar{\epsilon}_c$ was tested for a least-squares fit to ϵ_p . There were 231 different combinations of α, β, γ subject to $\alpha + \beta + \gamma = 1$ and incremental adjustments of 0.05. The combination $\alpha = 0.50$, $\beta = 0.10$, and $\gamma = 0.40$ produced the best fit. The poorest fit was given by $\alpha = \gamma = 0.00$ and $\beta = 1.00$. The 231 sets of parameters α, β, γ were then weighted; a weighting factor of 231 for the best fit and successive weighting downward to a factor of one for the poorest fit. The weighted average for the parameters

$$\alpha = 0.40, \beta = 0.21, \gamma = 0.39.$$

The general indication of α, β, γ is that the particles of Gypsum in the pellet are preferentially, but not totally, oriented so the (010) cleavage plane made the greatest contribution to ϵ_p . It is physically reasonable that grinding the Gypsum to produce a powder produced irregularly shaped platelets with (010) cleavage faces. When the Gypsum powder was poured in the die, and when the powder was compressed to form the pellet, the platelets naturally tended toward horizontal alignment; an alignment similar to leaves on the floor of the forest.

We also noted that all spectral features in $\bar{\epsilon}_c$ were also in ϵ_p . Also, there were no spectral features in ϵ_p that were not in $\bar{\epsilon}_c$. Any shifts in spectral features in ϵ_p compared to those in $\bar{\epsilon}_c$ were

quite small. The greatest disagreement between ϵ_c and ϵ_p occurred in the 180-500 cm^{-1} region. This could be due in part to the KK analysis of reflectance spectra that extended only to 180 cm^{-1} , or it could be due to relatively weak, broad, overlapping surface modes in the particles comprising the Gypsum pellet.

UV-VIS-NIR SPECTRA

Similar reflectance spectra were also obtained for the crystal in the 4,000-50,000 cm^{-1} region by use of a Perkin-Elmer E-System Spectrophotometer. Only one spectrum, that for the Y optical direction of the crystal, resembled a true reflectance spectrum. Beyond about 5,000 cm^{-1} the other spectra appear to be multiple reflectance superimposed with a transmittance spectrum. Physically, we attribute this to lower absorption coefficients in the near infrared and visible regions compared to those in the infrared. Lower absorption increases the penetration depth thus allowing for multiple reflections from particles in the pellet, and from successive planes or the back surface of the cleaved sample. The failure of the KK analysis (negative values of k) provided additional proof that the "reflectance" is higher than is physically allowable for first-surface specular reflection.

CONCLUSIONS

From the investigation we concluded that:

- (1) One can obtain a specular reflectance spectrum and subsequent dielectric function for a powder that has been compressed to a density comparable to that of the individual particles of the powder,
- (2) The material must be opaque in the spectral region in which the reflectance spectrum is to be measured,
- (3) The dielectric function of the compressed pellet will contain all the spectral features of the bulk material, and
- (4) The particle constituents of the compressed powder may be preferentially oriented thus predisposing the dielectric function of the pellet to be weighted more to specific orientations of uniaxial or biaxial materials.

Encouraged by this investigation of Gypsum we proceeded to obtain similar reflectance spectra for compressed pellets of Montmorillonite, Limonite, Kaolin, Illite, Colemanite, Pyrolusite, Kernite, Vermiculite, and Wavellite. These spectra are now being reduced to obtain complex refractive indices.

Support provided by the U.S. Army Research Office Contract DAAG-29-79-C-0131.

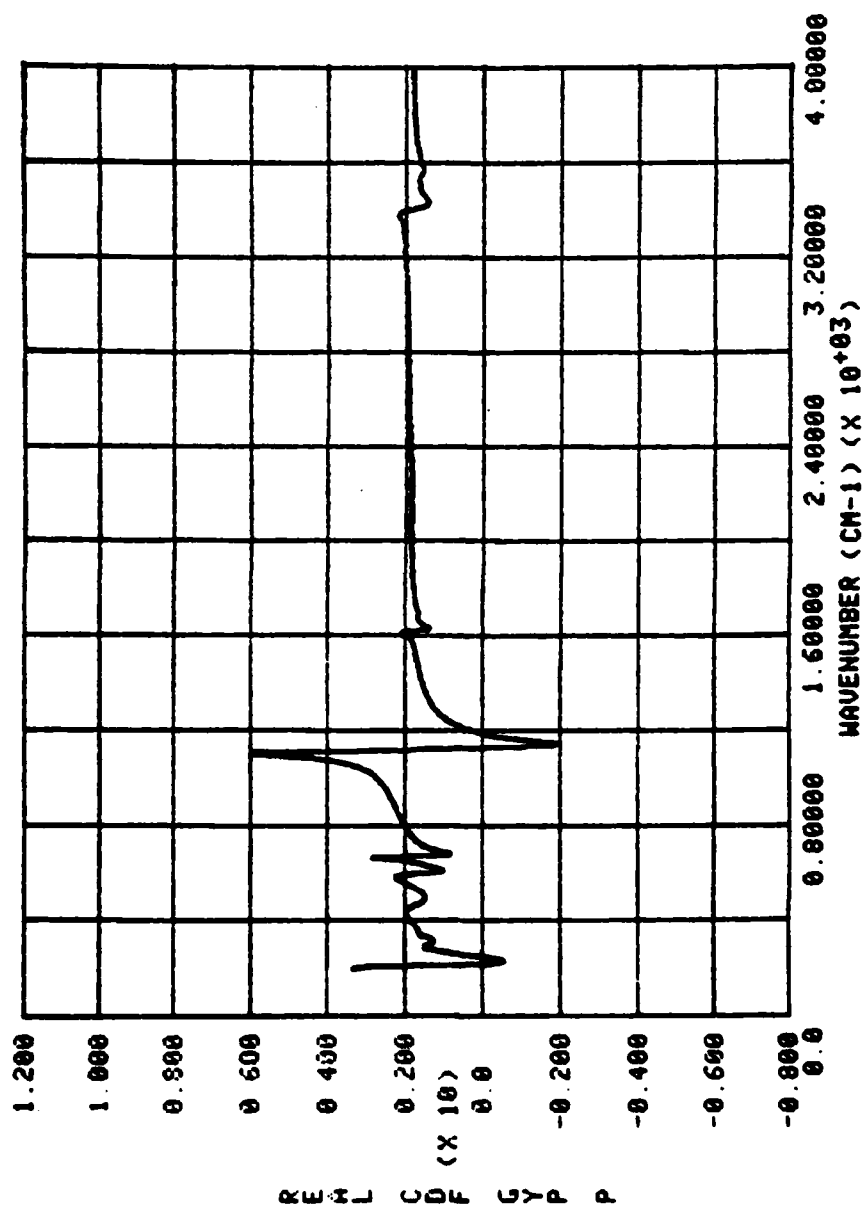


Figure 1. Real part of ϵ_p the complex dielectric function for the gypsum pellet.

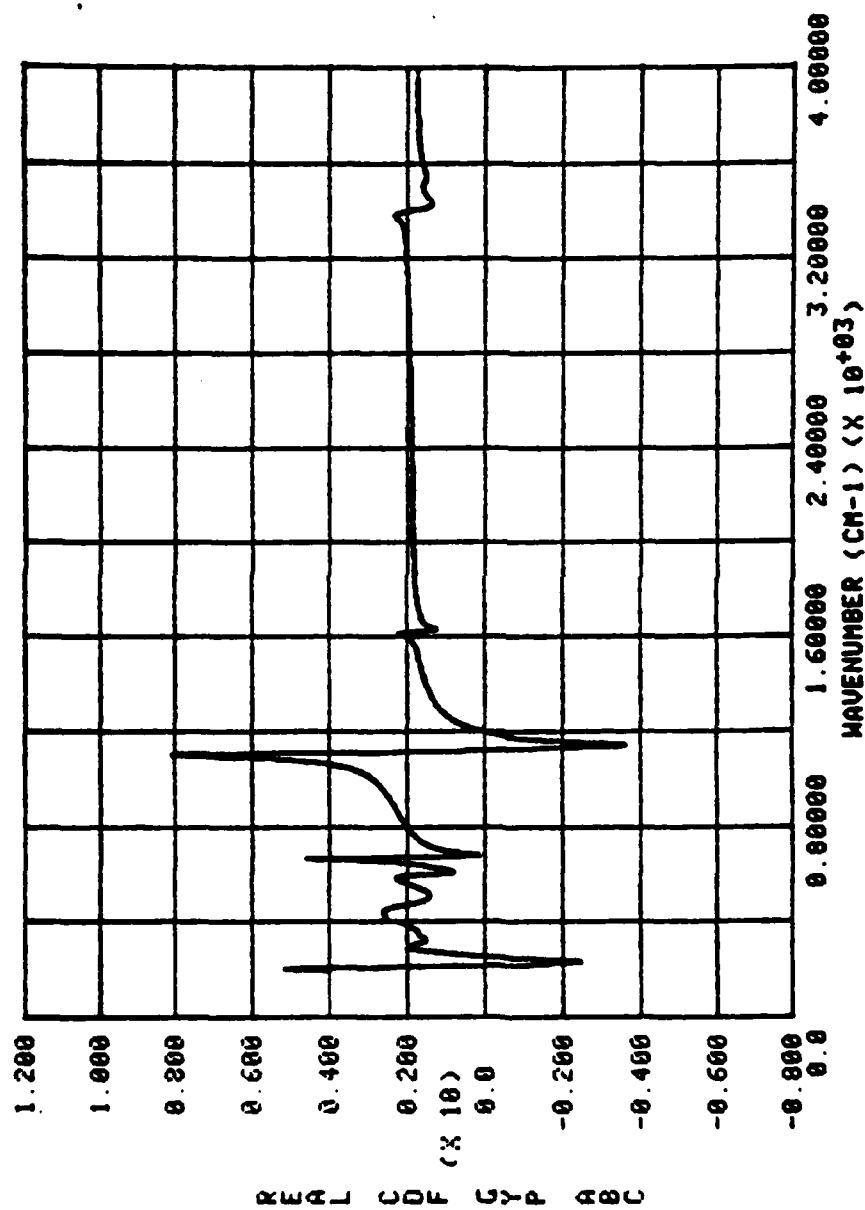


Figure 2. Real part of $\bar{\epsilon}_c$ the composite dielectric function; $\alpha = 0.40$,
 $\beta = 0.21$, and $\gamma = 0.039$.

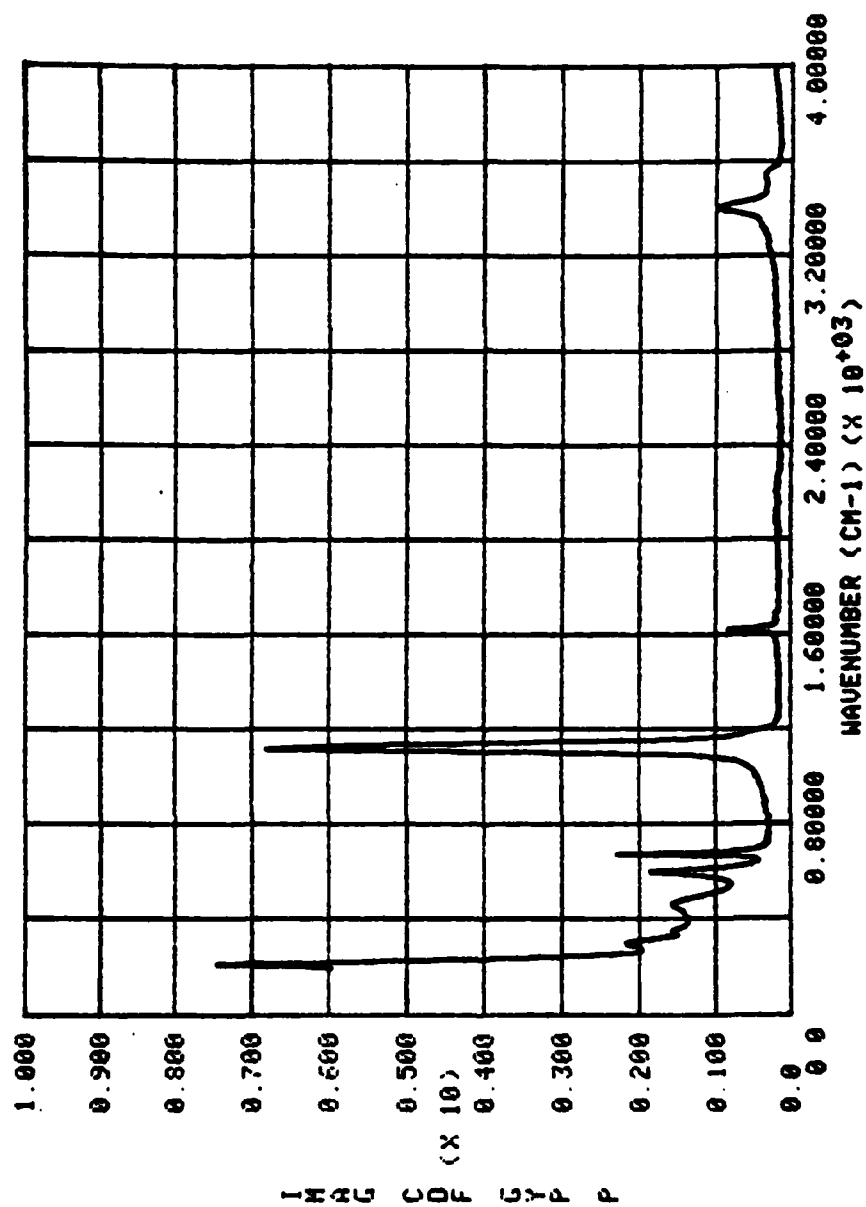


Figure 3. Imaginary part of ϵ_p the complex dielectric function for the gypsum pellet.

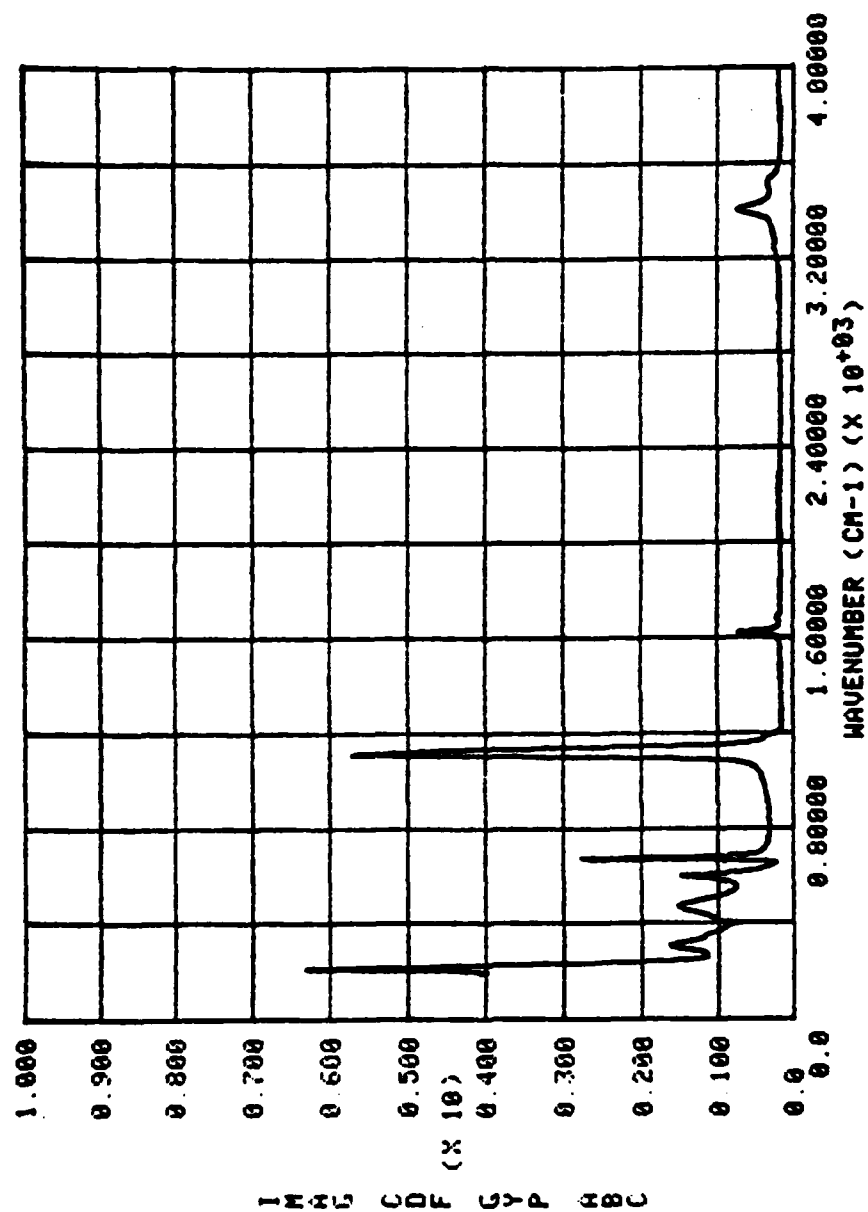


Figure 4. Imaginary part of $\bar{\epsilon}_c$ the composite dielectric functions; $\alpha = 0.40$, $\beta = 0.21$, and $\gamma = 0.39$.

INFRARED OPTICAL PROPERTIES OF GYPSUM

A THESIS IN
Physics

Presented to the Faculty of the University
of Missouri-Kansas City in partial fulfillment of
the requirements for the degree of

MASTER OF SCIENCE

by
RICHARD L. STRECKER

B.A., Benedictine College, 1980

Kansas City, Missouri
1982

INFRARED OPTICAL PROPERTIES OF GYPSUM

Richard L. Strecker, Master of Science
University of Missouri-Kansas City, 1982

ABSTRACT

The optical properties of crystalline and powdered gypsum were studied in the infrared region. Gypsum is an optically biaxial (+) crystal with monoclinic, prismatic-2/m layered structure. It possesses a perfect (010) cleavage and two less distinct cleavages.

Relative reflectance spectra were measured in the 180-4000 cm^{-1} region for radiant flux polarized parallel to each of the three principal optic directions of a crystal gypsum sample. A powder was obtained from the same sample material and compressed to produce a pellet. A relative reflectance spectrum was obtained for this powder sample. The complex index of refraction and the complex dielectric function for each direction and for the powder were obtained using Kramers-Kronig techniques. The four complex dielectric function spectra were normalized and a composite crystal dielectric function was developed using the description

$$\bar{\epsilon}_c(\omega) = A\bar{\epsilon}_x(\omega) + B\bar{\epsilon}_y(\omega) + C\bar{\epsilon}_z(\omega)$$

where c denotes composite, x, y, and z denote the optical directions and A, B, and C are adjustable coefficients. The coefficients were

systematically varied and a fitting routine performed to find the $\bar{\epsilon}_c$ which best agreed with the powder complex dielectric function, $\bar{\epsilon}_p$. The optimum coefficients were determined to be $A = 0.44$, $B = 0.12$, and $C = 0.44$. This result indicates that the powder dielectric function closely resembles the dielectric functions from the XZ plane and implies that the powder surface is predominantly comprised of (010) cleavage platelets.

Normalization factors and the above coefficients were applied to the non-normalized real and imaginary parts of the crystal dielectric functions to obtain a final composite crystal dielectric function. Visual and numerical comparisons of the composite and powder dielectric functions were found to be very satisfactory.

This abstract of about 275 words is approved as to form and content.

Marvin R. Querry, Ph.D.

The undersigned, appointed by the Dean of the School of Graduate Studies, have examined a thesis entitled "Infrared Optical Properties of Gypsum," presented by Richard L. Strecker, candidate for the degree of Master of Science, and hereby certify that in their opinion it is worthy of acceptance.

Marvin R. Querry, Ph.D.
Department of Physics

Date

James M. Phillips, Ph.D.
Department of Physics

Date

John R. Urani, Ph.D.
Department of Physics

Date

TABLE OF CONTENTS

ABSTRACT	ii
LIST OF ILLUSTRATIONS	vi
LIST OF TABLES	viii
ACKNOWLEDGEMENT	ix
Chapter	
I INTRODUCTION	1
II EXPERIMENTAL RESULTS	5
Description of Gypsum ($\text{CaSO}_4 \cdot 2\text{H}_2\text{O}$)	5
Sample Preparation	12
Measurement of Reflectance Spectra	12
III THEORETICAL METHODS	27
Monochromatic Waves in Conducting Media	27
Peterson-Knight Transformations	28
Determination of Complex Refractive Index	30
IV ANALYSIS OF COMPLEX DIELECTRIC FUNCTION	48
Composite Crystal Complex Dielectric Function	48
Computational Methods	65
V CONCLUSION	81
REFERENCES	83
VITA	84

LIST OF ILLUSTRATIONS

Figure

1.	Crystallographic Axes of Gypsum	7
2.	Optical Directions and Crystallographic Axes of Gypsum .	11
3.	Relative Reflectance of Gypsum - X Direction	20
4.	Relative Reflectance of Gypsum - Y Direction	22
5.	Relative Reflectance of Gypsum - Z Direction	24
6.	Relative Reflectance of Gypsum - Powder	26
7.	Index of Refraction of Gypsum - X Direction	33
8.	Index of Refraction of Gypsum - Y Direction	35
9.	Index of Refraction of Gypsum - Z Direction	37
10.	Index of Refraction of Gypsum - Powder	39
11.	Extinction Coefficient of Gypsum - X Direction	41
12.	Extinction Coefficient of Gypsum - Y Direction	43
13.	Extinction Coefficient of Gypsum - Z Direction	45
14.	Extinction Coefficient of Gypsum - Powder	47
15.	Real Dielectric Function of Gypsum - X Direction	50
16.	Real Dielectric Function of Gypsum - Y Direction	52
17.	Real Dielectric Function of Gypsum - Z Direction	54
18.	Real Dielectric Function of Gypsum - Powder	56
19.	Imaginary Dielectric Function of Gypsum - X Direction . .	58
20.	Imaginary Dielectric Function of Gypsum - Y Direction . .	60

21.	Imaginary Dielectric Function of Gypsum - Z Direction . .	62
22.	Imaginary Dielectric Function of Gypsum - Powder	64
23.	Real Composite Dielectric Function of Gypsum	73
24.	Real Dielectric Function of Gypsum - Powder	75
25.	Imaginary Composite Dielectric Function of Gypsum	77
26.	Imaginary Dielectric Function of Gypsum - Powder	79

LIST OF TABLES

1. Best Fit Coefficients for Composite Dielectric Function 70

ACKNOWLEDGEMENTS

I would like to thank the faculty of the Physics Departments at Benedictine College and the University of Missouri-Kansas City for their efforts and inspiration.

I especially thank Dr. Marvin Querry for his assistance and advice during this project. His careful and helpful manner have been enjoyed inside and outside the classroom.

I also thank my colleagues at UMKC Physics for their friendship and encouragement throughout this research.

Finally, I thank my parents, Bill and Theresa, for making this all possible and worthwhile.

CHAPTER I

INTRODUCTION

The major motivation for this project is to determine if the optical properties of a bulk crystalline mineral can be predicted from an analysis of a powdered sample of the same material. This subject is of importance because of a desire to identify a material without requiring optimum crystal samples for examination. It is also of interest to determine the relationship between different natural states of a material and their interaction with electromagnetic phenomena. Of concern is whether this interaction is similar for bulk crystalline and powdered dust forms.

Gypsum was chosen for this study because it is a common crystalline mineral which has been generally well researched. Because of characteristics in the crystalline structure, gypsum lends itself well to an examination of the individual optical directions. The samples obtained polished well and provided excellent reflection surfaces. In addition, gypsum is a rather general mineral in the crystallographic sense and it is hoped that an examination of it may provide results which are applicable to other minerals as well.

The material was examined for this project in the infrared region primarily to take advantage of the availability of sophisticated spectroscopic equipment capable of analysis in the infrared. The

the powder dielectric function was quite satisfactory. Each prominent feature for the powder was nearly echoed, both qualitatively and quantitatively, by the composite crystal dielectric function.

The final objective of the project was an analysis of the optical results based on crystallographic considerations of the mineral. Specifically, it was desired to distinguish which physical characteristics of the crystal and of the powder were responsible for the parameters found using the fitting techniques. This analysis would hopefully provide analytical criteria for predicting the optical properties of other mineral systems in powdered form.

It was initially believed that the nature of this project was original. A comparison of the optical properties of a mineral material in crystalline and powdered forms had yet to be completed. An initial effort to find similar studies was made by M. R. Querry and the author with no success. An interactive computer based search was completed by Dialog Information Services of Palo Alto, California through the University of Missouri-Kansas City library. Five mineralogical and physics abstracts services were accessed. None of the descriptions provided by this search indicated that similar projects had been undertaken.

Two reference manuals describing crystallographic and optical properties of mineral systems, by Deer, Howie and Zussman ^{1/} and Hurlbut and Klein ^{2/}, were used to develop the descriptions of gypsum found in the next chapter.

The theoretical and computational methods used in this project to determine the optical constants of a material are well documented in the literature. The time-domain method described by Peterson and Knight ^{3/}

is shown to be equivalent to the Kramers-Kronig method. The method for determining the optical constants from the relative reflectance and phase angle values was developed by Querry et al. ^{4/} .

CHAPTER II

EXPERIMENTAL METHODS

Description of Gypsum ($\text{CaSO}_4 \cdot 2\text{H}_2\text{O}$)

Gypsum is the most abundant of sulphate minerals. It occurs generally in large masses in association with limes and shales in evaporite deposits. Gypsum is typically colorless but is occasionally tinted brown or gray or pale shades of red, yellow, or blue due to impurities. It is considered transparent to translucent and is given a Mohs' scale of hardness rating of 2, indicating it to be one of the softer minerals. Although it is found in most parts of the world it is primarily produced in the United States, France, Canada, England, and the Soviet Union. Its primary commercial use is in the manufacture of Plaster of Paris.

Gypsum is a monoclinic crystal which implies three unequal crystallographic axes; two of which, a and c, are inclined to each other at an oblique angle, $\beta = 114^\circ 12'$ (See Figure 1). These axes both lie perpendicular to the third axis, b. Gypsum is further classified as a $2/m$ prismatic crystal which indicates the two-fold rotation symmetry of the b axis and that the a and c axes lie in a mirror plane. The axial lengths of the unit cell constructed using the three shortest vectors are; $a = 6.28 \text{ \AA}$, $b = 15.15 \text{ \AA}$, and $c = 5.67 \text{ \AA}$. These result in the axial ratios $a:b:c = 0.414:1:0.374$.

Gypsum has a perfect cleavage at (010) and less distinct cleavages

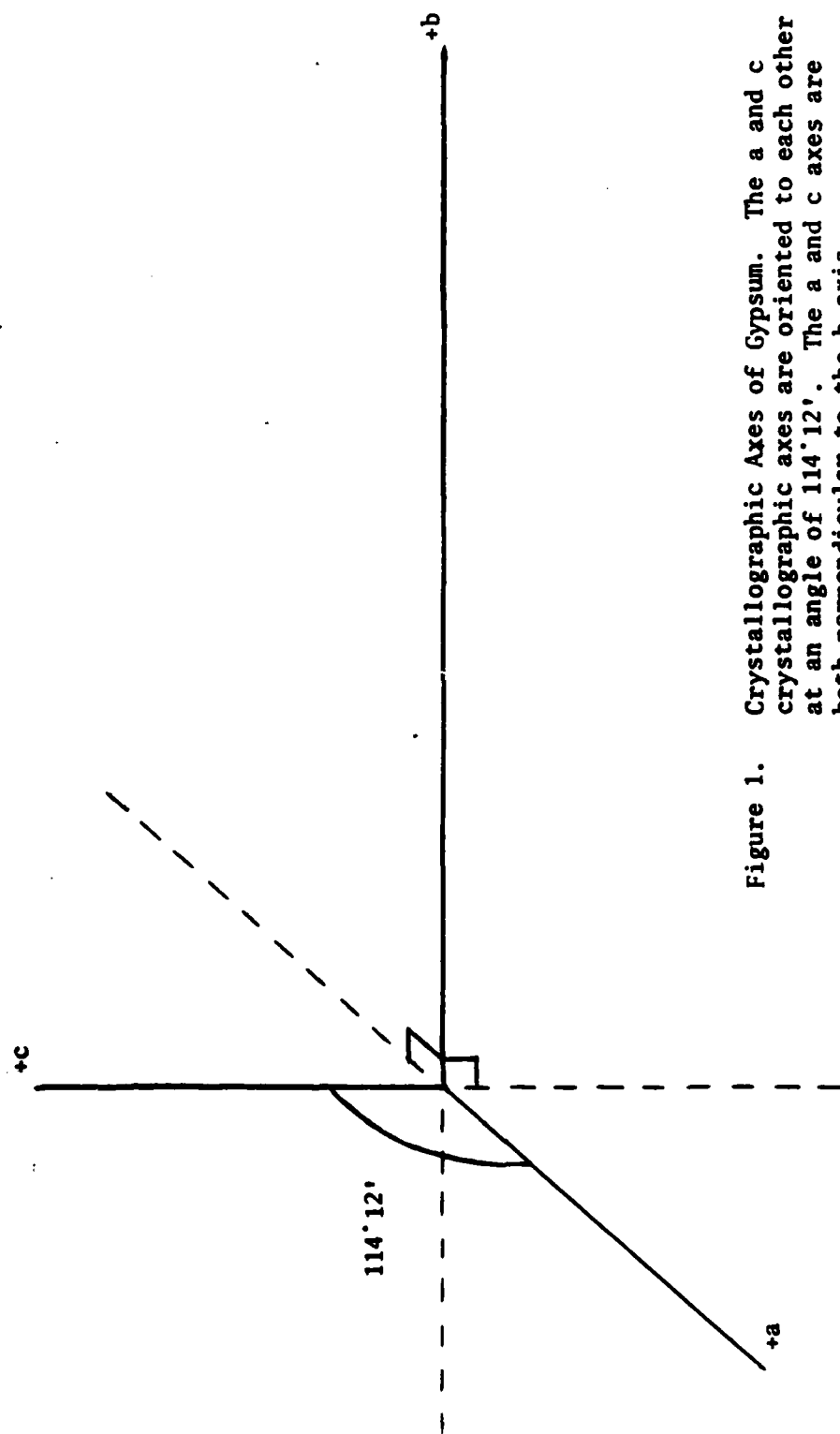


Figure 1. Crystallographic Axes of Gypsum. The a and c crystallographic axes are oriented to each other at an angle of $114^{\circ}12'$. The a and c axes are both perpendicular to the b axis

at (100) and (011). The perfect cleavage is provided by sheets of adjacent layers comprised of Ca^{++} ions and tetrahedral SO_4^{--} ions. Between successive sheets the water molecules are hydrogen bonded to the oxygens in the sulphate groups. Each Ca^{++} ion is thus coordinated by six oxygens of SO_4 groups and by two water molecules. Each water molecule links a Ca^{++} ion to an oxygen in the same sheet and to an oxygen in an adjacent sheet. The perfect cleavage results between the water molecules.

Gypsum is an optically biaxial (+) crystal which indicates that the crystal has two directions in which light travels with zero birefringence. In any direction other than these two electromagnetic waves propagating through gypsum travel as two rays with perpendicular vibrations. These two rays differ in velocity according to which direction they travel through the crystal. The vibration direction of the faster and of the slower rays are at right angles to each other and are designated X and Z, respectively. The vibration direction perpendicular to the plane of X and Z, corresponding to the vibration of an intermediate velocity ray, is designated as Y.

Due to the velocity differences in each of these directions, there are accordingly three indices of refraction corresponding to the different optical directions. The indices α , β , and γ are associated with the optical directions X, Y, and Z, respectively; $\alpha = 1.520$, $\beta = 1.523$, and $\gamma = 1.530$ at the wavelength of the Sodium D lines.

In gypsum, as in all other monoclinic crystals, the Y optical direction corresponds to the b crystallographic axis. The XZ plane is therefore identical to the plane defined by the a and c crystal axes.

The angle between the optical X direction and the crystallographic c axis is -37° . The negative sign indicates that the X direction lies between the +c axis and the -a axis (See Figure 2).

An important consideration is to note the parallel nature of the XZ plane and the ac plane. The importance is that the (010) cleavage plane in gypsum corresponds to the XZ optical plane as well as to the ac crystallographic plane. A desirable experimental result is that the optical properties, specifically the reflectance, may be determined from an excellent cleaved surface in the X and Z directions.

In addition, when the gypsum sample is powdered, it is hypothesized that the crystal will easily separate along the cleavage planes and then break further into small platelets having XZ surfaces perpendicular to the Y direction. When the powder is compressed into pellet form for optical examination it is unlikely that the platelets will line up vertically, or parallel to the compression forces. If this were to occur, the platelets would probably continue to break until a more stable arrangement was found. Rather, the platelets would probably shuffle together horizontally with their surfaces perpendicular to the compression forces.

The result of this alignment is that the pellet surface to be examined will largely be a collection of XZ platelets. This leads to an initial assumption that the optical properties of the powdered pellet will primarily be due to characteristics of the X and Z optical directions and be less influenced by characteristics of the Y direction.

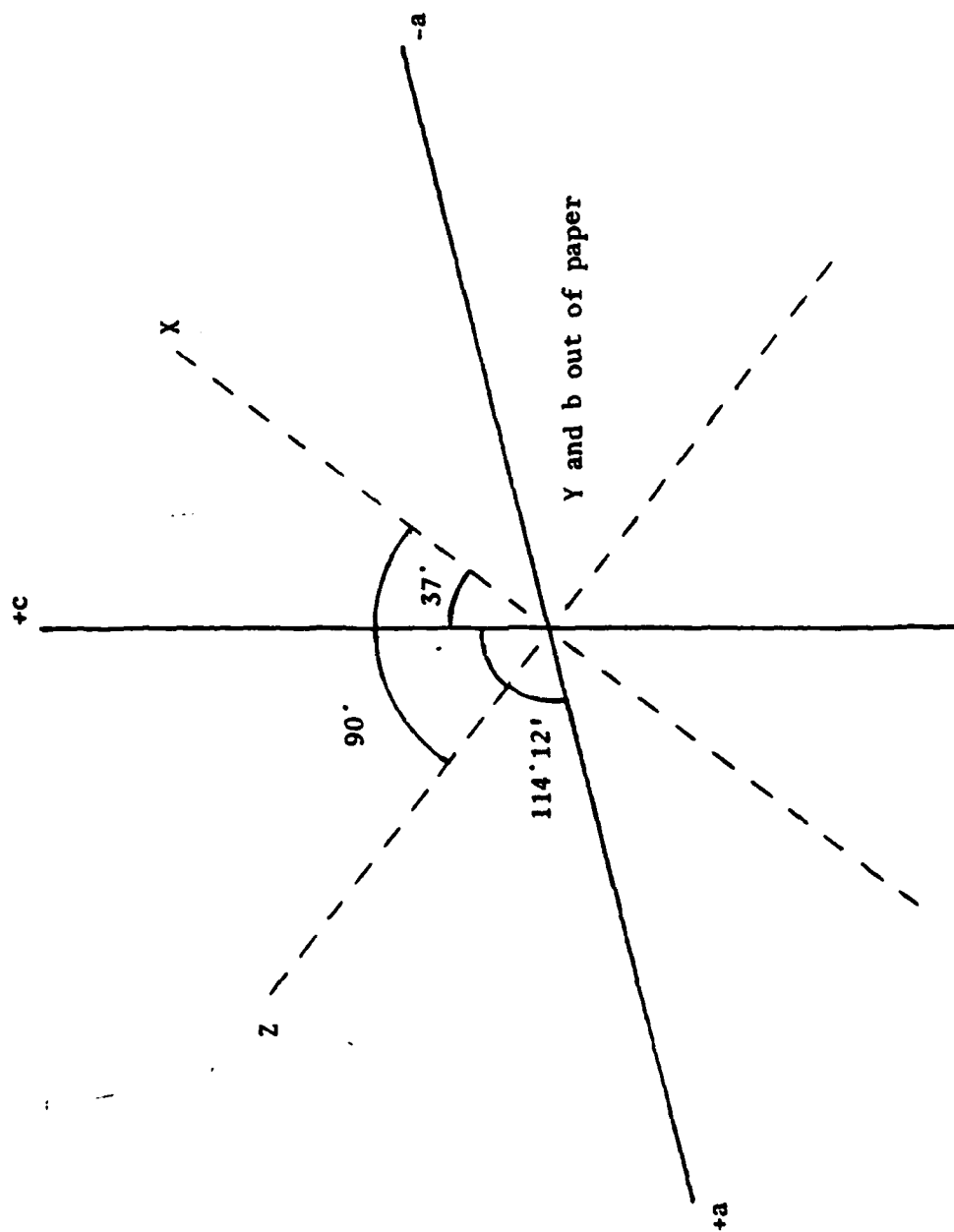


Figure 2.

Optical Directions, and Crystallographic Axes of Gypsum.
 The Y optical direction is parallel to the b crystallographic axis and both are directed out of the paper. The XZ plane and the ac plane are parallel and lie in the plane of the paper in the Figure. Note that the X direction lies between the +c and -a axes at an angle of 37' from the +c axis.

Sample Preparation

The gypsum material to be used in the project was initially examined by R. Coveney, Department of Geosciences, University of Missouri-Kansas City. Crystallographic determination of the a, b, and c axes was completed and samples providing XZ and XY surfaces were obtained. The XZ surface was cleaved at the (010) cleavage plane and was clearly evidenced by a natural shine. The XY surface sample was cut from the same large sample piece. The surface was polished by J. Potter, Department of Physics, University of Missouri- Kansas City using a series of polishing compounds until a large percentage of the surface damage due to the cut was removed.

The density of the crystal samples was 2.30 g/cm^3 . Each of the crystal samples were approximately 6 mm thick and provided ample cross sectional area for examination with the experimental equipment.

The same large sample piece was used to provide the powder for examination. The powder was ground by R. Coveney using conventional methods and a pellet was produced from the powder using a hydraulic press. Several pellets were manufactured and one providing an optimum reflectance surface was chosen for optical examination.

The powder pellet sample measured 0.75 mm in thickness, was 13.00 mm in diameter and had a mass of 0.210 grams. Density = 2.11 g/cm^3 .

Measurement of Reflectance Spectra

The crystal samples were securely fixed to circular platforms of outside diameter 28 mm, inside diameter 11 mm, and of thickness 4.8 mm. These dimensions were required to mount the samples in the

reflectance accessory to be discussed below.

The lower face of the platform was beveled from the outer diameter to the inner diameter. The inner circular opening at the top of the bevel provided for optical examination of the sample surface. A flat black adherent was applied to the beveled surface to avoid reflectance from the mount itself.

The gypsum pellet was mounted in a similar device which additionally was indented to accommodate the pellet. This mount was fitted with a removable top plate used to hold the pellet in place.

The primary experimental instrument used was the Perkin-Elmer PE-580 B Infrared Spectrophotometer. This instrument is double beam ratio recording device which provides a record of the transmission or reflectance of a sample as a function of frequency. The system is capable of being purged with nitrogen gas or dry air to eliminate spurious data, contributed especially by atmospheric H_2O and CO_2 gases.

Source radiation for the spectrophotometer is provided by a ceramic tube heated by an internal element to approximately $1200^{\circ}C$. This provides a continuous source of radiation largely in the infrared. This radiation is then divided into reference and sample beams by a chopper mirror. The reference beam follows an unaffected path while the sample beam is reflected and absorbed by the material being examined.

The reference and reflected beams are recombined by a second chopper mirror and the combined beam is directed toward a grating monochromator which disperses the beam into its spectral components. A polarization accessory for the spectrophotometer allows the operator

to eliminate all radiation not polarized corresponding to the optical axis being examined. The radiation corresponding to the wavenumber selected by the grating is then passed through a filter which rejects unwanted radiation which is also diffracted by the grating.

This radiation is then focused onto a blackened gold-leaf thermocouple detector. The thermoelectric voltage produced by the radiation absorption of the thermocouple is representative of the intensity of radiation reaching the detector. The chopped signal from the detector is processed electronically to give separate sample and reference beam signals. A ratiometer produces the ratio of the two signals which is the reflectance value for the sample.

The reflectance recorder and the grating monochromator scan mechanism are driven in synchronism by a single scan motor. Internal corrections assure that the wavenumber and corresponding reflectance information are accurately recorded at a variety of scan speeds.

The spectrophotometer is additionally equipped with scaled plotting capability which indicates the reflectance ratio data as a function of frequency in wavenumber units. The data are recorded using the disk memory capability of the spectrophotometer companion Perkin-Elmer Data Station.

For examination of sample reflectance the mounted samples are fitted in a Perkin-Elmer Combination Beam Condenser and Specular Reflectance Accessory. This device is necessary to use the spectrophotometer in the reflectance capacity. First surface aluminum mirrors are used to focus and condense the sample beam before incidence with the sample. The reflected radiation is then directed to the

second chopper mirror. The beam was directed to the sample surface at an angle of incidence of $\theta = 6.5^\circ$.

Preliminary trial runs for each of the sample types were made to examine the general features of the reflectance spectra and the behavior of the experimental equipment. Guidelines and procedural techniques were developed to insure the quality and validity of the data obtained.

The first of these guidelines was to insure adequate warm up time for the equipment electronics, for the source and for the detector. The second guideline was to insure adequate time for the system to purge itself of troublesome atmospheric gases. These two checks were accomplished by taking spectra at various time intervals after the equipment was turned on. When the spectrum from an initial test agreed with that from a much later test the wait time for the initial test was determined to be sufficient.

The procedures were carefully examined to insure that the polarizing accessory was passing radiation corresponding to the desired optical direction. The initial identification of the optical directions was done with crystallographic techniques and these directions were marked. Fine tuning on the directions was accomplished by identifying reflectance peaks for each direction and then slightly turning the sample in the beam until the maximum reflectance at the peaks was found. This method "zeroed in" on lattice characteristics responsible for the reflectance peaks.

The next tests were made to determine appropriate time scale settings for the reflectance scans through the spectrum. This insured that the time response for the equipment electronics was not a limiting factor for the validity of the data. This check was accomplished by

examining the spectra taken using different time scales. When the spectrum from a faster scale closely agreed with a more extended time spectrum the faster scale was determined to be sufficient.

Computational methods to determine the index of refraction and the complex dielectric function from the relative reflectance data were used on the trial data to construct n and ϵ spectra. These computational methods will be discussed in more detail in Chapter 3. The n , k , and ϵ spectra were plotted and carefully examined for any evident discontinuous or non-physical characteristics.

It was found that the relative reflectance spectra for the X and Z directions contained a hump which centered for both at approximately 2600 cm^{-1} . The anomalous feature in the X spectrum was quite distinct and extended from roughly 2300 cm^{-1} to 2900 cm^{-1} . Over this frequency span the peak relative reflectance rose to 70% higher than a straight line joining the endpoints of the affected span. The relative reflectance for the Z direction contained a similar feature, although the peak reflectance was only 20% higher than a straight line correction.

As would be expected, these anomalies contributed to questionable features in the n , k , and complex ϵ values in the same region.

It was speculated that the additional reflectance was the result of radiation reflection from the back surface of the sample. This thought implies a relatively high transmission through the gypsum in the affected region. As noted previously, the XZ plane corresponds to the (010) cleavage plane for gypsum. The cleaved sample was very transparent through this plane, at least for visible radiation. The transmission "window" from 2300 cm^{-1} to 2900 cm^{-1} is not altogether surprising in view of these considerations.

The transmission was experimentally verified by removing the reflectance accessory from the spectrophotometer and examining the transmission spectra for the X and Z directions. The transmission windows expected were found in the regions specified by the reflectance humps.

A variety of corrections was discussed, including roughing up the second surface so that the transmitted radiation would scatter upon incidence at the second interface. Also considered was application of a coating to the second surface that would possibly absorb the transmitted radiation at the interface.

Attempts with other samples using the above methods yielded inconclusive results. Although the transmission decreased, this effect had little influence on the reflectance hump. The reflectance from the second surface was apparently still present.

It was decided to leave the experimental sample unaltered and to obtain the reflectance data without corrective action. After the data were obtained the results were corrected for the second surface reflectance by joining the unaffected regions on both sides of the anomalous region with a straight line. Preliminary results for the reflectance, the complex index of refraction, and the complex dielectric function using this correction proved satisfactory.

The data for the final set of relative reflectance spectra were acquired continuously to avoid deviations in the equipment response that might occur otherwise. The equipment was allowed to warm up and purge for one hour prior to any data acquisition. The reflectance data were obtained and converted to digital values at one cm^{-1} intervals

from 180 cm^{-1} to 4000 cm^{-1} for the aluminum mirror. The data were stored on a floppy disk memory using the terminal capability of the PE 580 B. Three runs for the aluminum mirror were completed.

The above procedures were completed for the crystal X, Y, and Z directions, for the powder sample, and for the zero. The data from the three runs for each of the samples were averaged at each wavenumber position. The average zero value at each wavenumber position was then subtracted from the average values for the gypsum samples and for the aluminum mirror. The corrected reflectance values for the samples were divided by the Al mirror reference values to obtain relative reflectance values throughout the spectrum (See Figures 3-6).

The relative reflectance data were transmitted to storage files on the University of Missouri Computer Network for further calculations.

As was noted when examining the preliminary runs, it was necessary to correct for transmission effects in the X and Z spectra in the region from about 2300 cm^{-1} to 2900 cm^{-1} . A straight line was drawn smoothly joining the endpoints of the spectra considered to be affected by the transmission. Points along this line were used in further analysis of the reflectance.

It is well known that aluminum does not reflect 100% of the incident radiation, nor does it reflect equally throughout the spectrum. Corrections were made on the relative reflectance for each sample using the absolute reflectance values for aluminum at different wavenumber positions as were determined by Smith et. al. 5/.

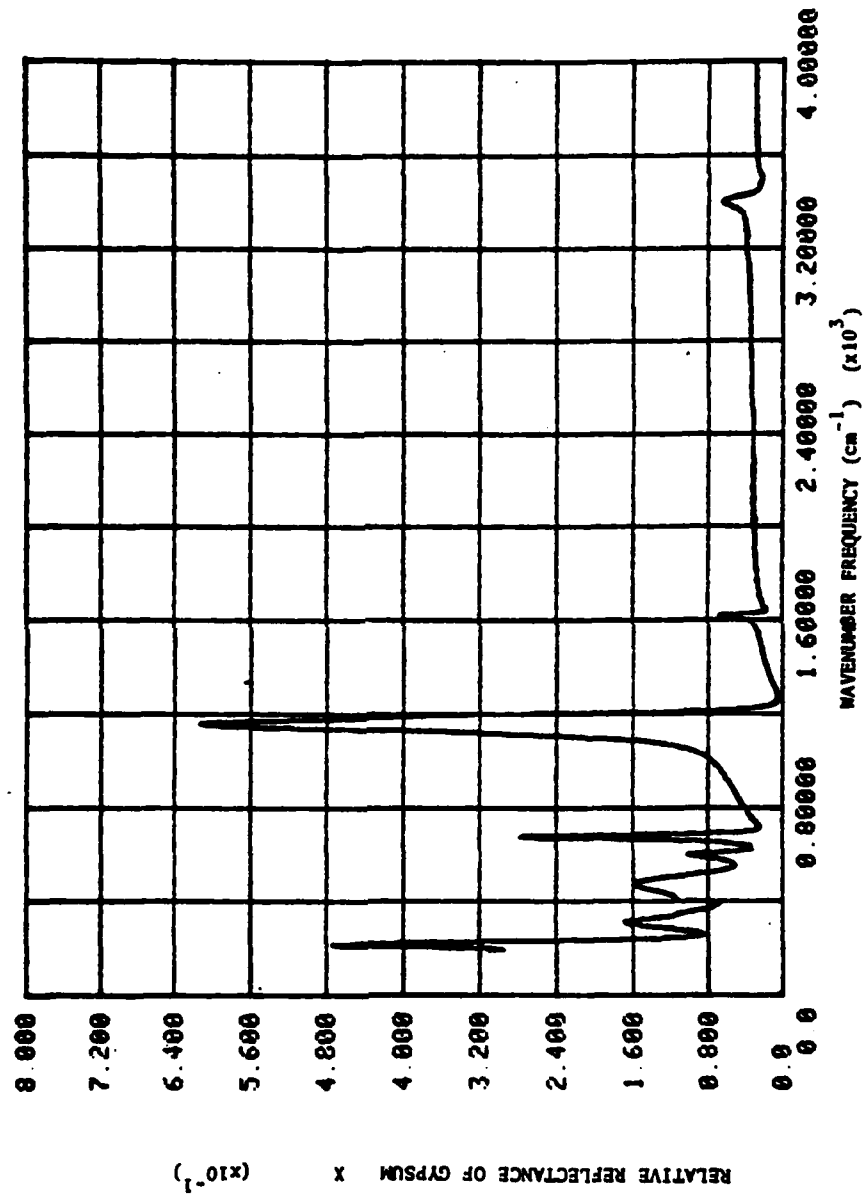


Figure 3. Relative Reflectance of Gypsum - X Direction

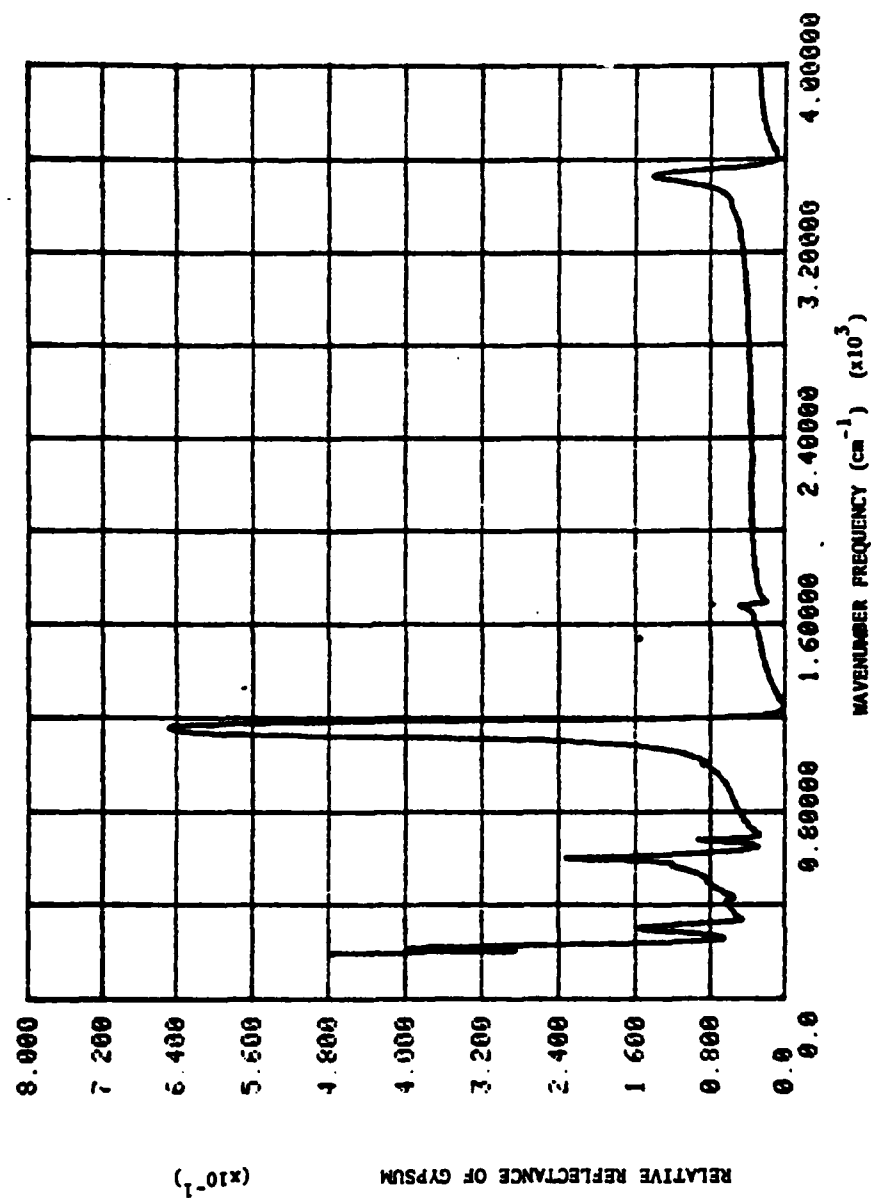


Figure 4. Relative Reflectance of Gypsum - Y Direction

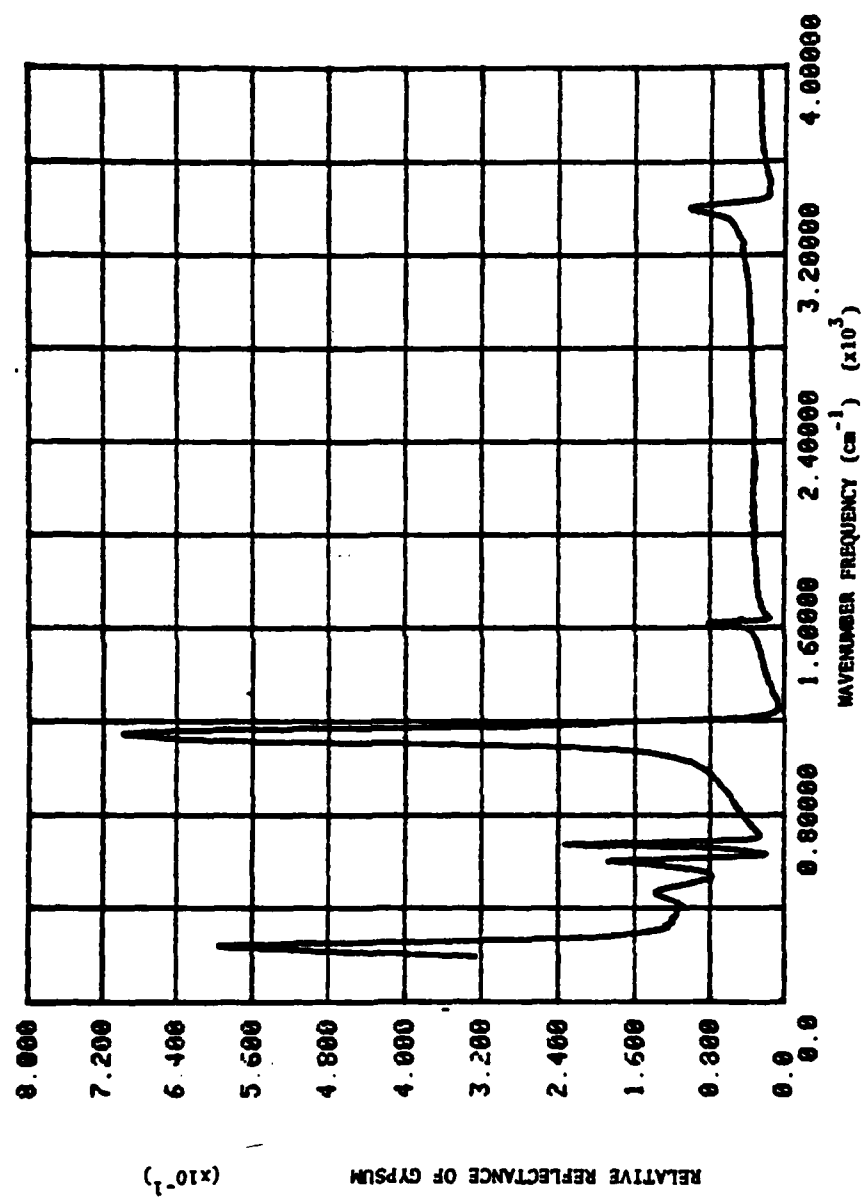


Figure 5. Relative Reflectance of Gypsum - Z Direction

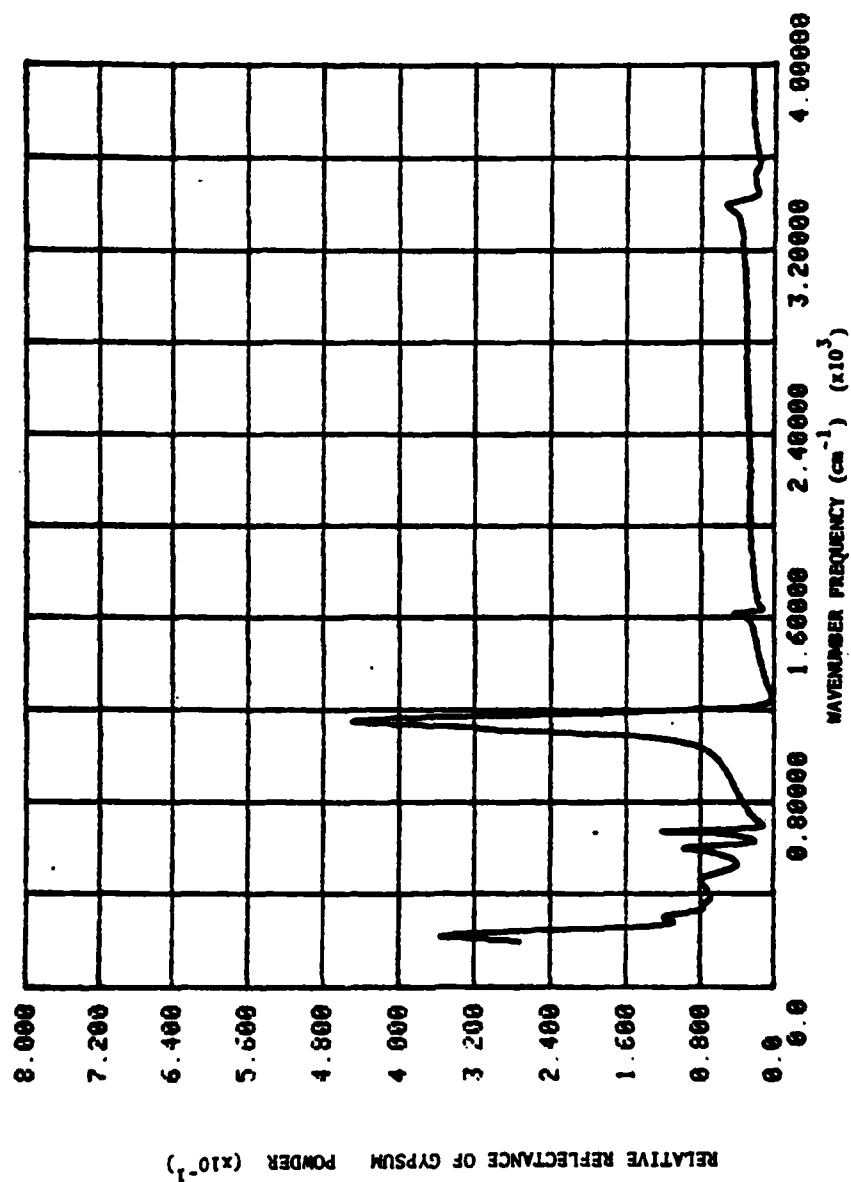


Figure 6. Relative Reflectance of Gypsum - Powder

CHAPTER III

THEORETICAL METHODS

Monochromatic Waves in Conducting Media

For monochromatic waves travelling in a nonconducting medium the simple index of refraction is defined in terms of the dielectric function of the medium according to the equation

$$n^2 = \epsilon \quad (1)$$

For similar waves in a conducting medium, the presence of an induced current density implies a necessary change in the generalized Ampere's Law from the Maxwell Equations. A result of this change is that the dielectric function of the conducting material takes on a complex nature due to the interaction of the medium and the electromagnetic wave. The relationship between the dielectric function and the index of refraction remains quite similar

$$N^2 = \epsilon_c \quad (2)$$

where the subscript c denotes complex. The complex index of refraction is

$$N = n + ik \quad (3)$$

and the complex dielectric function is

$$\epsilon_c = \epsilon_r + i\epsilon_i \quad (4)$$

The following relationships are evident:

$$\epsilon_r = n^2 - k^2, \quad (5)$$

$$\epsilon_i = 2nk, \quad (6)$$

$$n = \left(\frac{1}{2}(\epsilon_r + (\epsilon_r^2 + \epsilon_i^2)^{1/2}) \right)^{1/2}, \quad (7)$$

$$k = \left(\frac{1}{2}(-\epsilon_r + (\epsilon_r^2 + \epsilon_i^2)^{1/2}) \right)^{1/2}. \quad (8)$$

The important utility of these relationships is that simple calculations will lead from the complex dielectric function to the complex index of refraction, or vice-versa, if one of the quantities is known.

In this project Kramers-Kronig relations were used to determine the optical constants, n and k , for each crystal sample and for the powder sample at each wavenumber position in the infrared region. The relations above were used to determine the complex index of refraction.

Peterson-Knight Transformations

Kramers-Kronig methods for determining optical constants from relative reflectance spectra have been used for three decades. The fundamental relations were first advanced by Kramers and Kronig in 1927 ^{6/}.

Applications of these methods have been researched and are widely in use today. In 1973 Peterson and Knight ^{3/} derived a time-domain method procedure equivalent to the Kramers-Kronig procedure which is computationally more efficient. This analysis is known as the Peterson-Knight Fourier Transform Dispersion Relation.

The time-domain method is based on observations that a physical

systems response is zero for negative times (a causality relation) and may be expressed as the sum of two functions which are equal for positive times and opposite for negative times. Additionally, the Fourier transforms of the two functions are the real and imaginary parts of the same physical systems frequency response.

Peterson and Knight begin their development of the time-domain method noting that the impulse response of a system in the time domain, $I(t)$, after the input of an impulse may be represented as the Fourier transform of the frequency response, $F(\omega)$, to a sinusoidal input

$$I(t) = \frac{1}{2\pi} \int_{-\infty}^{\infty} d\omega F(\omega) e^{i\omega t} \quad (9)$$

where

$$F(\omega) = \int_{-\infty}^{\infty} dt I(t) e^{-i\omega t} \quad (10)$$

By imposing the causality relation, $I(t) = 0$ for $t < 0$ and by separating the frequency response into real and imaginary parts

$$F(\omega) = S(\omega) + iA(\omega) \quad (11)$$

Peterson and Knight show that $A(\omega)$ can be determined if $S(\omega)$ is known. With the proper operations in the time and frequency domains the resulting relationships between $S(\omega)$ and $A(\omega)$ are shown to be equivalent to the Kramers-Kronig relations for the real and imaginary parts of a complex function. The efficiency of the time-domain method relating two functions of physical interest provides a computational advantage over the Kramers-Kronig methods.

A computational algorithm relating the modulus, $\rho(\omega)$, of the complex reflectivity, $\rho(\omega)e^{i\phi(\omega)}$, to the phase, $\phi(\omega)$, was prepared by Querry et al. ^{4/} using the time-domain method. The principal relationship involved in the operation is

$$\phi(\omega_0) = P \left[\frac{\omega_0}{\pi} \int_0^{\infty} \frac{\ln \rho(\omega) d\omega}{\omega^2 - \omega_0^2} \right] \quad (12)$$

where P indicates the Cauchy principal value of the integral. The modulus, $\rho(\omega) = (R(\omega))^{1/2}$, is determined from the experimentally obtained values of the relative reflectance of the material. The condition that the integral must be evaluated for $0 < \omega < \infty$ is resolved satisfactorily by setting the reflectance values outside our experimental region equal to constants. The constants above and below the region were determined by averaging a set of reflectance values near the appropriate endpoints.

Determination of Complex Refractive Index

The complex reflectivity for a sample can be related to the complex index of refraction of the sample using the following Fresnel equation for normal incidence

$$\rho e^{i\phi} = (Z - \cos\theta)/(Z + \cos\theta) \quad (13)$$

where

$$Z = (N^2 - \sin^2\theta)^{1/2} \quad (14)$$

As noted earlier $\rho_{gyp} = (R_{gyp})^{1/2}$ where R_{gyp} is determined from our relative reflectance values according to the relation

$$R_{gyp} = \frac{R_{gyp}}{R_{A1}} \times R_{A1} \quad (15)$$

Solving equation (13) for Z we obtain

$$Z = \cos\theta (1 + \rho e^{i\phi}) / (1 - \rho e^{i\phi}) \quad (16)$$

and the complex index of refraction is described by

$$N = (Z^2 + \sin^2\theta)^{1/2} \quad (17)$$

A computational algorithm implementing these results to determine $N(\omega)$ if $\rho(\omega)$ and $\phi(\omega)$ are known was developed by Querry et. al.^{4/}. This algorithm has proved successful in a number of studies and will be used here to determine the complex index of refraction.

The real and imaginary parts of the complex index of refraction are plotted as a function of frequency for each of the samples (See Figures 7 - 14).

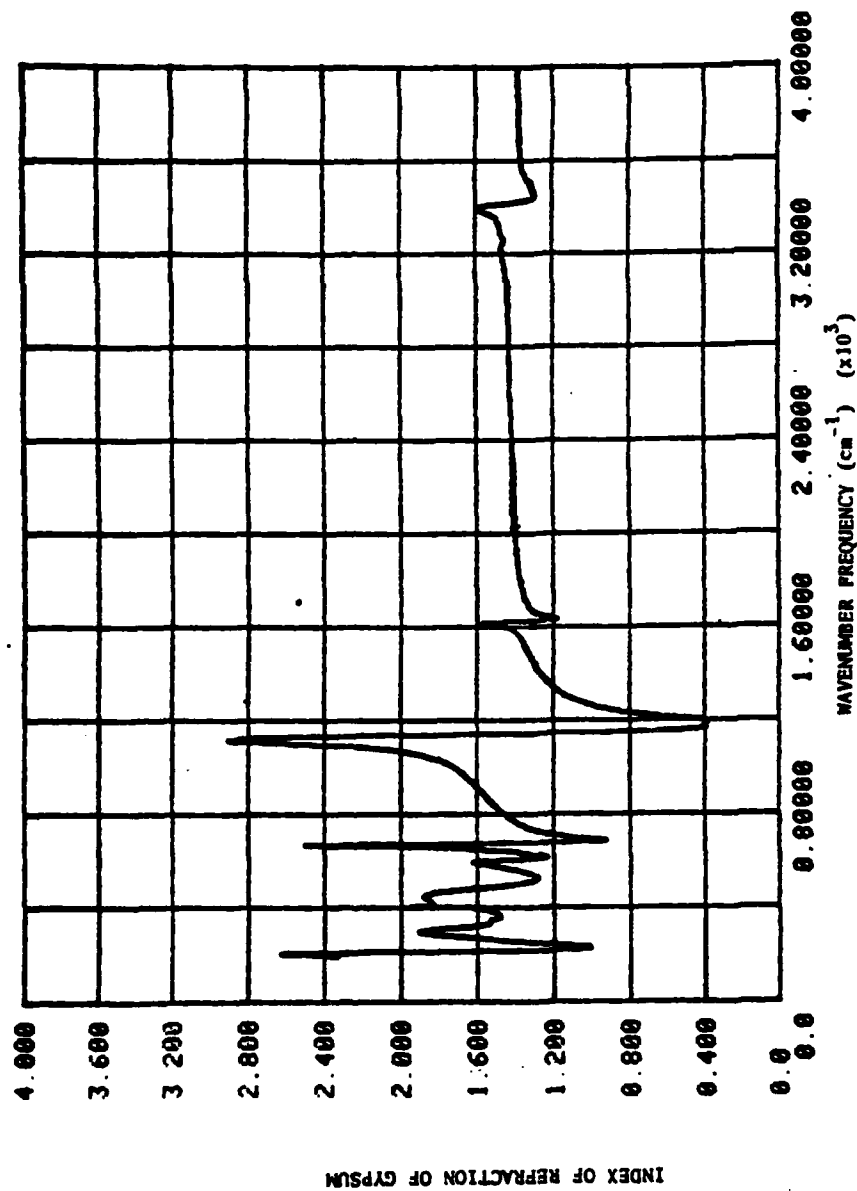


Figure 7. Index of Refraction of Gypsum - X Direction

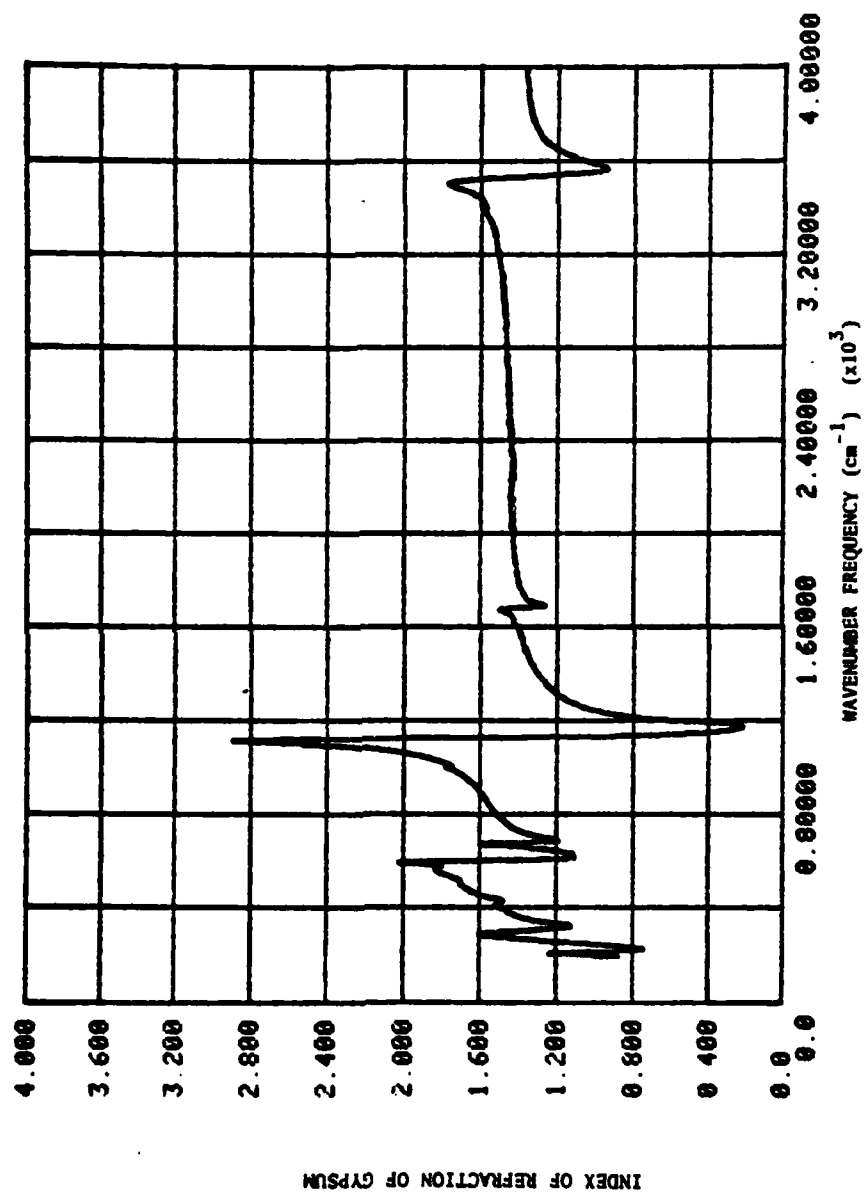


Figure 8. Index of Refraction of Gypsum - Y Direction

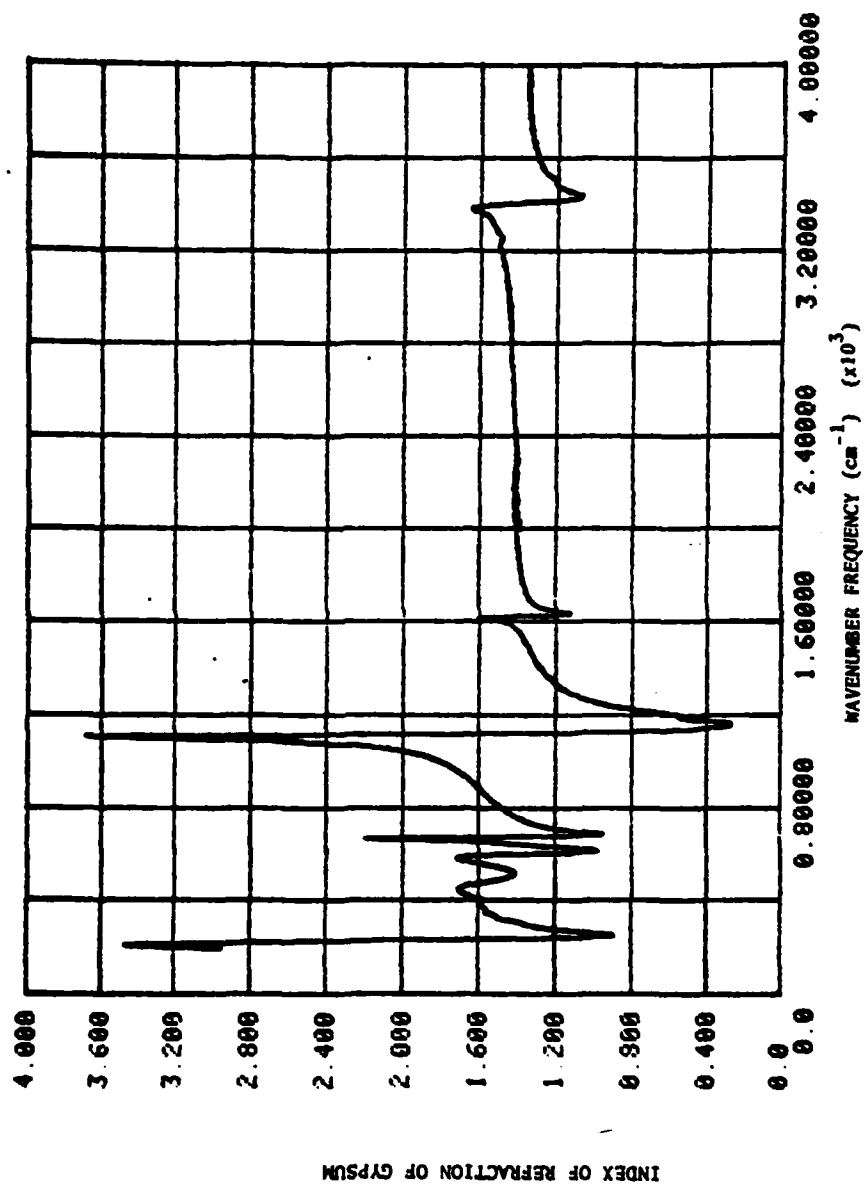


Figure 9. Index of Refraction of Gypsum - Z Direction

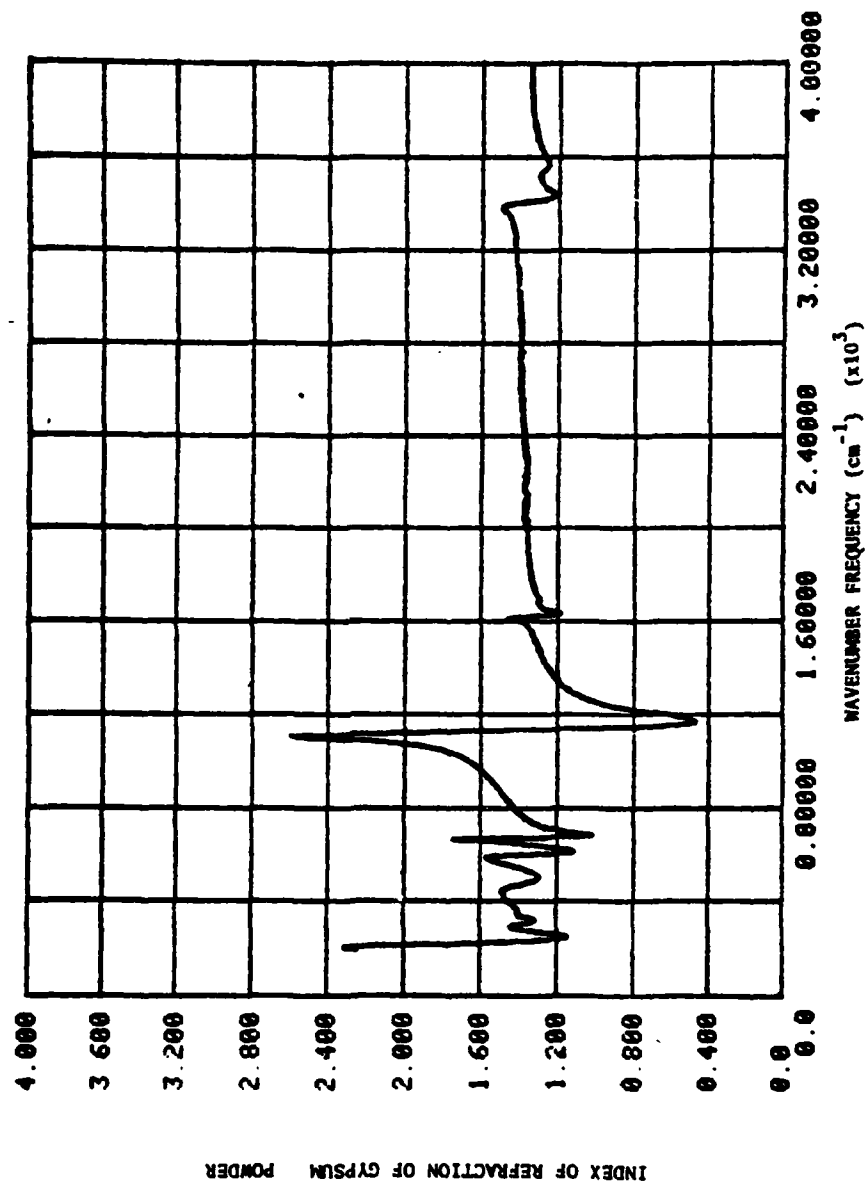


Figure 10. Index of Refraction of Gypsum - Powder

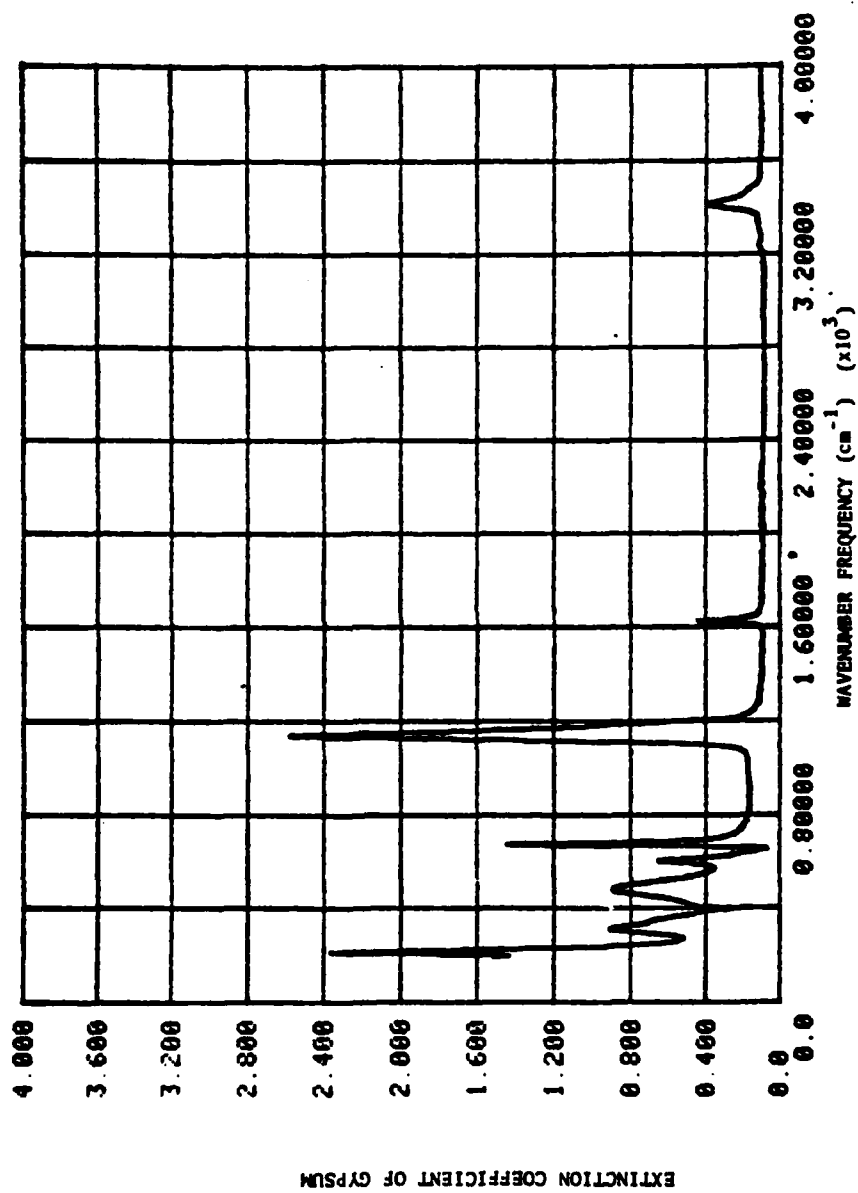


Figure 11. Extinction Coefficient of Gypsum - X Direction

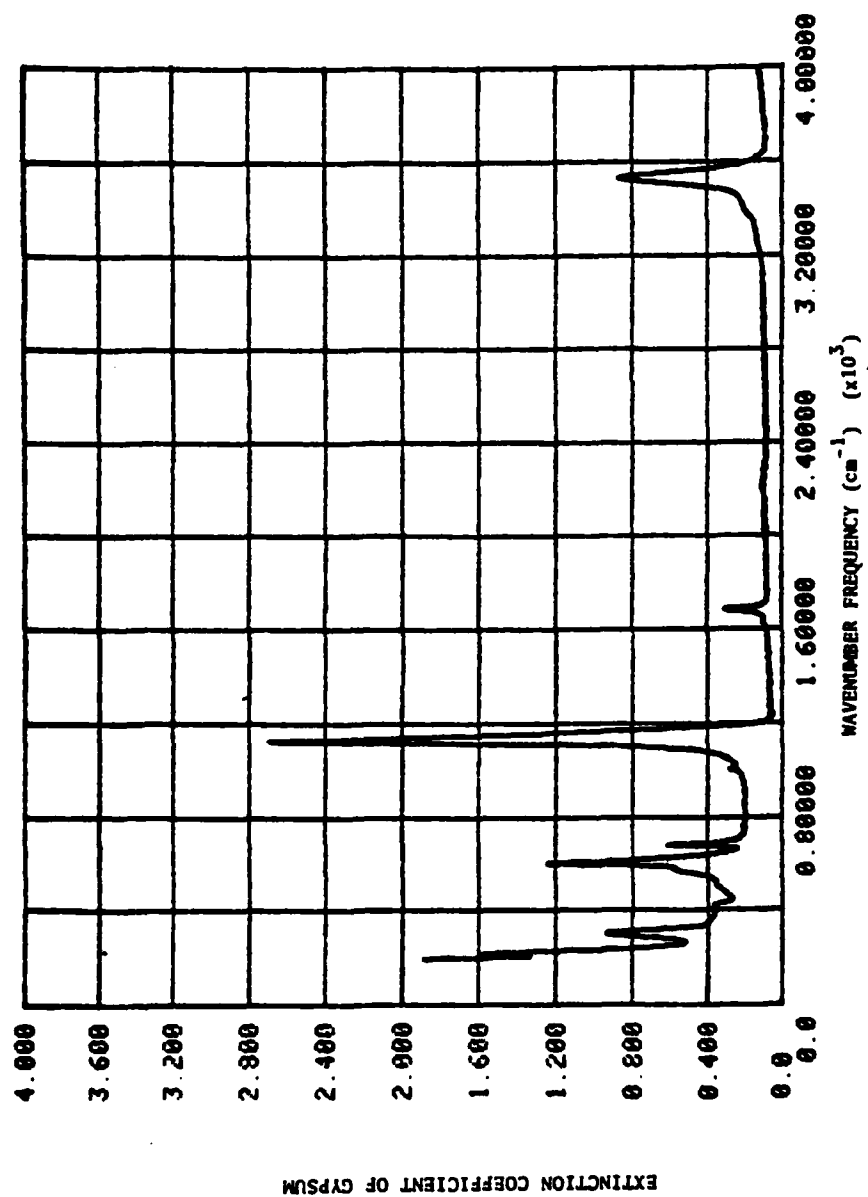


Figure 12. Extinction Coefficient of Gypsum - Y Direction

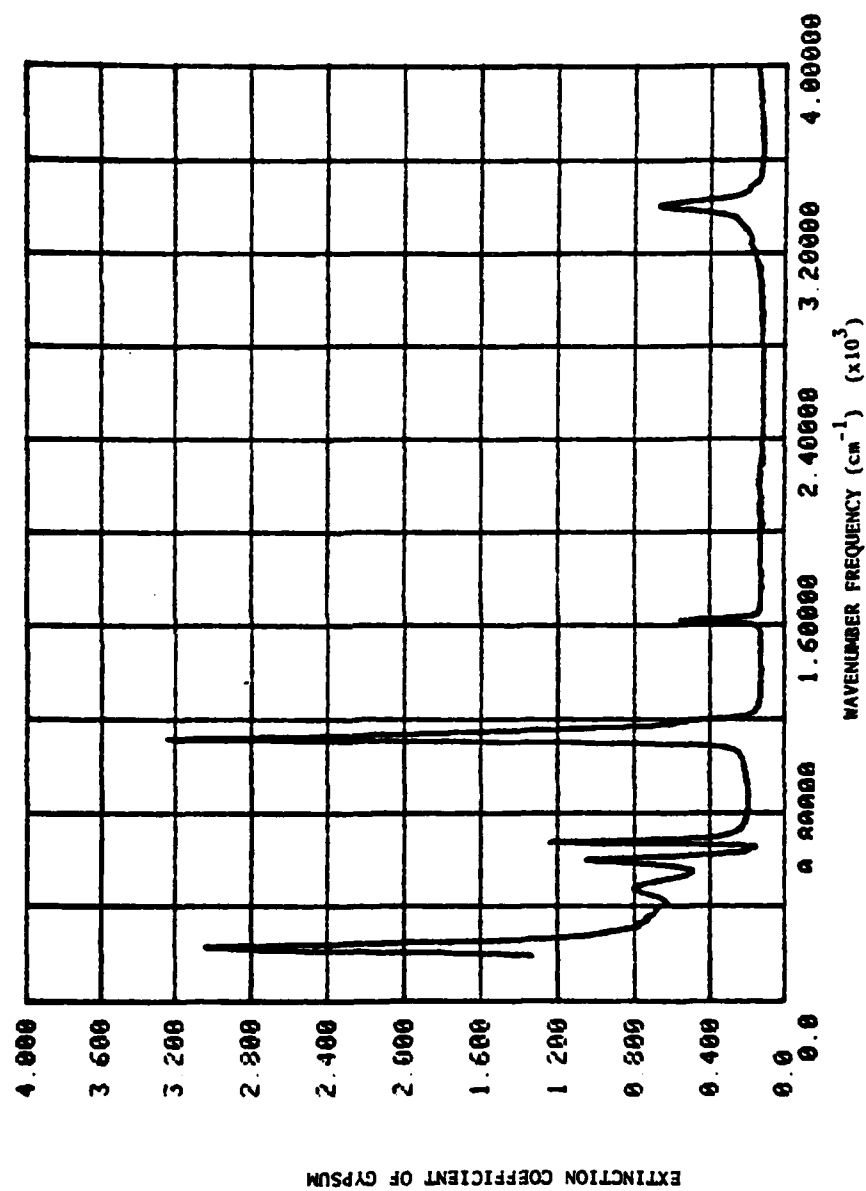


Figure 13. Extinction Coefficient of Gypsum - Z Direction

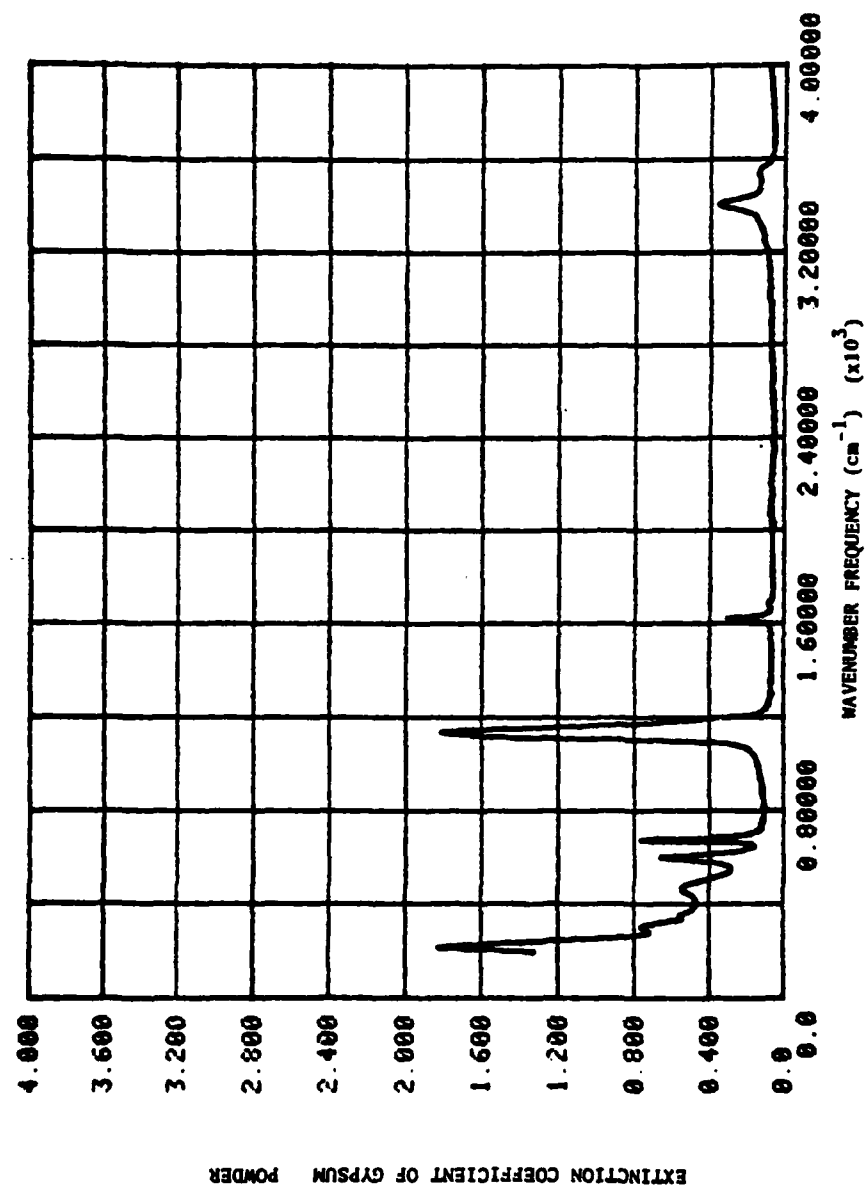


Figure 14. Extinction Coefficient of Gypsum - Powder

CHAPTER IV

ANALYSIS OF COMPLEX DIELECTRIC FUNCTION

Composite Crystal Complex Dielectric Function

The complex dielectric function was determined from the complex index of refraction according to the relationship discussed earlier

$$\epsilon = N^2 \quad (2)$$

(The subscript c indicating the complex nature of the dielectric function is no longer necessary for clarity.) This calculation was done for each of the crystal directions and for the powder.

The complex dielectric function for each of the samples was plotted as a function of frequency (See Figures 15-22). These graphical results provided incentive to continue the project and some verification of the initial speculations. The dielectric function for the powder resembled both the real and imaginary parts of the dielectric functions of the crystal. In addition, the dielectric function for the powder more closely resembled the functions for the X and Z directions than it did for the Y functions. This agrees well with the predictions made earlier based on the compression of the powder into pellet form.

The major goal of the project is to determine some combination of the complex dielectric functions of the crystal which would closely resemble the complex dielectric function of the powder. It is therefore

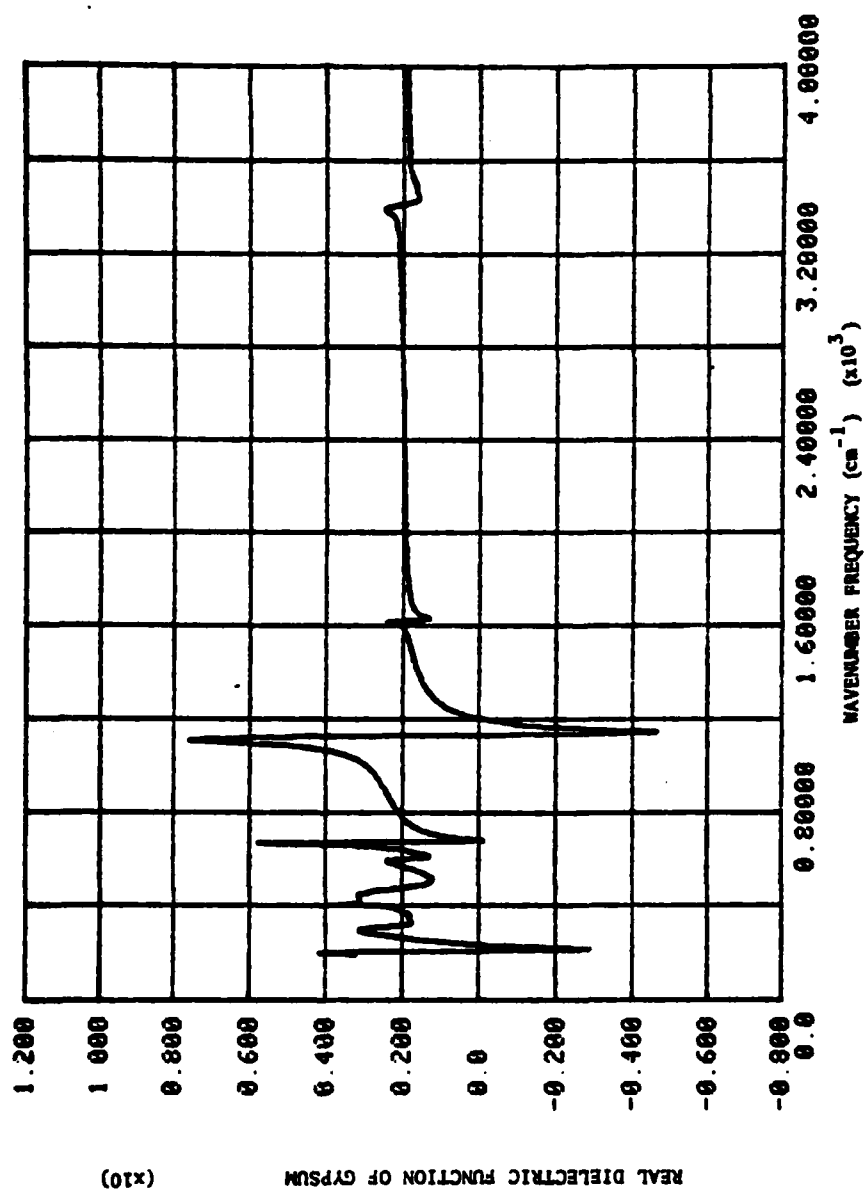


Figure 15. Real Dielectric Function of Gypsum - X Direction

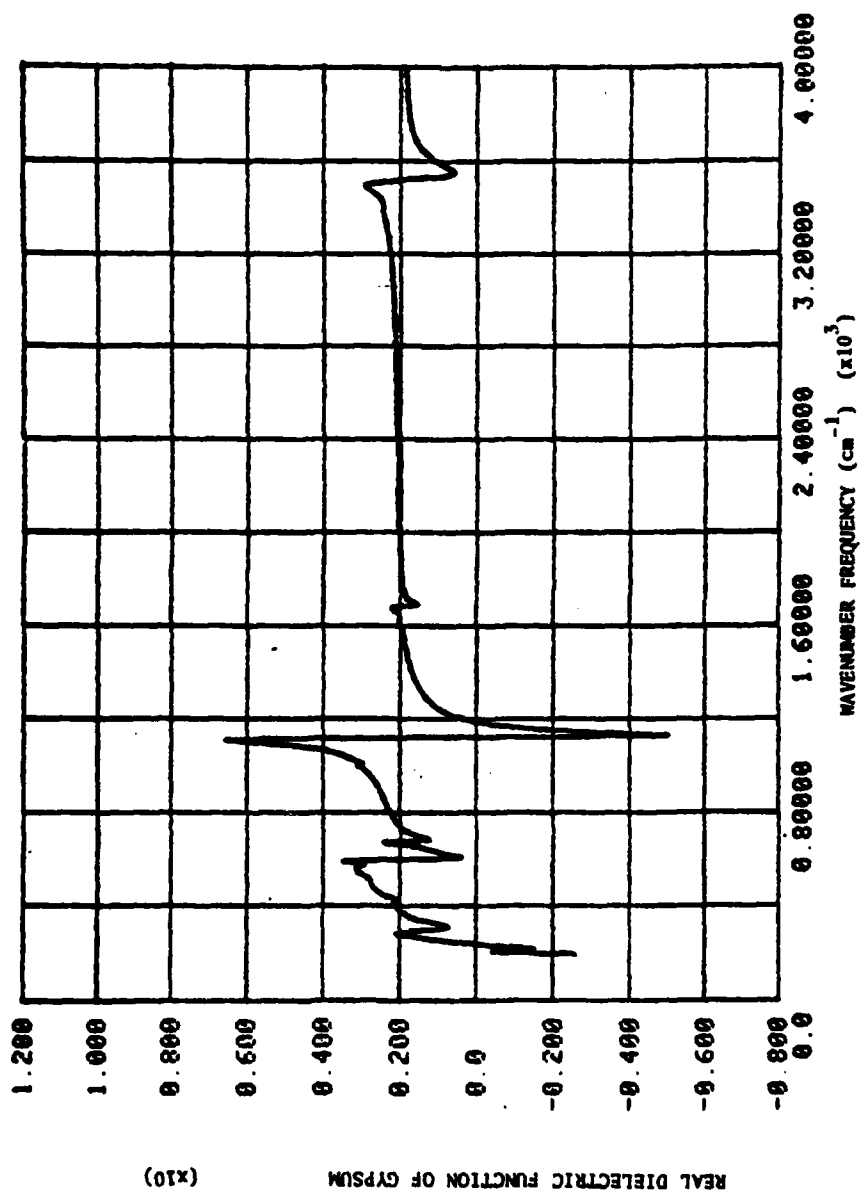


Figure 16. Real Dielectric Function of Gypsum - Y Direction

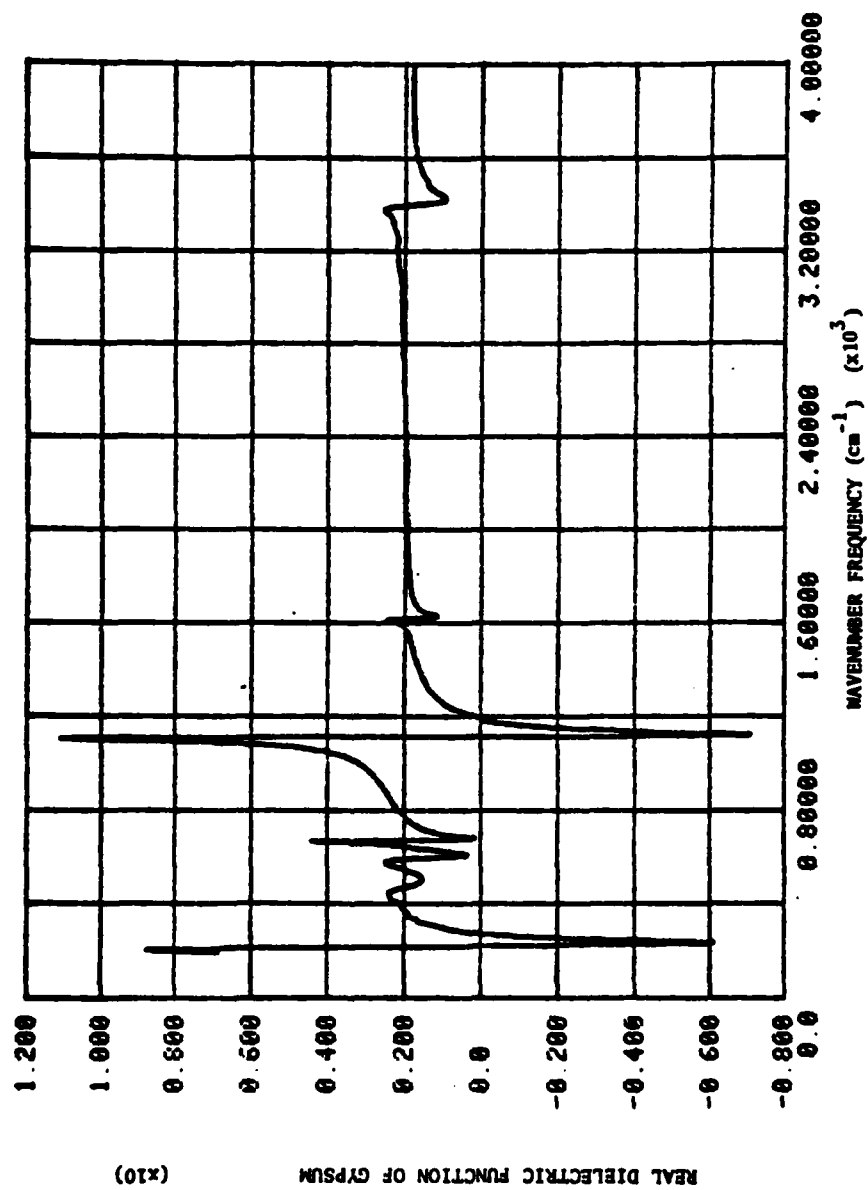


Figure 17. Real Dielectric Function of Gypsum - Z Direction

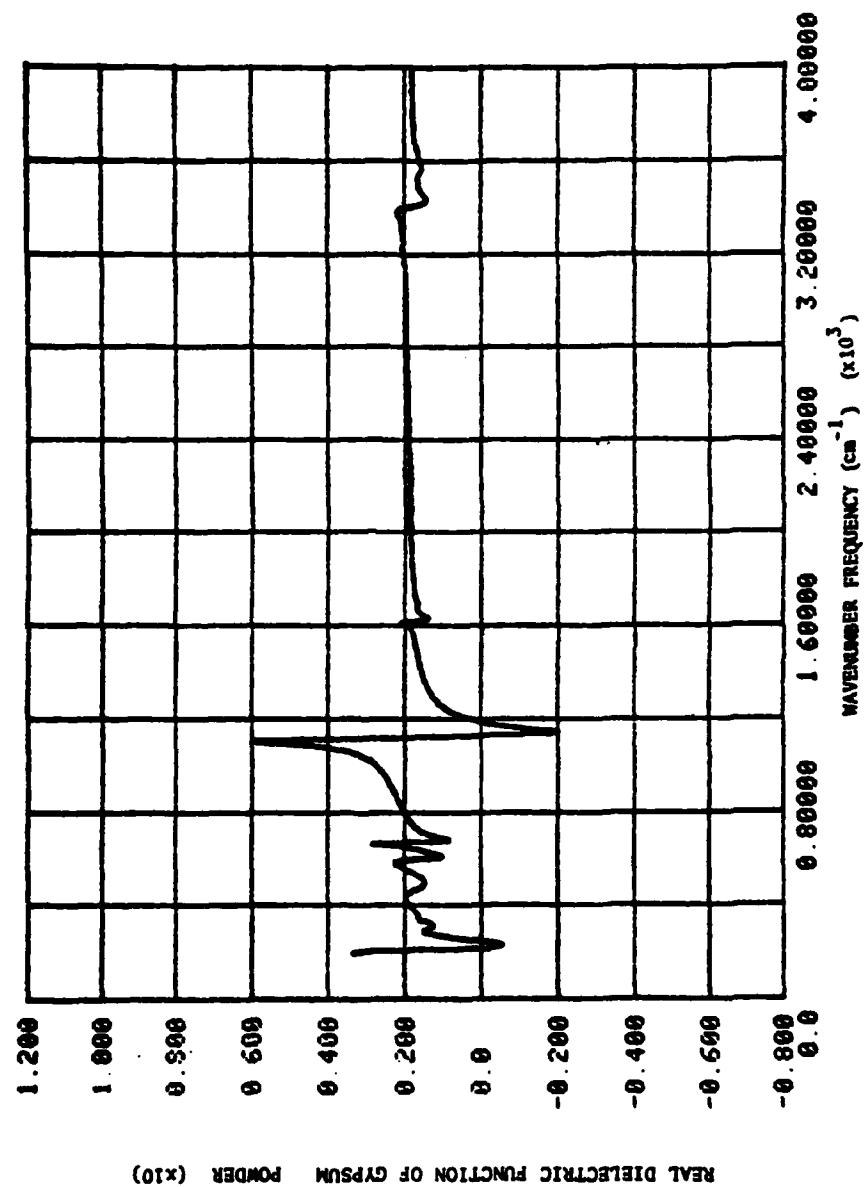


Figure 18. Real Dielectric Function of Gypsum - Powder

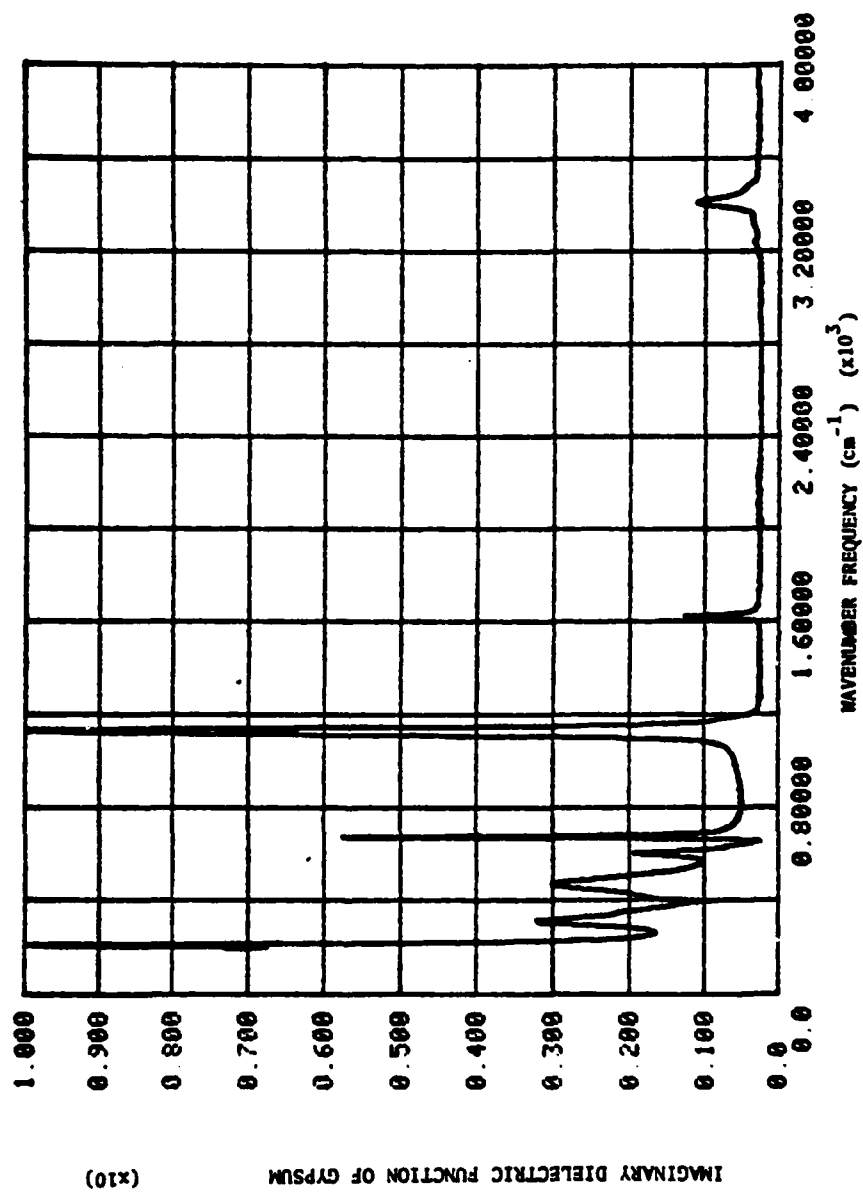


Figure 19. Imaginary Dielectric Function of Gypsum - X Direction

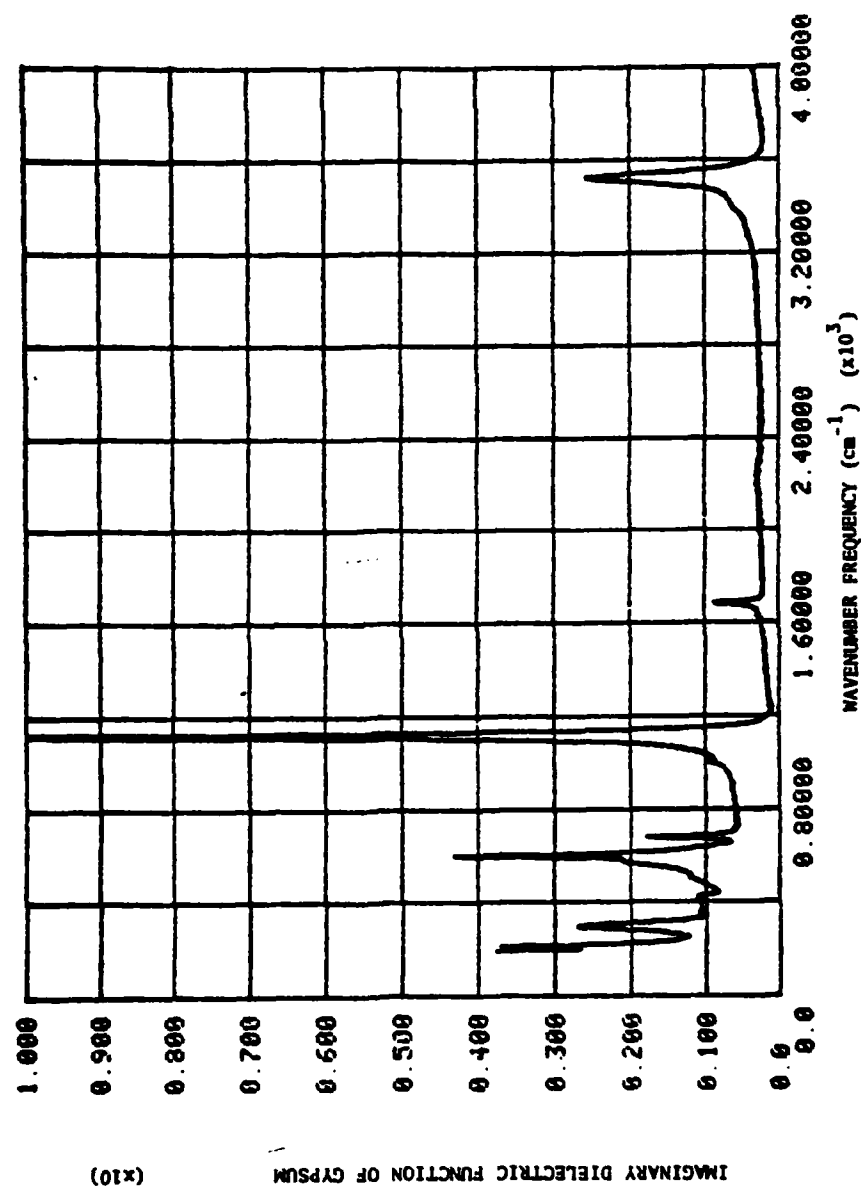


Figure 20. Imaginary Dielectric Function of Gypsum - Y Direction

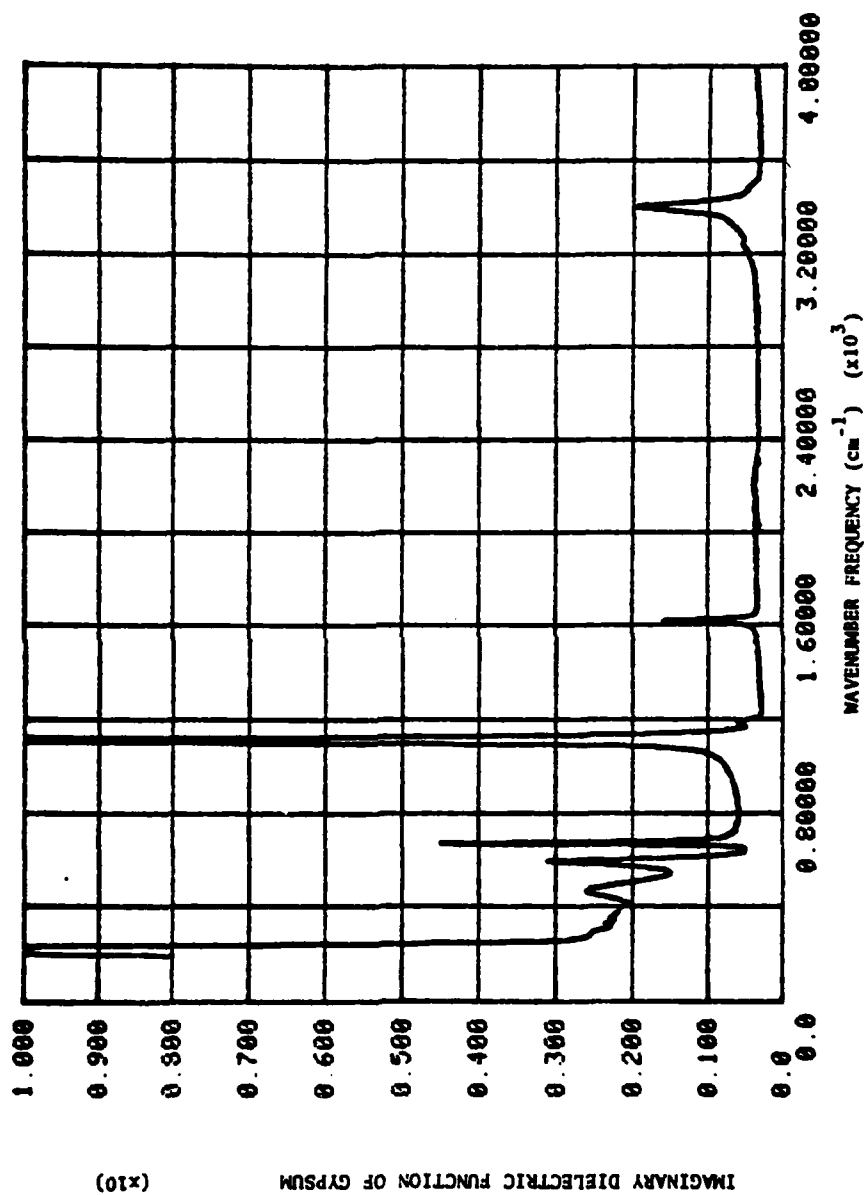


Figure 21. Imaginary Dielectric Function of Gypsum - Z Direction

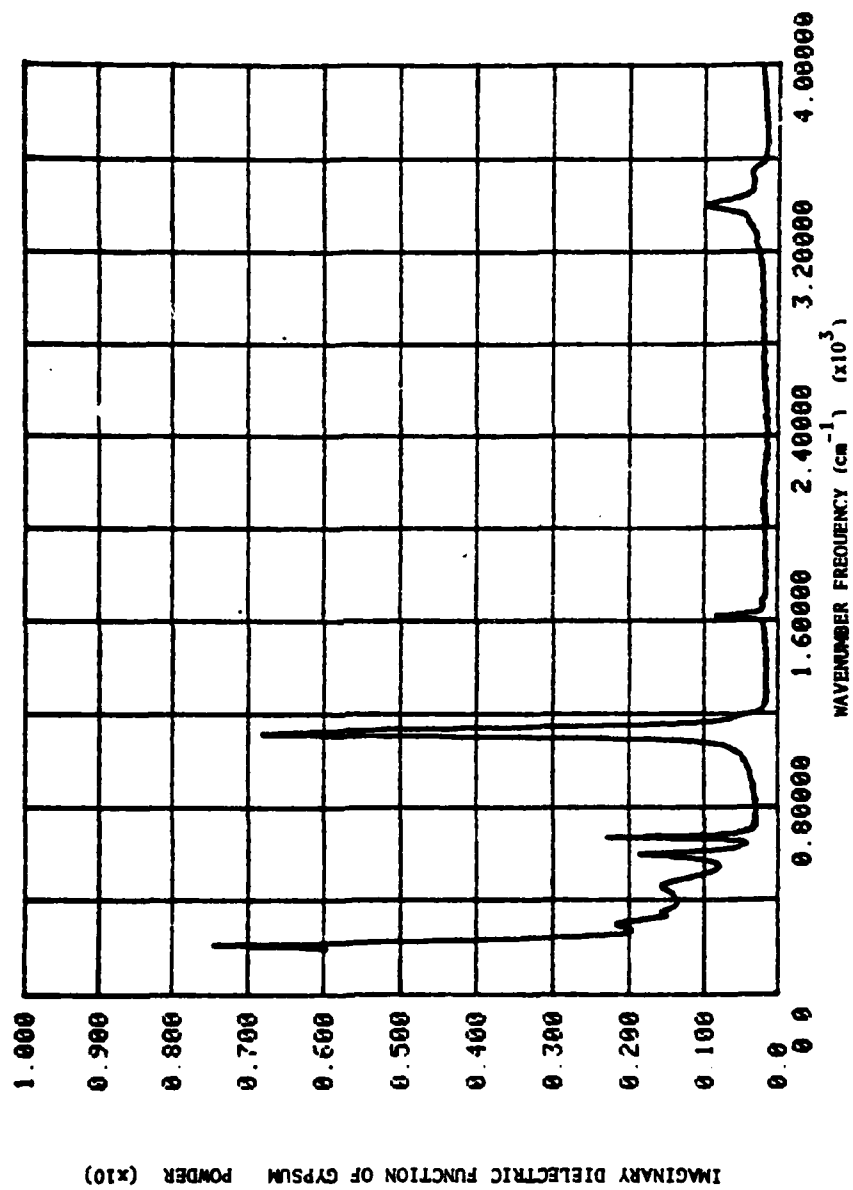


Figure 22. Imaginary Dielectric Function of Gypsum - Powder

AD-A133 530

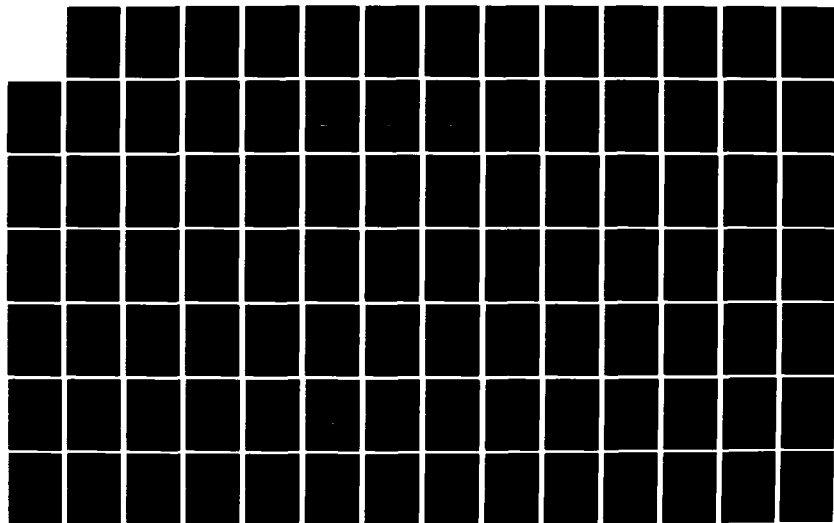
OPTICAL PROPERTIES OF NATURAL MINERALS AND OTHER
MATERIALS IN THE 350-500. (U) MISSOURI UNIV-KANSAS CITY
DEPT OF PHYSICS M R QUERRY AUG 83 ARO-16512.2-GS
DAG29-79-C-0131

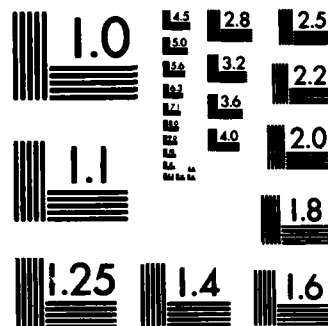
2/4

UNCLASSIFIED

F/G 8/7

NL





MICROCOPY RESOLUTION TEST CHART
NATIONAL BUREAU OF STANDARDS-1963-A

desired to find multiplicative coefficients A, B, and C for the crystal dielectric functions such that

$$\epsilon_p = A\epsilon_x + B\epsilon_y + C\epsilon_z \quad (18)$$

throughout the spectrum. The subscripts indicate the powder and the three optical directions. An additional condition is that $A + B + C = 1$. By adjusting these coefficients in a systematic fashion and utilizing the graphics equipment available through the University of Missouri Computer Network an attempt to computationally and visually determine the best combination of coefficients was made.

Computational Methods

It was determined that the powder, due to surface and density considerations, did not reflect at the same levels as did the polished crystals. The phenomenological model of $\epsilon(\omega)$ suggests that the dielectric function is dependent upon the density of oscillators in the material considered ^{7/}. This implies a dependence also on the mass density of the sample. Since the powder pellet is of lower density than the crystal samples we might therefore expect a lower $\epsilon(\omega)$ for the powder. The ratio of the densities is

$$\rho_p/\rho_c = 2.30 \text{ g/cm}^3 / 2.11 \text{ g/cm}^3 = 0.92 \quad (19)$$

The relative effect of the surface differences is uncertain, but is assumed to be present. The powder surface probably causes some scattering of the reflected beam.

In order to normalize the crystal data to the powder data

a normalization constant for the crystal dielectric functions was determined using a comparison with the powder over a relatively featureless region of the spectrum (1800 cm^{-1} to 2200 cm^{-1}). At each wavenumber position in this region the following ratios were determined;

$$R_x = \frac{\text{Re}(\epsilon_p)}{\text{Re}(\epsilon_x)} , \quad (20)$$

and

$$I_x = \frac{\text{Im}(\epsilon_p)}{\text{Im}(\epsilon_x)} . \quad (21)$$

The normalization constants for the X direction were then computed as the average of these ratios throughout the normalization region. This calculation was also completed for the Y and Z directions.

Although the real normalization constants for the X, Y, and Z directions (and correspondingly the imaginary constants) were slightly different, they were averaged to yield a single normalization for ϵ_r and a single normalization for ϵ_i ;

$$R = 0.934 \quad I = 0.598 . \quad (22)$$

The normalization for ϵ_r shows fairly good agreement with 0.92, the density ratio discussed earlier. The normalization for ϵ_i is in poorer agreement with the density ratio and indicates ϵ_i values which are only 60% of the values for the crystal. This effect can possibly be attributed to the low absorption of the crystal in this region. Multiple reflections by the powder particles could affect the absorption coefficient and ultimately the ϵ_i values.

A preliminary composite complex dielectric function for the crystal was determined by use of the normalized X, Y, and Z dielectric functions and by setting the coefficients A, B, and C equal to one third. The results were quite satisfactory as the composite dielectric function was very similar to the powder dielectric function.

The next step was an effort to find which coefficients would provide a best fit between the composite ϵ and the powder ϵ . The A, B, and C coefficients were incremented in 0.1 step intervals covering each possible combination. The composite ϵ was constructed for each set of coefficients according to the equation

$$\epsilon_c = R(A\epsilon_{xr} + B\epsilon_{yr} + C\epsilon_{zr}) + iI(A\epsilon_{xi} + B\epsilon_{yi} + C\epsilon_{zi}) \quad (23)$$

where the r and i subscripts indicate the real and imaginary parts of the dielectric functions, respectively. The subscript c on the left side of the equation distinguishes the composite crystal dielectric function. If we allow $\bar{\epsilon}$ to indicate the normalized dielectric functions then the description becomes

$$\bar{\epsilon}_c = A\bar{\epsilon}_x + B\bar{\epsilon}_y + C\bar{\epsilon}_z \quad (24)$$

A least squares routine was performed by comparing the real parts and the imaginary parts of the composite and powder dielectric functions at each wavenumber position in order to find the best fit. The real parts and the imaginary parts were necessarily separated during the least squares routine because of the nature of the complex squaring operation. Treating them separately implies that the real part of the

dielectric functions and the imaginary part of the dielectric functions are fit independently of each other. In a second operation, however, the quantitative results of the real fit and the imaginary fit were added together and a search was done to find the best agreement between $\bar{\epsilon}_c$ and ϵ_p . A pleasant indication was that the coefficients which provided the best fits for the real $\bar{\epsilon}_c$ and ϵ_p also generally gave the best fits for the imaginary $\bar{\epsilon}_c$ and ϵ_p . The best combination of coefficients was;

$$A = 0.50 \quad , \quad B = 0.20 \quad , \quad C = 0.30 \quad . \quad (25)$$

After examination of the plotted results using these coefficients it was thought that the large band feature at approximately 1130 cm^{-1} might be unreasonably prejudicing the least squares results. There was also some concern that two other large features below 1130 cm^{-1} might be causing similar difficulties. In order to examine the effect of the large band on the least squares fit it was decided to do an independent least squares examination on the region above 1450 cm^{-1} . The second fit serves a desire to qualitatively match $\bar{\epsilon}_c$ and ϵ_p . Without the influence of the dominant peak it was thought that the second fit would be predominantly affected by the exact placement of the more subtle features in the 1450 cm^{-1} to 4000 cm^{-1} region. It was also thought that the coefficients provided would yield a good qualitative match throughout the entire spectrum. The coefficients provided by the second fit were;

$$A = 0.50 \quad , \quad B = 0.10 \quad , \quad C = 0.40 \quad . \quad (26)$$

A visual comparison of $\bar{\epsilon}_c$ using these coefficients and ϵ_p was very encouraging. Features throughout the spectrum in $\bar{\epsilon}_c$ were closely echoed by ϵ_p .

A further least squares examination was done by adjusting the coefficients in 0.05 increments in a similar fashion. The best fit coefficients in this arrangement were again $A = 0.50$, $B = 0.10$, and $C = 0.40$. These were followed by $A = 0.45$, $B = 0.10$, and $C = 0.45$. The 50 best combinations of coefficients are listed in Table 1.

An examination of the best fit values generated by the least squares routine yields some important observations. The top group of fit values for the second region are very close together. The first five are separated by only 2.7%. So, although the designation of $A = 0.50$, $B = 0.10$, and $C = 0.40$ as the optimum coefficients is of some importance, the more important result is the trend of the first group of coefficients listed in the table. The trend definitely shows that the values of the coefficients A and C are very close. They are both significantly higher than the values for the coefficient B . However, the B coefficient is clearly non-negligible.

In order to examine these trends in more quantitative detail a further calculation was done. The coefficients were weighted according to their rank; i.e. the coefficients $A = 0.50$, $B = 0.10$, and $C = 0.40$ were given rank 231 (there were 231 possible combinations of coefficients). The coefficients with the worst fit, $A = 0.00$, $B = 1.00$, and $C = 0.00$ were given weight 1. The coefficients were multiplied by their assigned weight and these weighted coefficients were summed. The weighted sums for A , B , and C were then reduced such that $A + B + C = 1$. The results of this calculation were;

TABLE 1

BEST FIT COEFFICIENTS FOR COMPOSITE DIELECTRIC FUNCTION

1450-4000 cm^{-1} Region				180-4000 cm^{-1} Region			
A	B	C	FIT	A	B	C	FIT
0.50	0.10	0.40	8.856	0.50	0.15	0.35	476.34
0.45	0.10	0.45	8.938	0.55	0.10	0.35	477.26
0.45	0.15	0.40	9.095	0.55	0.15	0.30	482.11
0.55	0.10	0.35	9.103	0.50	0.20	0.30	488.03
0.40	0.15	0.45	9.108	0.45	0.20	0.35	488.87
0.40	0.10	0.50	9.348	0.60	0.10	0.30	489.64
0.50	0.15	0.35	9.411	0.60	0.05	0.35	491.62
0.35	0.15	0.50	9.449	0.50	0.10	0.40	497.45
0.60	0.10	0.30	9.678	0.45	0.15	0.40	503.14
0.55	0.15	0.30	10.055	0.55	0.05	0.40	505.20
0.35	0.10	0.55	10.087	0.45	0.25	0.30	507.38
0.30	0.15	0.55	10.119	0.65	0.05	0.30	510.60
0.55	0.05	0.40	10.120	0.40	0.25	0.35	514.83
0.50	0.05	0.45	10.271	0.65	0.00	0.35	519.41
0.60	0.05	0.35	10.298	0.55	0.20	0.25	519.75
0.65	0.10	0.25	10.582	0.60	0.15	0.25	520.44
0.45	0.05	0.50	10.750	0.40	0.20	0.40	522.27
0.35	0.20	0.45	10.780	0.60	0.00	0.40	526.39
0.65	0.05	0.30	10.804	0.50	0.25	0.25	532.50
0.40	0.20	0.40	10.837	0.65	0.10	0.25	534.57
0.60	0.15	0.25	11.028	0.40	0.30	0.30	540.18
0.30	0.20	0.50	11.053	0.70	0.00	0.30	545.00
0.25	0.15	0.60	11.117	0.45	0.10	0.45	550.20
0.30	0.10	0.60	11.154	0.50	0.05	0.45	551.35
0.45	0.20	0.35	11.222	0.35	0.30	0.35	554.23
0.40	0.05	0.55	11.558	0.35	0.25	0.40	554.83
0.70	0.05	0.25	11.638	0.45	0.30	0.25	558.69
0.25	0.20	0.55	11.653	0.70	0.05	0.25	562.14
0.70	0.10	0.20	11.814	0.40	0.15	0.45	562.50
0.50	0.20	0.30	11.935	0.55	0.00	0.45	565.93
0.65	0.15	0.20	12.329	0.60	0.20	0.20	584.04
0.20	0.15	0.65	12.444	0.35	0.35	0.30	586.41
0.25	0.10	0.65	12.550	0.35	0.20	0.45	588.23
0.20	0.20	0.60	12.582	0.55	0.25	0.20	590.19
0.35	0.05	0.60	12.695	0.65	0.15	0.20	591.34
0.75	0.05	0.20	12.801	0.40	0.35	0.25	598.32
0.60	0.00	0.40	12.887	0.30	0.30	0.40	600.84
0.55	0.20	0.25	12.977	0.75	0.00	0.25	603.14
0.65	0.00	0.35	12.995	0.30	0.35	0.35	607.07
0.55	0.00	0.45	13.107	0.50	0.30	0.20	609.77

$$A = 0.40 , \quad B = 0.21 , \quad C = 0.39 . \quad (27)$$

The nature of this calculation increases the relative value for B slightly. However, the exact result is not as important as the general indication. The A and C coefficients should be nearly equal and the B coefficient should be significantly lower.

Examining both the weighted coefficients and the actual best fit coefficients the following ranges seem reasonable;

$$A = 0.40 - 0.45 , \quad B = 0.10 - 0.15 , \quad C = 0.40 - 0.45 . \quad (28)$$

A representative set of coefficients within these ranges might be;

$$A = 0.44 , \quad B = 0.12 , \quad C = 0.44 . \quad (29)$$

The above coefficients and the normalizations previously determined were used to generate a final combination crystal dielectric function. This function over the infrared spectrum was then plotted along with the powder complex dielectric function using identical scales. (See figures 23-26). The visual results of this comparison were very favorable. The qualitative features of the two were almost exactly reproduced. The normalization had very nearly duplicated the quantitative nature of the spectra. The large sulphate band at 1130 cm^{-1} is the only large quantitative disparity. The only other significant disagreement between $\bar{\epsilon}_c$ and ϵ_p occurs in the $180 - 500 \text{ cm}^{-1}$ region. This could possibly be an effect of the average value of the reflectance used in the Kramers-Kronig analysis for frequencies below the experimental region. An extremely pleasing result was the almost perfect duplication

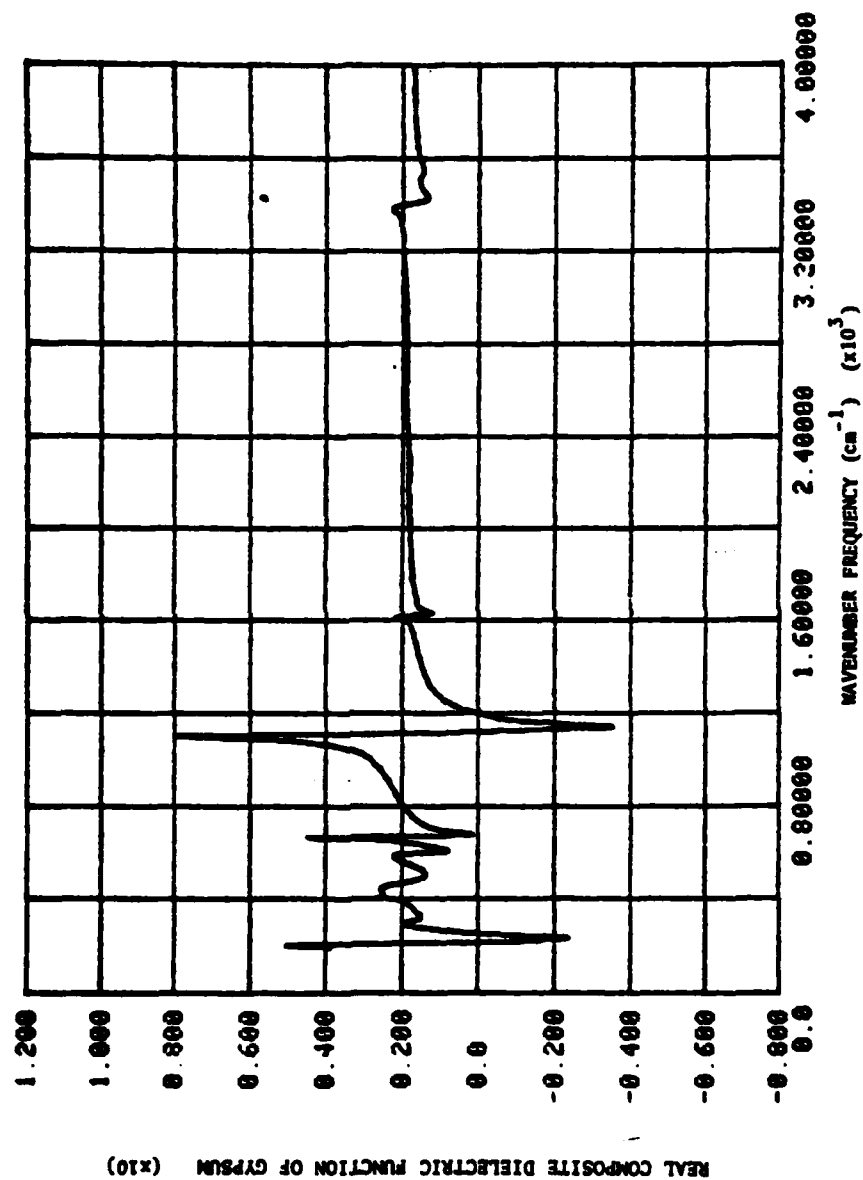


Figure 23. Real Composite Dielectric Function of Gypsum

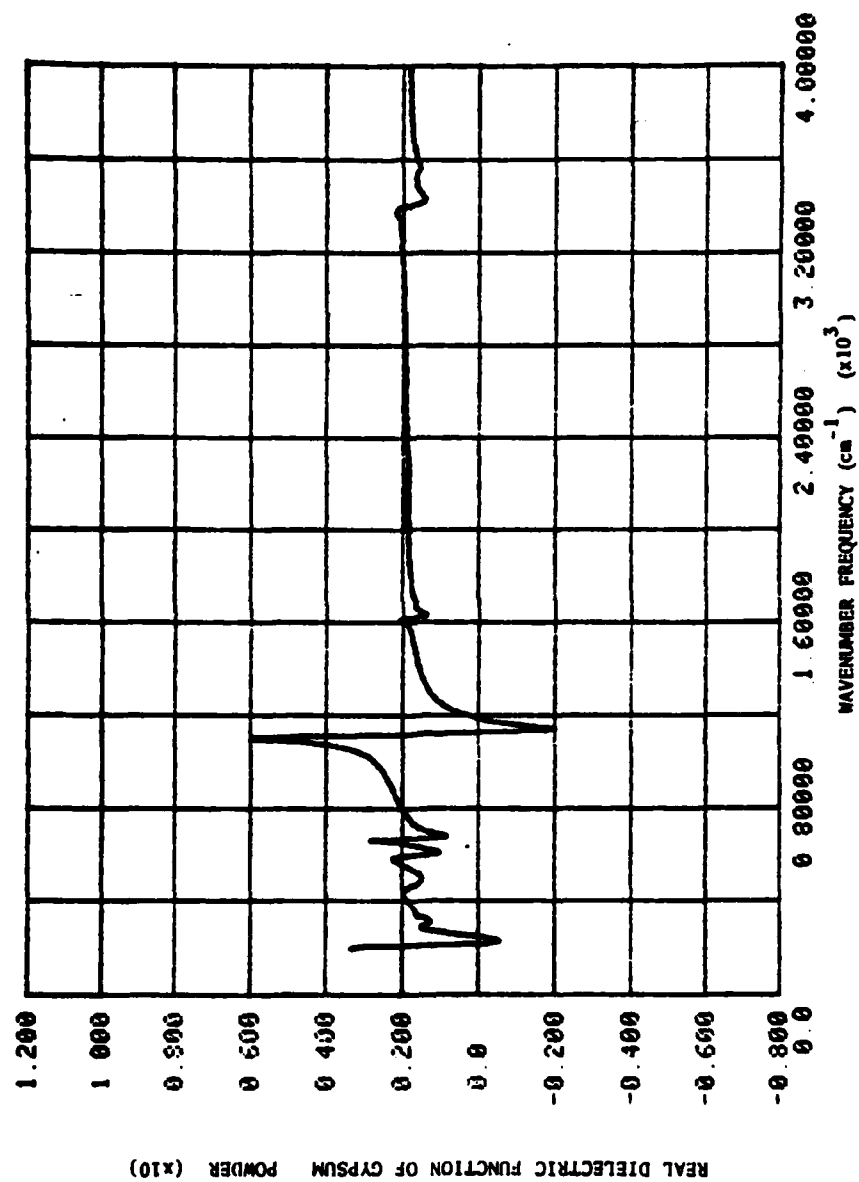


Figure 24. Real Dielectric Function of Gypsum - Powder

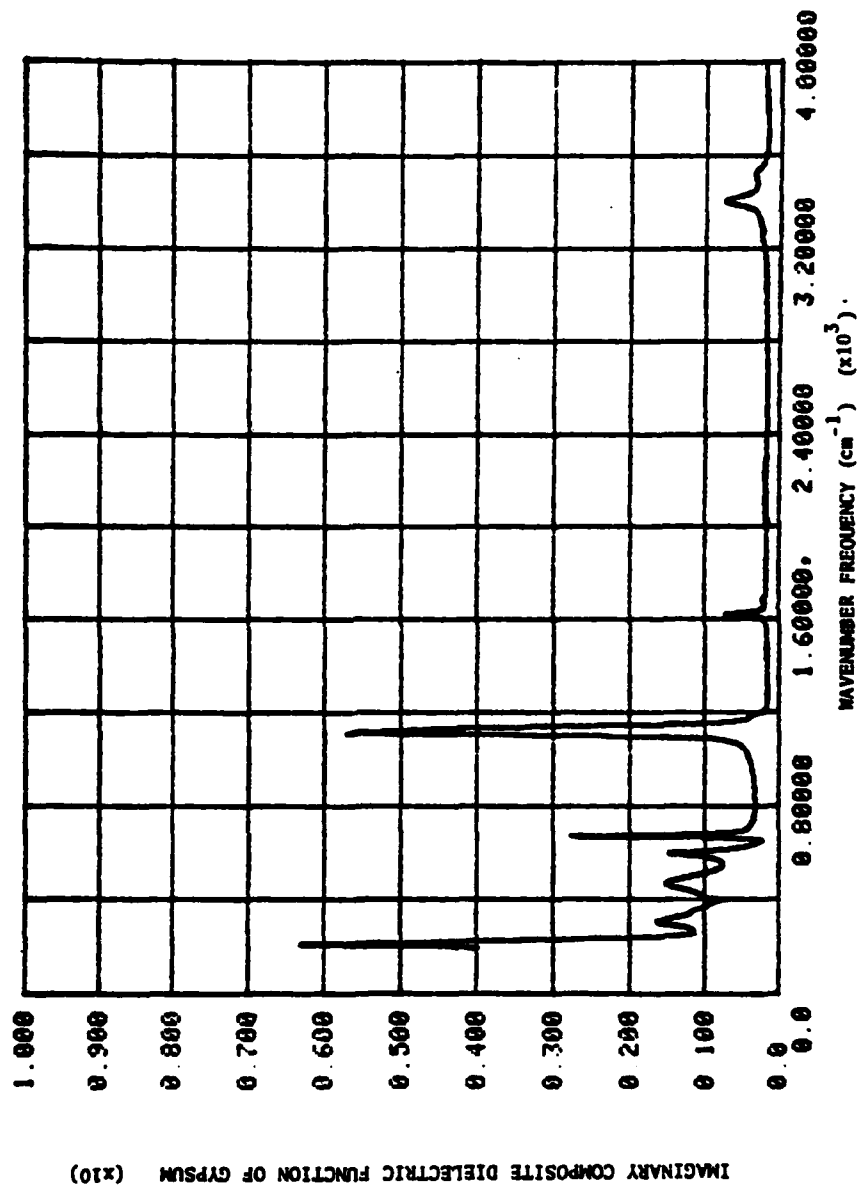


Figure 25. Imaginary Composite Dielectric Function of Gypsum

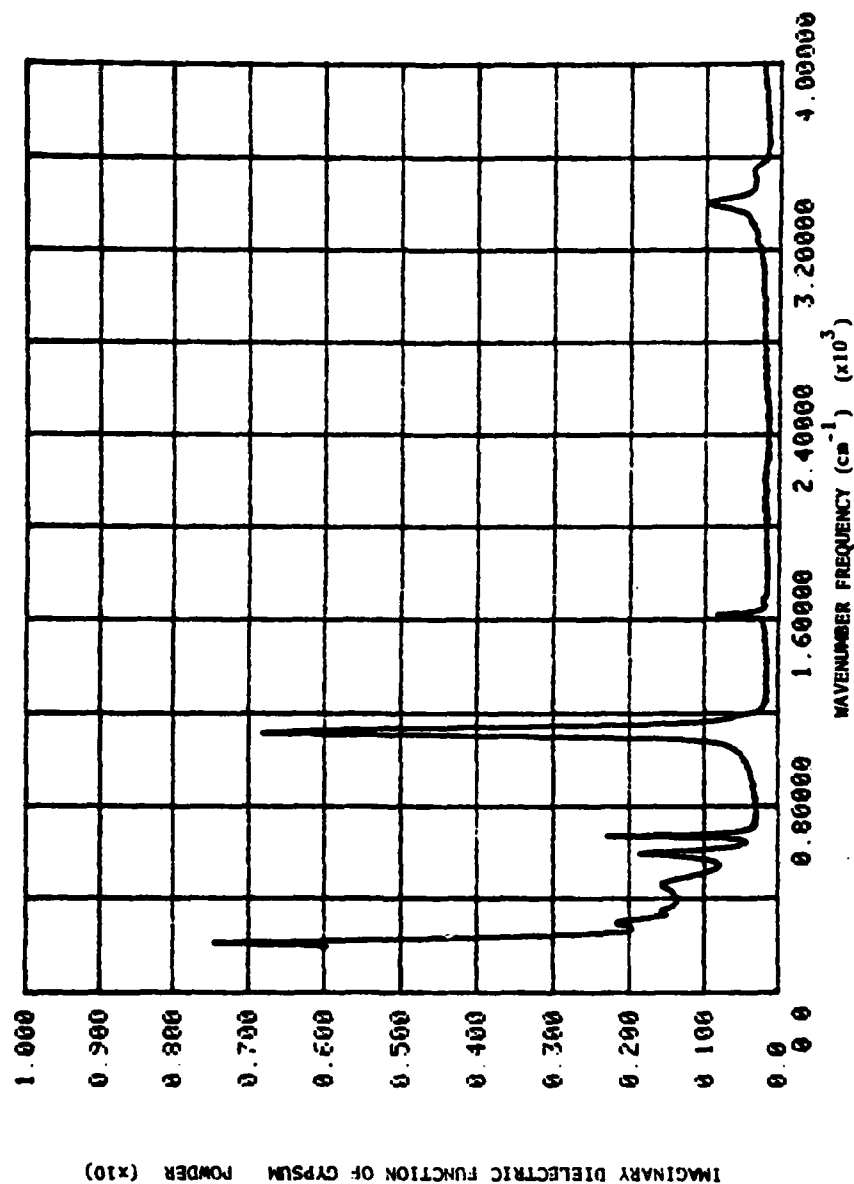


Figure 26. Imaginary Dielectric Function of Gypsum - Powder

of the two faceted feature at approximately 3300 cm^{-1} since one part of the feature can be identified with the X and Z optical directions and the smaller part is identified with the Y optical direction.

CHAPTER V

CONCLUSION

The results of this investigation are quite encouraging and are assumed to be valid. Although the comparison of the complex dielectric function for powdered and crystalline forms of a mineral material appears to be a novel project, the theoretical and computational methods employed in the bulk of the project have been used effectively in numerous experimental studies. The computational algorithm developed by Querry implementing the time-domain method forwarded by Peterson and Knight has been shown successful in determining the optical properties of materials. The additional computations for the comparison of the powder and crystal dielectric functions are straightforward.

The comparison provided results which are in excellent agreement with the predictions initially made from crystallographic analysis of the gypsum crystal. The powder complex dielectric function closely resembles the X and Z complex dielectric functions and gives strong evidence to support the hypothesis that the powdered sample particles are predominantly oriented in the pellet with the (010) cleavage platelets parallel to the sample surface. This is encouraging since it predicts that most other biaxial and uniaxial minerals will behave in a similar manner if they possess strong cleavage planes.

Another important result is the indication that gypsum and possibly other materials may be effectively identified in either powdered or crystalline forms. The dielectric function of the powder will contain all of the spectral features of the crystalline material. From the transmission effects noted in the X and Z reflectance spectra it is found to be necessary that the material be opaque in the spectral region considered or the data must be corrected for the transmission before the optical constants may be determined from Kramers-Kronig analysis. A practical result of the investigation is that the methods used here should be helpful in remote airborne identifications of surface soil composition similar to those done by Lindberg et al. ^{8/} and Doda et al. ^{9/}.

The study of the optical constants in the infrared region seems to indicate that the optical characteristics of a crystalline powder may be predicted if the crystal optical properties are known and if a knowledge of the crystal structure is available. However, the molecular activity responsible for the spectral characteristics in the infrared region differs from the activity responsible for optical responses in other regions. So while it seems plausible that our results and conclusions may be applicable to other spectral regions, it is possible that the break up of the regular crystal structure in the reduction to powder form may provide different effects in other regions.

REFERENCES

1. W. A. Deer, R. A. Howie, J. Zussman, Rock Forming Minerals, Vol. 5 (John Wiley and Sons, Inc., New York, 1962), pp. 202-218.
2. C. S. Hurlbut, C. Klein, Manual of Rock Forming Minerals (John Wiley and Sons, Inc., New York, 1977), pp. 321-322.
3. C. W. Peterson, B. W. Knight, J. Opt. Soc. Am. 63, 1238 (1973).
4. G. M. Hale, W. E. Holland, M. R. Querry, Appl. Opt. 12, 48 (1973).
5. D. Y. Smith, E. Shiles, M. Inokuti, "The Optical Properties of Metallic Aluminum," preprint.
6. R. de L. Kronig, Physica (Utr.) 3, 1009 (1936); H. A. Kramers, Atti Congr. Intern. Fisici, Como 2, 545 (1927).
7. J. D. Jackson, Classical Electrodynamics (John Wiley and Sons, Inc., New York, 1975), 2nd ed., p. 285.
8. J. D. Lindberg, M. S. Smith, Am. Mineral. 58, 1062 (1973).
9. D. D. Doda, A. E. S. Green, Appl. Opt. 20, 636 (1981).

VITA

Richard L. Strecker was born in Topeka, Kansas on March 7, 1958. He was educated in Topeka parochial schools and was graduated from Hayden High School in Topeka in 1976 after serving as student council president in 1975-1976. He accepted an academic scholarship from Benedictine College, Atchison, Kansas and was graduated from the same institution with a Bachelor of Arts degree in Physics in the spring, 1980.

Mr. Strecker accepted a graduate teaching assistantship in the Department of Physics at the University of Missouri-Kansas City and began studies in the graduate program there in the fall, 1980. He was a graduate research assistant during the summers of 1981 and 1982. He continued his involvement in the Society of Physics Students as president of the local chapter and was selected to Sigma Pi Sigma, the physics student honor society. Upon completion of the Master of Science degree Mr. Strecker plans to continue persuing academic interests in physics and education.

E. Crystalline Samples

1. Rutile O-Ray (E+C)

Rutile is an optically uniaxial (+) crystal of the $P4_2/mnm$ lattice and space group. The optical directions for the E- and O-rays are respectively parallel and perpendicular to the C-axis of the crystal. The reflectance spectrum was measured in the $180\text{--}4,000\text{ cm}^{-1}$ region for a polished (001) plane (O-ray) and spectral values of $N(\nu)$ were computed by use of the dispersion relations and the Fresnel equations. The reflectance spectrum is shown in Fig. E1-1 and the spectra for the real and imaginary parts of $N(\nu)$ are presented in Figs. E1-2 and E1-3, respectively. The natural Rutile crystal used for this investigation was black in color and possessed a metallic appearance after polishing.

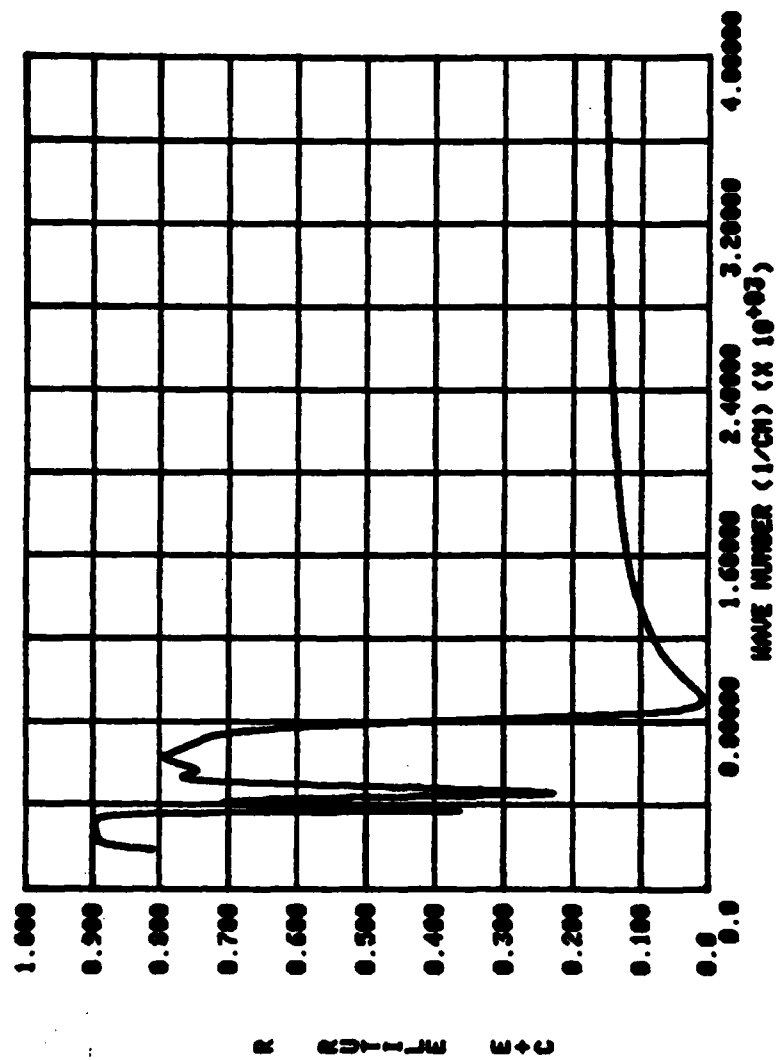


Figure E1-1. Reflectance spectrum of rutile (O-ray) in the 180-4,000 cm^{-1} wave number region.

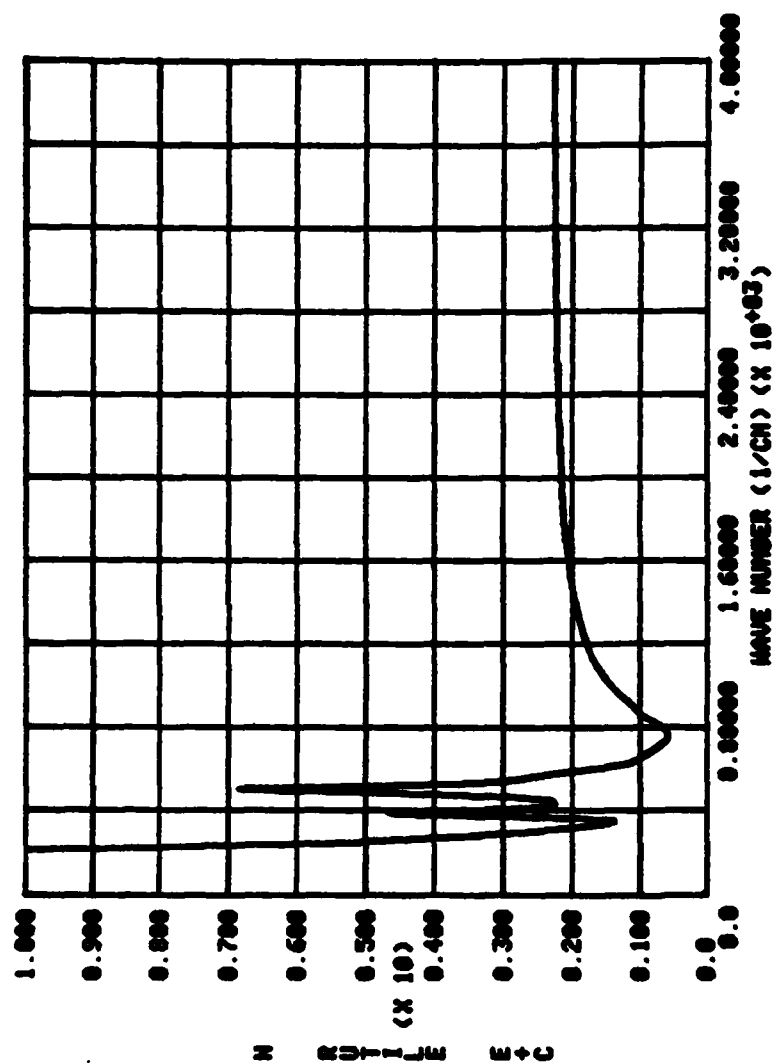


Figure E1-2. Index of refraction n of rutile (O-ray) in the 180-4,000 cm^{-1} wave-number region.

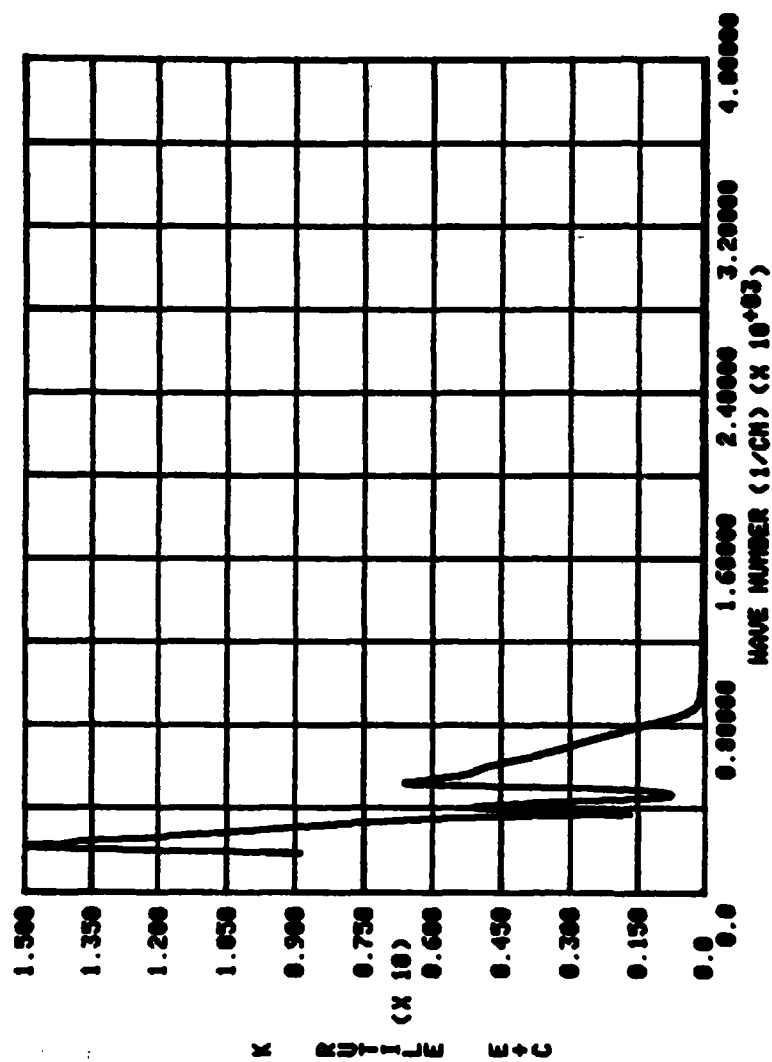


Figure E1-3. Extinction coefficient k of rutile (O-ray) in the 180-4,000 cm^{-1} wave-number region.

2. Calcite

Calcite is an optically uniaxial (-) hexagonal crystal of the $R\ 32/m$ lattice and space group. The optical directions for the E- and O-rays are respectively parallel and perpendicular to the c-axis of the crystal. The crystalline sample used in this investigation was cut parallel to the c-axis and then mechanically polished. Reflectance spectra were obtained for the E-ray (O-ray) with the incident radiant flux linearly polarized so that the electric vector was parallel (perpendicular) to the c-axis. The reflectance spectrum in the $180\text{--}4,000\text{ cm}^{-1}$ region for the O-ray (E-Ray) is presented in Fig. E2-1 (Fig. E2-4). The real and imaginary parts of $N(\nu)$ for the O-ray are presented in Figs. E2-2 and E2-3, respectively; and for the E-Ray in Figs. E2-5 and E2-6, respectively, values of $N(\nu)$ presented for the E-ray yielded non physical values for the phase shift $\phi(\nu)$ in the $875\text{--}900\text{ cm}^{-1}$ region. The absorption coefficient for the E-ray in the $875\text{--}900\text{ cm}^{-1}$ region is relatively small. We believe reflection from the back surface of the crystal was responsible for the non physical values of $\phi(\nu)$. Reflection from the back surface of the crystal was evident for both the E- and O-ray in the near infrared and visible regions. We therefore excluded from further analysis, and from this report, the reflectance spectra for Calcite in the near infrared and visible regions.

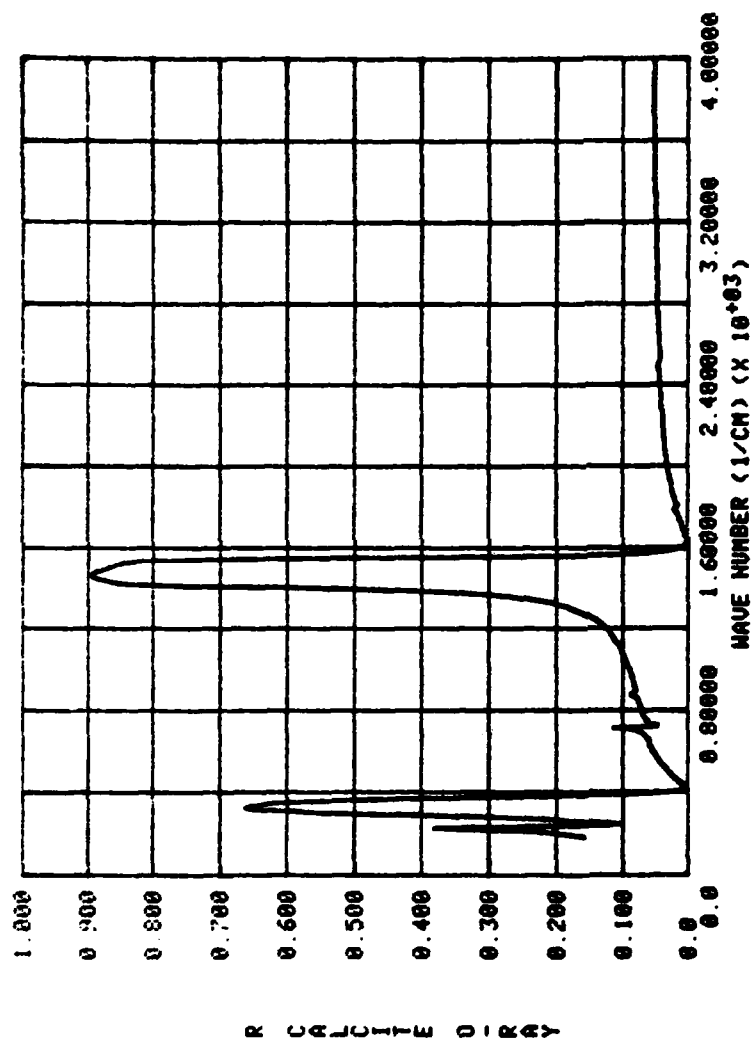


Figure E2-1. Reflectance spectrum of calcite (O-ray) in the 180-4,000 cm^{-1} wave-number region.

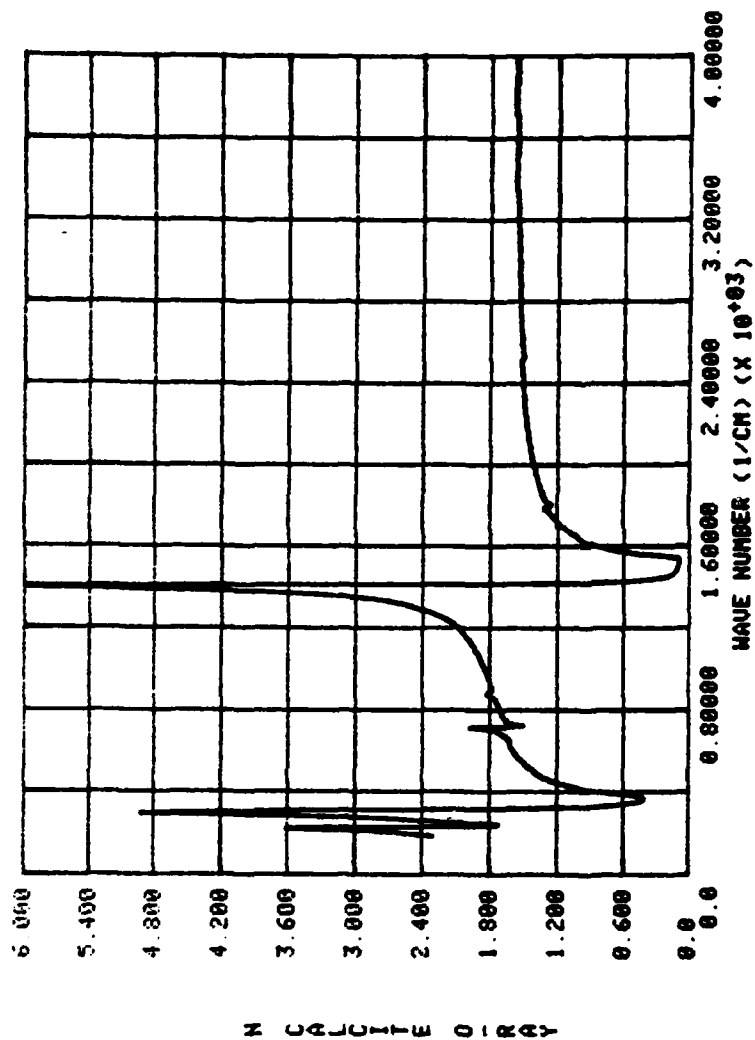


Figure E2-2. Index of refraction n of calcite (O-ray) in the $180\text{--}4,000\text{ cm}^{-1}$ wave-number region.

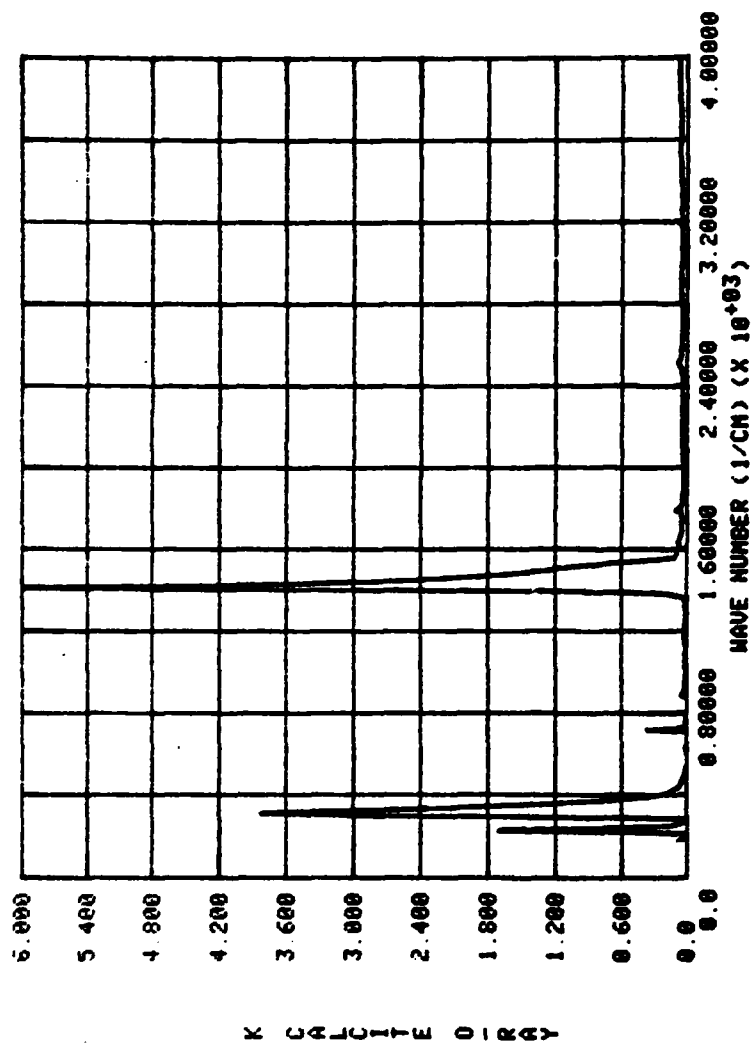


Figure E2-3. Extinction coefficient k of calcite (O-ray) in the 180-4,000 cm^{-1} wave-number region.

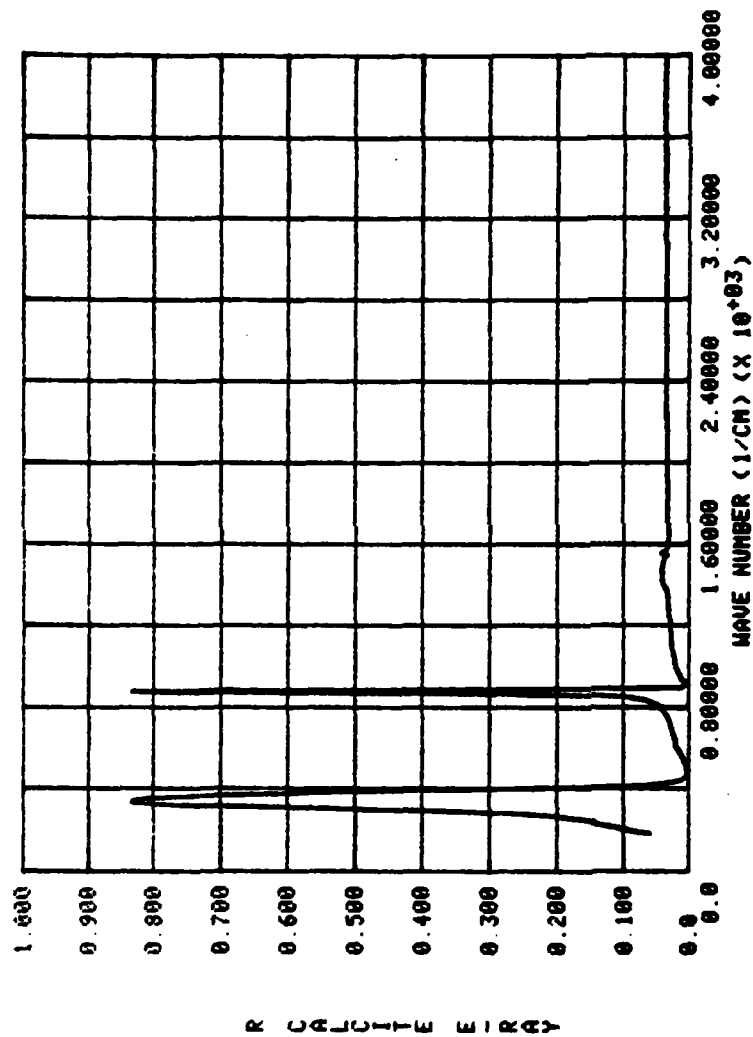


Figure E2-4. Reflectance spectrum of calcite (E-ray) in the 180-4,000 cm^{-1} wave-number region.

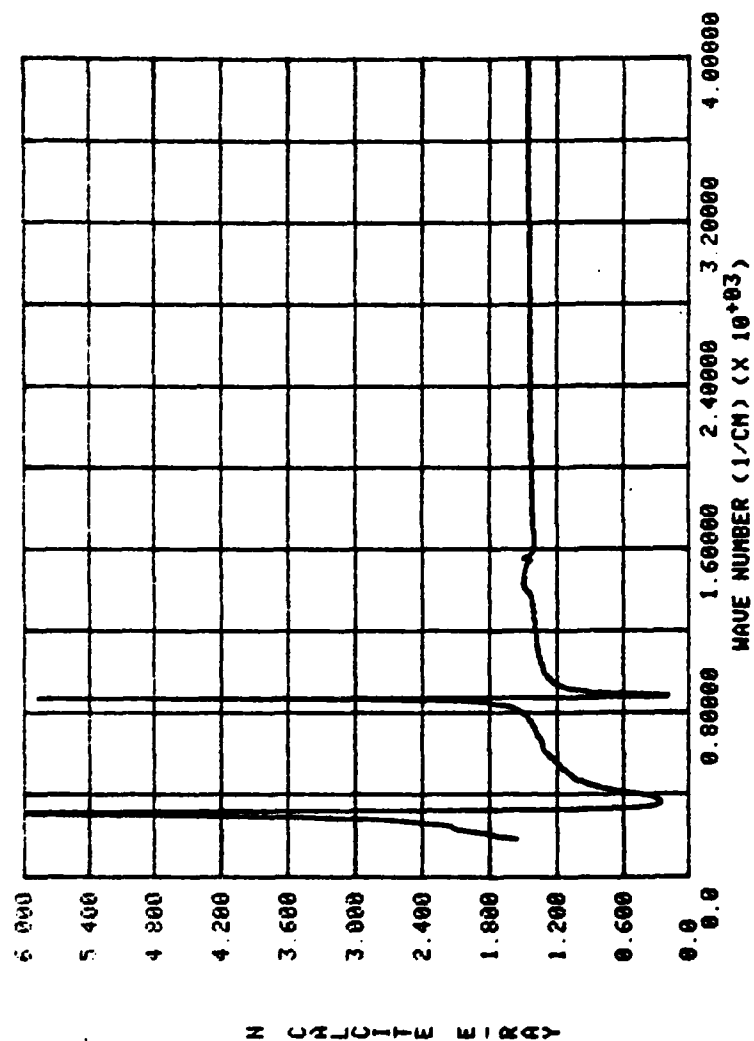


Figure E2-5. Index of refraction n of calcite (E-ray) in the 180-4,000 cm^{-1} wave-number region.

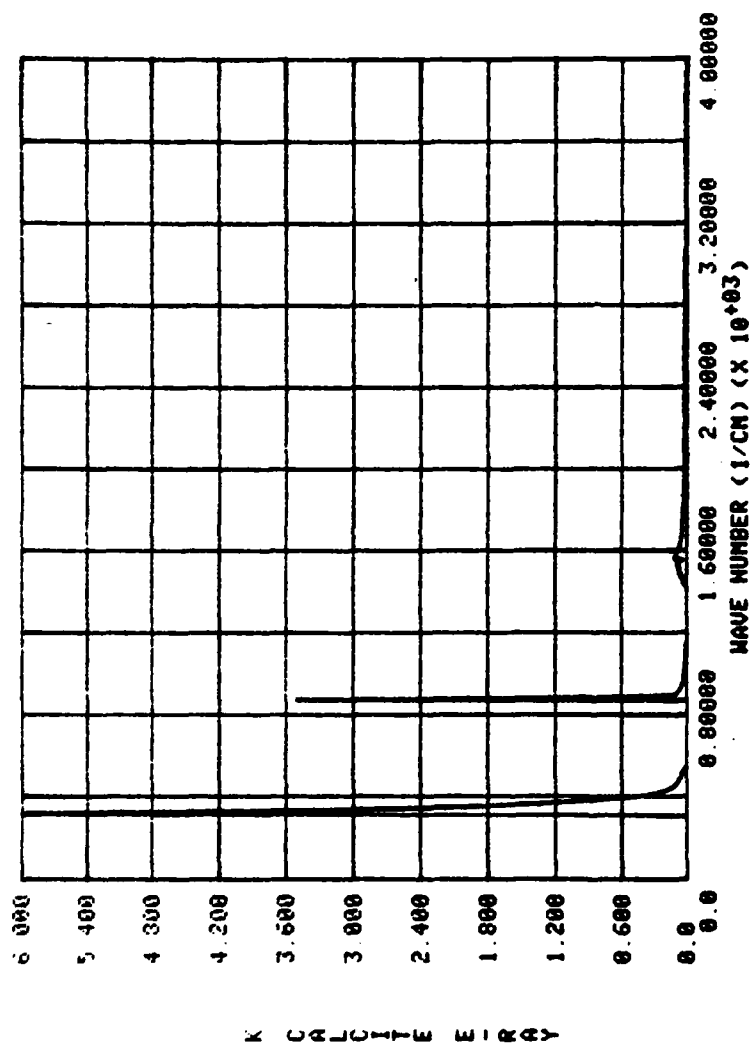


Figure E2-6. Extinction coefficient k of calcite (E-ray) in the 180-

4,000 cm^{-1} wave-number region.

3. Biotite

Biotite (Black Mica) is an optically biaxial (-) monoclinic crystal of the $C 2/m$ lattice and space group possessing perfect (001) cleavage. Two crystalline samples were prepared for this investigation; one was cut on the (100) plane the other on the (010) plane. The two samples were mechanically polished. The Y optical direction coincides with the b-axis of the crystal. The Z optical direction forms an angle of 0-9 degrees with the a-axis of the crystal. Thus reflectance spectra were obtained for linearly polarized radiant flux with the electric vector E parallel to the a, b, and c axes of the crystal. Reflectance spectra were obtained in the $180-40,000\text{ cm}^{-1}$ region. However, the reflectance spectra in the visible region contained an artifact due to a damaged calcite polarizer and those spectra were eliminated from further consideration. We now have a new uv-vis-nir spectrophotometer system on order and will remeasure the reflectance spectra of the Biotite with that instrument. The reflectance spectra for Biotite are shown in Figs. E3-1, E3-4, and E3-7 respectively for E parallel to the a, b, and c axes. The real and imaginary parts of $N(\nu)$ in the infrared region are shown in Figs. E3-2 and E3-3 for E parallel to a, in Figs. E3-5 and E3-6 for E parallel to b, and Figs. E3-8 and E3-9 for E parallel to c.

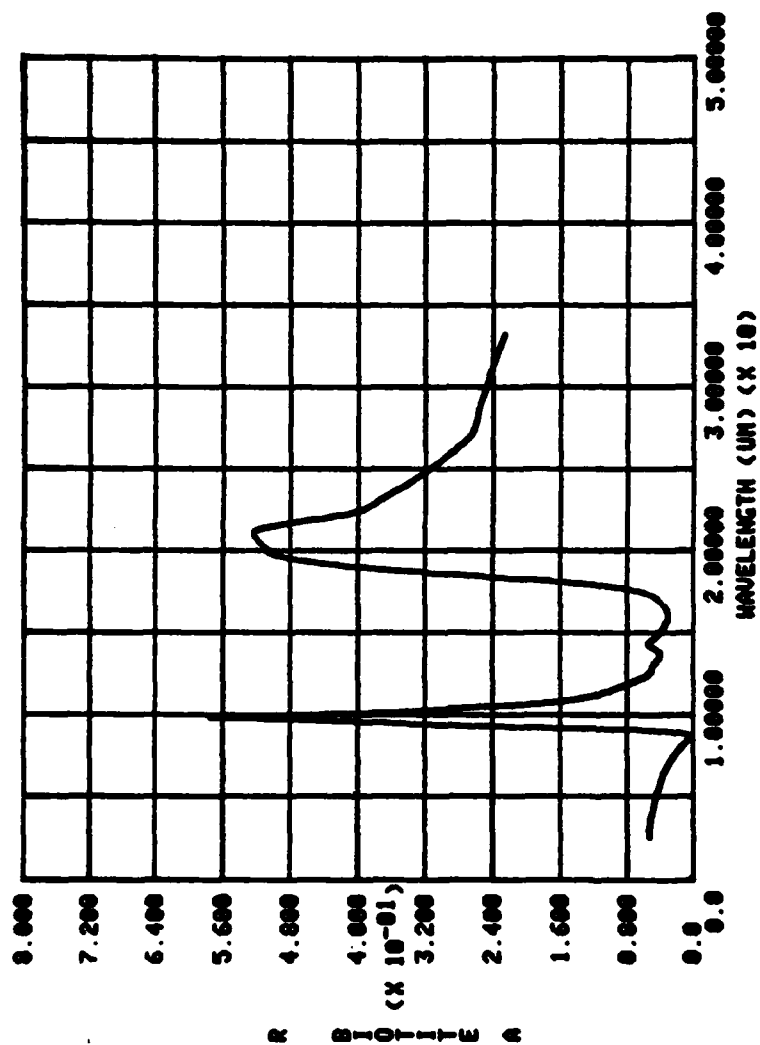


Figure E3-1. Reflectance spectrum of Biotite a-axis in the 2.5-33 μm wavelength region.

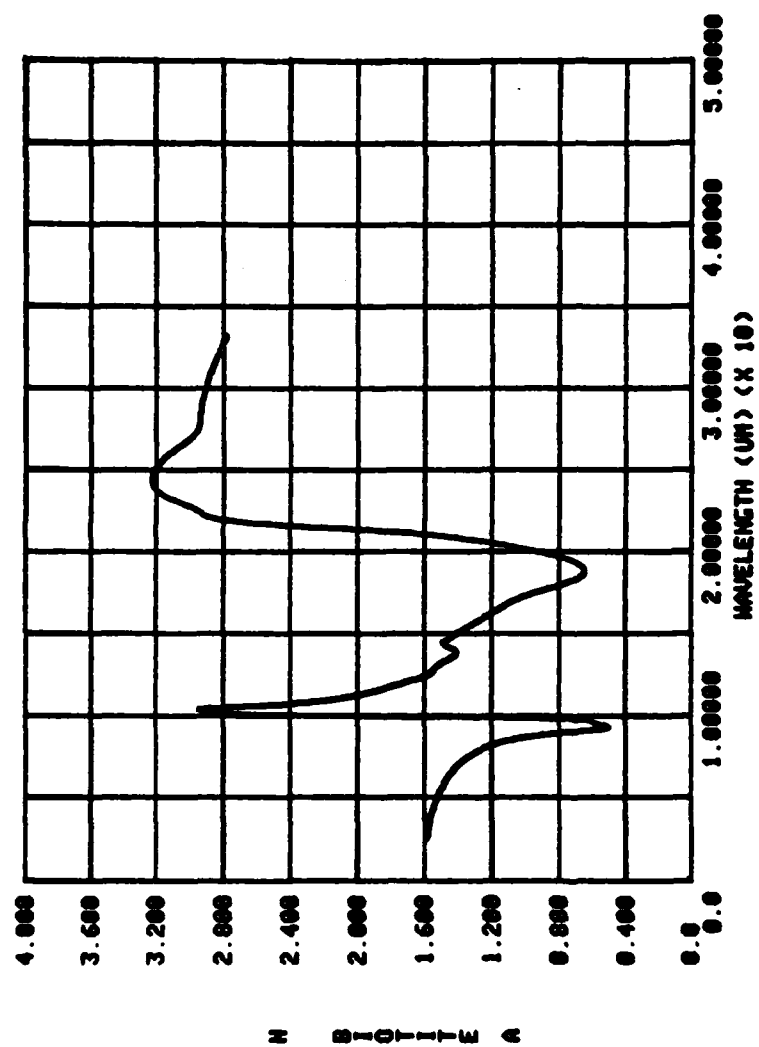


Figure E3-2. Index of refraction n of Biotite a-axis in the 2.5-33 μm wavelength region.

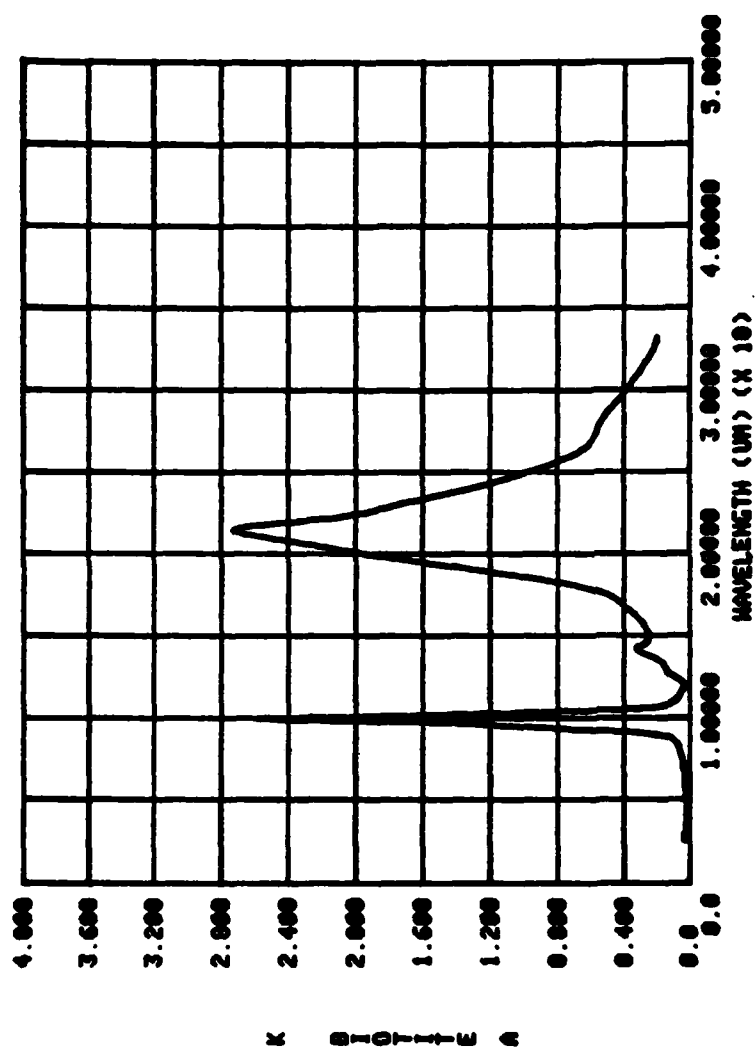


Figure E3-3. Extinction coefficient k of Biotite a-axis in the 2.5-33 μm wavelength region.

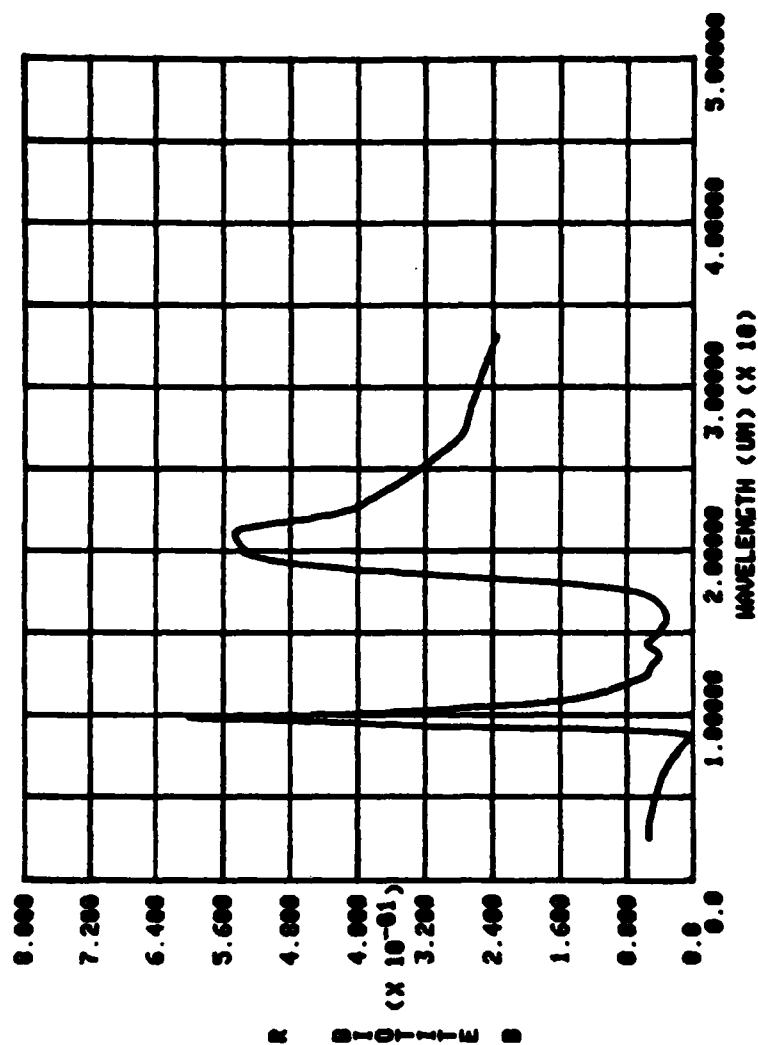


Figure E3-4. Reflectance spectrum of Biotite b-axis in the 2.5-33 μm wavelength region.

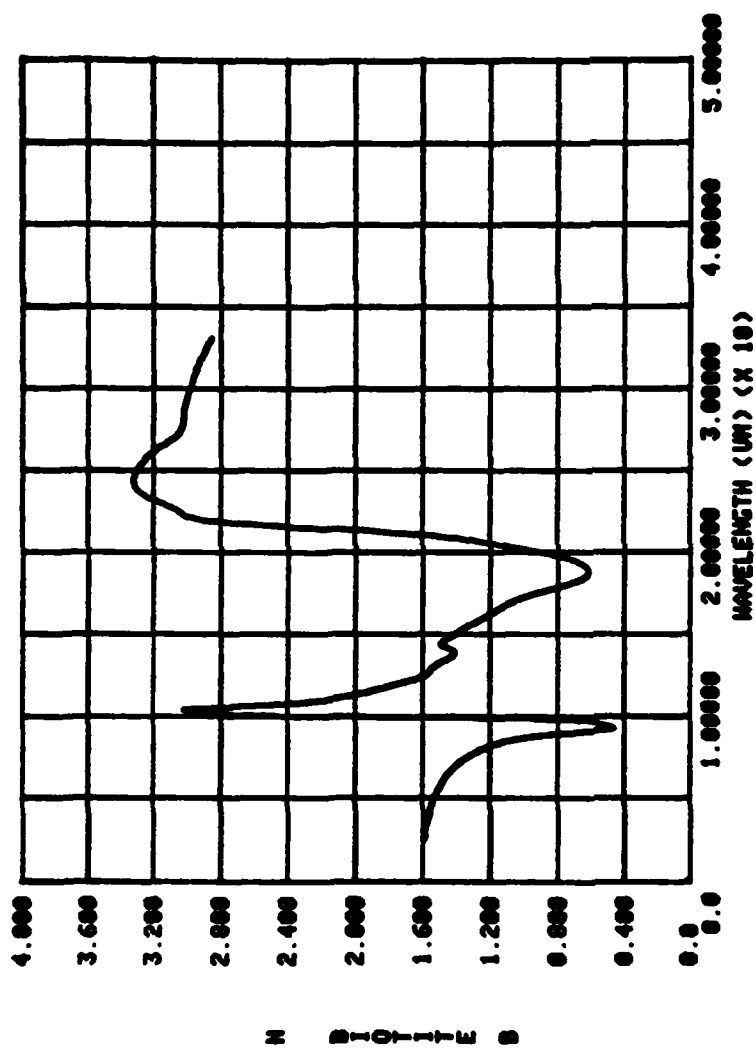


Figure E3-5. Index of refraction of n Biotite b-axis in the 2.5-33 μm wavelength region.

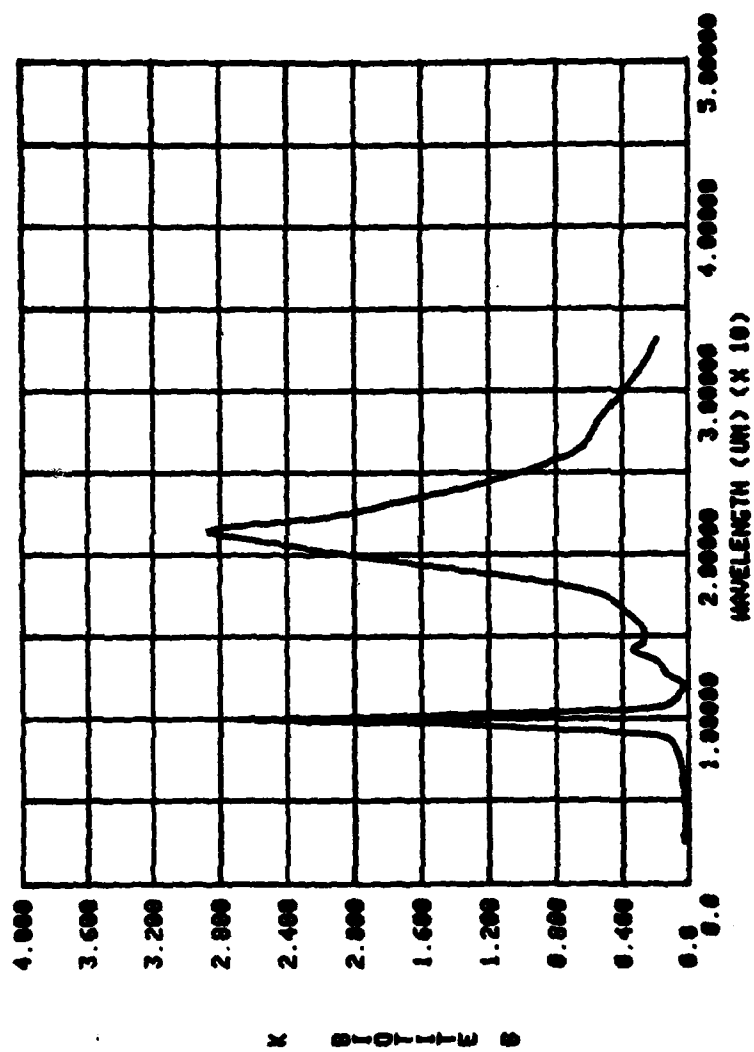


Figure E3-6. Extinction coefficient k of Biotite b-axis in the 2.5-33 μm wavelength region.

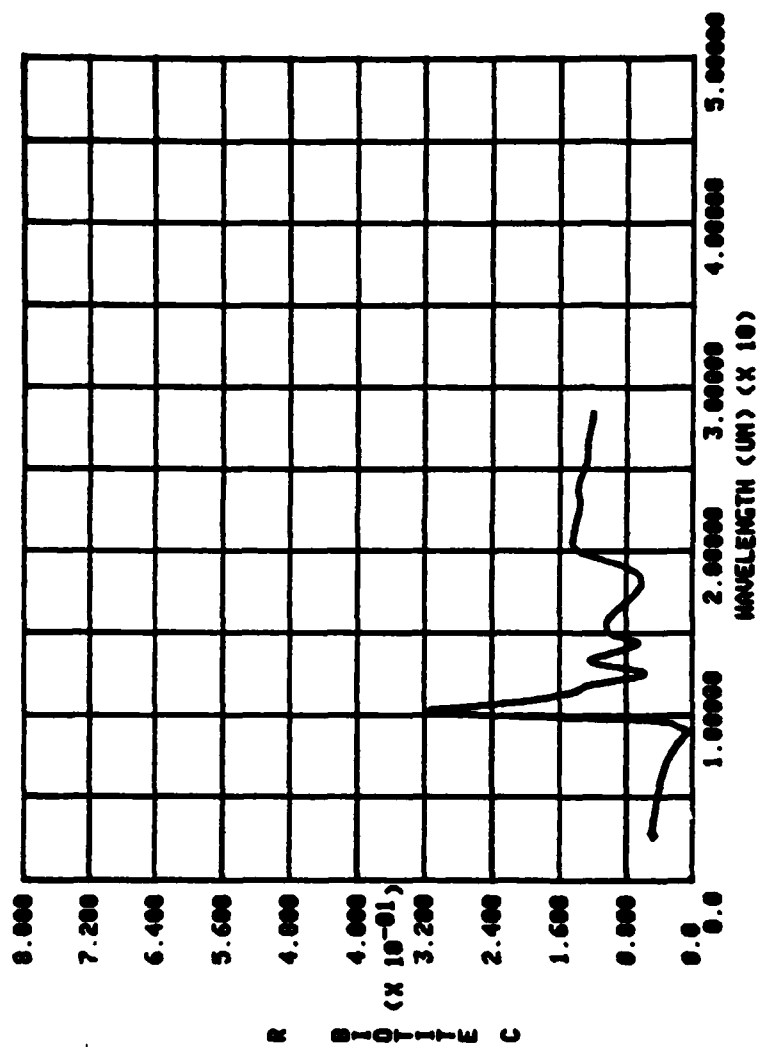


Figure E3-7. Reflectance spectrum of Biotite c-axis in the 2.5-28 μm wavelength region.

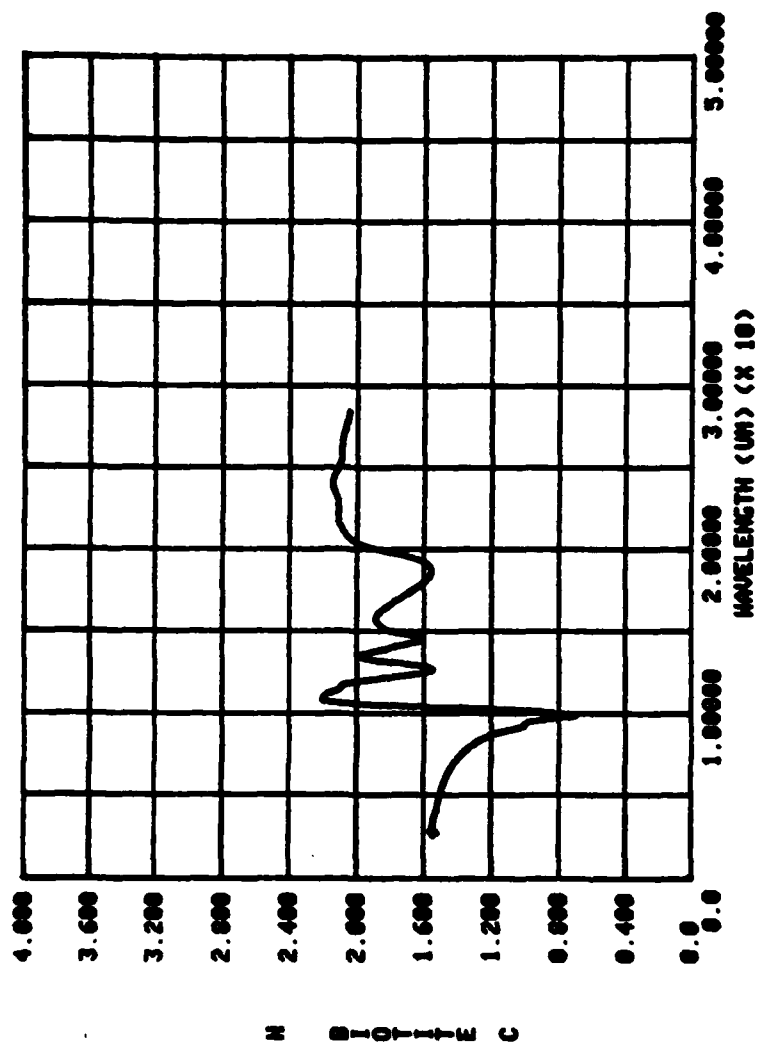


Figure E3-8. Index of refraction of Biotite c-axis in the 2.5-28 μm wavelength region.

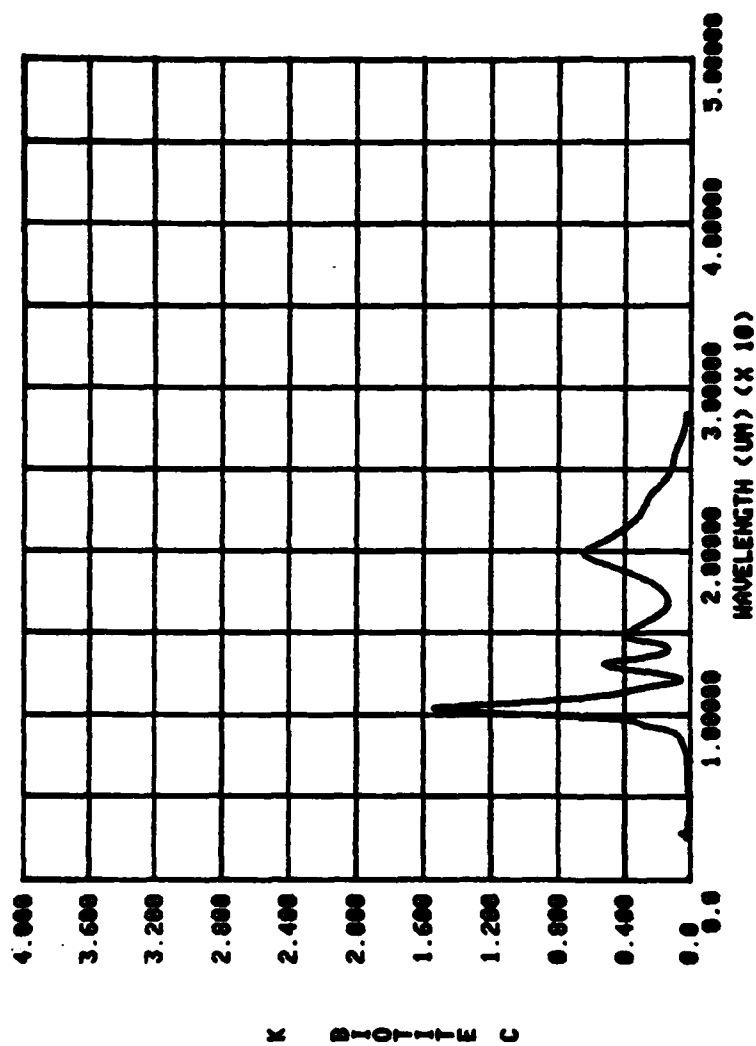


Figure E3-9. Extinction coefficient k of Biotite c-axis in the 2.5-28 μm wavelength region.

4. Phlogopite

Phlogopite is an optically biaxial (-) monoclinic crystal of the $C 2/m$ lattice and space group and possesses perfect (001) cleavage. Two crystal samples of phlogopite were prepared for this investigation; one was the (001) cleavage surface and the other was cut and polished parallel to the (100) plane. The Y optical direction coincides with the b-axis of the crystal, the X optical direction forms an angle of 0-5 degrees with the c axis of the crystal, and the Z optical direction forms an angle of 2-4 degrees with the a axis. Thus we obtained reflectance spectra for linearly polarized radiant flux with the electric vector E separately parallel to the a, b, and c axes. The reflectance spectra for E parallel to the a and b axes were obtained on the (001) cleaved surface, and for E parallel to the c axis on the cut and polished (100) surface. The reflectance spectra for E parallel to a, b, and c axes are presented in Figs. E4-1, E4-2, and E4-3, respectively.

The reflectance spectra presented in Figs. E4-1 and E4-2 show, in the $1,500-4,000\text{ cm}^{-1}$ region, characteristics of transmittance spectra rather than reflectance spectra. It appears that cleaving the crystal for the reflectance studies also broke some of the bonds between (001) lamellar planes that remained with the sample. This produced multiple internal reflections that are the source of the

interference fringes and the H_2O absorption bands in the $3,600\text{--}3,700\text{ cm}^{-1}$ region. All (001) cleaved surfaces yielded similar spectra.

The reflectance spectrum shown in Fig. E4-3 for E parallel to the c axis was obtained on the (010) surface which is perpendicular to the (001) cleavage. The interference fringes and absorption bands are not present in this spectrum.

Complex refractive indices were computed only for the spectrum in Fig. E4-3. The leakage of the single polarizer in the $180\text{--}400\text{ cm}^{-1}$ gave inconsistent values of $N(\nu)$ in this region. Thus $N(\nu)$ for E parallel to the c axis is presented in Figs. E4-4 and E4-5 only for the $400\text{--}4,000\text{ cm}^{-1}$ region.

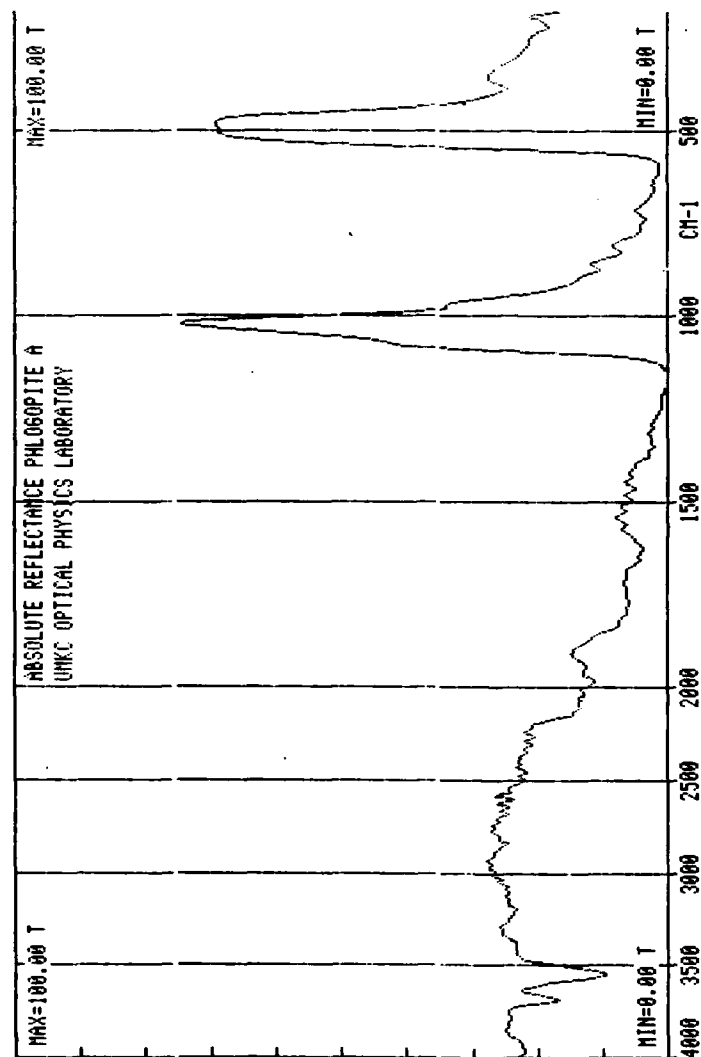


Figure E4-1. Reflectance spectrum of Phlogopite a-axis in the 180-4,000 cm^{-1} wave-number region.

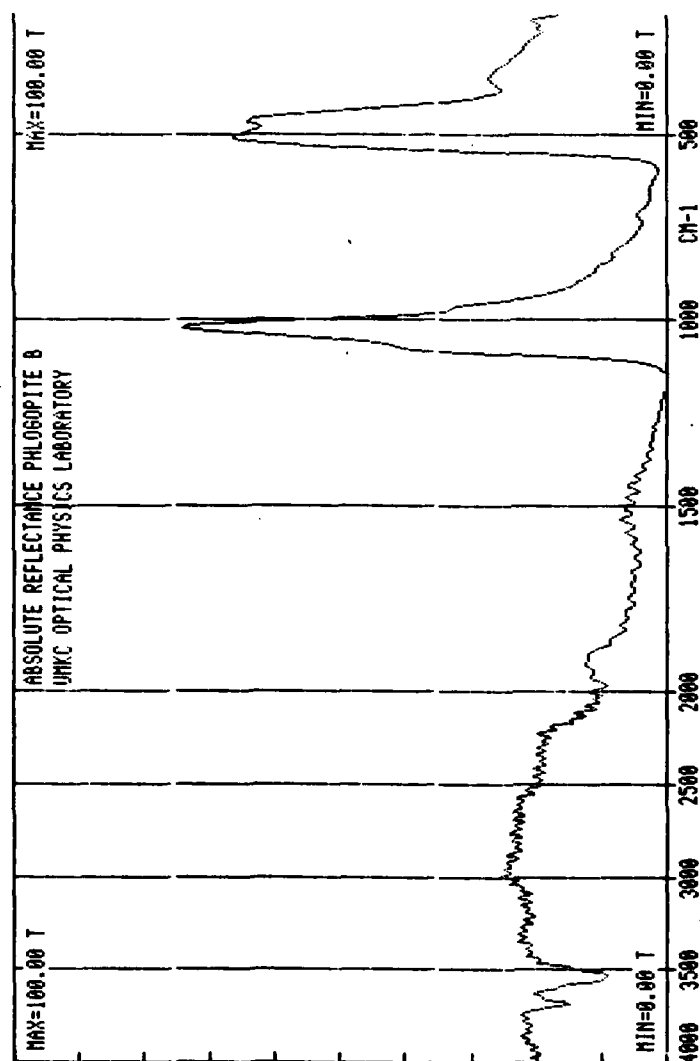


Figure E4-2. Reflectance spectrum of Phlogopite b-axis in the 180-4,000 cm^{-1} wave-number region.

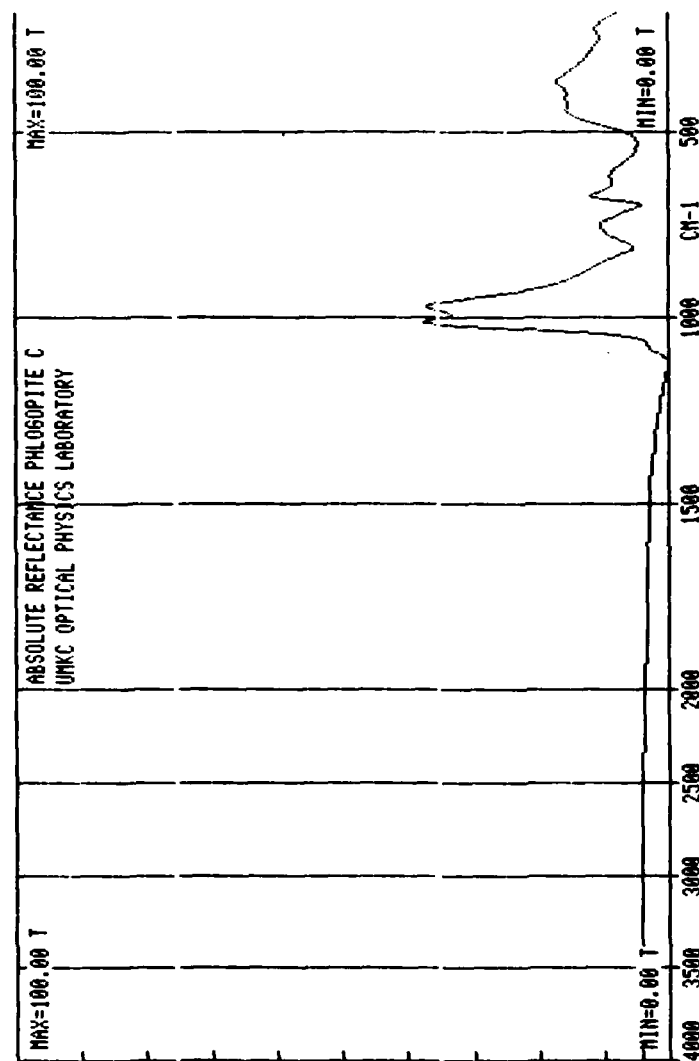


Figure E4-3. Reflectance spectrum of Phlogopite c-axis in the 180-4,000 cm^{-1} wave-number region.

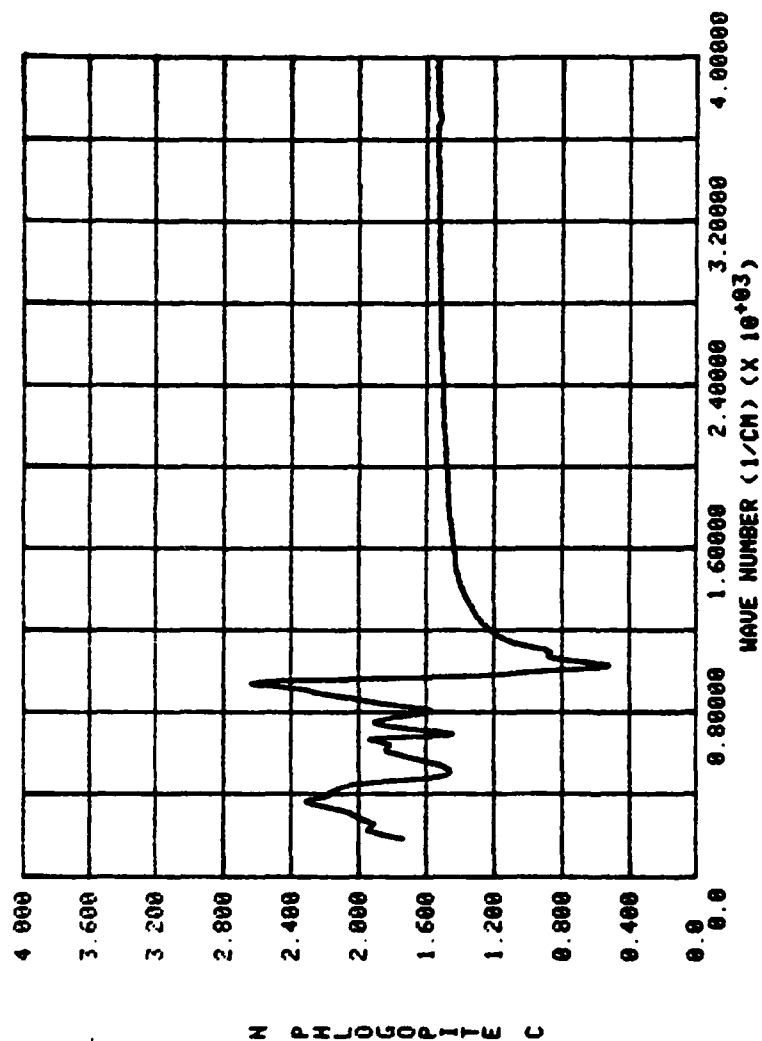


Figure E4-4. Index of refraction n of Phlogopite c-axis in the 180-4,000 cm^{-1} wave-number region.

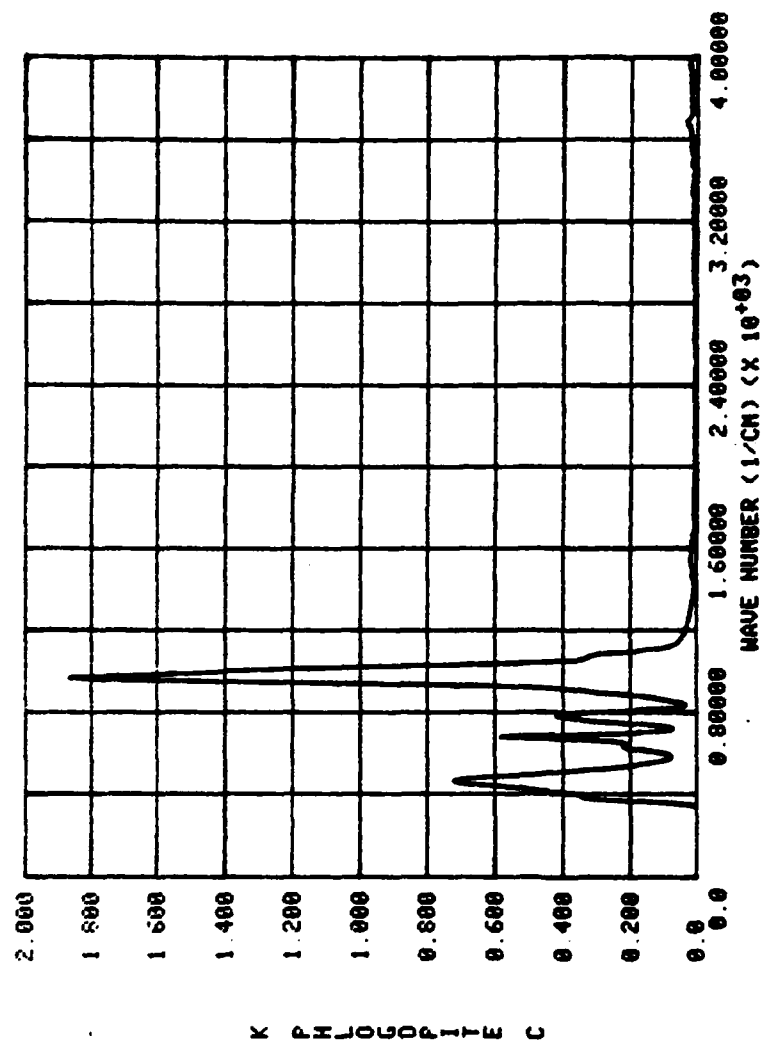


Figure E4-5. Extinction coefficient k of Phlogopite c-axis in the 180-

4,000 cm^{-1} wave-number region.

5. Muscovite

Muscovite is an optically biaxial (-) monoclinic crystal of the $C 2/m$ lattice and space group, and possesses perfect (001) cleavage. Two crystal samples of Muscovite were prepared, one was the (001) cleavage plane and the other was cut and polished parallel to the (010) plane. The Z optical direction corresponds to the b axis of the crystal, the X optical direction is at an angle from 0 to -5 degrees relative to the c axis, and the Y optical direction is at an angle of 1-3 degrees relative to the a axis. Thus we measured reflectance spectra of the (001) cleavage surface for radiant flux linearly polarized with the electric vector E parallel to the a and b crystal axes and reflectance spectra of the (010) plane with linear polarization parallel to the c axis. The reflectance spectrum for E parallel to the a axis is presented in Fig. E5-1 for the $400\text{--}4,000\text{ cm}^{-1}$ region and in Fig. E5-2 for the $180\text{--}400\text{ cm}^{-1}$ region. Note that in the $1,800\text{--}4,000\text{ cm}^{-1}$ region the spectrum in Fig. E5-1 has the appearance of a transmittance spectrum. Transmittance measurements on a thin cleaved (001) lamellar muscovite sample showed muscovite to possess less absorption in the $1,800\text{--}4,000\text{ cm}^{-1}$ region. Additionally, there are multiple interference fringes in $1,500\text{--}4,000\text{ cm}^{-1}$ region of the spectrum in Fig. E5-1. It thus appears that cleaving the crystal

for the reflectance studies also broke some of the bonds between (001) planes remaining with the sample and this produced multiple internal reflections and caused the interference fringes and also the water absorption bands in the $3,600\text{--}3,700\text{ cm}^{-1}$ region.

The reflectance spectrum for E parallel to the b axis is shown in Figs. E5-3 and E5-4. This spectrum (Fig. E5-3) was also acquired from the (001) cleavage surface and shows interference fringes and absorptions similar to those previously described in Fig. E5-1.

The reflectance spectrum for E parallel to the c axis is shown in Figs. E5-5 and E5-6. This spectrum was acquired from the cut and polished (010) surface, i.e. perpendicular to the (001) cleavage planes. The interference fringes and absorptions are not present in Fig. E5-5. However, the reflectance at the peaks near $1,050$ and 550 cm^{-1} is about 35% which is lower than was expected. We attribute this to the extreme difficulty encountered in preparing a specular surface perpendicular to the cleavage planes, although we have no other spectra to compare.

Complex refractive indices $N(\nu)$ were obtained only for the reflectance spectrum shown in Fig. E5-5. Leakage of the single polarizer used in the $180\text{--}400\text{ cm}^{-1}$ region gave inconsistent values of $N(\nu)$ in this lower frequency region. $N(\nu)$ for E parallel to the c axis are presented in Fig. E5-7 and E5-8.

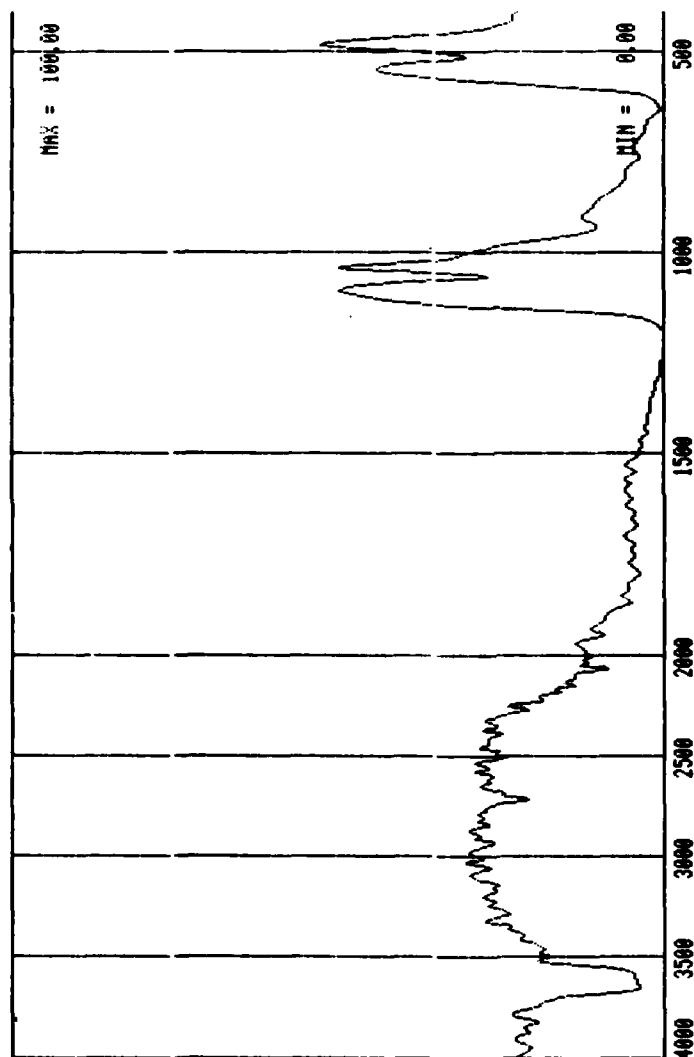


Figure E5-1. Reflectance spectrum of Muscovite a-axis in the 400-4,000 cm^{-1} wave-number region.

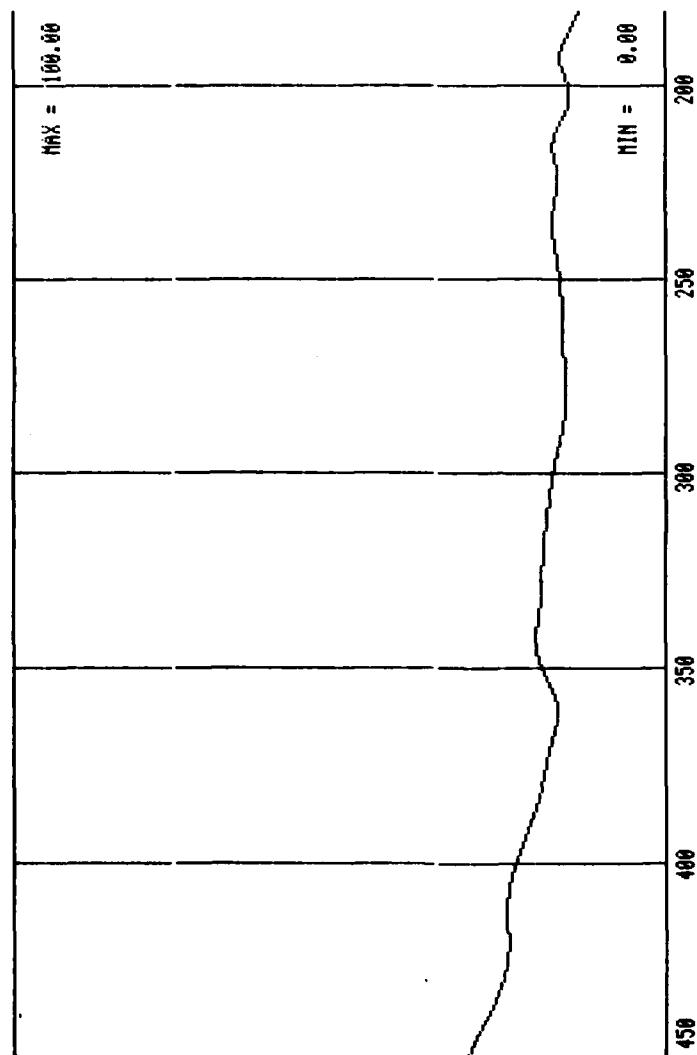


Figure E5-2. Reflectance spectrum of Muscovite a-axis in the 180-450 cm^{-1} wave-number region.

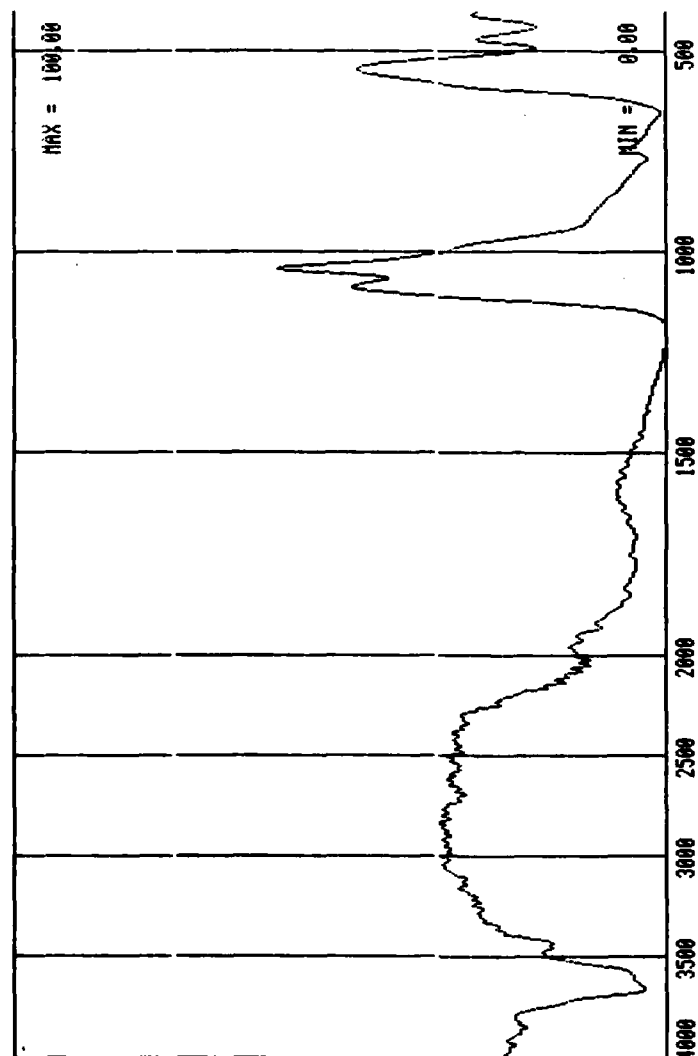


Figure E5-3. Reflectance spectrum of Muscovite \hat{b} -axis in the 400-4,000 cm^{-1} wave-number region.

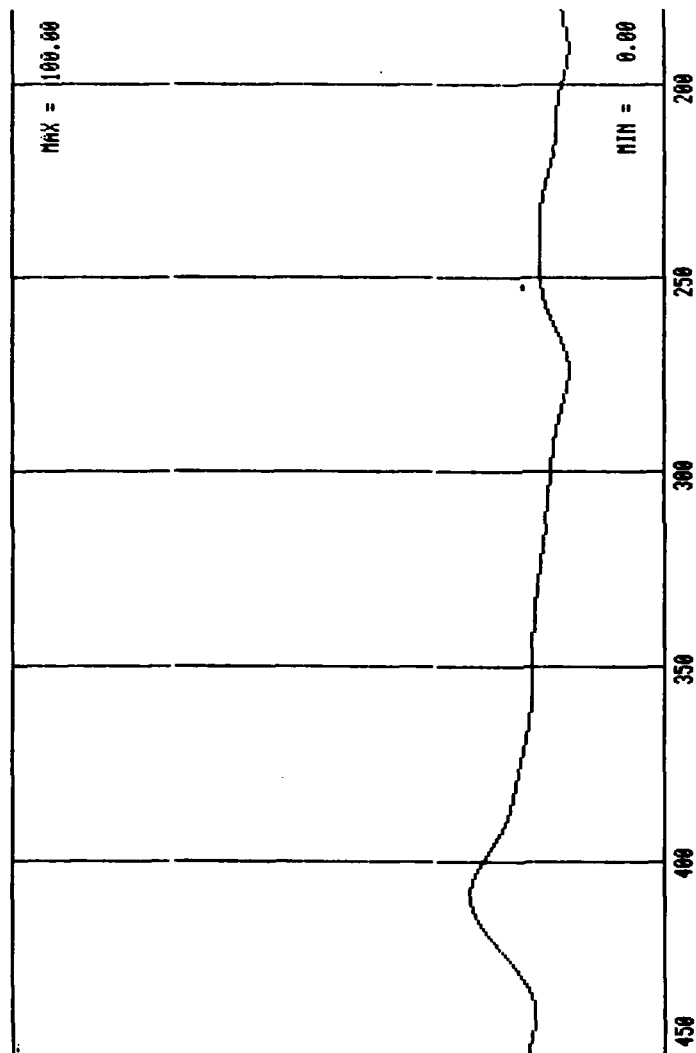


Figure E5-4. Reflectance spectrum of Muscovite b-axis in the 180-450 cm^{-1} region.

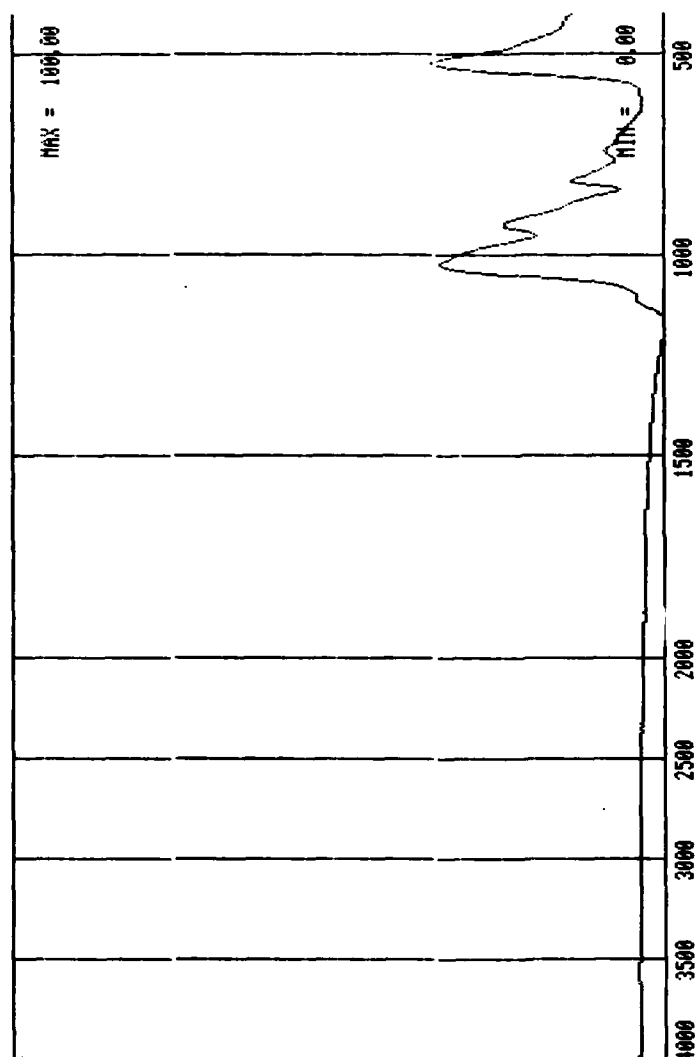


Figure E5-5. Reflectance spectrum of Muscovite c-axis in the 400-4,000 cm^{-1} wave-number region.

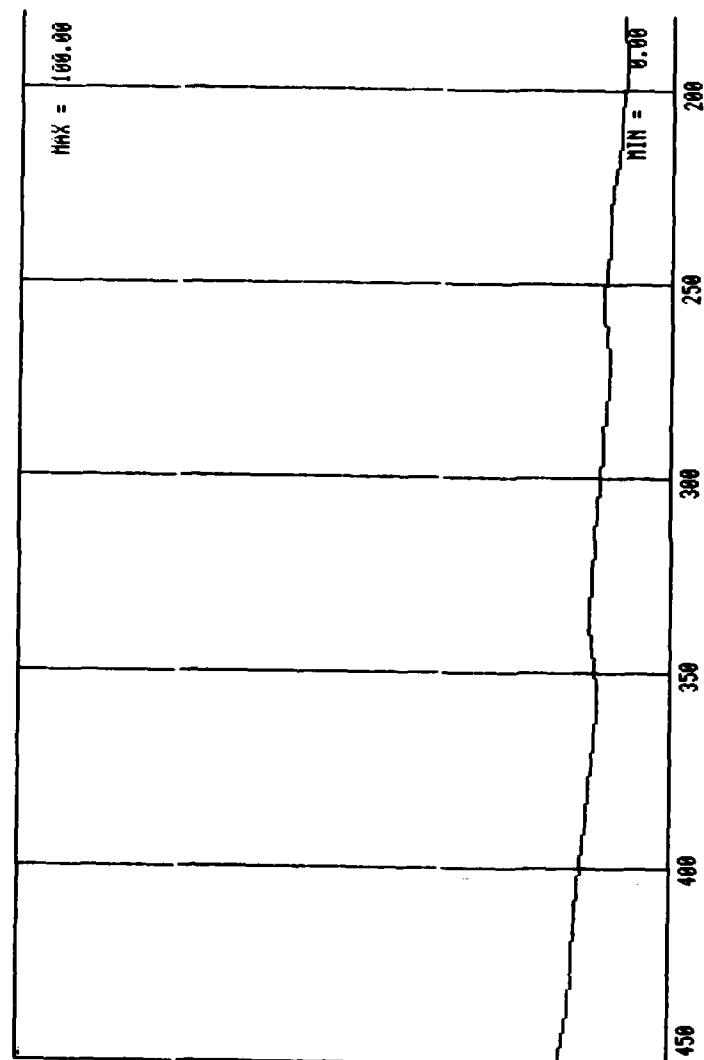


Figure E5-6. Reflectance spectrum of Muscovite c-axis in the 180-400 cm^{-1} wave-number region.

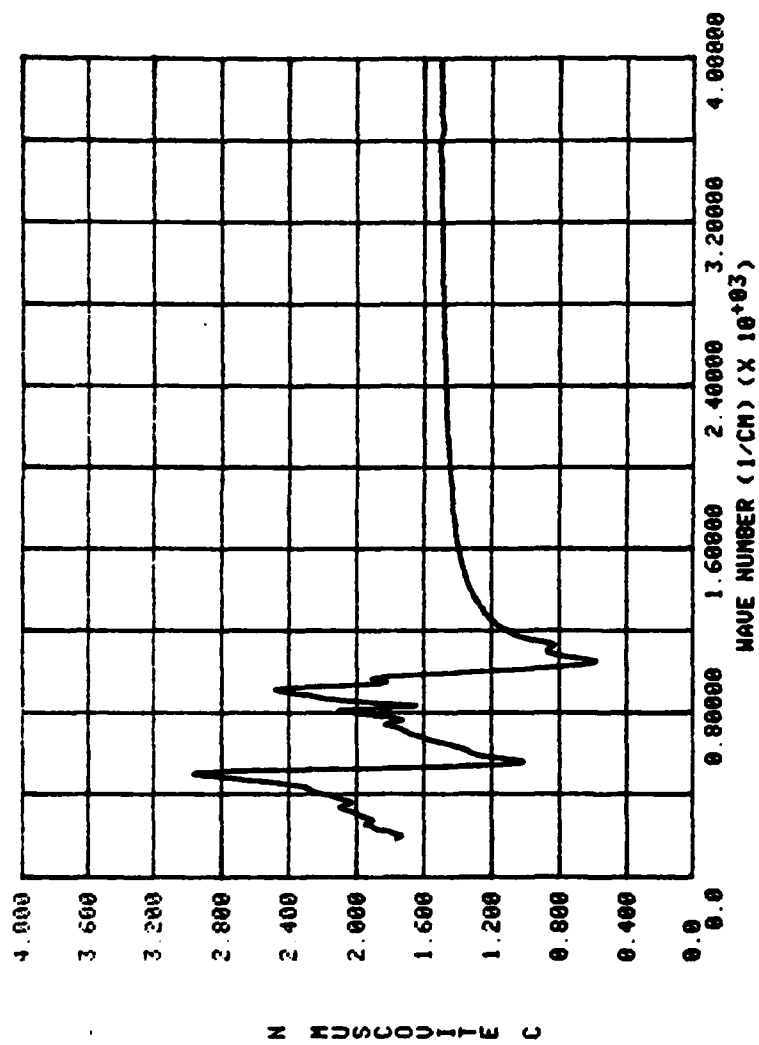


Figure E5-7. Index of refraction n of Muscovite o-axis in the 180-4,000 cm^{-1} wave-number region.

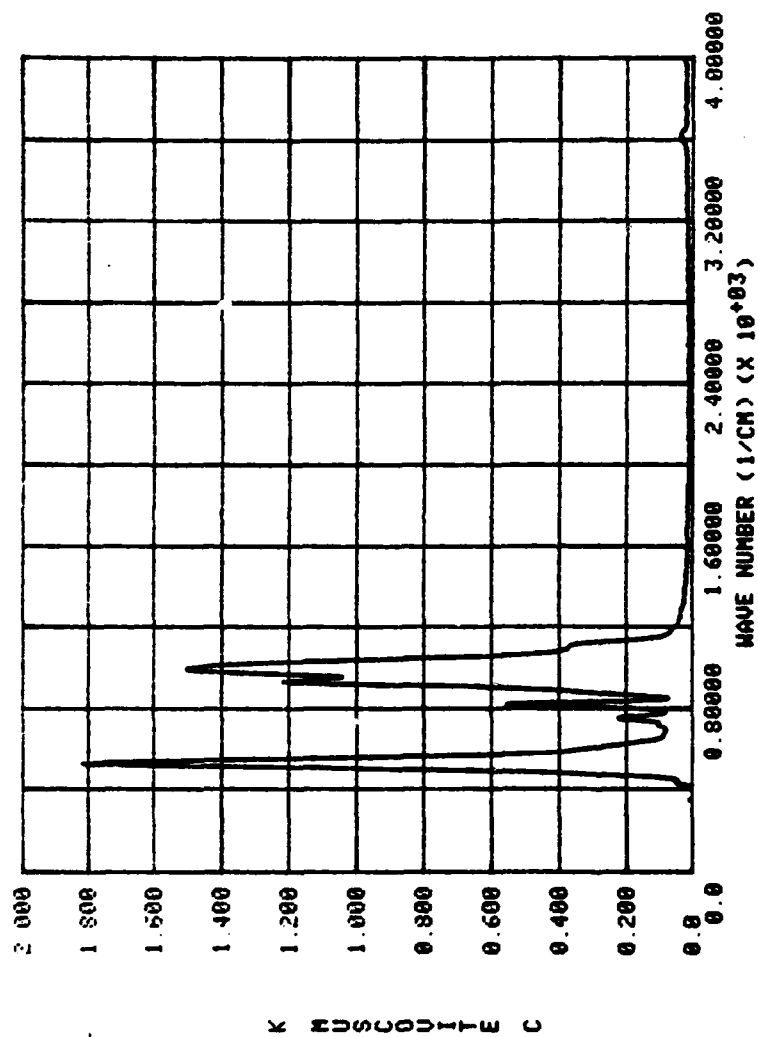


Figure E5-8. Extinction coefficient k of Muscovite c-axis in the 180-4,000 cm^{-1} wave-number region.

F. Powder/Pellet Samples

Many natural minerals occur in nature only as small crystals, i.e. powders, that preclude preparation of bulk crystalline samples suitable for reflectance measurements. The clay minerals are examples. Also the clay minerals are relatively soft and if large crystalline specimens could be acquired they could not be polished by use of conventional methods. In order to obtain reflectance spectra of such minerals they were reduced to powder by grinding and the powder was then formed into a 13 mm diameter pellet by placing the powder between polished stainless steel rams in a die and applying pressure with a hydraulic press. The 13 mm die was rated for a maximum of 10 tons of force applied to the pellet. Most pellets, however, were pressed by applying 8 tons of force.

For such pellets two primary traits are desirable. First, the pellet should have a specular surface, and second, most natural minerals are either optically uniaxial or biaxial thus a random orientation of the particles within the pellet is preferable. The specular surface is necessary because rough surfaces reflect incident radiant flux in both specular and diffuse components. The application of the Fresnel equations to determine $N(\nu)$ implicitly assumes that there is no diffuse reflectance. If diffuse reflectance is present, then values of $N(\nu)$ for dielectric minerals computed from measurements of the specular component will have $n(\nu)$ too small and $k(\nu)$ too large. The random orientation of particles within the pellet is desirable so that $N(\nu)$ is representative of all

TABLE V. Data for natural minerals pressed into pellets

Mineral	Hardness	ρ_m (g.cm ³)	ρ_p (g/cm ³)	ρ_p/ρ_m	n_D	n_p (589 nm)	n_p (2.5 μ m)
Colemanite	8T	4.5	2.40	2.06	0.858	1.586 – 1.614	1.301 (1.356) 1.311 (1.368)
Gypsum	8T	2.0	2.32	2.10	0.905	1.5205 – 1.5296	1.344 (1.381)
Illite	8T	2.0	2.70–2.78	2.46	0.894	1.555 – 1.610	1.195 (1.174) 1.331 (1.367)
Kaolin	8T	2.0–2.5	2.57–2.68	2.13	0.810	1.553 – 1.570	1.263 (1.326) 1.341 (1.426)
Kernite	8T	2.5	1.73	1.91	1.10	1.454 – 1.488	1.285 (1.256) 1.283 (1.254)
Limonite (Al.)	8T	5.0–5.5	4.09–4.48	2.97	0.694	2.150 – 2.415	1.225 (1.335) 1.40 (1.619)
Limonite (Ga.)	8T	5.0–5.5	4.09–4.48	2.40	0.561	2.150 – 2.415	
Montmorillonite	8T	1.0–2.0	1.98–2.06	2.19	1.10	1.475 – 1.534	
Pyrolusite	8T	1.0–2.0	4.75	3.48	0.732	1.303 – 1.623	1.176 (1.244) 1.418 (1.604)
Vermiculite (Cn.)	3T	1.5–2.0	2.26–2.35	1.95	0.848	1.525 – 1.581	
Vermiculite (Id.)	3T	1.5–2.0	2.26–2.35	2.00	0.869	1.525 – 1.561	
Wavellite	8T	3.5–4.0	2.31–2.46	2.00	0.851	1.520 – 1.561	1.259 (1.315) 1.235 (1.283)
Gypsum	14T	2.0	2.32	2.21	0.952	1.5205 – 1.5296	1.420 (1.444)
Pyrolusite	16T	1.0–2.0	4.75	3.44	0.724	1.303 – 1.623	1.882 (1.998)

optical directions within the crystal. The effect of surface roughness on measurements of specular reflectance has been investigated by Bennet et. al. (1961).

This method of pressing pellets, measuring their specular reflectance, and computing $N(\nu)$ from the reflectance spectrum was previously applied by Toon (1977) to montmorillonite and by Volz (1973) to $(\text{NH}_4)_2 \text{SO}_4$. Toon (1976) has suggested that although diffuse reflectance is present with pellet surfaces one may be able to obtain values of $N(\nu)$ from the specular reflectance that are adequate for Mie scattering computations.

The purpose of this investigation was to determine the validity of $N(\nu)$ obtained from measurements of the specular component of reflectance from pellet surfaces. Natural minerals investigated by use to the pellet method are listed in column 1 of Table V. The hardness (Mohs Scale) and density ρ_m of these minerals are listed in columns 2 and 3, respectively. The density of the pellets ρ_p and the ratio ρ_p / ρ_m are listed in columns 4 and 5, respectively. The range of refractive indices $n(\nu)$ at 589 nm wavelength (Sodium D lines) for the mineral is listed in column 6 and for the pellet in column 7. In column 7 values n in parenthesis have been corrected for density by applying the Lorentz- Lorenz formula

$$\frac{(n^2-1)}{(n^2-2)} = \frac{\rho_m (n_p^2-1)}{\rho_p (n_p^2+2)} \quad (12)$$

which provides

$$n^2 = (1 + 2a)/(1 - a), \quad (13)$$

where

$$a = \frac{\rho_m (n_p^2 - 1)}{\rho_p (n_p^2 + 2)}. \quad (14)$$

Similarly, values of n_p at 2.5 μm are listed in column 8 of Table V.

Values of $k(v)$ for these minerals are not available in the literature

thus similar comparisons for $k(v)$ could not be made.

1. Gypsum

A part of the investigations of gypsum were discussed in Section VD. Additional investigations of the optical properties of gypsum in the infrared are described in this section. Those additional investigations consisted of additional reflectance measurements on the same gypsum pellet discussed in Section VD. The pellet, however, was repressed with 14 tons of force applied to the 13 mm pellet rather than 8 tons. These will be referred to as the 14T and 8T pellets. Also, transmittance measurements were made for minute quantities of gypsum mixed with KBr and pressed into 13 mm dia. pellets.

The specular reflectance spectra of gypsum pellets pressed with 8 tons and 14 tons of force and the ratio of the specular reflectance of the 8T pellet to that of the 14T pellet is shown in Fig. F1-1. We conclude from the ratio reflectance spectrum shown in Fig. F1-1 that (1) the 14T pellet provided greater specular reflectance throughout the spectrum, (2) there are possible slight shifts in the infrared bands for the 8T and 14T pellets, and (3) the 14T pellet had a much smoother surface. The decrease in relative reflectance with increasing wave number (decreasing wavelength) indicates that the 14T pellet should yield superior values of $N(\nu)$ for gypsum "powder". Values for $n(\nu)$ and $k(\nu)$ computed by Kramers-Kronig methods

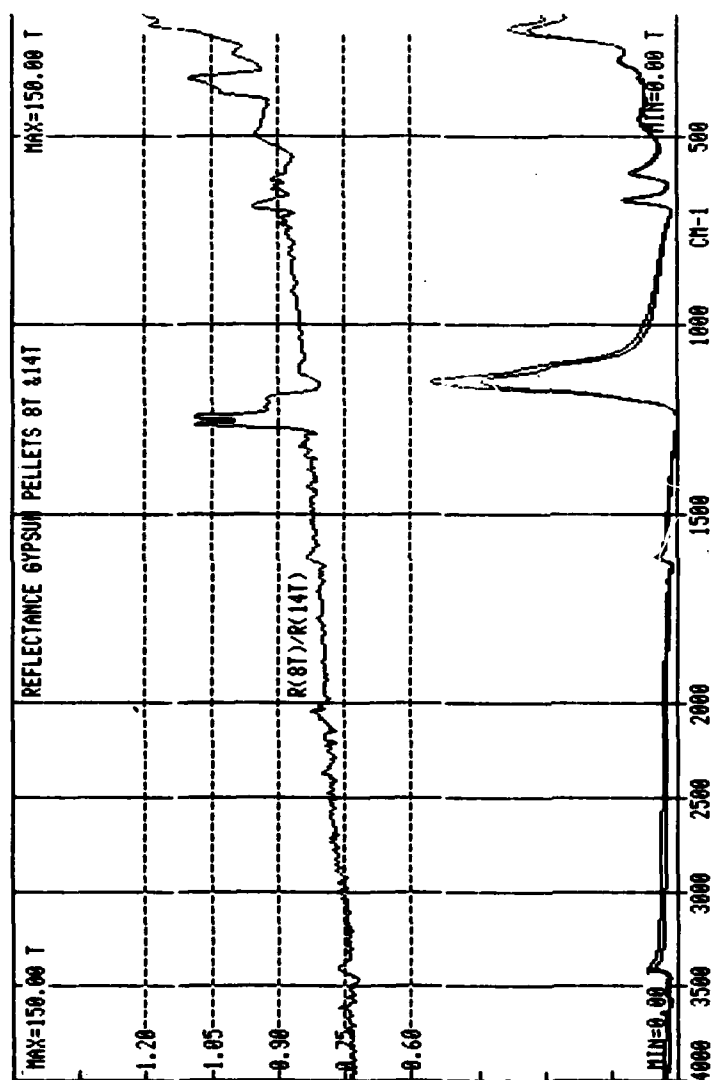


Figure F1-1. Reflectance spectra $R(8T)$ and $R(14T)$ of the 8T and 14T gypsum pellets, and ratio reflectance $R(8T)/R(14T)$ in the 180-4,000 cm^{-1} wave-number region.

applied to the specular reflectance spectrum of the 14T pellet are presented in Figs. F1-2 and F1-3, respectively.

The specular reflectance R at normal incidence for a smooth surface is given by

$$R = \frac{(n-1)^2 + k^2}{(n+1)^2 + k^2} . \quad (15)$$

Thus we see that measurements of R are sensitive to k^2 where k is the imaginary part of $N(\nu)$. If $k = 0.05$, then $k^2 = 0.0025$ and reflectance measurements with some degree of confidence in the fourth significant digit would be required to determine k . Typical uncertainty in our reflectance measurements is $(\Delta R/R) = 0.025$, which, at best, provides some degree of confidence in the third significant digit. An analysis of uncertainties in $\Delta N = \Delta n + i\Delta k$ was presented in Section VC.

In order to determine better values of k for Gypsum powder we mixed varying minute quantities of Gypsum powder with KBr and pressed the mixtures into 13 mm dia. pellets. Thirteen separate gypsum/KBr pellets were formed and transmittance spectra were obtained in the $300-4,000 \text{ cm}^{-1}$ region. Transmittance spectra for three of the pellets are shown in Fig. F1-4. From the thirteen transmittance spectra four spectra were chosen which possessed the least scattering that is characteristic of some KBr pellets.

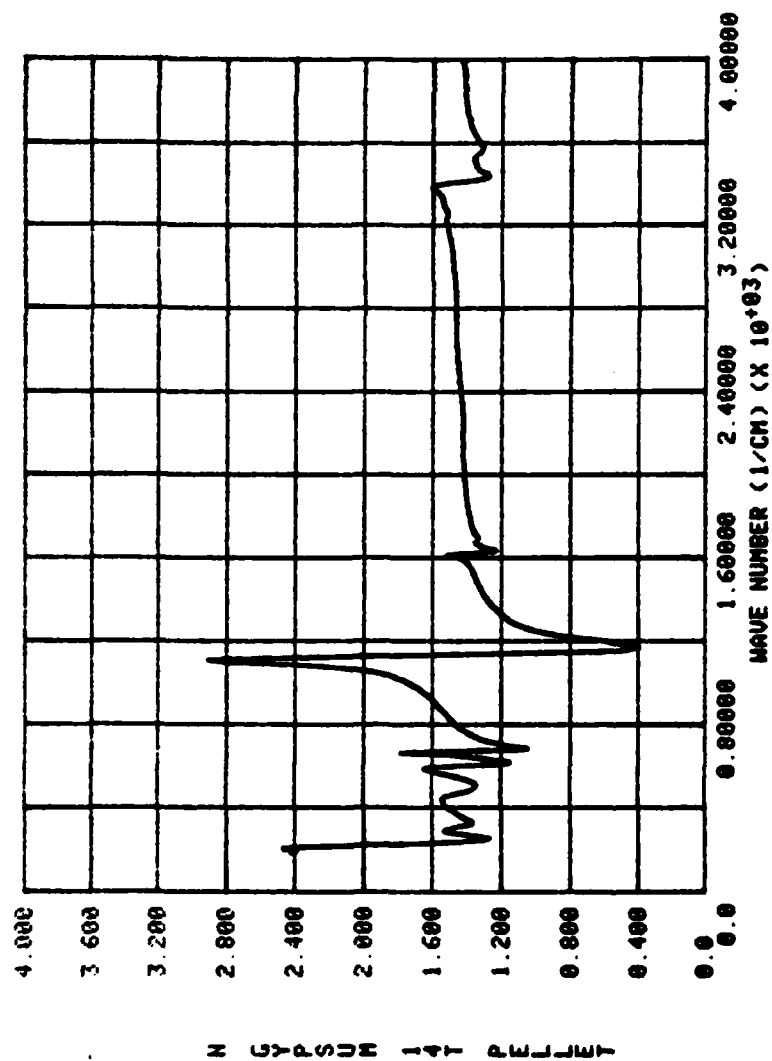


Figure F1-2. Index of refraction n of the 14T gypsum pellet in the 180-4,000 cm^{-1} wave-number region.

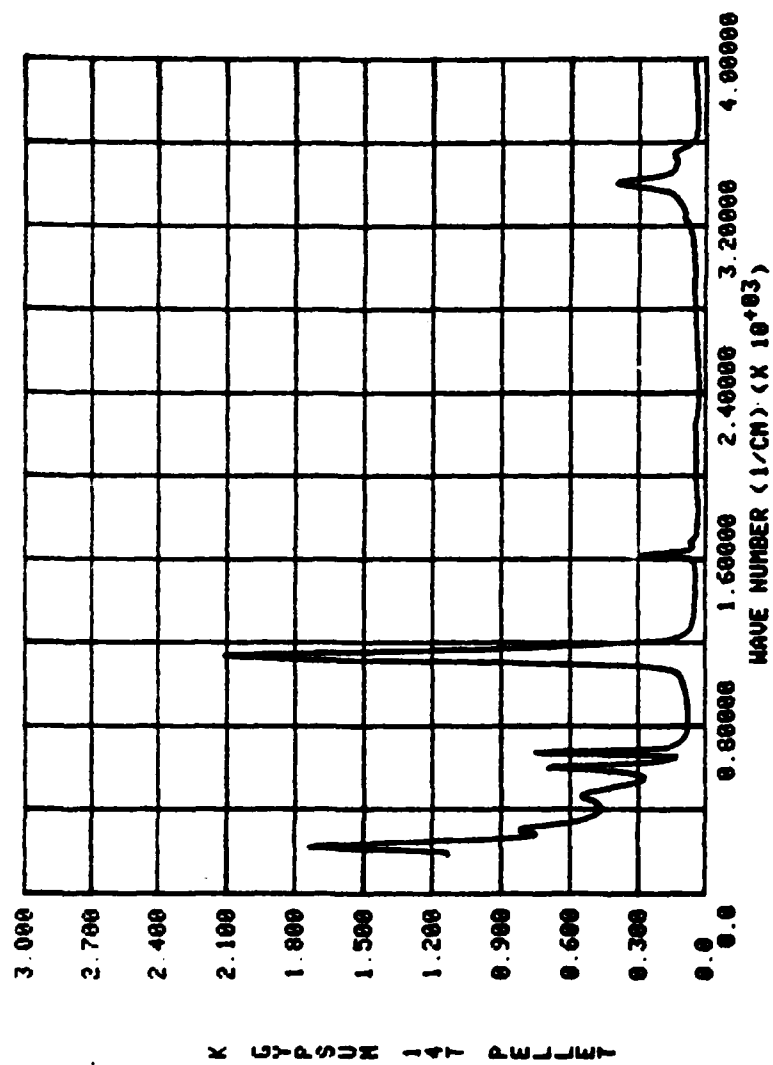


Figure F1-3. Extinction coefficient k of the 14T gypsum pellet in the 180-4,000 cm^{-1} wave-number region.

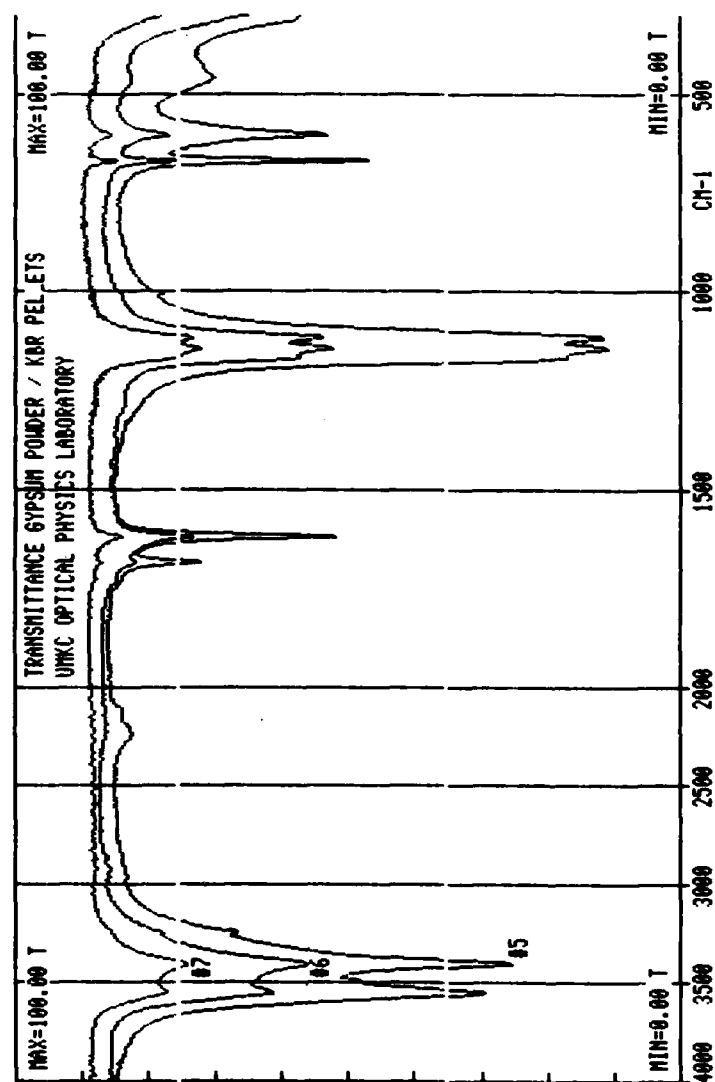


Figure F1-4. Transmittance spectra of three of the gypsum-powder/KBr pellets in the 300-4,000 cm⁻¹ wave-number region.

These four transmittance spectra were converted to absorbance spectra and the six possible subtractions of one absorbance spectrum from another were made, this resulted in six difference spectra. Three absorbance spectra and the six difference spectra are shown in Figs. F1-5 & F1-6. The three difference spectra possessing the least scattering were then chosen for further analysis. Before we describe the analysis of the three chosen difference spectra, let us cast the procedures in this paragraph into mathematical form.

Let us assume that the fractional transmittance T through a gypsum/KBr pellet is given by

$$T = \frac{(1-R)^2 e^{-\alpha x}}{1-R^2 e^{-2\alpha x}}, \quad (16)$$

where R is the reflectance of the surfaces of the KBr pellet, α is an attenuation coefficient due to absorption by the gypsum and scattering by the gypsum and KBr particles, and x we assign to the effective thickness of the gypsum in the pellet. Let us further assume that n for the KBr is 1.4-1.5 so that $R=0.04$ and $R^2=0.0016$. Furthermore, the largest that $e^{-2\alpha x}$ will be is 1 corresponding to $\alpha=0$; thus we may write for our gypsum/KBr pellet

$$T = (1-R)^2 e^{-\alpha x}. \quad (17)$$

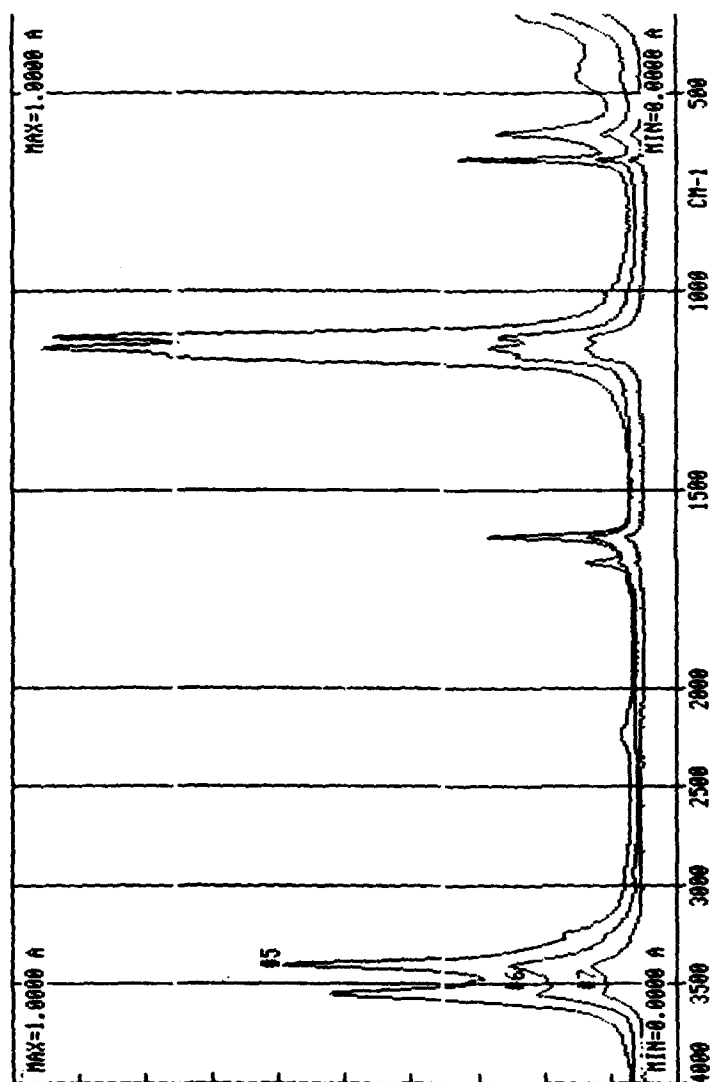


Figure F1-5. Absorbance spectra of three of the gypsum-powder/KBr pellets in the 300-4,000 cm^{-1} wave-number region.

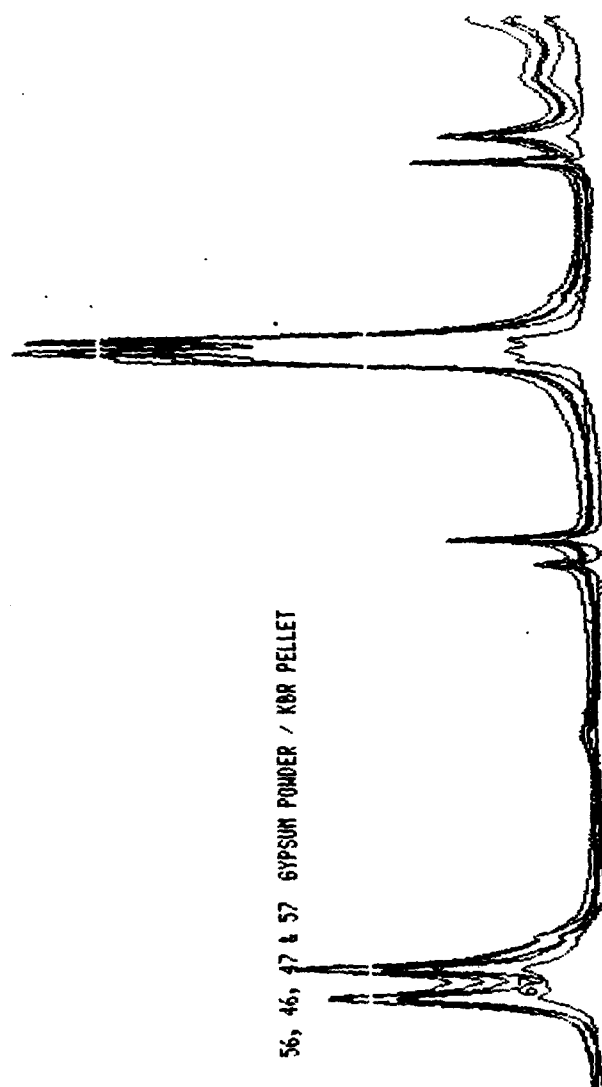


Figure F1-6. Five difference spectra obtained from four absorbance spectra for the gypsum-powder/KBr pellets in the 300-4,000 cm^{-1} wave-number region.

The absorbance $A = -\log(T)$, where \log represents \log of base 10; thus

$$A = -2 \log (1-R) + \alpha x c \quad (18)$$

$$= -2 \log(1-R) + c\alpha_a x + \alpha_s t c, \quad (19)$$

where we have recast αx into the form $\alpha x = \alpha_a x + \alpha_s t$ which represents absorption a and scattering s , and $c = 0.43429$. Again, x represents the effective thickness of the gypsum and t is the thickness of the gypsum/KBr pellet. A difference between two absorbance spectra is

$$A_2 - A_1 = -2 \log[(1-R_2)/(1-R_1)] + c\alpha_a (x_2 - x_1) + (c\alpha_s t)_2 - (c\alpha_s t)_1 \quad (20)$$

Assuming $R_1 = R_2$ and $(\alpha_s t)_1 = (\alpha_s t)_2$ we have

$$A_2 - A_1 = c\alpha_a (x_2 - x_1); \quad (21)$$

$$= c4\pi k\nu (x_2 - x_1). \quad (22)$$

Thus, if the gypsum/KBr pellets are adequately prepared the difference spectra $A_2 - A_1$ is directly proportional to k . However, one can not measure the effective thickness x of the gypsum in the pellet.

We now return to the further analysis of the three

difference spectra. The primary difference between two difference spectra is in the factors x_2-x_1 which cannot be measured. Two of the three difference spectra were thus normalized to the third difference spectrum. The normalization factor was an average of such factors determined at the centers of the strong absorption bands of gypsum where k is relatively large. The average of the three normalized difference spectra was divided by $4\pi v$ throughout the $300-4,000 \text{ cm}^{-1}$ region. This process produced the relative k spectrum shown in Fig. F1-7 and F1-8. Actually the relative k spectrum is a product $ck\Delta x$ spectrum. The smoothed fractional standard deviation $\Delta k/k$ is shown in Fig. F1-9; $\Delta k/k$ was obtained as a byproduct of averaging the three normalized difference spectra. The ordinate scale for $\Delta k/k$ in Fig. F1-9 is from 0 to 1.0; note that $\Delta k/k$ is very large in regions where k is very small but is less than $\Delta k/k$ for KK analysis for small k .

It is impossible to determine the effective thickness x of the Gypsum in the pellets. Thus we applied a calibration factor to the relative k spectrum shown in Figs. F1-7 and F1-8. The calibration factor was determined in the following manner. Values of k were available from Kramers-Kronig analysis of the reflectance spectrum of the Gypsum pellets. At the centers of four of the strong infrared bands the ratios of k values from KK analysis to

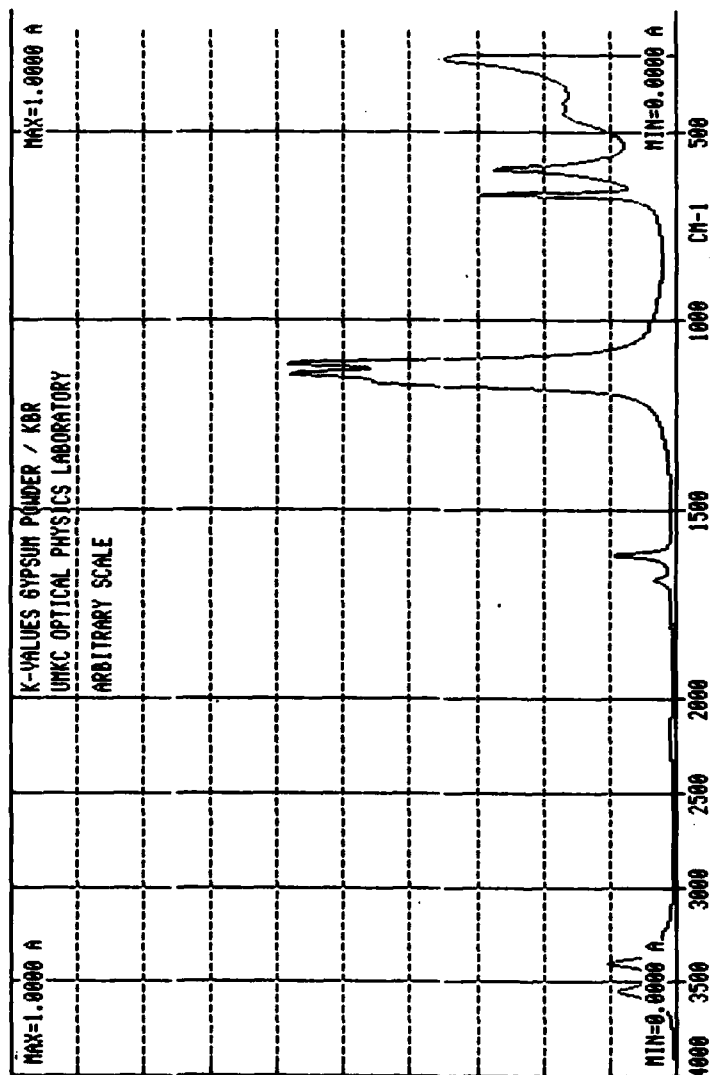


Figure F1-7. Relative k spectrum for gypsum from the average of three normalized difference spectra of the gypsum-powder/KBr pellets; 300-4,000 cm^{-1} wave-number region.

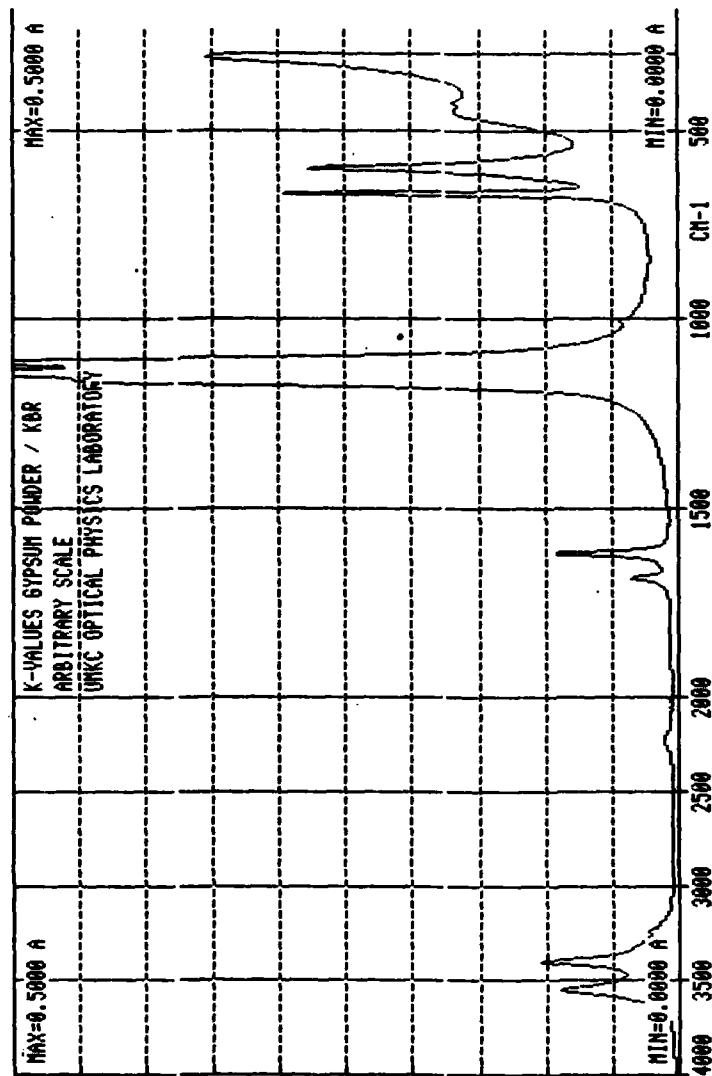


Figure F1-8. Relative k spectrum for gypsum from the average of three normalized difference spectra of the gypsum-powder/KBR pellets, expanded ordinate scale; 300-4,000 cm^{-1} wave-number region.

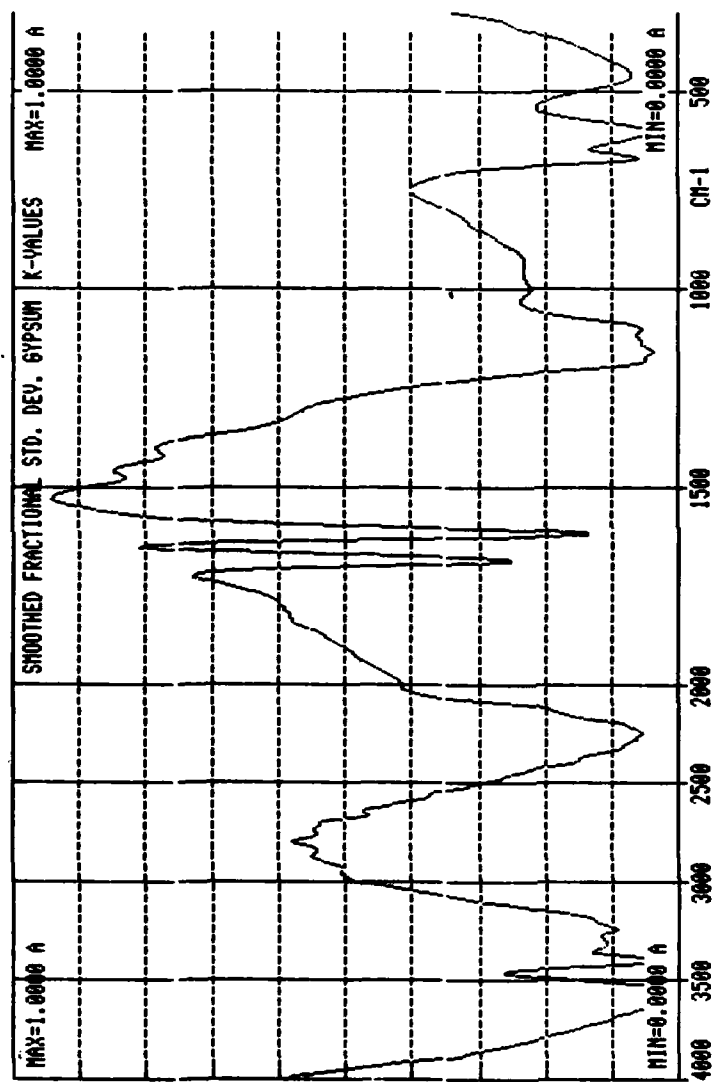


Figure F1-9. Smoothed fractional standard deviation Dk/k obtained from the three normalized difference spectra; $300-4,000\text{ cm}^{-1}$ wave-number region.

relative k values were computed and averaged. The average of the four ratios was the calibration factor applied to the relative k spectrum throughout the $300\text{--}4,000\text{ cm}^{-1}$ region. The calibration factor corresponded to $1/c\Delta x$. Values of k determined in this manner are shown graphically as the dashed line in Fig. F1-10. The solid line in Fig. F1-10 is the k spectrum determined by KK analysis of the reflectance spectrum of the 8T Gypsum pellet.

We noted from Fig. F1-10 that the infrared band at $3,550\text{ cm}^{-1}$, which is a characteristic of the Y optical direction of Gypsum, is stronger from the transmittance measurements of the Gypsum/KBr pellet than from KK analysis of the reflectance spectrum of the 8T pellet. We attribute this to a more random orientation of the Gypsum particles in the Gypsum/KBr pellet than in the 8T Gypsum pellet. Preferred (010) orientation of the Gypsum particles in the 8T pellet was described in Section VD of this report. Also, we note from Fig. F1-10 that in spectral regions where k is relatively small that k values from the transmittance measurements yield more accurate values of k . There is a general increase in base level k values for KK analysis from about $1,300\text{ cm}^{-1}$ to $4,000\text{ cm}^{-1}$ which would be expected as diffuse reflectance increases as frequency increases. The diffusely reflected radiant flux will be interpreted by the KK algorithms as absorption and k values

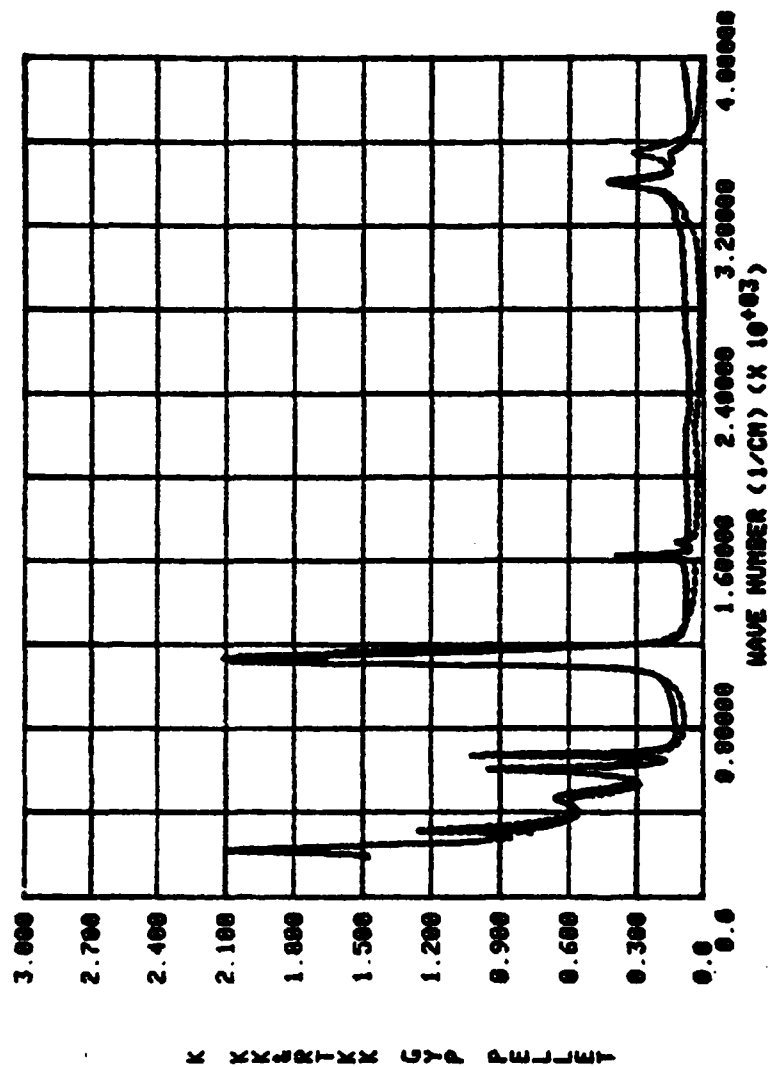


Figure F1-10. Comparison of k spectra for gypsum obtained from KK analysis (solid line) of the reflectance spectrum of the 8T pellet and from transmittance (dashed line) measurements of the gypsum-powder/KBr pellets, 300-4,000 cm^{-1} region.

will thus increase as diffuse reflectance increases. This is exactly the situation that we observe with the 8T Gypsum pellet.

Next, we determined values of n that were consistent with the calibrated k spectrum from the transmittance measurements and with the reflectance spectrum of the 8T pellet. This was accomplished by using the Fresnel reflectance equation

$$R = \frac{(Z - \cos \theta)(Z^* + \cos \theta)}{Z + \cos \theta}^2 \quad (23)$$

$$Z^2 = N^2 - \sin^2 \theta. \quad (24)$$

Values of n were systematically adjusted by use of a least squares method in Eqns. (23) and (24) until the measured value of R was obtained. The n spectrum thus obtained is the dashed curve in Fig. F1-11. The solid-line curve in Fig. F1-11 is the n spectrum of the 8T pellet. Differences in the two n spectra in Fig. F1-10 were attributed to differences in the orientation of Gypsum particles in the Gypsum/KBr pellet and the 8T Gypsum pellet.

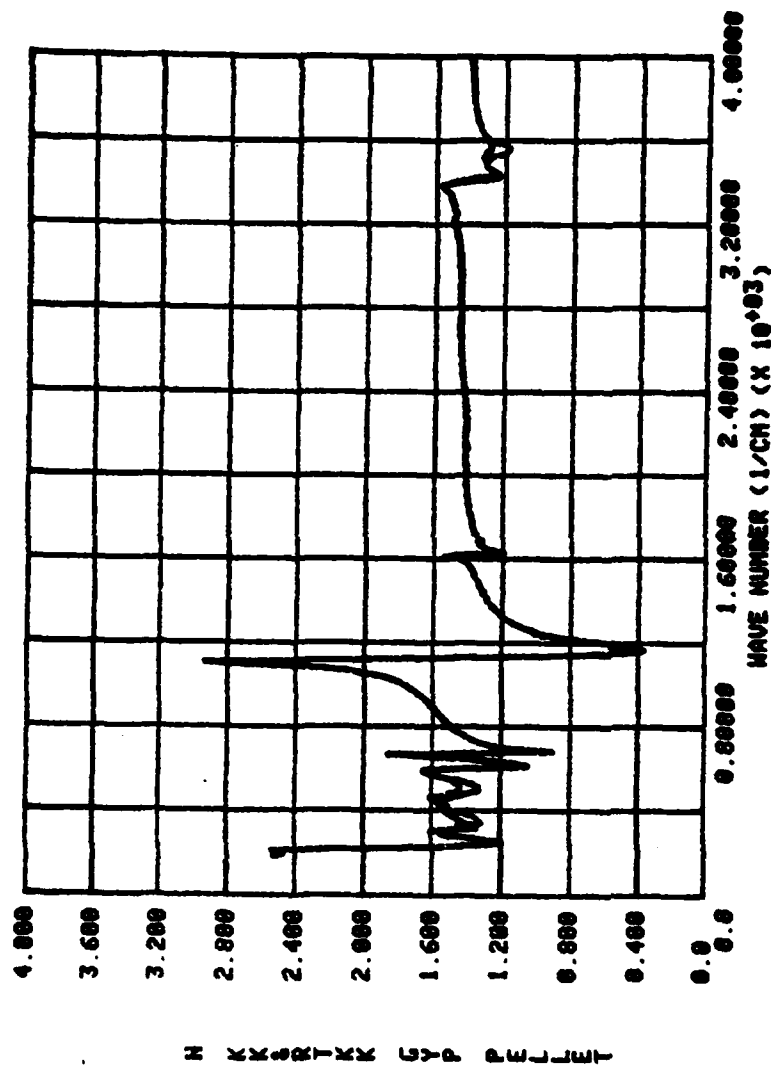


Figure F1-11. Comparison of n spectra for gypsum obtained from KK analysis (solid line) of the reflectance spectrum of the 8T pellet and from application of the fresnel equation (dashed line) to the k spectrum from transmittance measurements and the reflectance spectrum of the pellet; 300-4,000 cm^{-1} region.

2. Pyrolusite

Pyrolusite MnO_2 is a tetragonal optically uniaxial opaque mineral of the $4/m\ 2/m\ 2/m$ lattice and space group and has a structure the same as that of Rutile. Pyrolusite is rarely found in well developed crystals. Our Pyrolusite sample was black in color and took on a metallic luster when pressed into pellets. Two pellets were prepared; one with 8 tons of force and the other with 16 tons of force applied to the 13 mm dia. surface. The powder used to prepare the 16T pellet was much smaller in particle size than that used for the 8T pellet. The 16T pellet possessed a more metallic luster than the 8T pellet due to the smaller particle size and the factor of 2 increase in the pressure used to form the pellet.

The reflectance spectrum for the 8T Pyrolusite pellet is shown in Fig. F2-1 for the 0.2-50 μm wavelength range. The real and imaginary parts of N obtained by applying KK analysis to the reflectance spectrum of the 8T pellet are presented in Figs. F2-2 and F2-3, respectively.

The reflectance spectra of the 8T and 16T Pyrolusite pellets in the $180\text{--}4,000\text{ cm}^{-1}$ spectral range are presented in Fig. F2-4. The ratio reflectance spectrum $R(8T)/R(16T)$ of Pyrolusite in the $180\text{--}4,000\text{ cm}^{-1}$ spectral range is shown in Fig. F2-5. Note that the 8T pellet specularly reflected much less than the 16T pellet at nearly all spectral

positions. The shape of the reflectance spectrum for the 16T pellet and the visual appearance of the 16T pellet suggest that there was probably increasing diffuse reflectance as the frequency increased. However, black metallic materials such as graphite exhibit decreasing reflectance with increasing frequency through the infrared and visible spectral regions. The reflectance of black metallic Pyrolusite will probably bear some similarities to that of graphite and decrease with increasing frequency from about $2,000\text{ cm}^{-1}$ in the infrared to about $50,000\text{ cm}^{-1}$ in the ultraviolet.

Spectral values of n and k from KK analysis of the reflectance spectrum of the 16T pellet are presented graphically in Figs. F2-6 and F2-7, respectively.

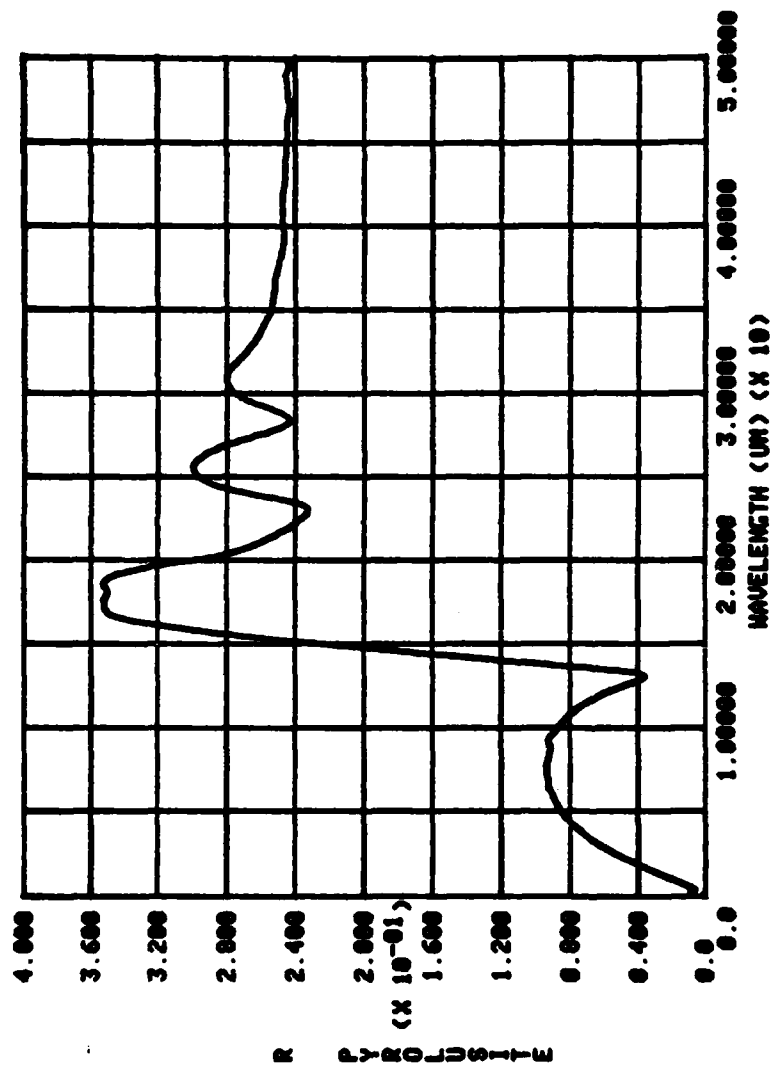


Figure F2-1. Reflectance spectrum of the 8T Pyrolusite pellet in 0.2-50 μm wavelength region.

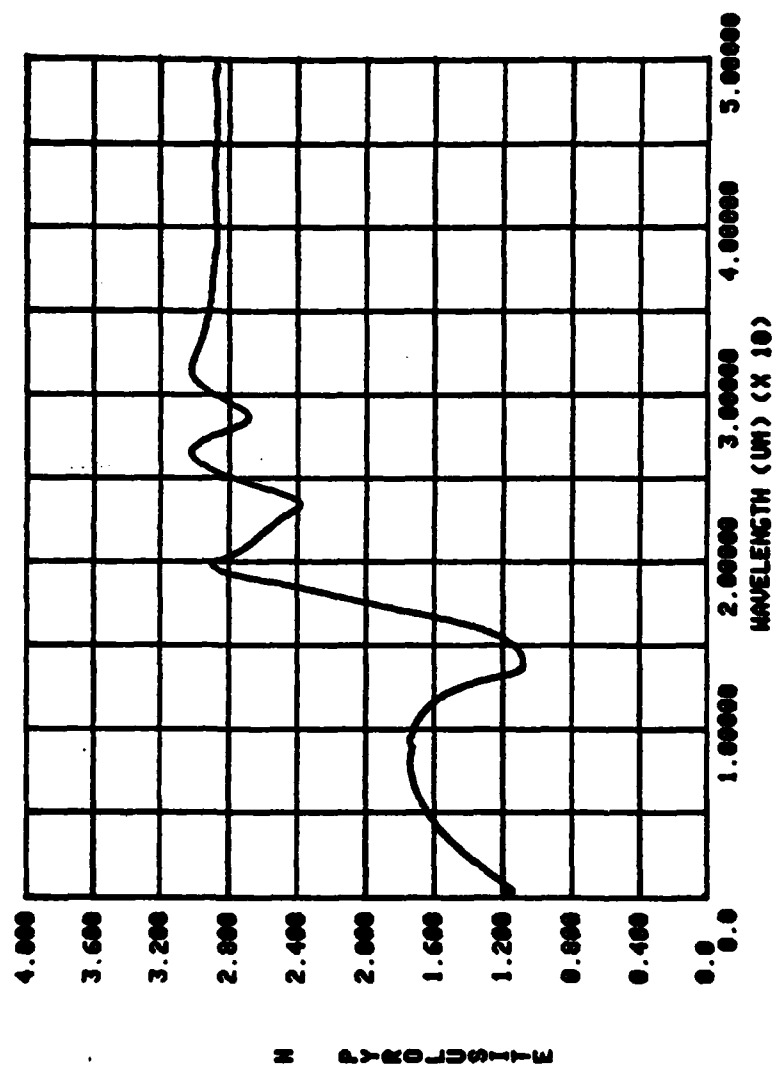


Figure F2-2. Index of refraction n of the 8T Pyrolusite pellet in the 0.2-50 μm wavelength region.

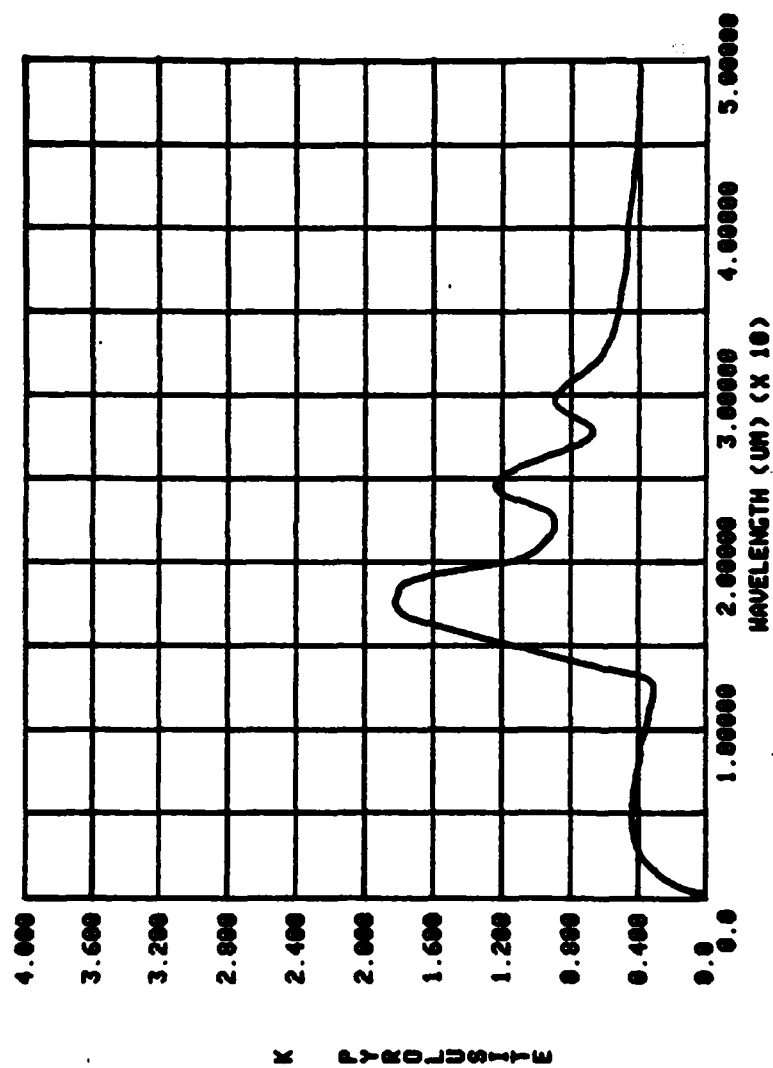


Figure F2-3. Extinction coefficient k of the 8T Pyrolusite pellet in the 0.2-50 μm wavelength region.

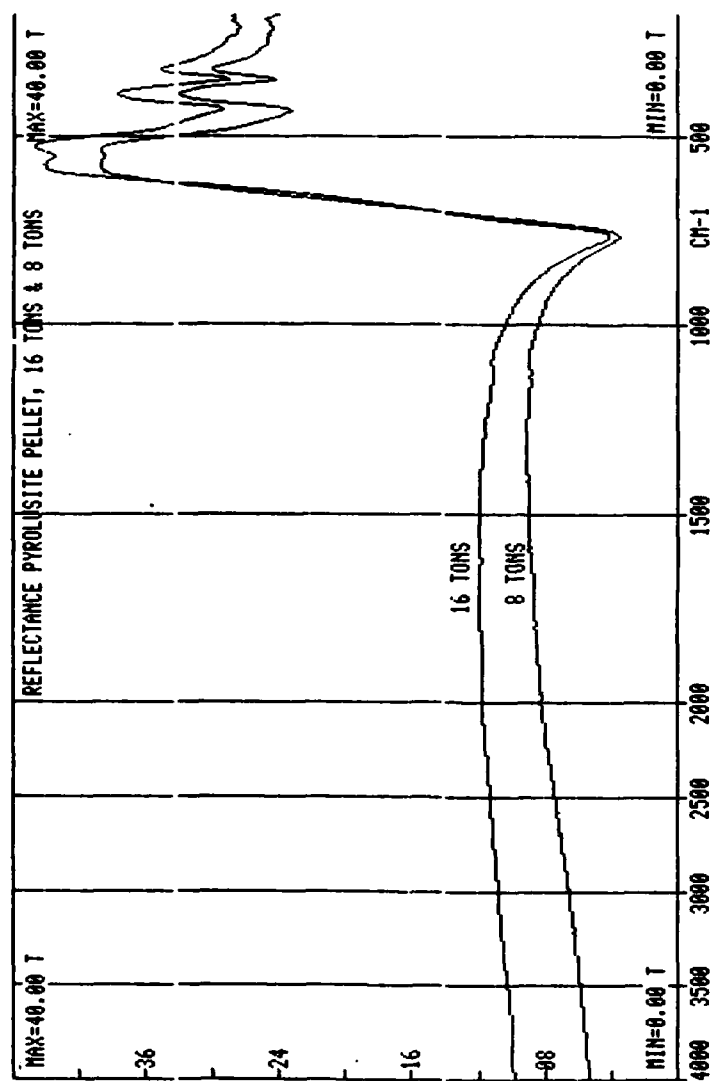


Figure F2-4. Reflectance spectra of the 8T and 16T Pyrolusite pellets in the 180-4,000 cm^{-1} wave-number region, (55-2.5 μm).

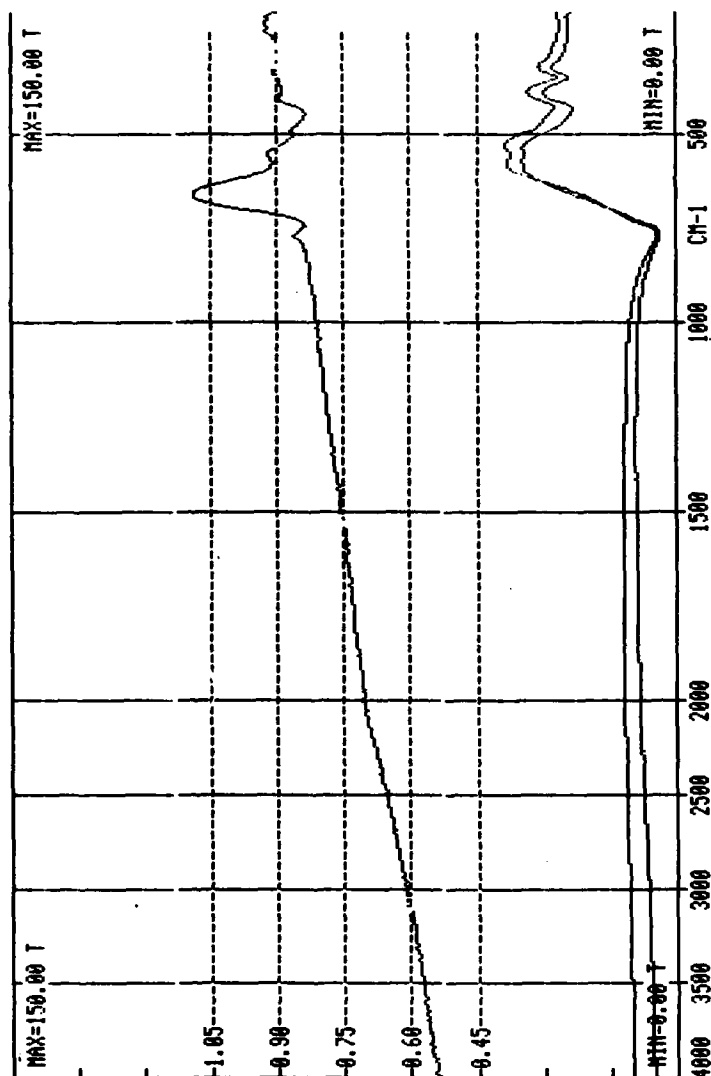


Figure F2-5. Ratio reflectance spectrum $R(8T)/R(16T)$ for Pyrolusite in the 180-4,000 cm^{-1} wave-number region.

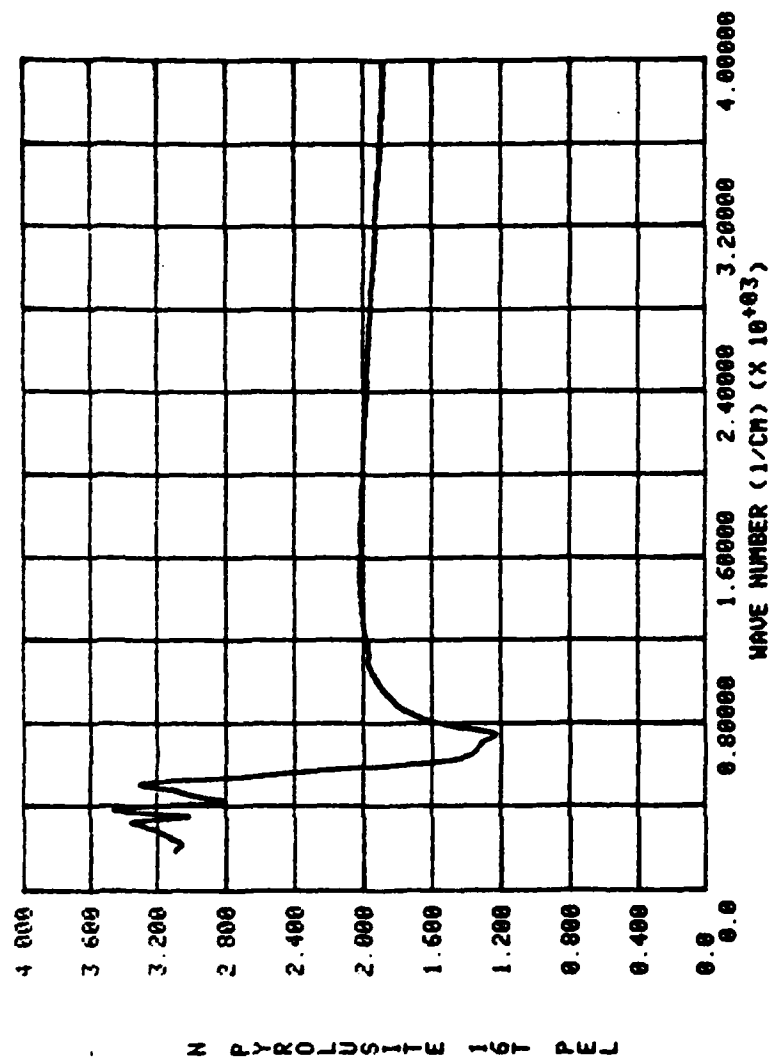


Figure F2-6. Index of refraction n for the 16T Pyrolusite pellet in the 180-4,000 cm^{-1} wave-number region.

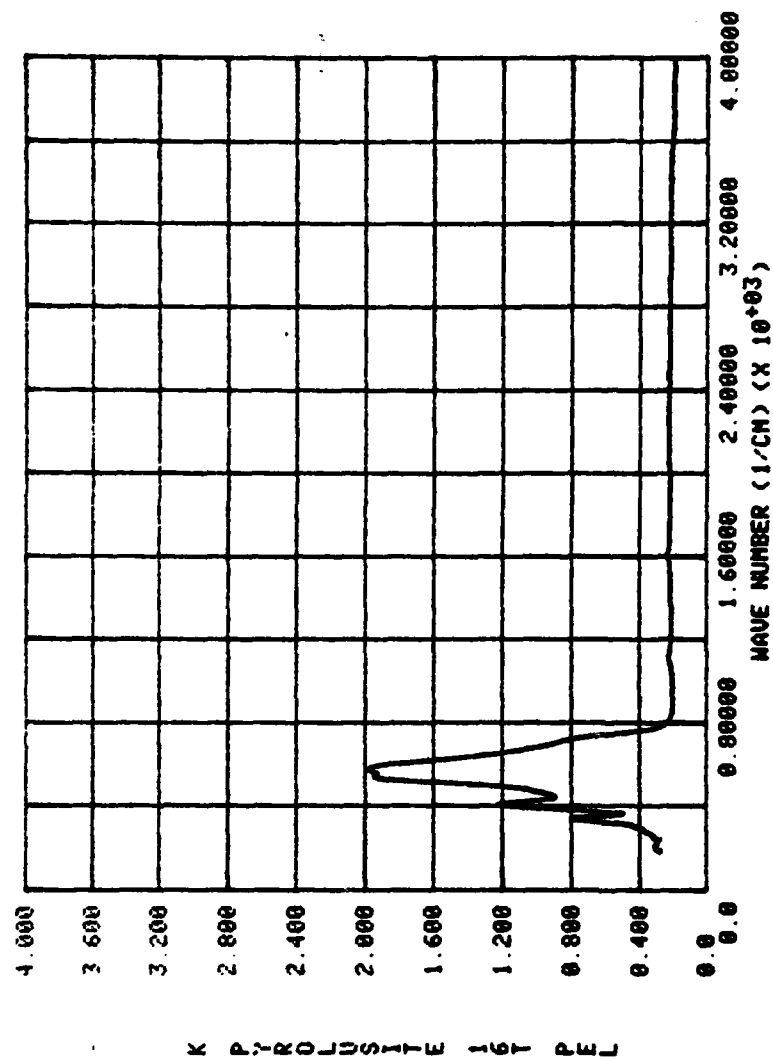


Figure F2-7. Extinction coefficient k for the 16T Pyrolusite pellet in the $180\text{--}4,000 \text{ cm}^{-1}$ wave-number region.

3. Alabama Limonite

Limonite is primarily composed of Goethite (α -FeOOH). Limonite ($\text{FeOOH} \cdot n\text{H}_2\text{O}$) is a mineralogy field term referring to natural hydrous iron oxides of uncertain identity. The reflectance spectrum in the 0.2-50 μm wavelength region for an 8T Alabama Limonite pellet is shown in Fig. F3-1. Spectral values of n and k determined by applying KK analysis to the reflectance spectrum of the 8T Alabama Limonite pellet are presented graphically in Figs. F3-2 and F3-3, respectively. The sample was yellow-orange in color. An 8T Georgia Limonite pellet had similar optical properties.

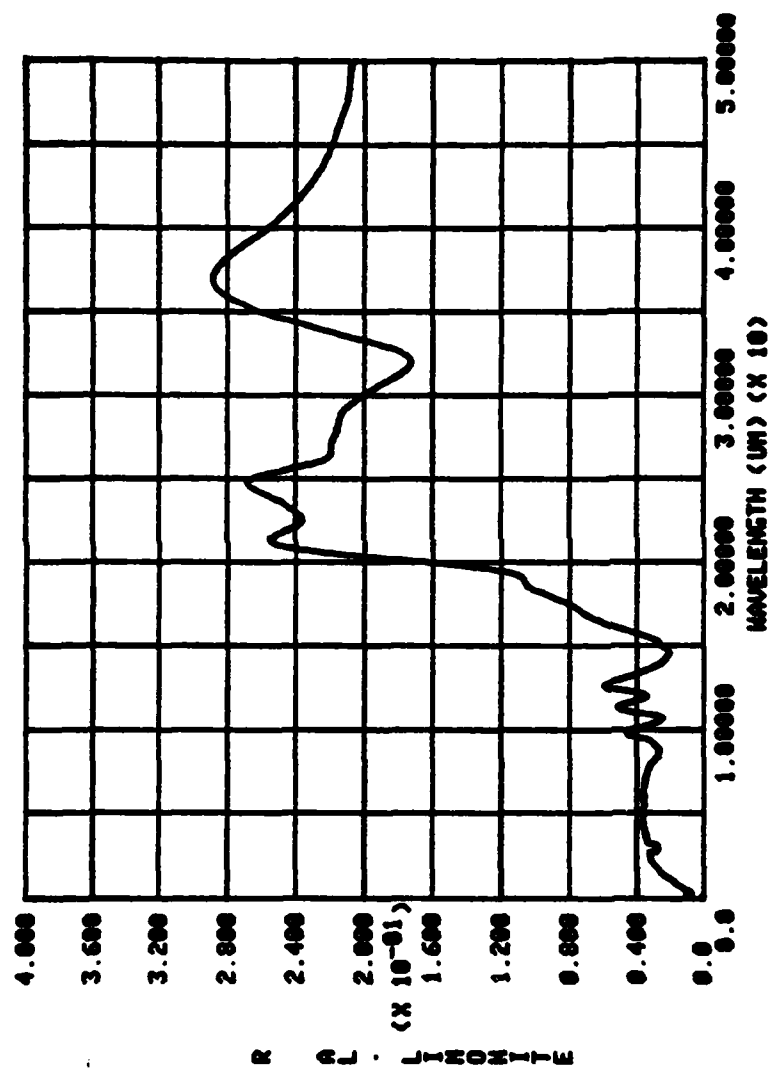


Figure F3-1. Reflectance spectrum of Alabama Limonite 8T pellet in the 0.2-50 μm wavelength region.

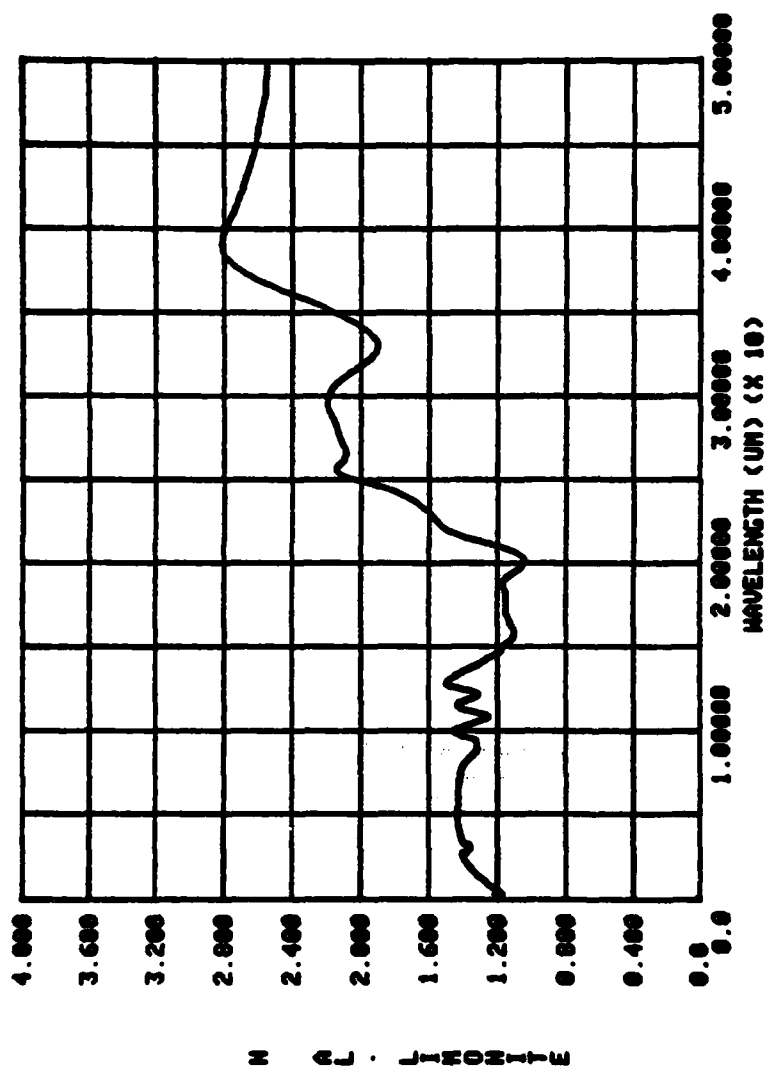


Figure F3-2. Index of refraction n of the 8T Alabama Limonite pellet in the 0.2-50 μm wavelength region.

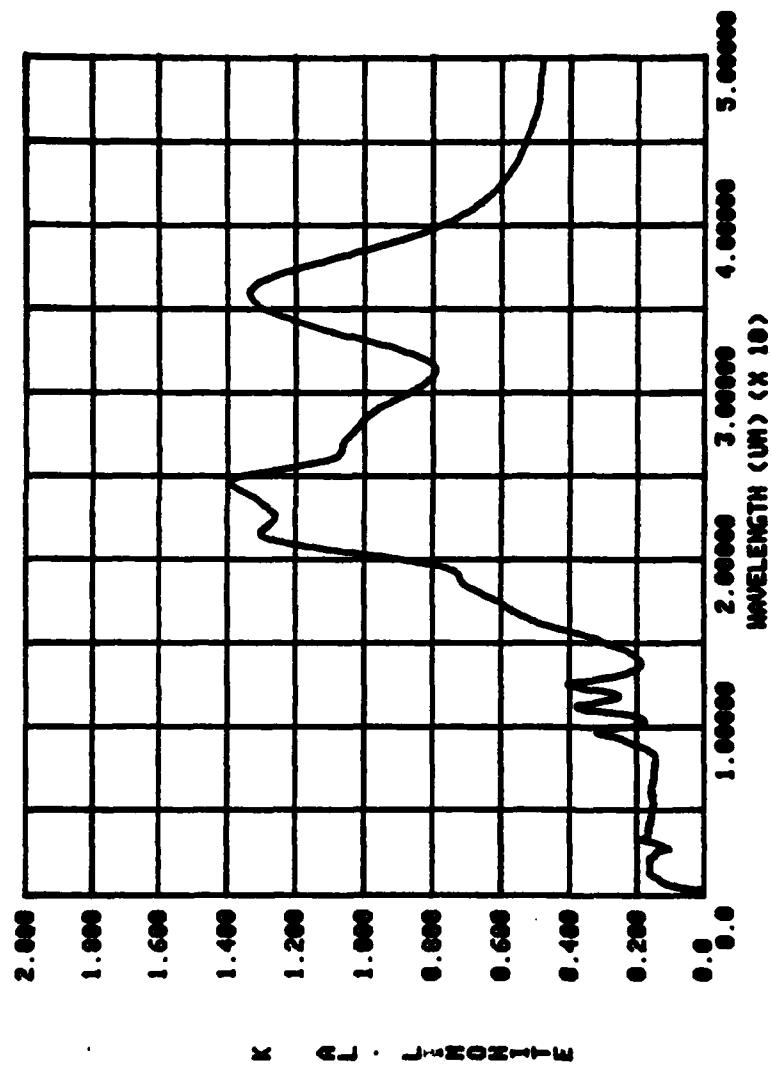


Figure F3-3. Extinction coefficient k of the 8T Alabama Limonite pellet
in the 0.2-50 μm wavelength region.

4. Kaolin

Kaolin, a member of the clay mineral group, is composed primarily of Kaolinite which is Triclinic and thus optically biaxial. The specular reflectance spectrum at 6.5 deg. angle of incidence in the 0.2-50 μm wavelength region for an 8T Kaolin pellet is shown in Fig. E4-1. Spectral values of n and k from KK analysis of the reflectance spectrum of the 8T Kaolin pellet are presented graphically in Figs. F4-2 and F4-3, respectively.

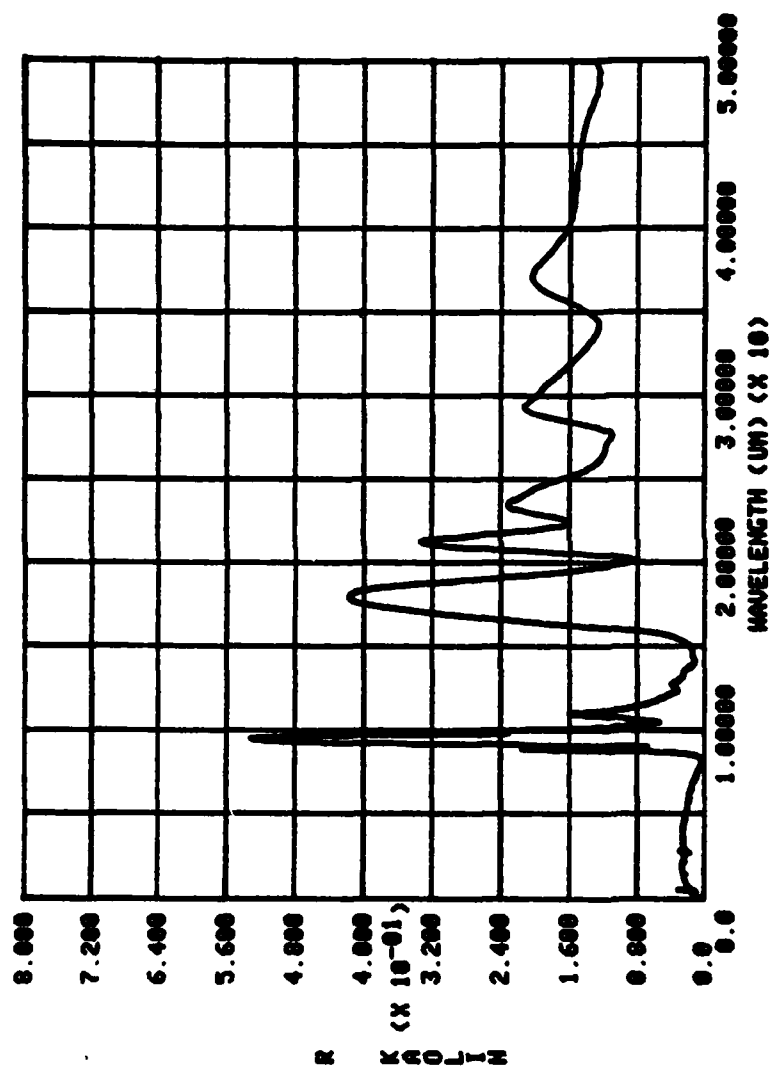


Figure F4-1. Reflectance spectrum of the 8T Kaolin pellet in the 0.2-50 μm wavelength region.

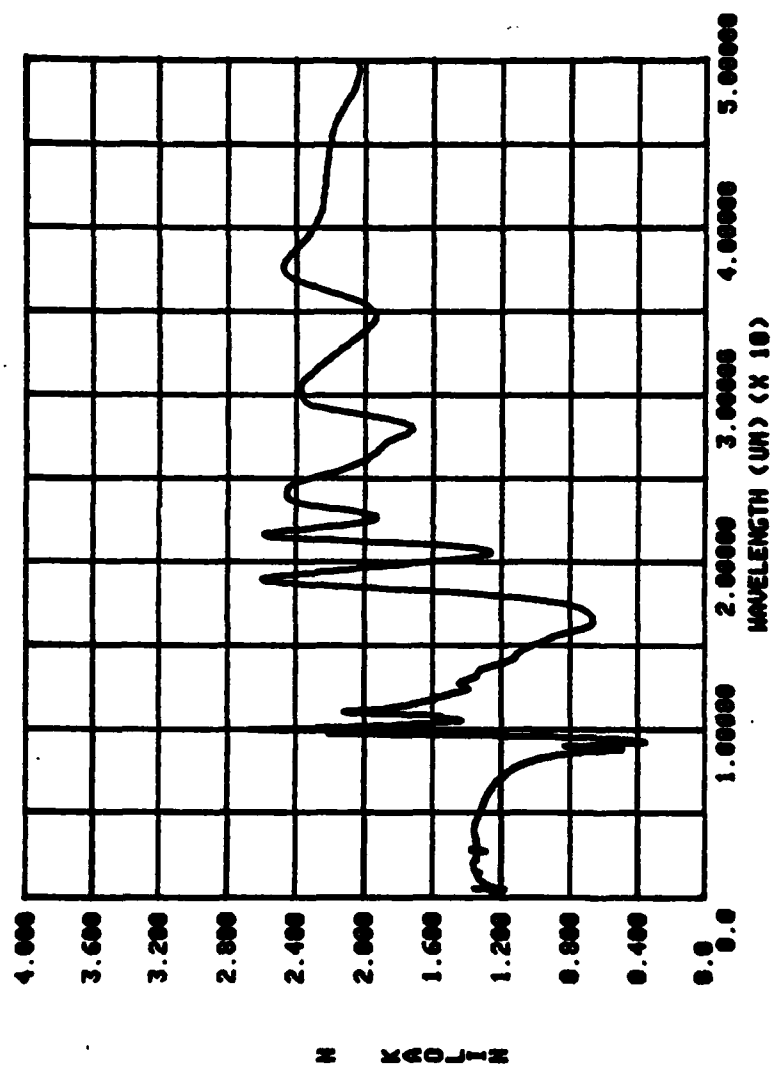


Figure P4-2. Index of refraction n of the 8T Kaolin pellet in the 0.2-50 μm wavelength region.

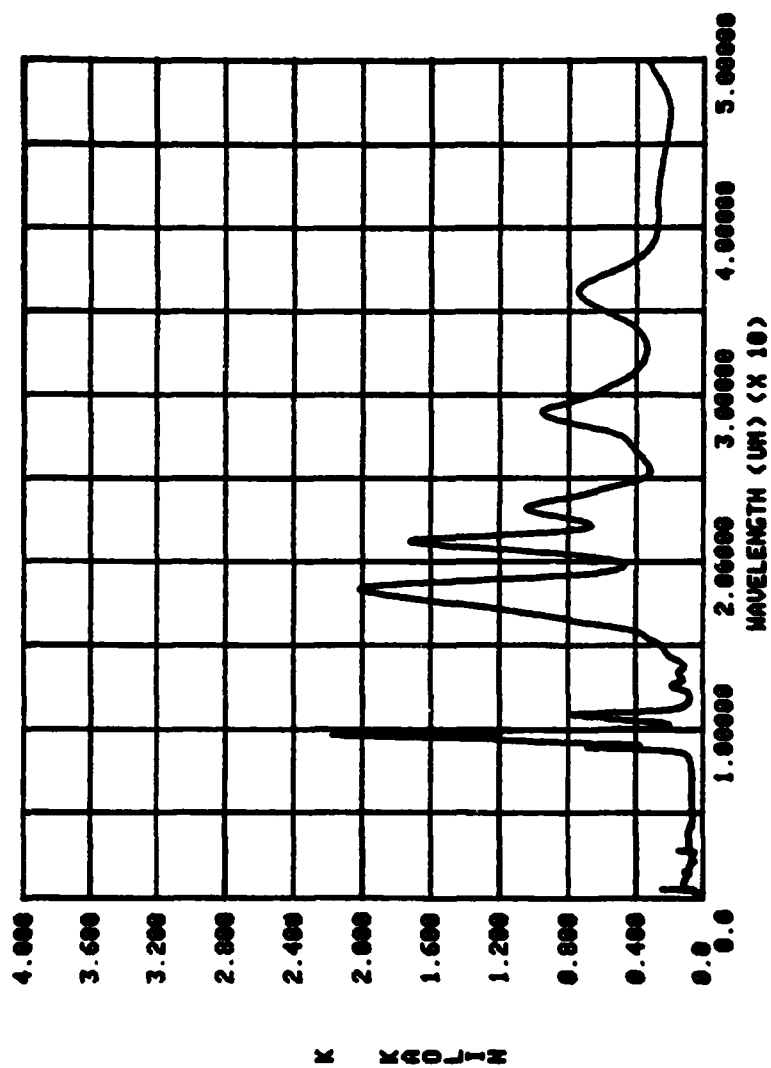


Figure F4-3. Extinction coefficient k of the 8T Kaolin pellet in the 0.2-50 μm wavelength region.

5. Illite

Illite is an hydromuscovite mineral of clay particle size (2 μm). Hydromuscovite is a monoclinic optically biaxial crystal with perfect (001) cleavage and a hardness of 2. The specular reflectance spectrum at 6.5 deg. angle of incidence in the 0.2-50 μm wavelength region for an 8T Illite pellet is shown in Fig. F5-1. Spectral values of n and k obtained by KK analysis of the reflectance spectrum of the 8T Illite pellet are presented graphically in Figs. F5-2 and F5-3, respectively.

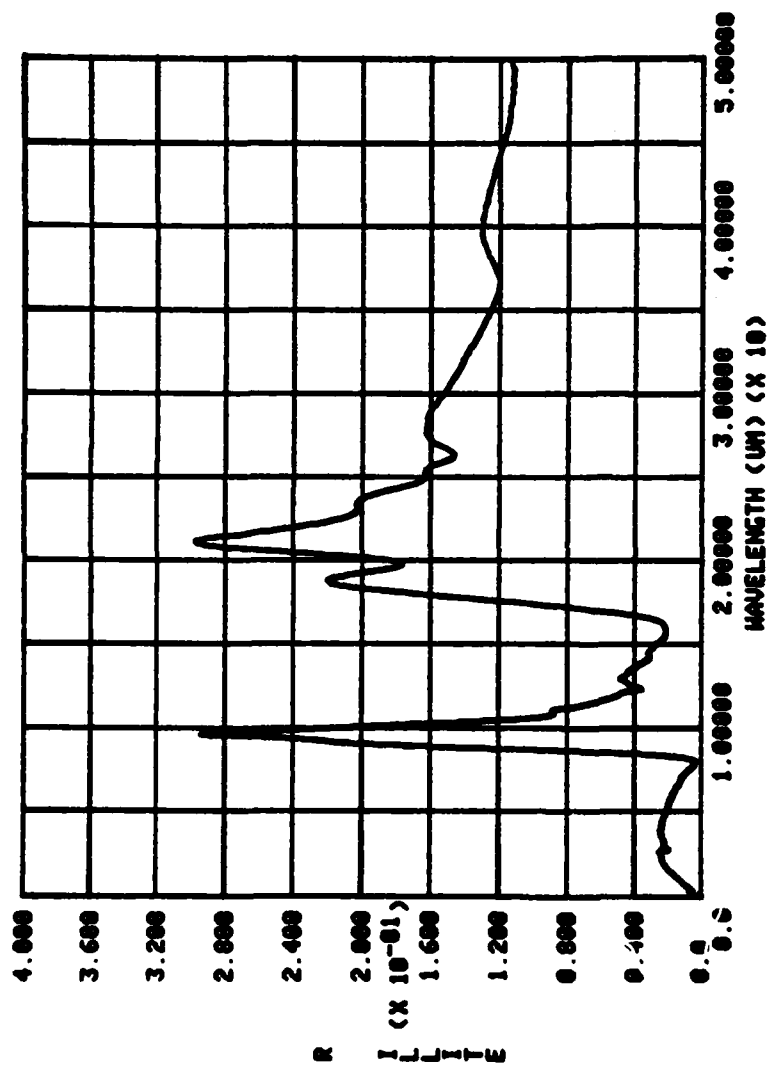


Figure F5-1. Reflectance spectrum of the 8T Illite pellet in the 0.2-50 μm wavelength region.

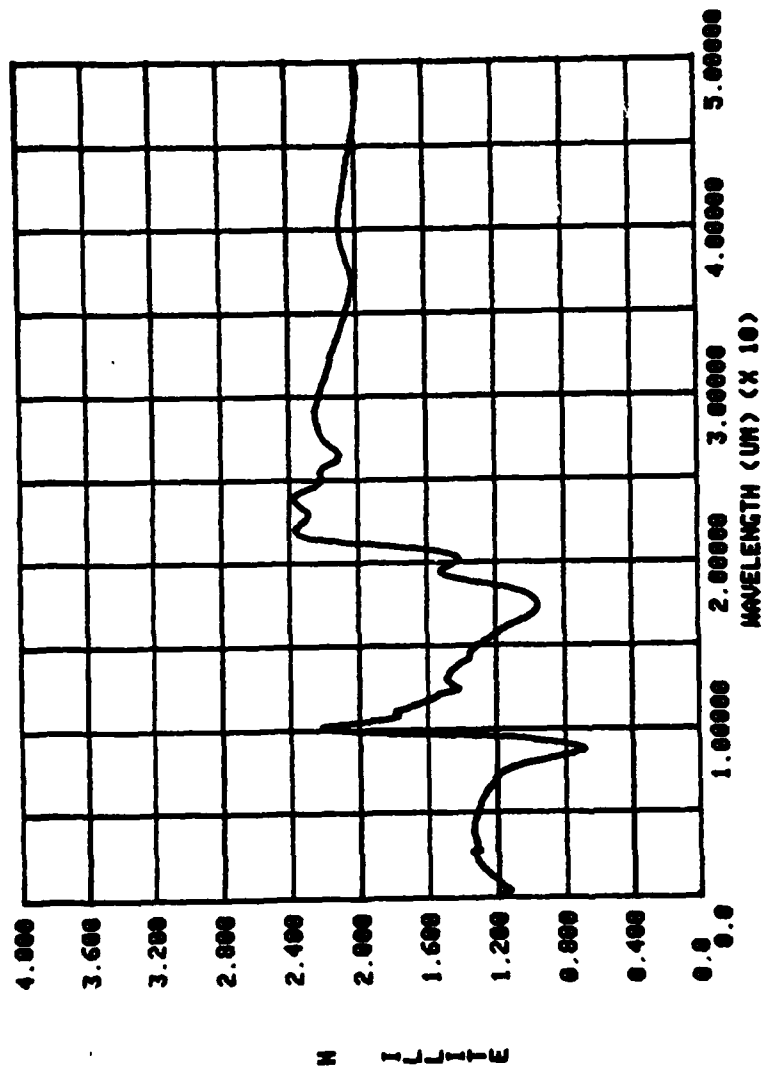


Figure F5-2. Index of refraction n of the 8T Illite pellet in the 0.2-50 μm wavelength region.

AD-A133 530

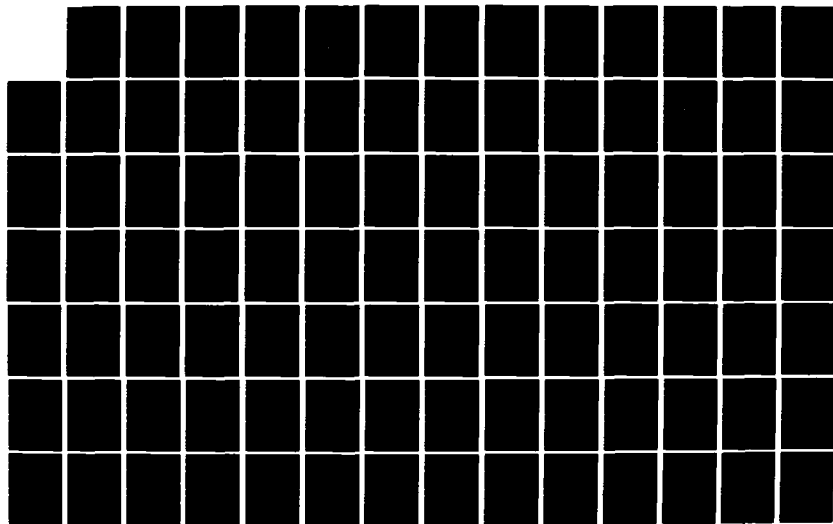
OPTICAL PROPERTIES OF NATURAL MINERALS AND OTHER
MATERIALS IN THE 350-500 (U) MISSOURI UNIV-KANSAS CITY
DEPT OF PHYSICS H R QUERRY AUG 83 ARO-16512.2-G5
DAAG29-79-C-0131

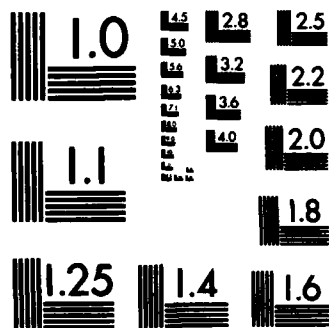
3/4

UNCLASSIFIED

F/G 8/7

NL





MICROCOPY RESOLUTION TEST CHART
NATIONAL BUREAU OF STANDARDS-1963-A

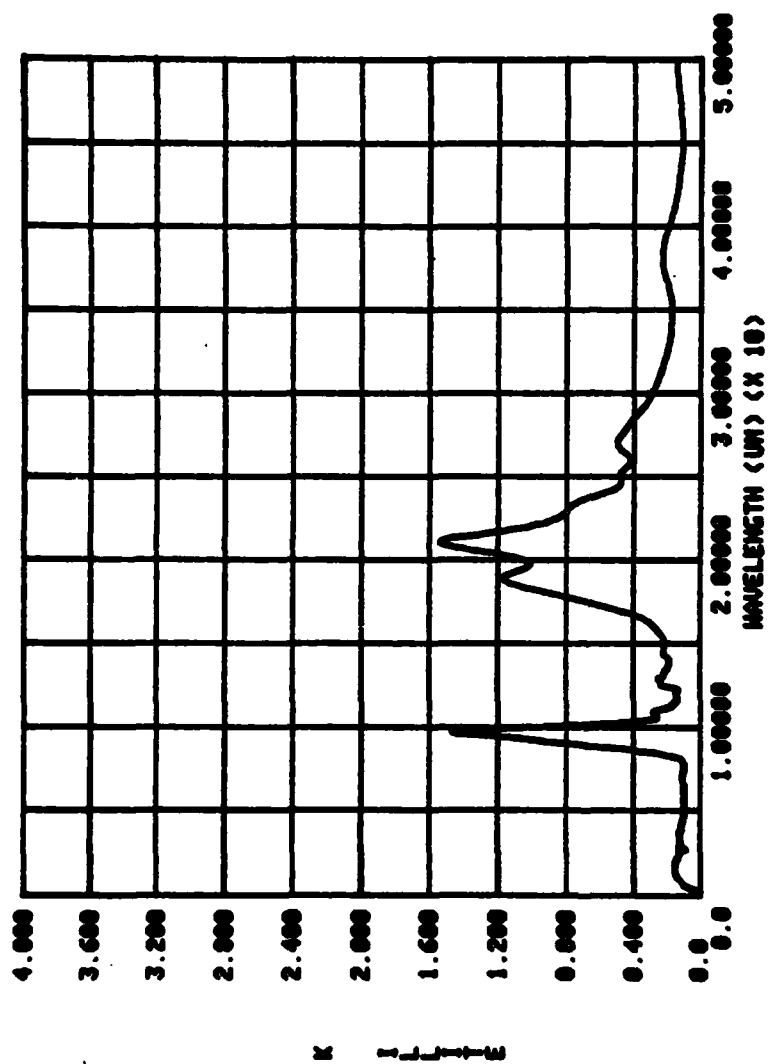


Figure F5-3. Extinction coefficient k of the 8T Illite pellet in the 0.2-50 μm wavelength region.

6. Colemanite

Colemanite is a monoclinic optically biaxial crystal of the $2/m$ lattice and space group. It is transparent colorless to white in color. The specular reflectance at 6.5 deg. angle of incidence in the 0.2-50 μm wavelength region for an 8T Colemanite pellet is shown in Fig. F6-1. Spectral values of n and k obtained from KK analysis of the reflectance spectrum of the 8T Colemanite pellet are presented graphically in Figs. F6-2 and F6-3, respectively.

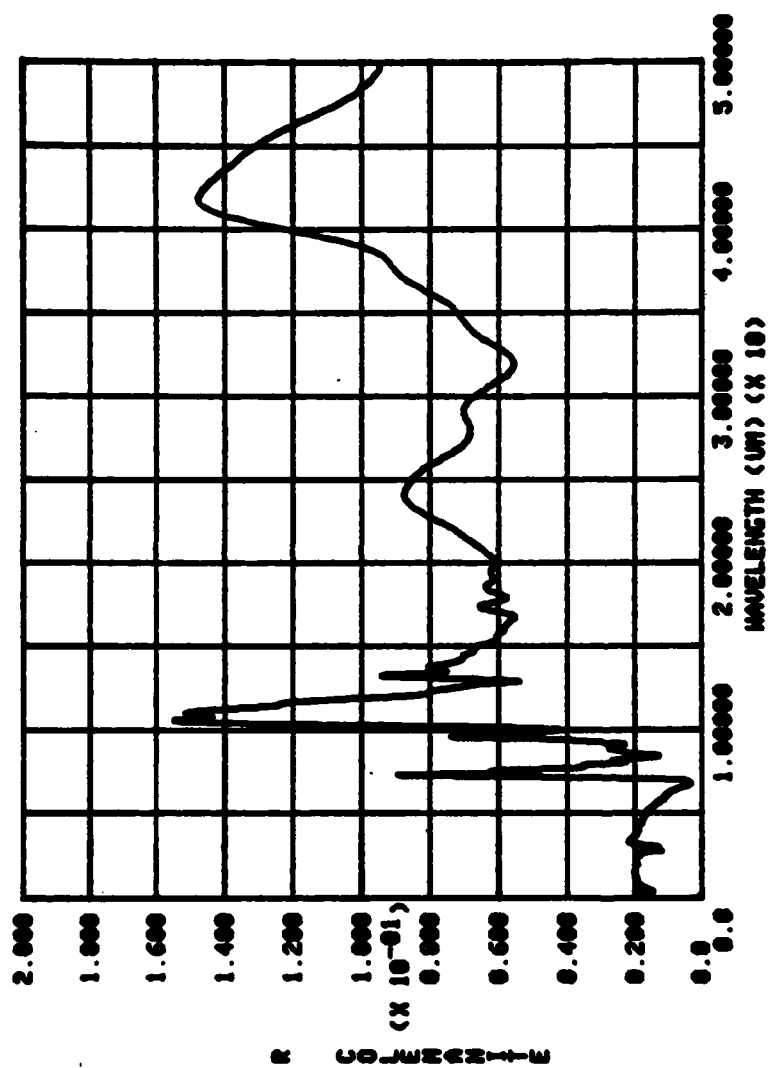


Figure F6-1. Reflectance spectrum of the 8T Colemanite pellet in the 0.2-50 μm wavelength region.

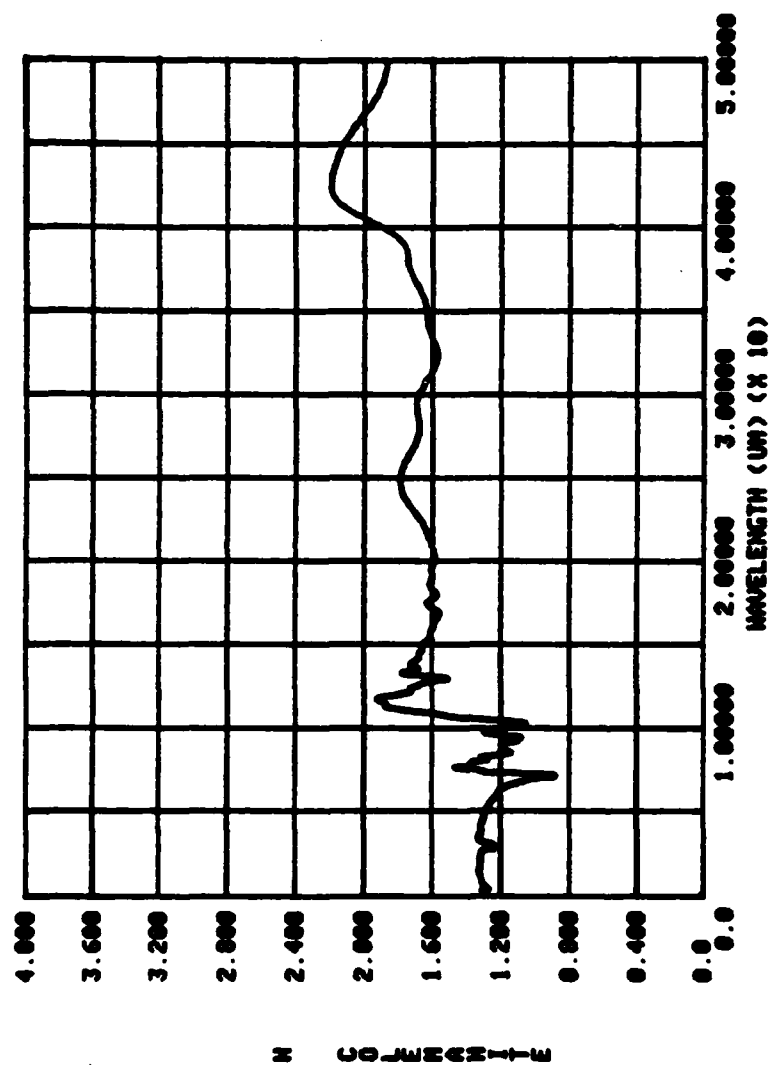


Figure F6-2. Index of refraction n of the 8T Colemanite pellet in the
the 0.2-50 μm wavelength region.

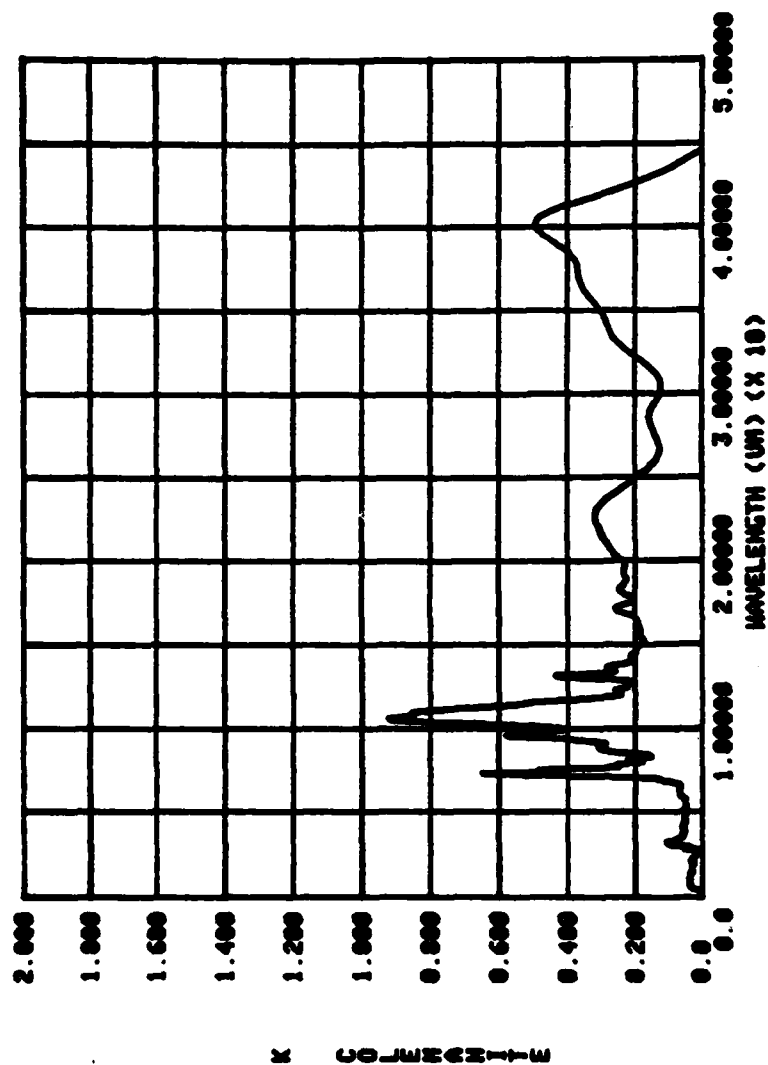


Figure F6-3. Extinction coefficient k of the 8T Colemanite pellet in the 0.2-50 μm wavelength region.

7. Kernite

Kernite is a monoclinic optically biaxial mineral which is found in nonmarine evaporites and salt pans; it is a metamorph of Boxax. The specular reflectance spectrum at 6.5 deg. angle of incidence in the 0.2-50 μm wavelength region is shown in Fig. F7-1. Spectral values of n and k obtained from KK analysis of the reflectance spectrum of the 8T Kernite pellet are presented graphically in Figs. F7-2 and F7-3, respectively.

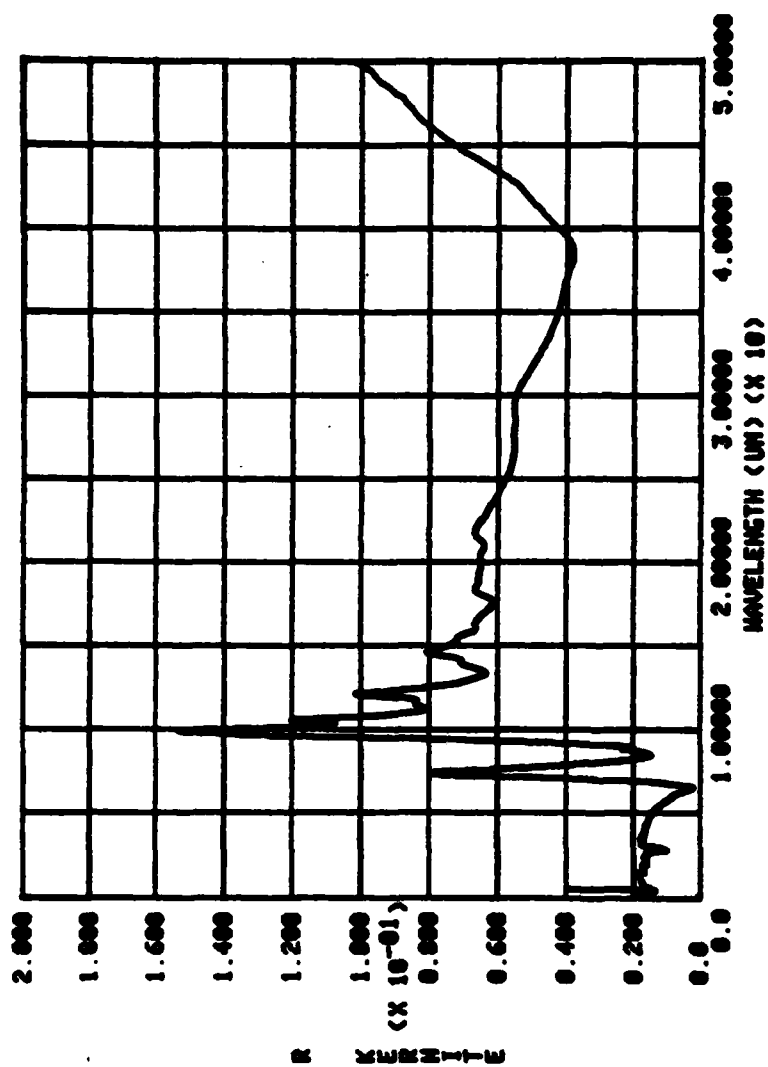


Figure F7-1. Reflectance spectrum of the 8T Kernite pellet in the 0.2-50 μm wavelength region.

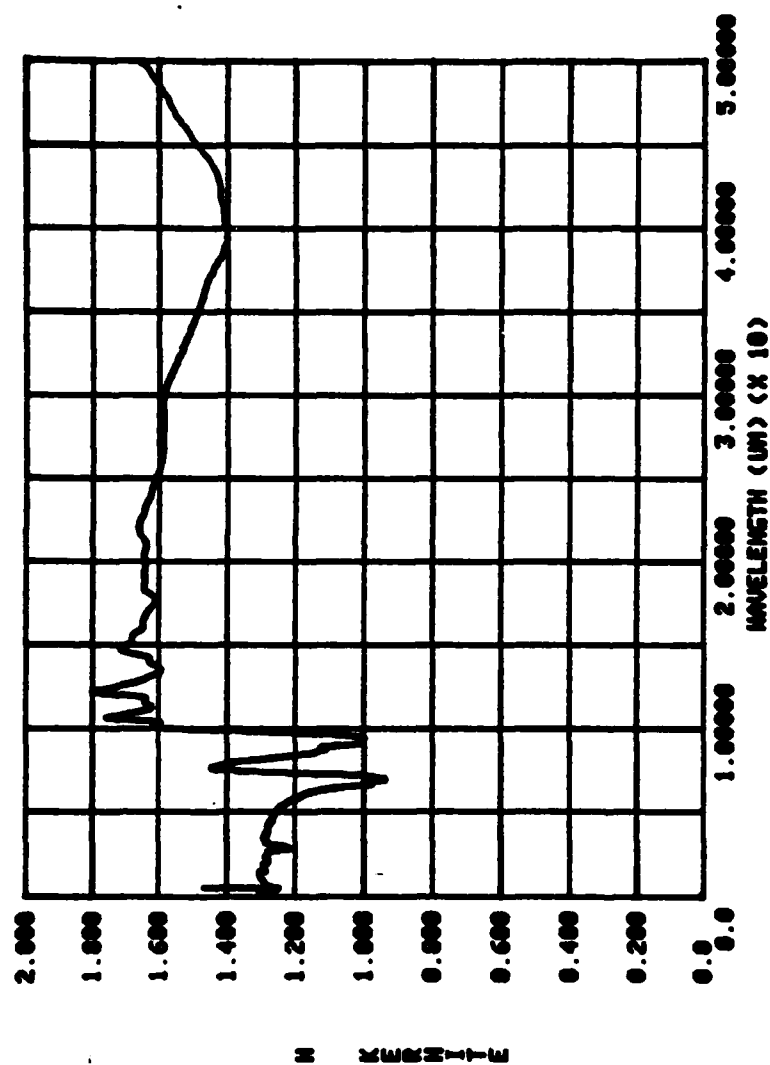


Figure F7-2. Index of refraction n of the 8T Kernite pellet in the 0.2-50 μm wavelength region.

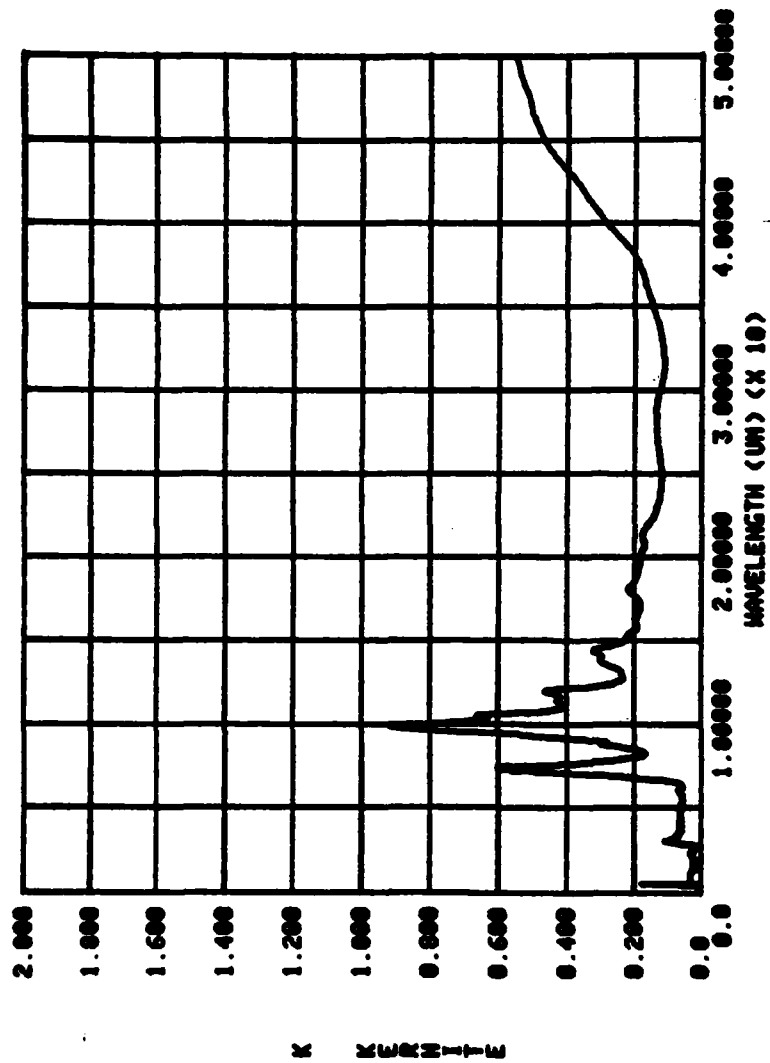


Figure F7-3. Extinction coefficient k of the 8T Kernite pellet in the 0.2-50 μm wavelength region.

8. Wavellite

Wavellite is an orthorhombic optically biaxial crystal of the $2/m\ 2/m\ 2/m$ lattice and space group. Single crystals of wavellite are rare. The specular reflectance spectrum at 6.5 deg. angle of incidence in the 0.2-50 μm wavelength region for an 8T wavellite pellet is shown in Fig. F8-1. Spectral values of n and k obtained by KK analysis of the reflectance spectrum of the 8T wavellite pellet are presented in Figs. F8-2 and F8-3, respectively.

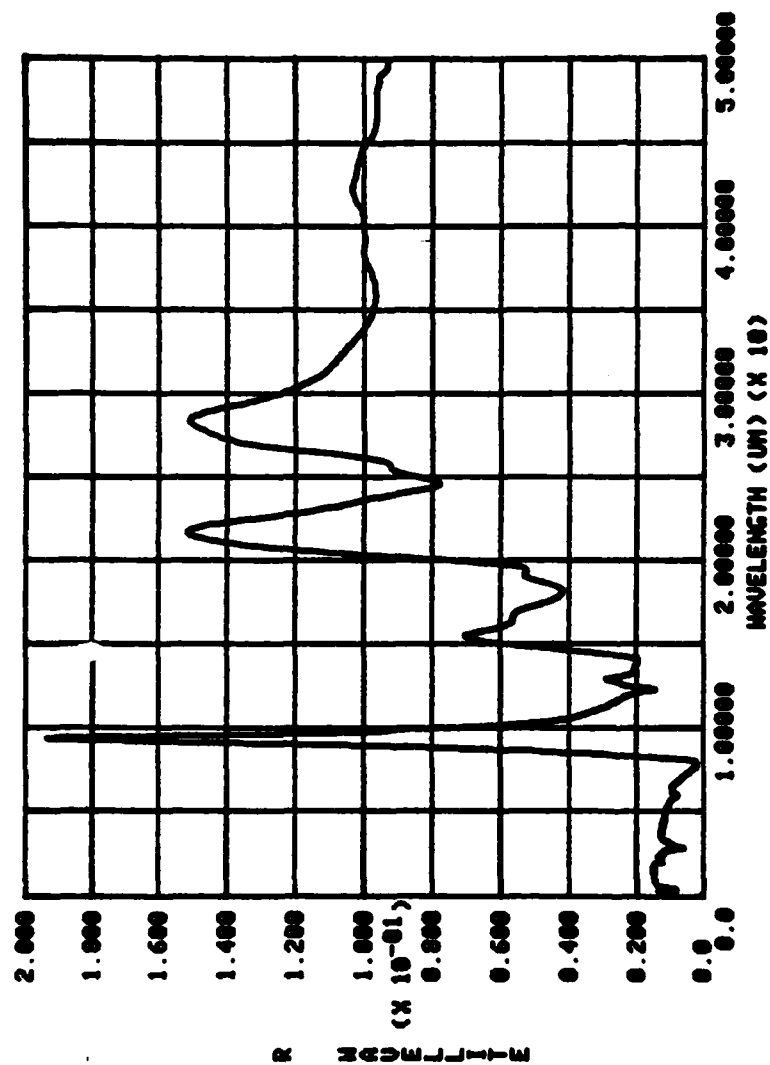


Figure F8-1. Reflectance spectrum of the 8T Wavellite pellet in the 0.2-50 μm wavelength region.

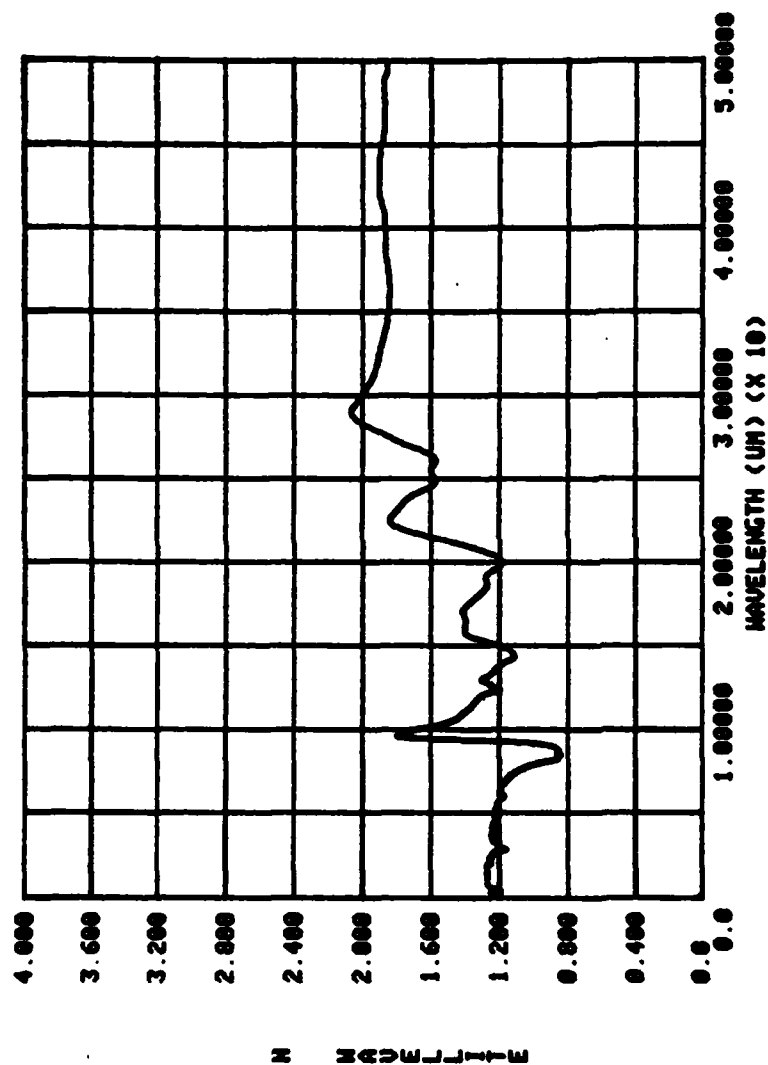


Figure F8-2. Index of refraction n of the 8T Wavellite pellet in the 0.2-50 μm wavelength region.

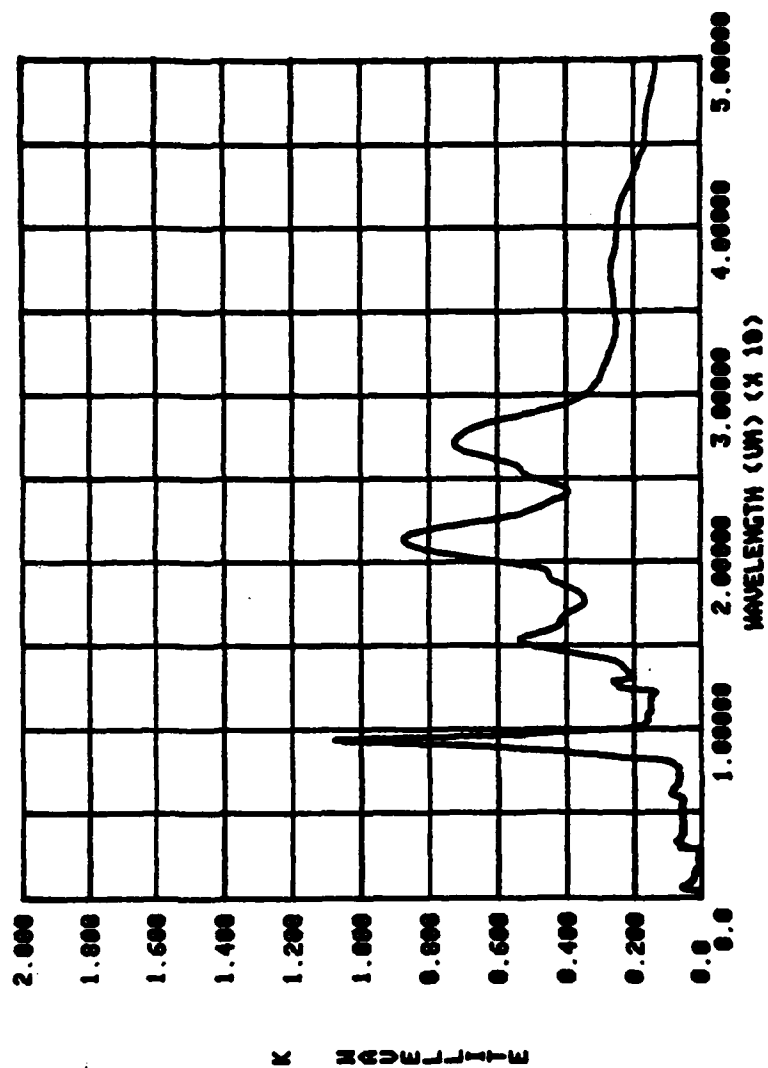


Figure F8-3. Extinction coefficient k of the 8T Wavellite pellet in the 0.2-50 μm Wavellite region.

9. Montmorillonite

Montmorillonite is a monoclinic optically biaxial clay mineral. The specular reflectance spectrum of 6.5 deg. angle of incidence in the 2.5-50 μm wavelength region is shown in Fig. F9-1 for the 8T pellet. Spectral values of n and k obtained from KK analysis of the reflectance spectrum of the 8T montmorillonite pellet are presented graphically in Figs. F9-2 and F9-3, respectively. The reflectance spectrum was also measured in the 0.2-2.5 μm wavelength region but was judged to be in error and thus is not included in this report.

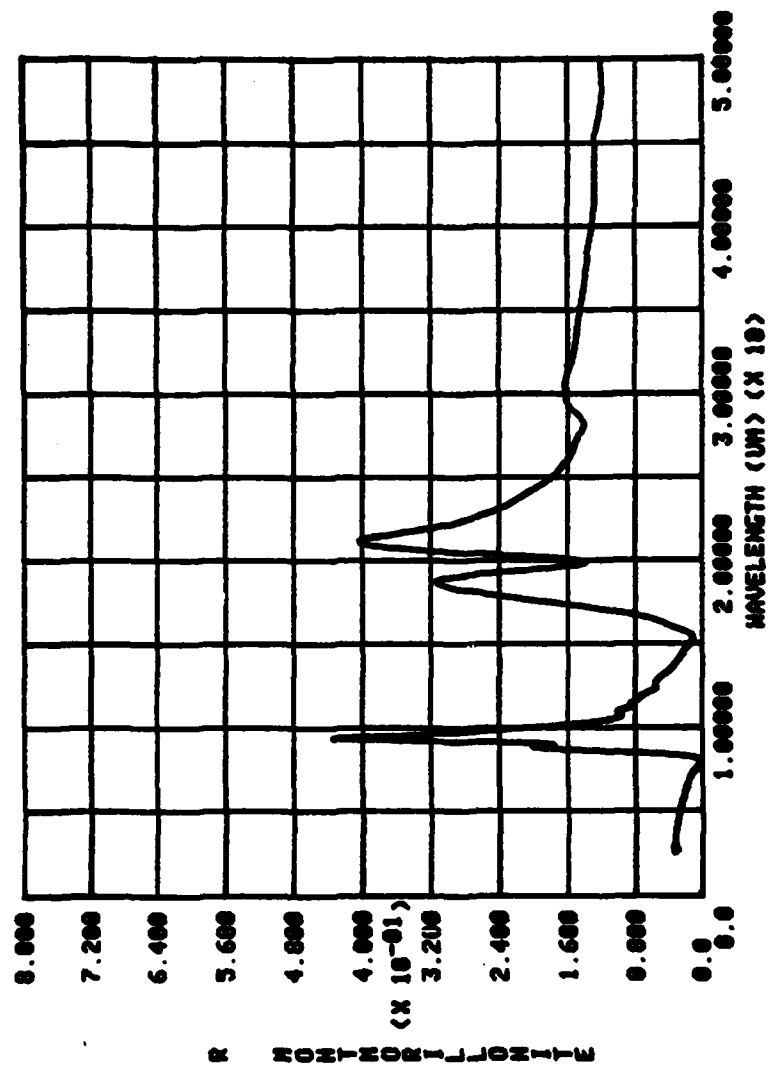


Figure F9-1. Reflectance spectrum of the 8T Montmorillonite pellet in the 2.5-50 μm wavelength region.

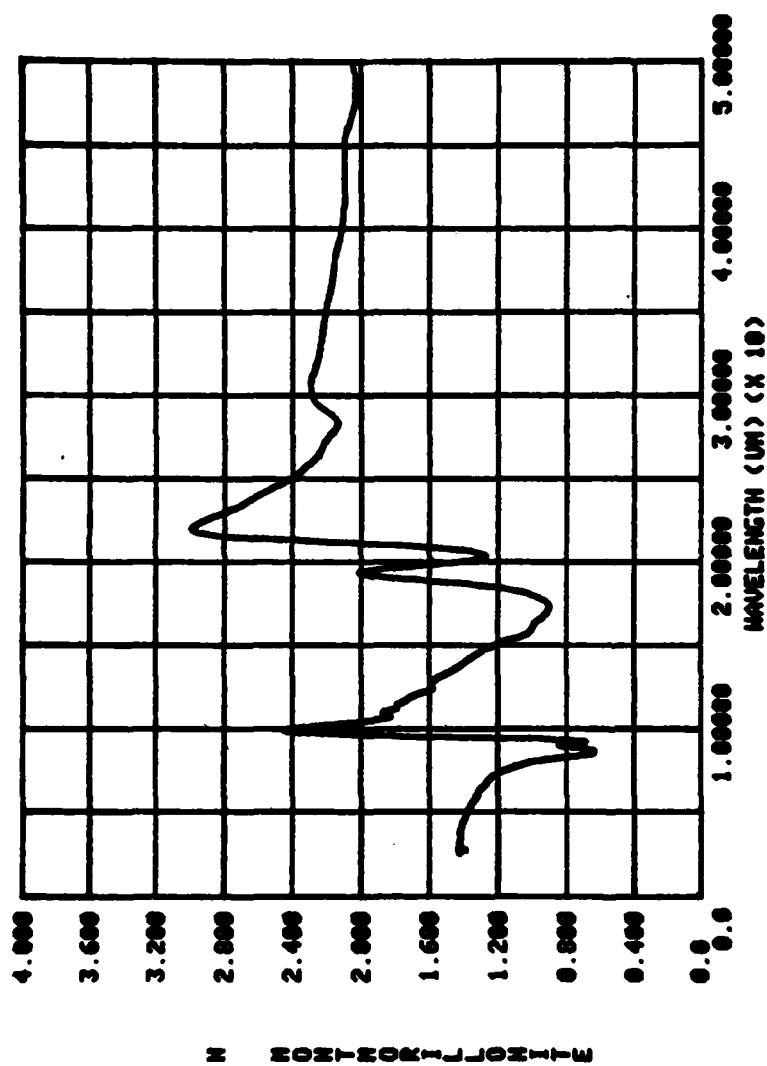


Figure F9-2. Index of refraction n of the 8T Montmorillonite pellet in the 2.5-50 μm wavelength region.

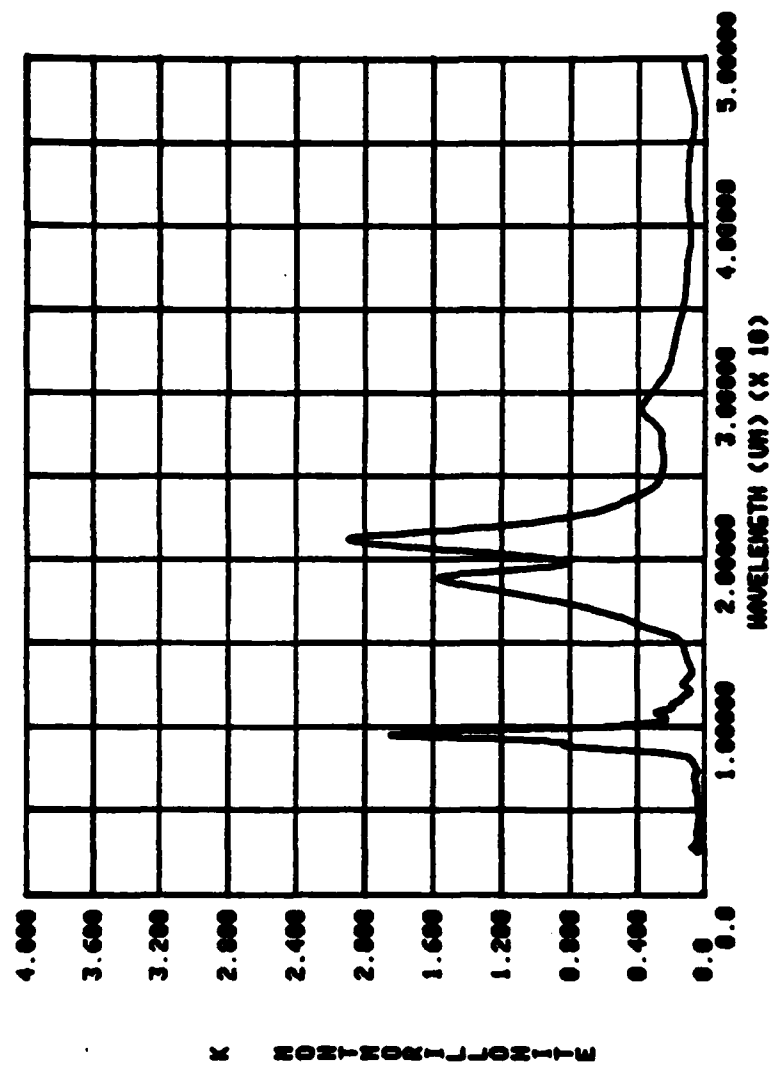


Figure F9-3. Extinction coefficient k of the 8T Montmorillonite pellet in the 2.5-50 μm wavelength region.

10. Vermiculite

Vermiculite is an altered form of Biotite with a structure similar to that of talc. Pellets of Vermiculite were very difficult to separate from the stainless steel rams between which the pellets were pressed. Only at very low relative pressure could the separation be made and then some of the Vermiculite would stick to the rams thus yielding a poor surface. Two pellets, a 3T pellet of Idaho Vermiculite and a 3T pellet of Connecticut Vermiculite were pressed and reflectance spectra were obtained. The spectra were of such poor quality due to the roughness of the surface that they were not included in this report.

Any future investigations of the optical properties of Vermiculite should be transmittance measurements of cleaved natural crystals. However, this would yield only the optical properties in the Y and Z optical directions and not in the X optical direction.

11. Chalcedony

Chalcedony is a term referring to several fibrous varieties of low quartz. Our sample was solid and appeared to be a polycrystalline material with red to pink colored impurities. The sample was cut, polished, and the reflectance spectrum at 6.5 deg. angle of incidence was measured throughout the 0.2-50 μm wavelength region. The reflectance spectrum for the 0.2-2.5 μm region is shown in Fig. F11-1, and for the 2.5-55 μm (5,000-180 cm^{-1}) region in Fig. F11-2. The KK analysis of reflectance spectrum yielded negative values of k in some spectral regions, particularly in the band near 0.3 μm . We believe that band may thus be due to fluorescence (emission) rather than reflection. Because this problem was not fully understood values of n and k were not presented here.

G. Diesel Fuel

The reflectance spectra of diesel fuel at 6.5 degrees angle of incidence was remeasured during this contract in order to eliminate some spectral artifacts due to vapor from the water standard that was used for previous measurements of reflectance. A first surface aluminum mirror was used for these measurements. The absolute reflectance of diesel fuel is shown in Fig. G-1 for the 180-4,000 cm^{-1} spectral region. Spectral values of n and k obtained from KK analysis of the reflectance spectrum are presented graphically in Figs. G-2 and G-3, respectively.

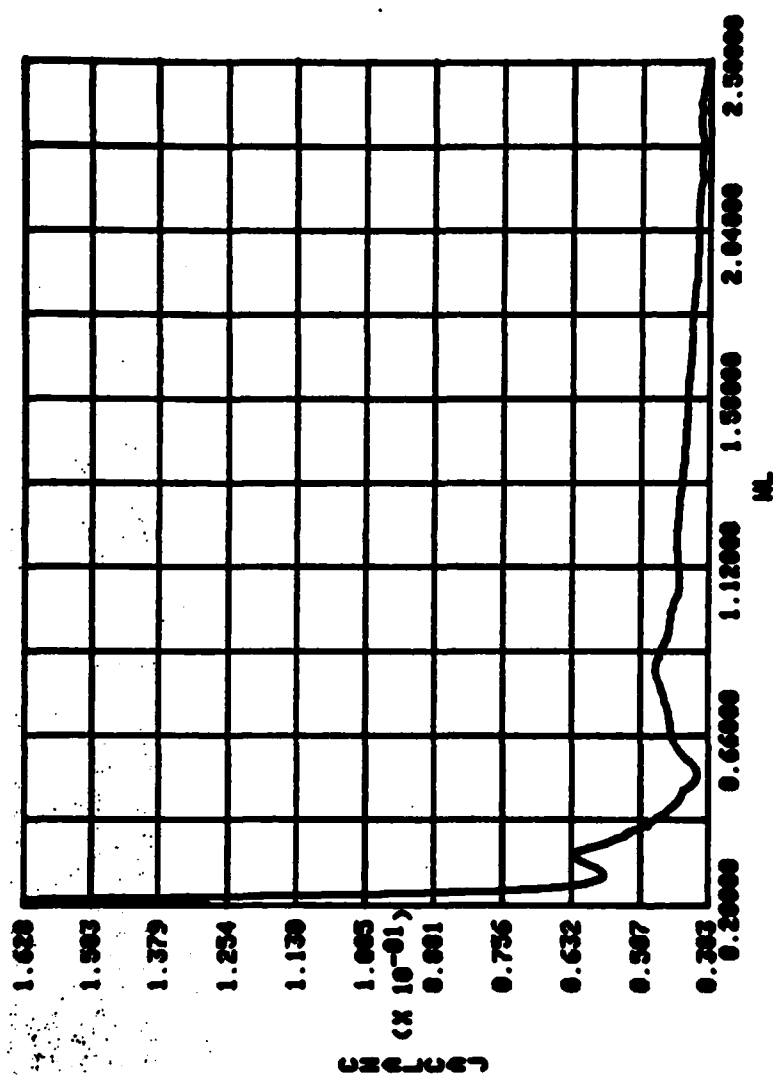


Figure F11-1. Reflectance spectrum of Chalcedony in the 0.2-2.5 μm wavelength region.

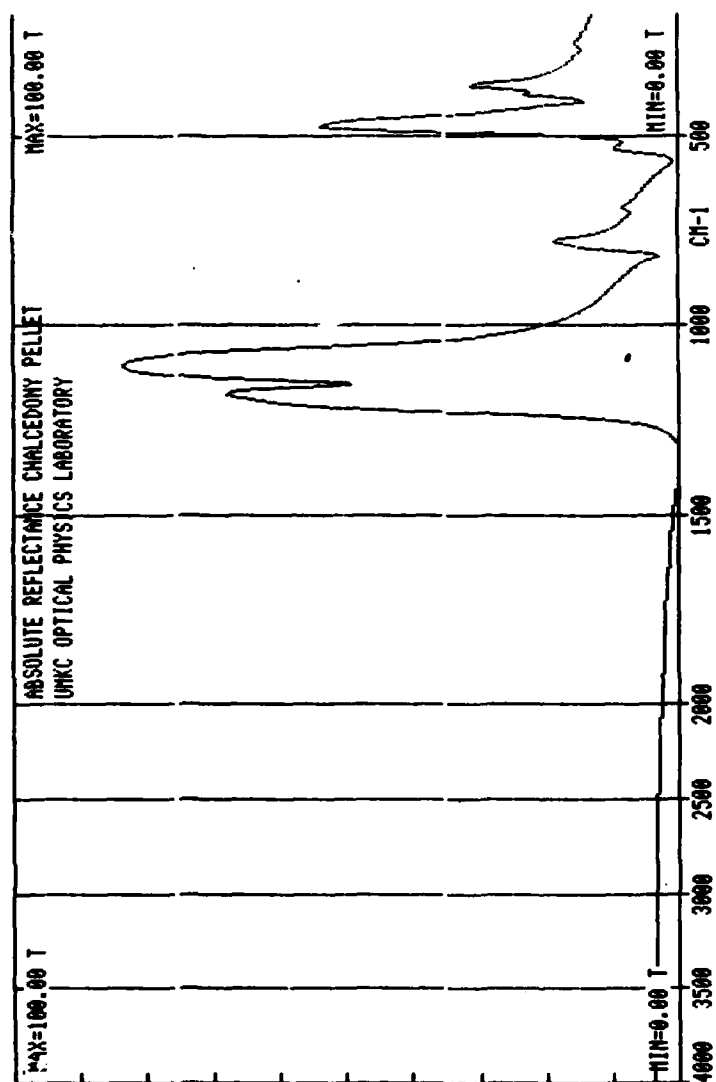


Figure F11-2. Reflectance spectrum Chalcedony in the 180-4,000 cm^{-1} wave-number region (55-2.5 μm).

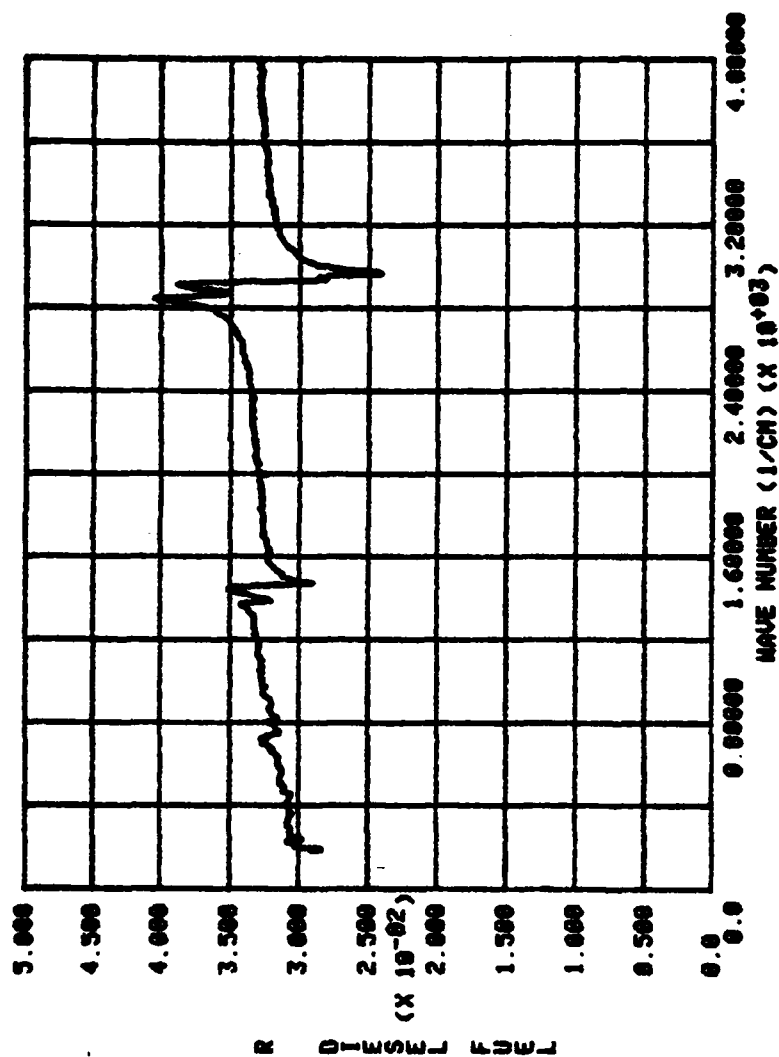


Figure G1. Reflectance spectrum of diesel in the 180-4,000 cm^{-1} wave-number region.

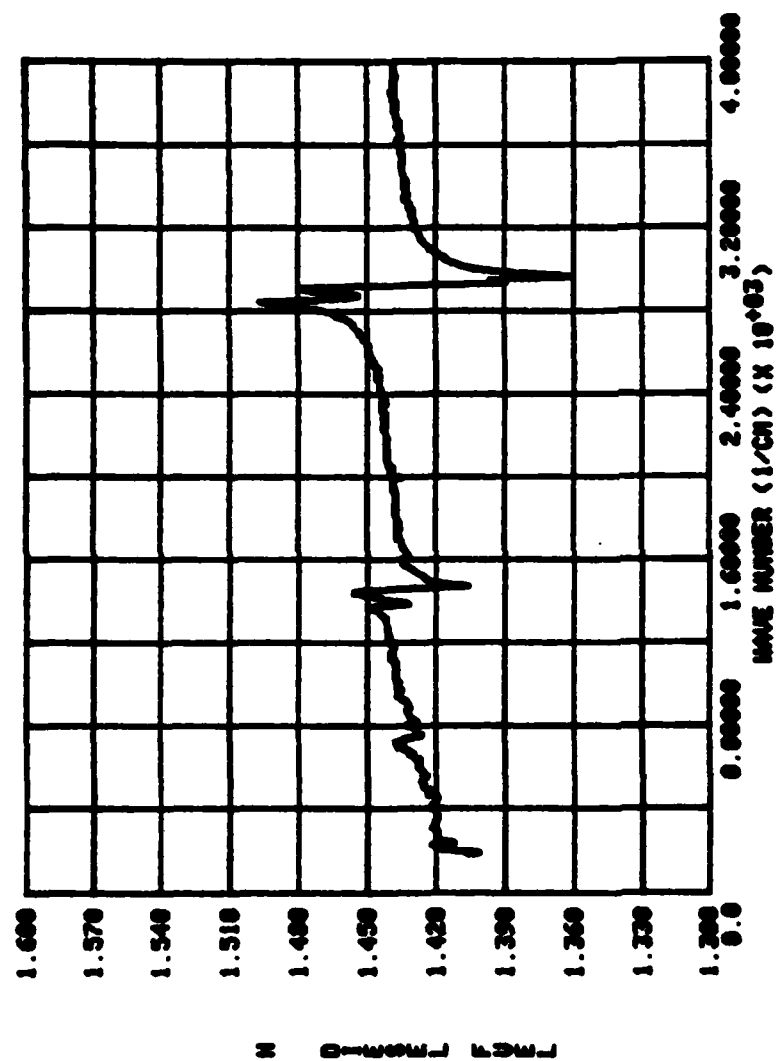


Figure G2. Index of refraction n of diesel fuel in the $180\text{--}4,000 \text{ cm}^{-1}$ wave-number region.

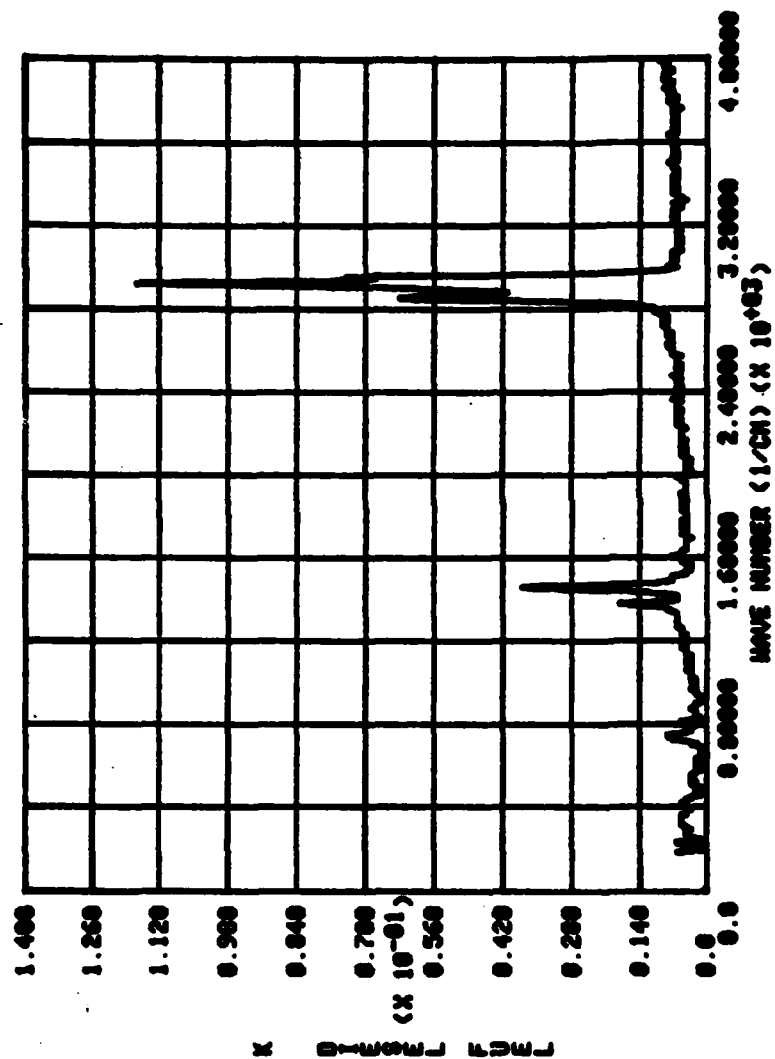


Figure G3. Extinction coefficient k of diesel fuel in the 180-4,000 cm^{-1} wave-number region.

H. ZnCl₂/H₂O Solutions and H₃PO₄/H₂O Solutions

We had previously measured the reflectance spectra and computed spectral values of n and k in the 2-33 μm wavelength region for 20/80, 30/70, 40/60, 50/50, 65/35, and 75/25 percent by weight ZnCl₂/H₂O solutions. During this contract we measured the reflectance spectra of similar solutions in the 0.2-2.0 μm wavelength region and computed values of n . Values of k for these solutions were too small to determine accurately by use of reflectance measurements and therefore are not presented here. The reflectance spectra and spectral values of n for these ZnCl₂/H₂O solutions are presented graphically in Figs. H-1 - H-12.

Similarly reflectance spectra were measured and spectral values of n were determined for 5/95, 10/90, 20/80, 40/60, 50/50, 65/35, 75/25, and 85/15 percent by weight H₃PO₄/H₂O solutions. The reflectance spectra and spectral values of n for the H₃PO₄/H₂O solutions are presented graphically in Figs. H-13 - H-18.

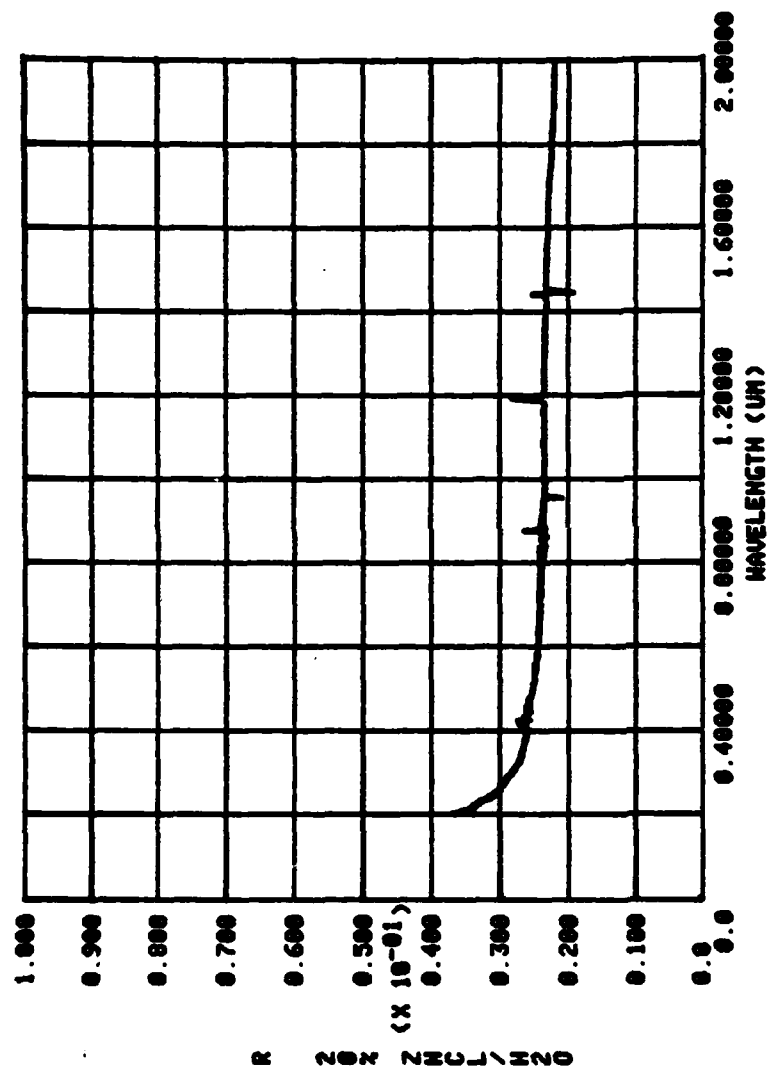


Figure H1. Reflectance spectrum of the 20/80% ZnCl₂/H₂O solution in the 0.2-2.0 μm wavelength region.

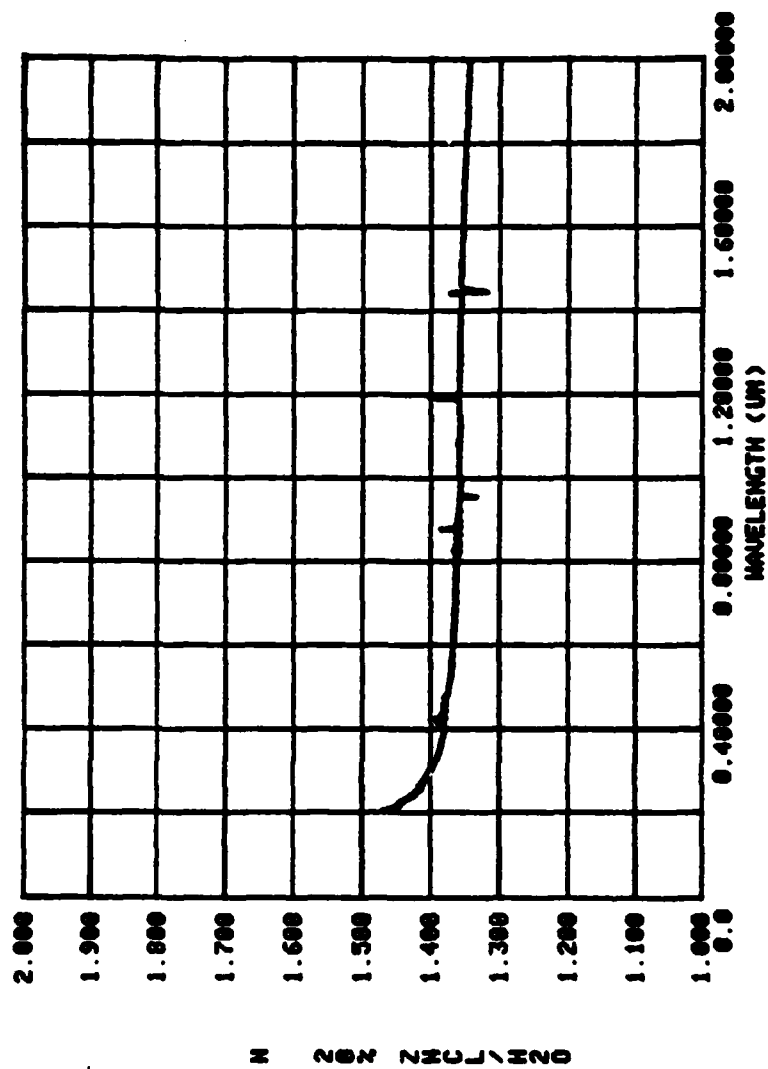


Figure H2. Index of refraction n of the 20/80% $\text{ZnCl}_2/\text{H}_2\text{O}$ solution in the 0.2-2.0 μm wavelength region.

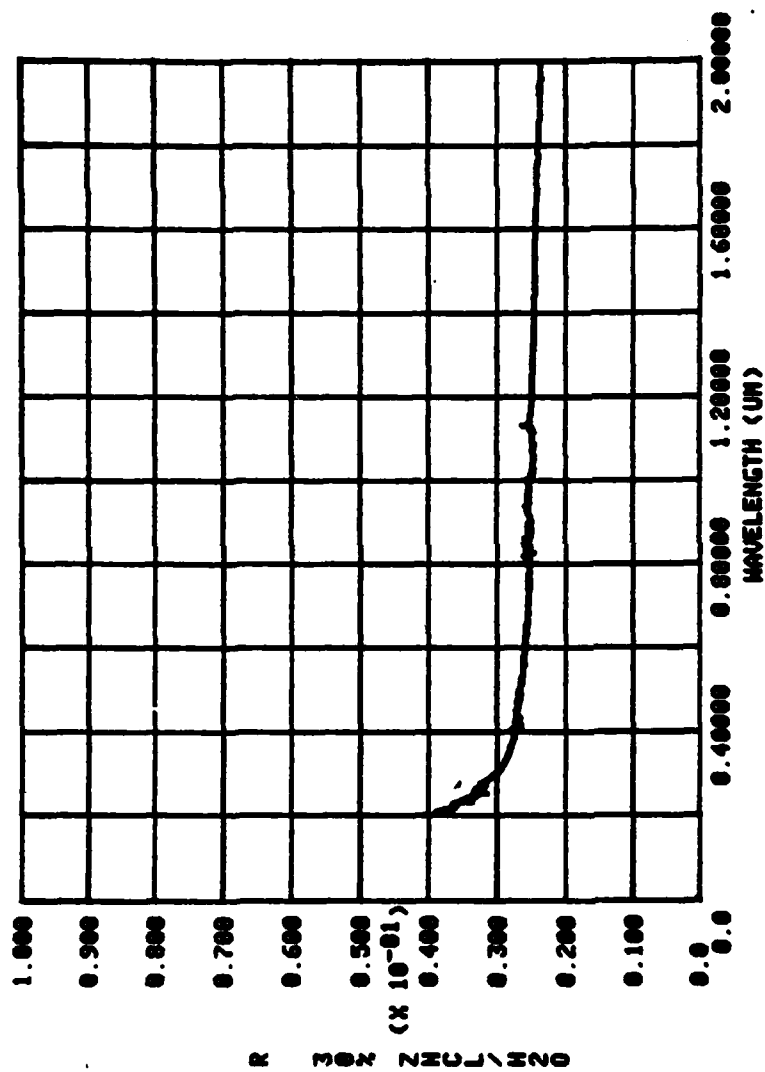


Figure H3. Reflectance spectrum of the 30/70% ZnCl₂/H₂O solution in the 0.2-2.0 μ m wavelength region.

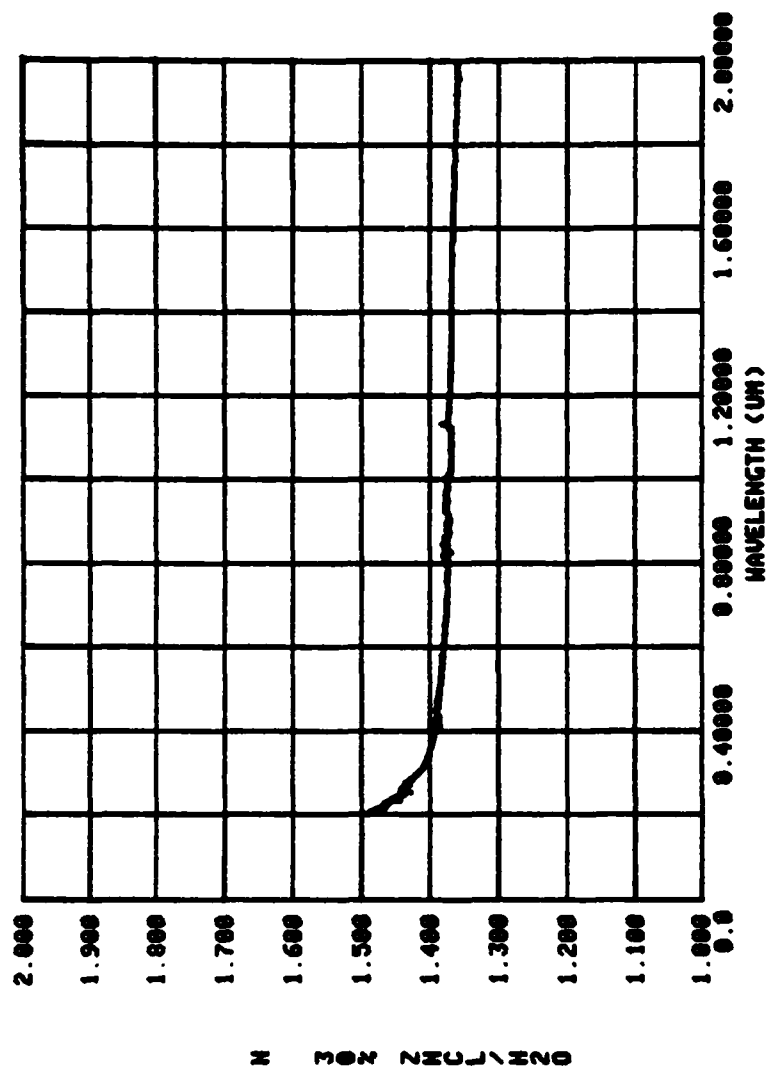


Figure H4. Index of refraction n of the 30/70% $\text{ZnCl}_2/\text{H}_2\text{O}$ solution in the 0.2-2.0 μm wavelength region.

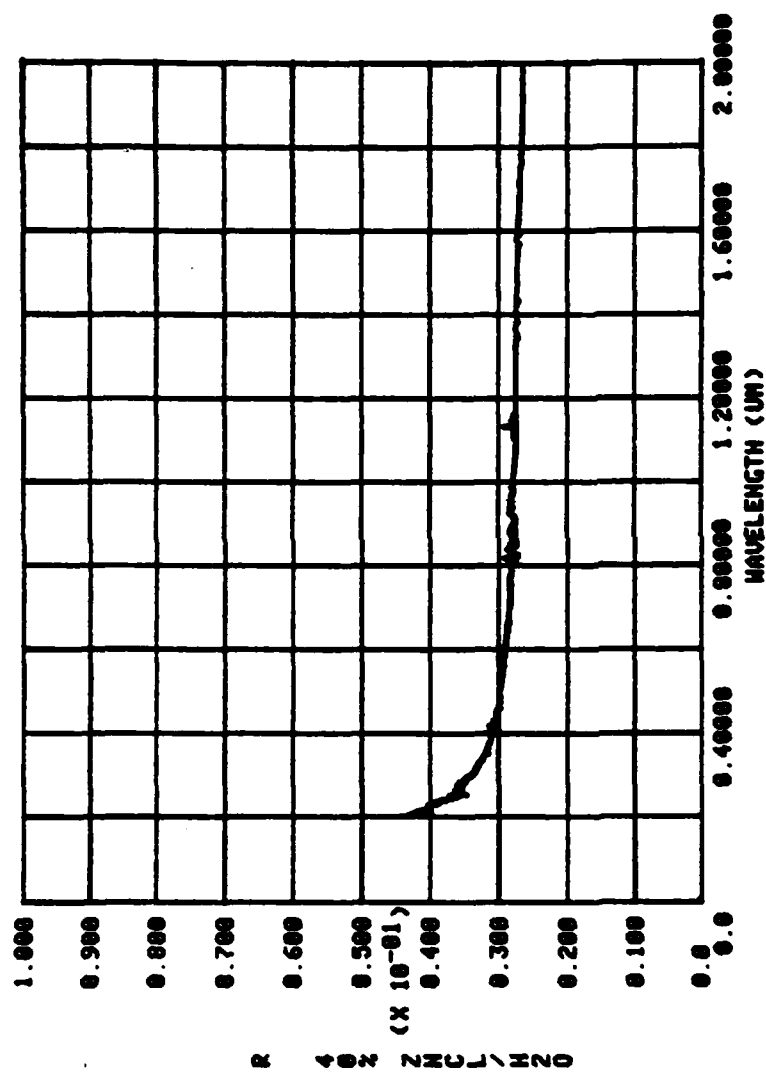


Figure H5. Reflectance spectrum of the 40/60% ZnCl₂/H₂O solution in the 0.2-2.0 μm wavelength region.

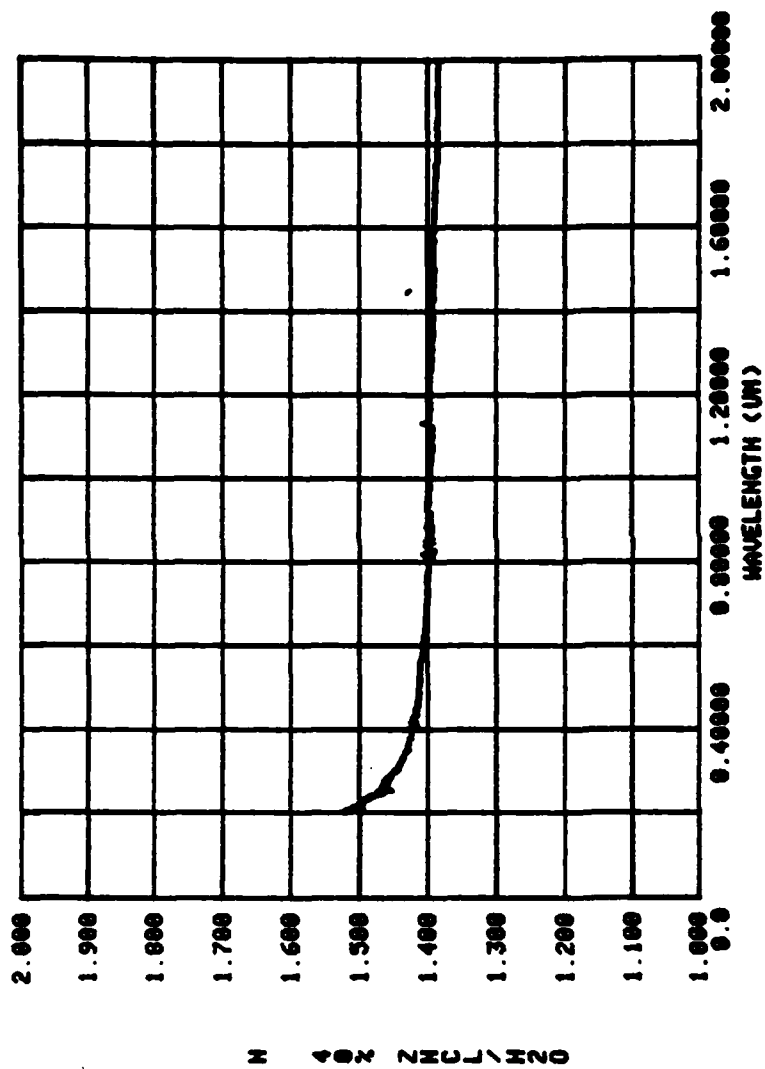


Figure H6. Index of refraction n of the 40/60% $\text{ZnCl}_2/\text{H}_2\text{O}$ solution in the 0.2-2.0 μm wavelength region.

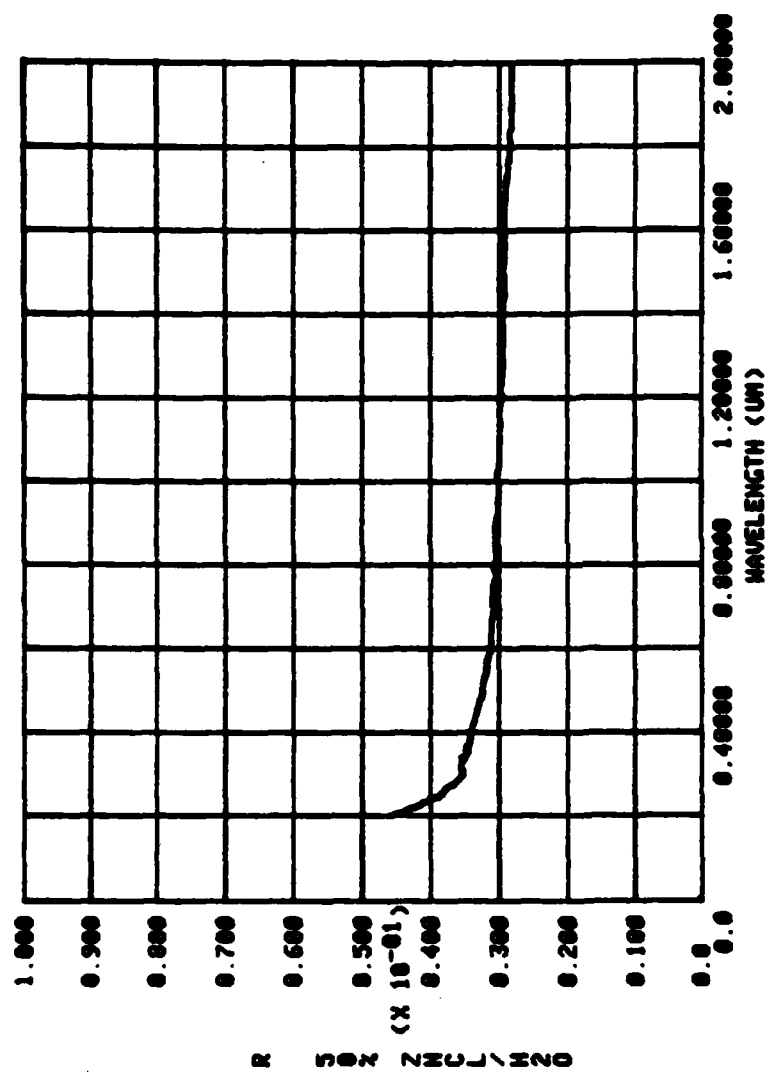


Figure H7. Reflectance spectrum of the 50/50% $\text{ZnCl}_2/\text{H}_2\text{O}$ solution in the 0.2-2.0 μm wavelength region.

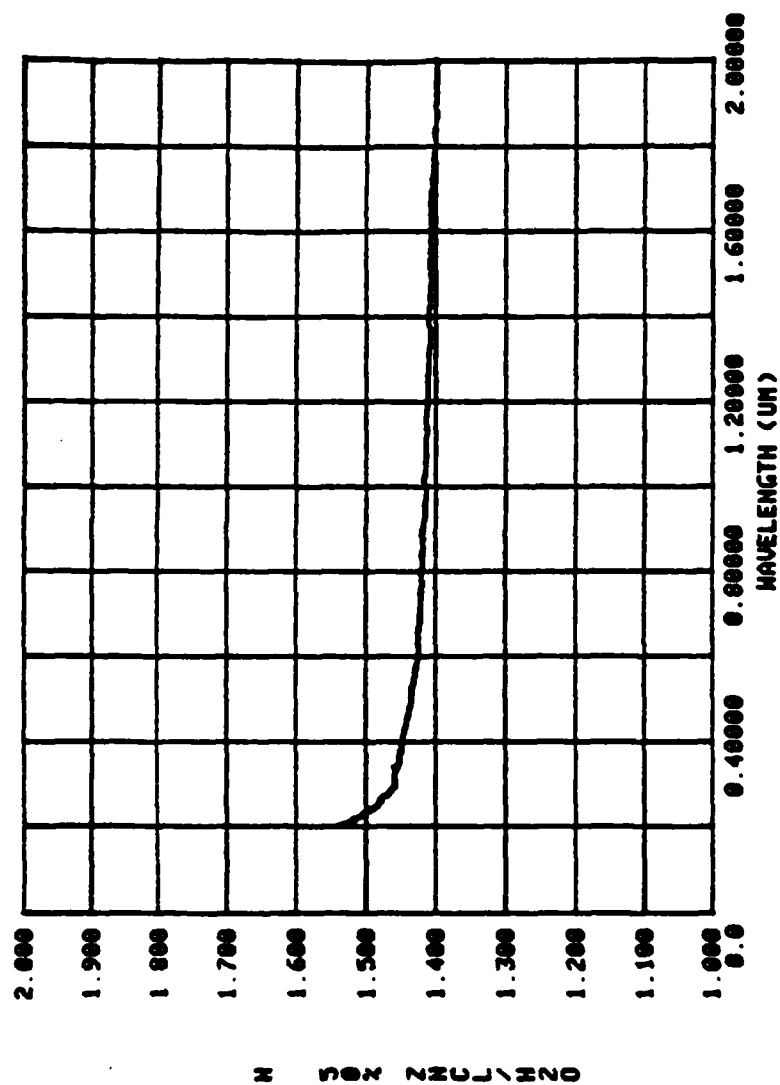


Figure H8. Index of refraction n of the 50/50% $\text{ZnCl}_2/\text{H}_2\text{O}$ solution in the 0.2-2.0 μm wavelength region.

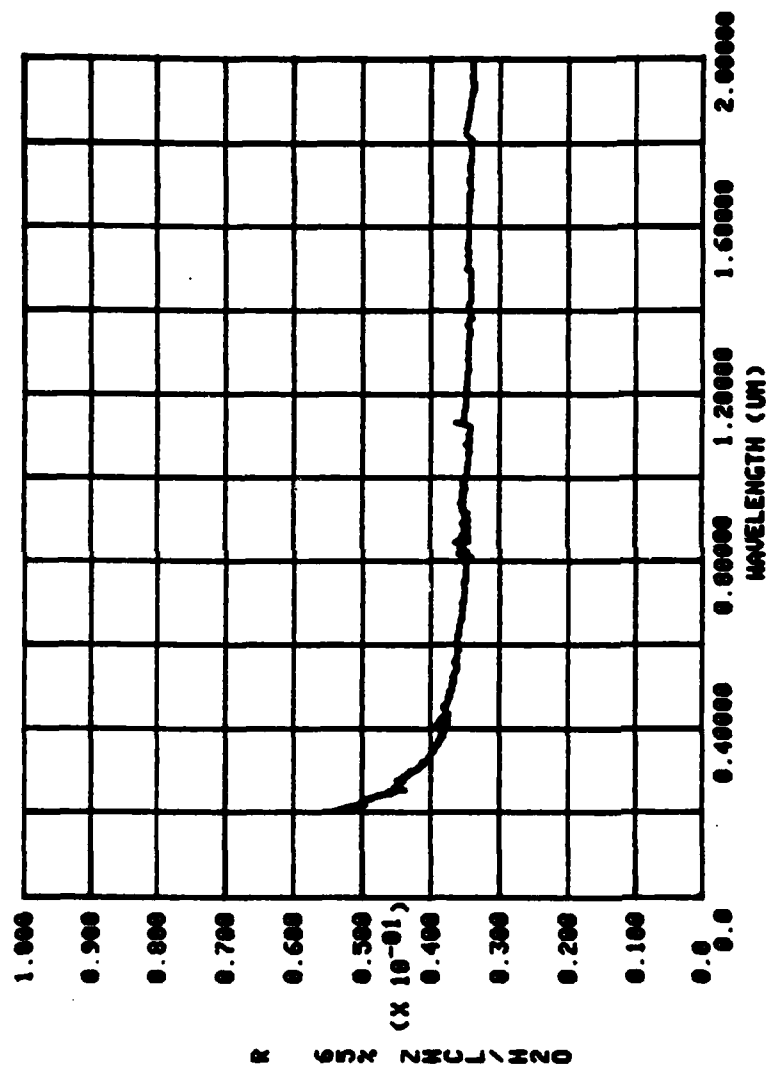


Figure H9. Reflectance spectrum of the 65/35% $\text{ZnCl}_2/\text{H}_2\text{O}$ solution in the 0.2-2.0 μm wavelength region.

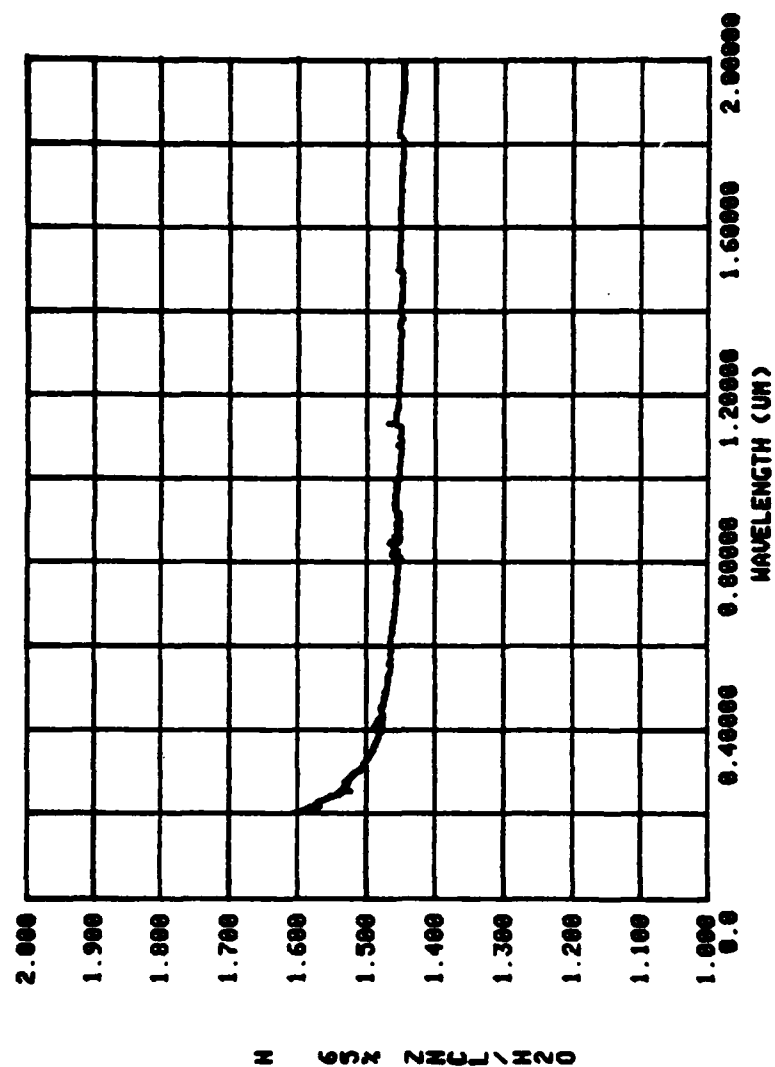


Figure H10. Index of refraction n of the 65/35% $\text{ZnCl}_2/\text{H}_2\text{O}$ solution in the 0.2-2.0 μm wavelength region.

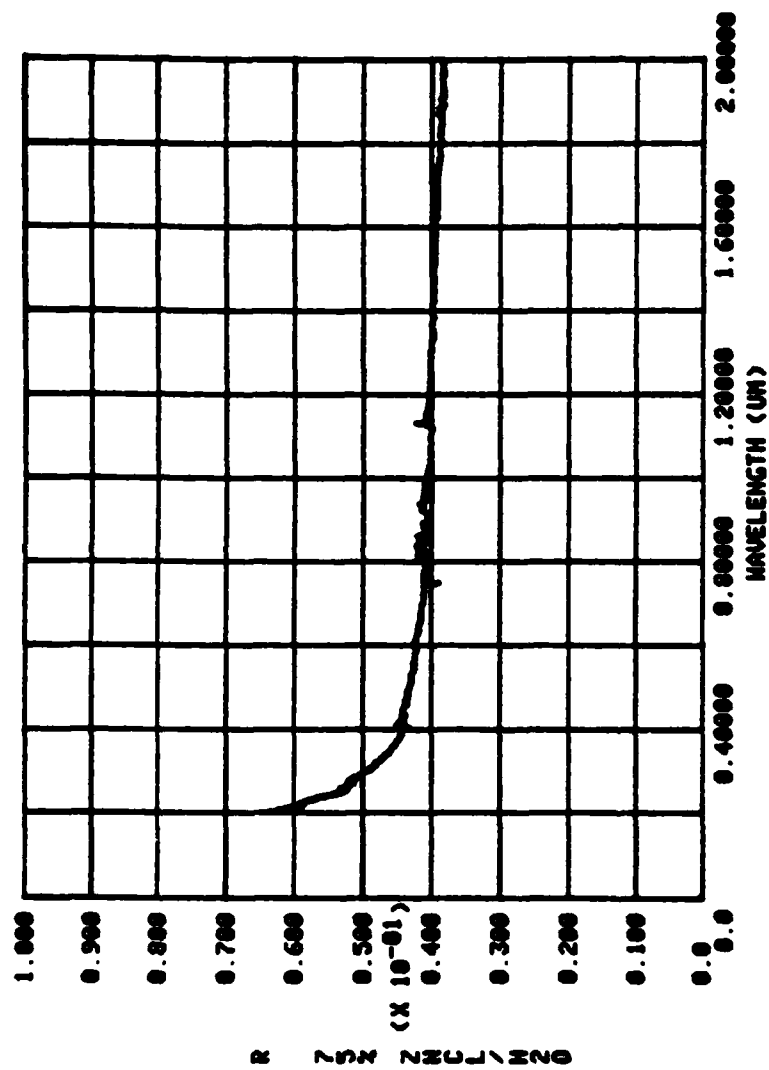


Figure H11. Reflectance spectrum of the 75/25% $\text{ZnCl}_2/\text{H}_2\text{O}$ solution in the 0.2-2.0 μm wavelength region.

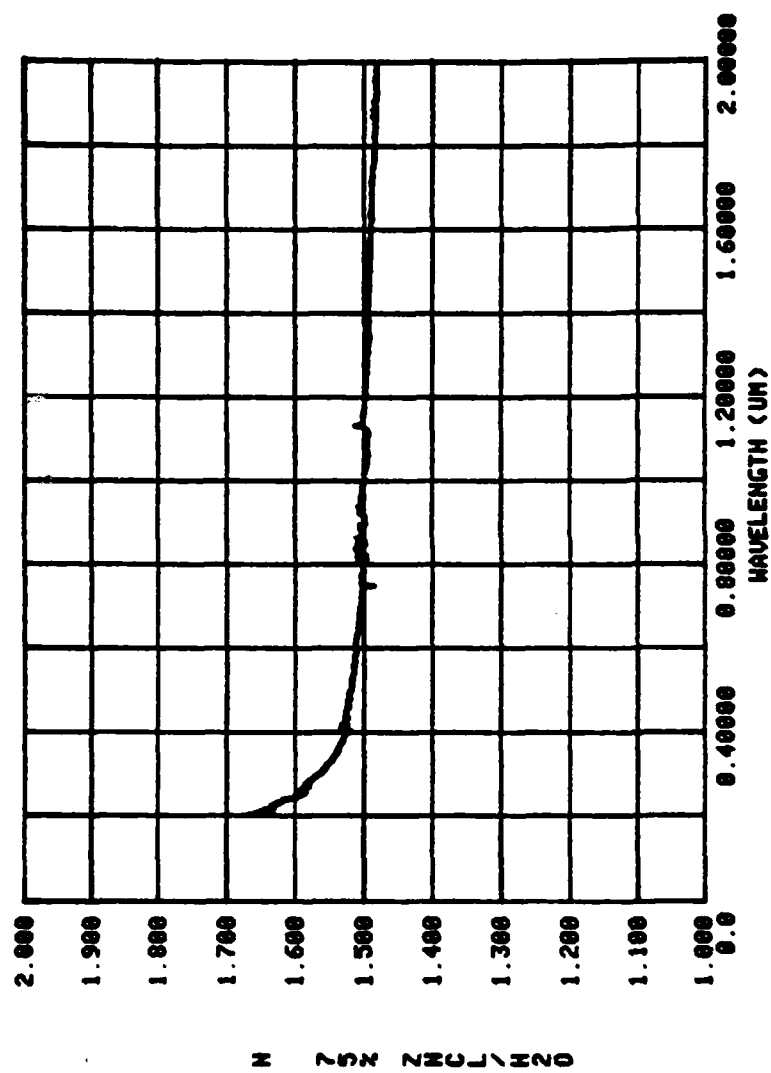


Figure H12. Index of refraction of the 75/25% $\text{ZnCl}_2/\text{H}_2\text{O}$ solution in the 0.2-2.0 μm wavelength region.

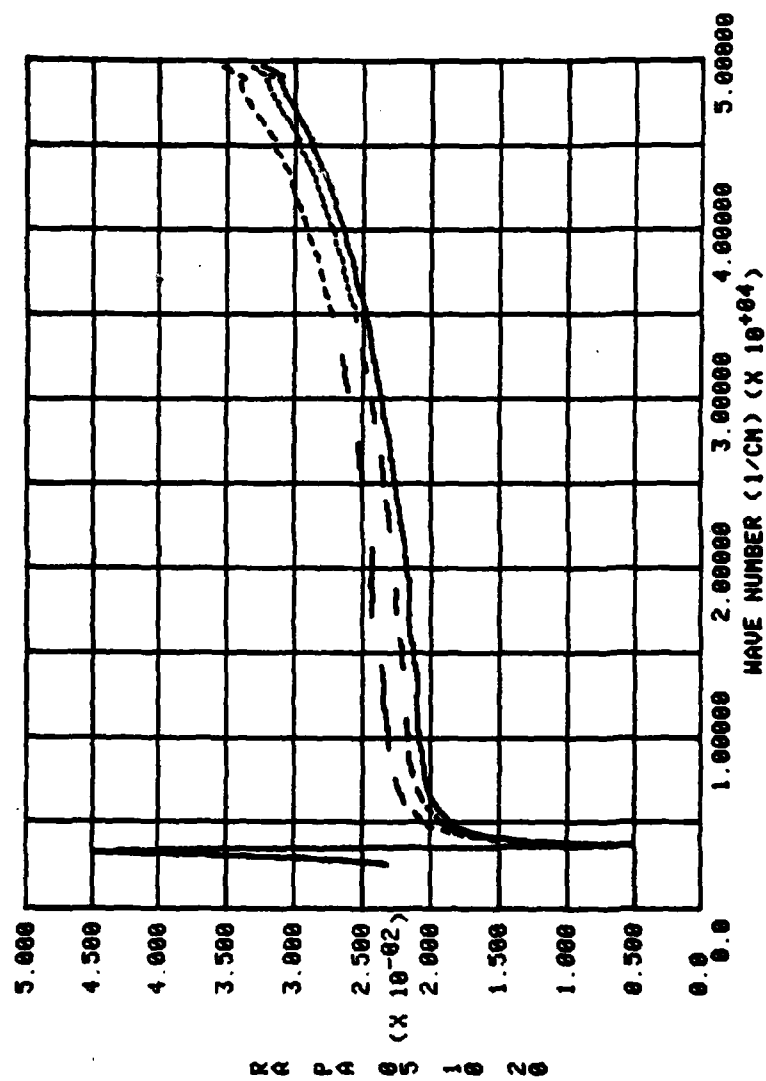


Figure H 13. Reflectance spectra of the 05/95, 10/90, and 20/80% $\text{H}_3\text{PO}_4/\text{H}_2\text{O}$ solutions in the 2,500-50,000 cm^{-1} wave-number region.

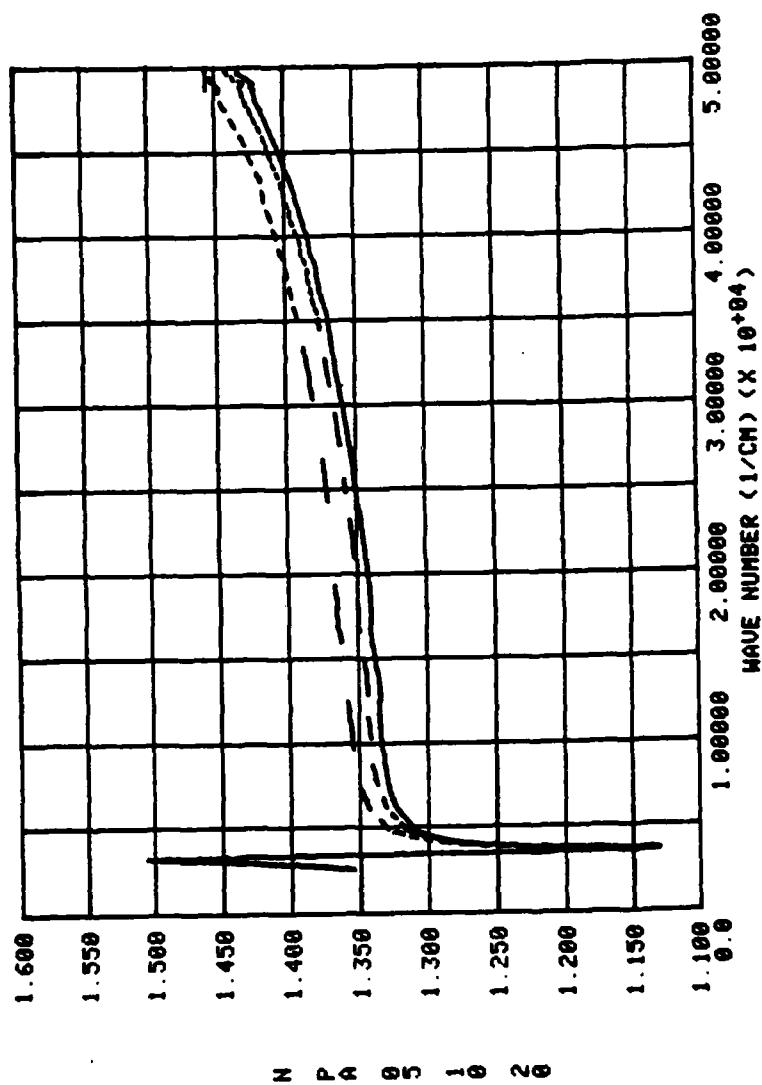


Figure H14. Index of refraction n of the 05/95, 10/90, and 20/80% $\text{H}_3\text{PO}_4/\text{H}_2\text{O}$ solution in the 2,500–50,000 cm^{-1} wave-number region

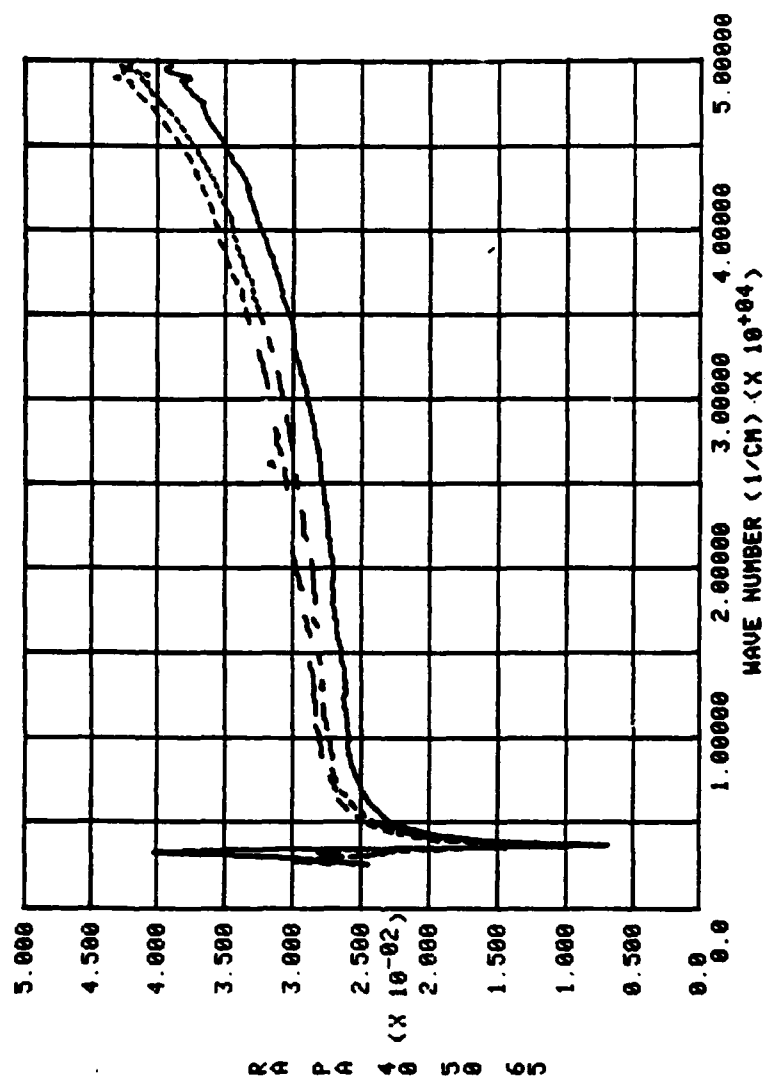


Figure H15. Reflectance spectra of the 40/60, 50/50, and 65/35% $\text{H}_3\text{PO}_4/\text{H}_2\text{O}$ solutions in the 2,500-50,000 cm^{-1} wave-number region.

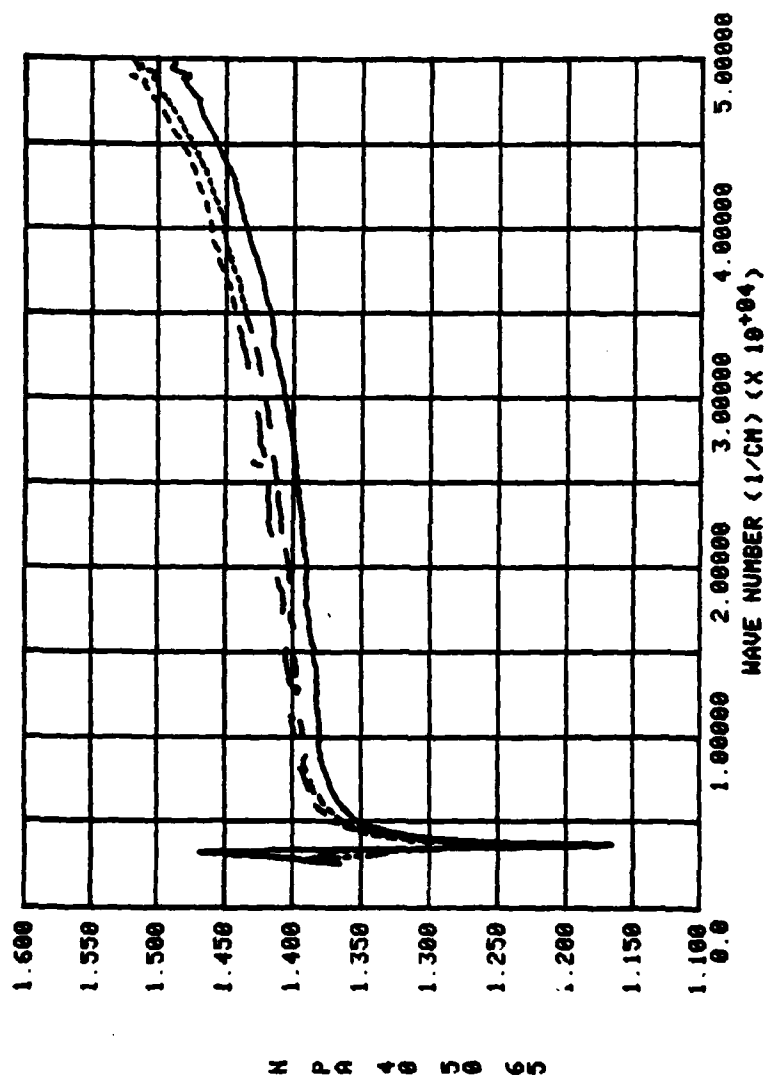


Figure H16. Index of refraction n of the 40/60, 50/50, and 65/35% $\text{H}_3\text{PO}_4/\text{H}_2\text{O}$ solutions in the 2,500–50,000 cm^{-1} wave-number region.

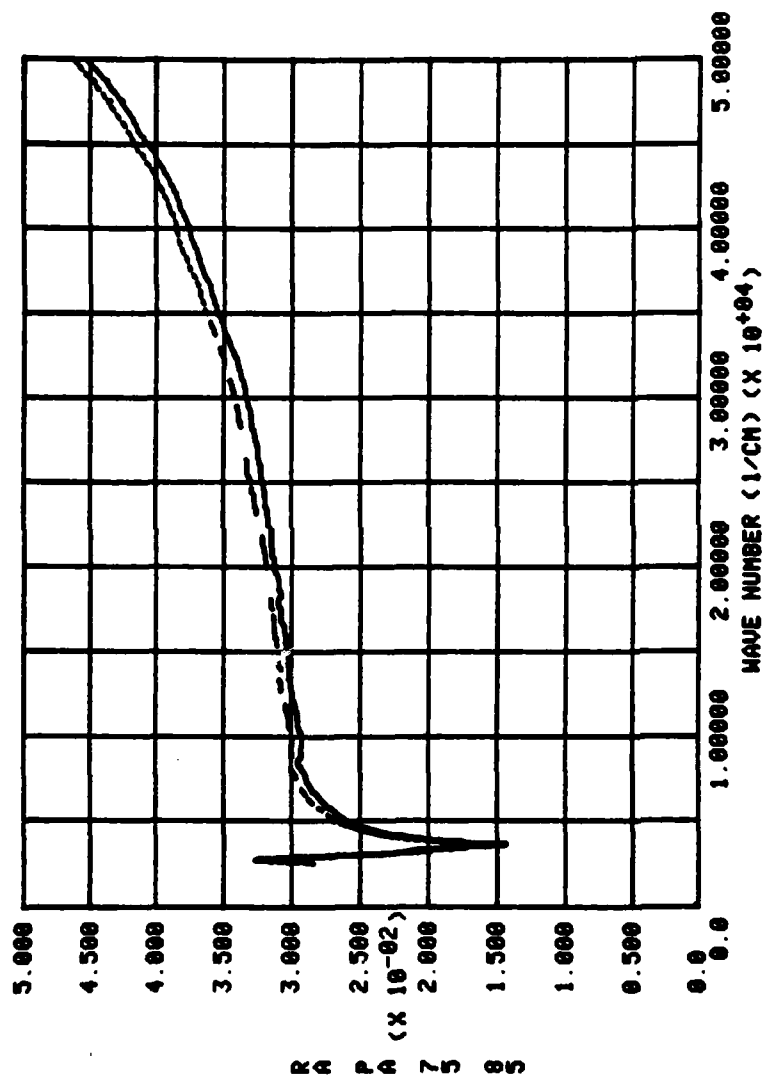


Figure H17. Reflectance spectra of the 75/25 and 85/15% $\text{H}_3\text{PO}_4/\text{H}_2\text{O}$ solutions in the 2,500-50,000 cm^{-1} wave-number region.

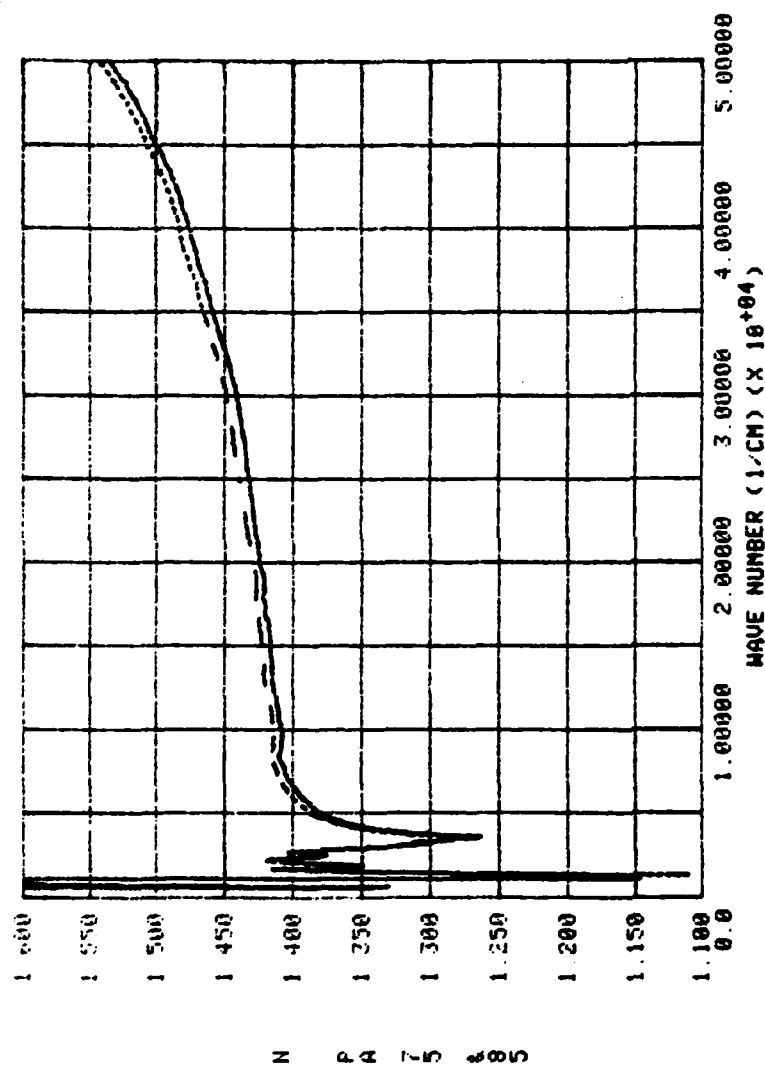


Figure H18. Index of refraction n of the 75/25 and 85/15% $\text{H}_3\text{PO}_4/\text{H}_2\text{O}$ solutions in the 300–50,000 cm^{-1} wave-number region.

J. Complex Refractive Indices of Water

Hale and Querry (1973) previously published values of the complex refractive index of water in the 200 nm to 200 μ m wavelength range. Their investigation was based on a KK analysis of a k spectrum for water compiled from about 80 papers in the scientific literature. The KK analysis provided spectral values of n. Other measurements of the optical properties of water have been published since 1973. Thus we have incorporated these new values of k into the k spectrum and determined the complex refractive index of water in the 10^{-3} to 10^6 cm^{-1} range. The following M.S. thesis by Mr. David Segelstein describes our updated investigations of the complex refractive index of water.

THE COMPLEX REFRACTIVE INDEX OF WATER

A THESIS IN
Physics

Presented to the Faculty of the University
of Missouri-Kansas City in partial fulfillment of
the requirements for the degree

MASTER OF SCIENCE

by
DAVID J. SEGELSTEIN

B.A., Columbia University, 1971
J.D., University of Missouri-Kansas City, 1975

Kansas City, Missouri
1981

THE COMPLEX REFRACTIVE INDEX OF WATER

David J. Segelstein, Master of Science

University of Missouri-Kansas City, 1981

ABSTRACT

A spectrum of the imaginary part of the complex index of refraction for water as a function of wave number was compiled from the literature and theoretical considerations. The spectrum ranged from 10^{-6} through 10^8 cm^{-1} . The curve was adjusted within the limits of error for the data used until an electronic sum rule gave proper results. The spectrum was then appropriately Fourier transformed to yield the real part of the complex refractive index. The results of several calculations over various ranges were combined into one spectrum over the range 10^{-3} through 10^6 cm^{-1} . Both real and imaginary parts are presented in graphical and tabular form.

This abstract of 106 words is approved as to form and content.

Marvin R. Query

The undersigned, appointed by the Dean of the School of Graduate Studies, have examined a thesis entitled "The Complex Refractive Index of Water," presented by David J. Segelstein, candidate for the degree Master of Science, and hereby certify that in their opinion it is worthy of acceptance.

Marvin R. Query, Ph.D.
Department of Physics

Date

John R. Urani, Ph.D.
Department of Physics

Date

Wai Yim Ching, Ph.D.
Department of Physics

Date

TABLE OF CONTENTS

ABSTRACT	ii
LIST OF ILLUSTRATIONS	vi
LIST OF TABLES	viii
ACKNOWLEDGMENTS	ix

Chapter

I. INTRODUCTION	1
Survey of the Literature	2
Description of the Research	4
II. ACQUISITION OF DATA	6
The Middle Range	6
Low Frequency Data	8
High Frequency Data	10
Application of the Sum Rule	12
III. THEORETICAL METHODS	23
The Complex Refractive Index	23
The Lambert Absorption Coefficient	31
The Kramers-Kronig Relations as Obtained from the Response Function	33
The Lorentz Oscillator Model	44
Analytic Properties of $N(\omega)$	48
The Kramers-Kronig Relations as Obtained from the Cauchy Integral Formula	59
The Real Part of $N(\omega)$ as a Fourier Transform	64
The Electronic Sum Rule	66
IV. NUMERICAL METHODS	70
The Numerical Computation of $n(\omega)$ from $k(\omega)$	70
Calculations	75

V. RESULTS	116
VI. CONCLUSION	162
REFERENCES	165
VITA	167

LIST OF ILLUSTRATIONS

1.	The Absorption Spectrum in the Region of Adjustment	15
2.	Detail of Figure 1	17
3.	The Absorption Spectrum in Full	19
4.	The Value of the Sum Rule Integral	21
5.	An Illustration of Increased Resolution by Reducing the Range	80
6.	The Spectrum Calculated for the Range 0 to $5 \times 10^6 \text{ cm}^{-1}$. . .	82
7.	The Spectrum Calculated for the Range 0 to $5 \times 10^5 \text{ cm}^{-1}$. . .	84
8.	The Spectrum Calculated for the Range 0 to $5 \times 10^4 \text{ cm}^{-1}$. . .	86
9.	The Spectrum Calculated for the Range 0 to $5 \times 10^3 \text{ cm}^{-1}$. . .	88
10.	The Spectrum Calculated for the Range 0 to $5 \times 10^2 \text{ cm}^{-1}$. . .	90
11.	The Spectrum Calculated for the Range 0 to $5 \times 10^1 \text{ cm}^{-1}$. . .	92
12.	The Spectrum Calculated for the Range 0 to 5 cm^{-1}	94
13.	The Spectrum Calculated for the Range 0 to $5 \times 10^{-1} \text{ cm}^{-1}$. .	96
14.	An Illustration of Inaccuracy as an Endpoint Is Approached	98
15.	Fitting Low Frequency Results	100
16.	The Transition in the Region of 10^{-1} cm^{-1}	102
17.	The Transition in the Region of 1 cm^{-1}	104
18.	The Transition in the Region of 10 cm^{-1}	106
19.	The Transition in the Region of 10^2 cm^{-1}	108
20.	The Transition in the Region of 10^3 cm^{-1}	110

21.	The Transition in the Region of 10^4 cm^{-1}	112
22.	The Transition in the Region of 10^5 cm^{-1}	114
23.	The Final Spectrum from 0 to 10^6 cm^{-1}	146
24.	The Final Spectrum from 0 to 10^5 cm^{-1}	148
25.	The Final Spectrum from 0 to 10^4 cm^{-1}	150
26.	The Final Spectrum from 0 to 10^3 cm^{-1}	152
27.	The Final Spectrum from 0 to 10^2 cm^{-1}	154
28.	The Final Spectrum from 0 to 10 cm^{-1}	156
29.	The Final Spectrum from 0 to 1 cm^{-1}	158
30.	The Final Spectrum from 0 to 10^{-1} cm^{-1}	160

LIST OF TABLES

1. The Complex Refractive Index from 10^{-3} to 10^6 cm^{-1} 116

ACKNOWLEDGMENTS

I would like to thank the faculty of the Physics Department of the University of Missouri-Kansas City for struggling so tirelessly to bring me to this point. I would especially thank Dr. Marvin Querry, who is the most patient individual I have ever met, for his generous and warm guidance whenever it was requested. I would also express my gratitude to the entire staff of the University of Missouri-Kansas City Computer Center for their kind tolerance of my constant pestering, and for their always competent assistance.

CHAPTER I

INTRODUCTION

Water is one of earth's most common and important substances. Information concerning its optical properties is of great significance in many areas of science and engineering. Knowledge of its properties is a first step, for example, in the ability to interpret data on aqueous solutions, including the oceans and the atmosphere. Water is also interesting because it serves as a challenging object for the application of the full analytical power of classical electromagnetic theory. One tool in the analysis of its optical properties is the complex refractive index $N(\nu)$ as a function of wave number:

$$N(\nu) \equiv n(\nu) + ik(\nu) \quad (1.1)$$

where the wave number, ν , is defined as the inverse of wavelength, and has units of cm^{-1} . From $N(\nu)$ one can calculate a variety of optical properties such as reflectance, transmittance, emittance, and Mie scattering parameters at any spectral location.

The purpose of the research described in this thesis was a determination of $N(\nu)$ for water throughout the wave number region of from 10^{-3} to 10^6 cm^{-1} . This corresponds to a frequency range of from 10^7 to 10^{16} Hz , a wavelength range of from 100 \AA to 10 m . This task has been undertaken previously by other investigators, but not over such a broad spectral region.

Survey of the Literature

In 1973, Hale and Querry¹ reported optical constants for the region 50 to $5 \times 10^4 \text{ cm}^{-1}$ (200 nm to 200 μm wavelength). They compiled a composite spectrum of $k(\nu)$, the extinction coefficient, from 58 sources representing data reported over a span of 81 years prior to their paper. This spectrum was transformed by Kramers-Kronig analysis to a spectrum of $n(\nu)$ for the region reported.

Some of the data used by Hale and Querry were incomplete or postulated. For example, a Gaussian-shaped absorption band was postulated for $k(\nu)$ with a peak in the area of $1.25 \times 10^6 \text{ cm}^{-1}$ (80 \AA wavelength). This would be the peak associated with the K-edge for electronic absorption. Also, the higher wave-number side of an absorption peak reported at approximately $1.2 \times 10^5 \text{ cm}^{-1}$ was postulated to be of Gaussian shape and appropriate width. These deficiencies were recognized by Hale and Querry, and were the basis for their implication that more and better data were needed for more accurate determination of $N(\nu)$.

Since the 1973 paper by Hale and Querry, there have been additional compilations of $n(\nu)$, $k(\nu)$, or $\alpha(\nu)$, the latter being the Lambert absorption coefficient. It is defined in terms of I , the intensity, as the fractional decrease in intensity over distance:

$$\alpha(\nu) \equiv -\frac{1}{I} \frac{dI}{dx} = 4\pi k(\nu)\nu \quad (1.2)$$

Of the more recent literature, the following are notable:

A report by Heller, Hamm, Birkhoff, and Painter² appeared in

1974. The authors obtained $n(\nu)$, $k(\nu)$, $\epsilon_r(\nu)$, and $\epsilon_i(\nu)$, the latter two being the real and imaginary parts of the dielectric function, $\epsilon(\nu)$, for the range 6.1×10^4 to $2.1 \times 10^5 \text{ cm}^{-1}$ (48 to 163 nm wavelength). Reflectance was measured and the above constants were calculated by Kramers-Kronig analysis.

A 1975 paper by Downing and Williams³ reported values for $n(\nu)$, $k(\nu)$, and $\alpha(\nu)$ for the region 10 to 5000 cm^{-1} (2 μm to 1 mm wavelength). The values of $k(\nu)$ were obtained by measurement and by calculation from reflectance data. The results for $n(\nu)$ were determined by either Kramers-Kronig analysis or by calculation from reflectance and phase shift data, depending on whether accurate values of $k(\nu)$ were available for the particular region.

A communication by Kopelevich⁴ reported in 1976 discussed the range 1.7×10^4 to $4 \times 10^4 \text{ cm}^{-1}$ (250 to 600 nm wavelength). The author criticized the values of $k(\nu)$ used by Hale and Querry in their 1973 paper. The claim was that water samples in the measurements relied upon were not pure enough. Kopelevich asserted that lower values of $k(\nu)$ were inherently better because they indicated a more pure sample.

A 1977 report by Afsar and Hasted⁵ gave $\alpha(\nu)$, $k(\nu)$, and $n(\nu)$ for the range 6 to 450 cm^{-1} (22 μm to 1.7 mm wavelength). These were calculated from reflectance data obtained by use of a Fourier-transform spectrophotometer, with an improved liquid cell and a more accurately measured reference interferogram, as compared with earlier measurements of the same type.

In a paper published in 1978, Querry, Cary, and Waring⁶ reported

values for $\alpha(\nu)$ for the region 1.5×10^4 to $2.4 \times 10^4 \text{ cm}^{-1}$ (418 to 640 nm wavelength). These were experimental data obtained by a split-pulse laser method of measuring attenuation.

Tam and Patel⁷ gave values for $\alpha(\nu)$ for the interval 1.44×10^4 to $2.24 \times 10^4 \text{ cm}^{-1}$ (446 to 694 nm wavelength) in a paper published in 1979. The technique used was pulsed dye-laser optoacoustic spectroscopy. The method eliminated the detection of spurious attenuation due to scattering.

In addition to the above data, there are relations which can be used to obtain reasonable data for optical constants. For example, in the region below approximately 10^5 cm^{-1} , the semi-empirical Cole-Cole equation⁸ gives sound values for the real and imaginary parts of the dielectric function. In the neighborhood of the oxygen K-edge, at $4.35 \times 10^6 \text{ cm}^{-1}$, the shape of the absorption curve above and below the discontinuity can be obtained from an empirical equation which gives the mass absorption coefficient as a power of wavelength.⁹ One can find the height of the discontinuity from an empirically obtained relationship between the jump in the mass absorption coefficient across the K-edge and the atomic number.¹⁰ Given these determinations, one needs only some data in the vicinity of the discontinuity to fix the position of the curve. These data are available.

Description of the Research

With the addition of the above data, it was hoped that a more reliable spectrum of $N(\nu)$ could be obtained. The program was, first, to obtain reasonable values for $\alpha(\nu)$, or equivalently $k(\nu)$, from the

literature and the relations mentioned above. These values would span the range from 10^{-6} cm^{-1} , the end of the spectrum obtained from the Cole-Cole equation, to 10^{15} cm^{-1} , the region for which the power law relation gives reasonable predictions. The compilation of this $\alpha(\nu)$ spectrum is described in Chapter II.

This spectrum of $\alpha(\nu)$ was tested for accuracy by use of a sum rule describing the contributions of electronic absorption. The spectrum was adjusted in the region from the low wave-number side of the absorption peak at $1.14 \times 10^5 \text{ cm}^{-1}$ to the bottom of the K-edge discontinuity. The adjustment was made, well within the experimental error stated for the data used, until the electronic sum rule indicated ten electrons.

The $\alpha(\nu)$ spectrum was then appropriately Fourier transformed to give $n(\nu)$ for the range 10^{-3} to 10^6 cm^{-1} . The Fourier transform technique is equivalent to conventional Kramers-Kronig analysis, as is shown in Chapter III. The advantage is in the ability to use the digital FAST FOURIER TRANSFORM yielding equivalent results with much less computing time.

The theoretical development of the Kramers-Kronig relations, their extension to a Fourier transform relationship, and the electronic sum rule derivation are presented in Chapter III. The application to direct computation is described in Chapter IV. Spectral values of $N(\nu)$ are presented in tabular and graphical form in Chapter V. The results are discussed in Chapter VI.

CHAPTER II

ACQUISITION OF DATA

The Middle Range

So as not to discard the baby with the bath water, the absorption spectrum used by Hale and Query was retained except where better data were available. Replacement of data began in the visible region.

A significant area of contention has been the purity of water samples for experimental determination of extinction coefficients in the visible region. The question involves how much intensity is lost due to scattering, a phenomenon which is aggravated by the presence of particles, bubbles, or other impurities. That was the substance of the objection by Kopelevich to the data used by Hale and Query. The difficulty is neatly avoided by the technique of optoacoustic spectroscopy, as used by Tam and Patel. The method relies on the generation of transient acoustic waves by any material which absorbs a light pulse. Data were obtained by detection and comparison of sound waves over the particular range of frequencies of input light. The light source was a pulsed dye laser. Since there is no reliance on the intensity of light surviving passage through the sample, scattering is not involved. Tam and Patel measured only absorption.

The data of Tam and Patel were incorporated into the spectrum. The next task was to find values for $\alpha(\nu)$ which joined continuously

with that data. At the lower end, $1.44 \times 10^4 \text{ cm}^{-1}$, the data of Tam and Patel joined almost precisely with that of Hale and Querry. Nothing additional was required. At the high end, however, $2.24 \times 10^4 \text{ cm}^{-1}$, there was no real agreement among investigators up to the area of $5 \times 10^4 \text{ cm}^{-1}$. After considering data of many researchers, it was found that the most reasonable and the smoothest curve connecting the two areas was obtained by averaging the data of Lenoble and Saint-Guilly¹¹ with that quoted by Kopelevich.

The range from 5×10^4 to $6.49 \times 10^4 \text{ cm}^{-1}$ was left intact with the data of Hale and Querry. There seems to be much agreement as to the values for that region, as is graphically illustrated by Painter, Birkhoff, and Arakawa in Figure 4 of their 1969 paper.¹²

In the range 6.49×10^4 to $2.06 \times 10^5 \text{ cm}^{-1}$, the data of Heller, Hamm, Birkhoff, and Painter were used because, at the lower end, the curve fit quite accurately in position and shape with the data below that. Also, as this was the region which would have the greatest effect in adjustments to conform to the sum rule, an inability to reach ten electrons while staying within the experimental error quoted by Heller et al. would have indicated that the data there were inappropriate. Because conformity with the sum rule constraint was obtained while remaining well within the error bars, it was evident that the data were appropriate.

The range above $2.06 \times 10^5 \text{ cm}^{-1}$ is discussed under "High Frequency Data" below. For the other extreme, the part of the spectrum from 10^{-6} to 5 cm^{-1} is discussed below in the section entitled "Low Frequency Data."

From 5 to 500 cm^{-1} , data from Afsar and Hasted were used. Their

work represents probably the first comprehensive investigation of that range of the spectrum. Further, their technique was advanced as compared with earlier measurements.

To join with the data of Afsar and Hasted, the values of $\alpha(\nu)$ obtained by Robertson and Williams¹³ fit quite well. In addition, their work was a direct experimental determination of absorption via transmittance measurements. The values of Robertson and Williams were used where they differed from those used by Hale and Querry, namely in the ranges 5×10^2 to 10^3 cm^{-1} and 3.3×10^3 to $4 \times 10^3 \text{ cm}^{-1}$.

Low Frequency Data

The behavior of a polar liquid in an alternating field is treated by Debye in his book Polar Molecules.¹⁴ By calculating the distribution function for orientation of the molecules, Debye obtained the following expressions¹⁵:

$$\epsilon' = \epsilon_0 + \frac{\epsilon_1 - \epsilon_0}{1 + x^2} \quad (2.1)$$

$$\epsilon'' = \frac{(\epsilon_1 - \epsilon_0)x}{1 + x^2} \quad (2.2)$$

$$x = \left(\frac{\epsilon_1 + 2}{\epsilon_0 + 2} \right) \omega \tau \quad (2.3)$$

where $\epsilon' = \epsilon_r$, $\epsilon'' = -\epsilon_i$, τ = the "relaxation time" for the orientation of the molecules, ω = the angular frequency of the applied field, ϵ_0 = the high frequency value for ϵ , and ϵ_1 = the static dielectric constant.

The characteristic relaxation time for water at room temperature was calculated by Debye to be approximately 2.5×10^{-11} seconds.¹⁶ This corresponds to a wavelength of the order of one cm. In this region, and for longer wavelengths, the Debye equations should yield good predictions, approaching the low frequency limit smoothly.

A significant improvement over the Debye relation was made by Cole and Cole in their paper published in 1941. They first wrote the Debye equations in the form⁸

$$\epsilon^* = \epsilon_{\infty} + \frac{\epsilon_0 - \epsilon_{\infty}}{1 + i\omega\tau_0} \quad (2.4)$$

where ϵ^* is the complex dielectric function, ϵ_{∞} is the high frequency limit, and ϵ_0 is the static limit. Then the authors showed that better results are obtainable by writing¹⁷

$$\epsilon^* = \epsilon_{\infty} + \frac{\epsilon_0 - \epsilon_{\infty}}{1 + (i\omega\tau_0)^{1-\alpha}} \quad (2.5)$$

where α and τ_0 are parameters to be determined.

This equation can be used directly to calculate values for the dielectric function, and hence the complex refractive index, in the vicinity of the frequency corresponding to the relaxation time. Values for the parameters ϵ_0 , ϵ_{∞} , τ_0 , and α are available, for example, from Water, a Comprehensive Treatise,¹⁸ there obtained from experimental results. The values of the parameters in that reference were used in the Cole-Cole equation to calculate the extinction coefficient for

the range 10^{-6} to 5 cm^{-1} .

High Frequency Data

In the soft x-ray region, data are scarce. However, the evidence indicates a relationship of the form⁹

$$\frac{\mu}{\rho} = K\lambda^{\frac{n}{Z}m} + \frac{\sigma}{\rho} \quad (2.6)$$

for the mass absorption coefficient, μ/ρ . σ/ρ is the attenuation due to scattering. This yields, since $\mu = \alpha$,

$$\alpha = \rho K\lambda^{\frac{n}{Z}m} + \sigma \quad (2.7)$$

or if scattering is subtracted out, $(\alpha - \sigma) = \alpha$, and

$$\alpha = A\nu^{-n} \quad (2.8)$$

Thus, the Lambert absorption coefficient is given by some negative power of wave number.

Engström suggests a value for n for the soft x-ray region of somewhat less than three. In the data used for this thesis, n was found to be 2.2297 in the area between 2.1×10^5 and $4.3 \times 10^6 \text{ cm}^{-1}$ (the latter location being the bottom of the K-edge), a range corresponding to ultra-soft x-rays. Above the K-edge, n was found to be 2.6257.

This power law relationship was applied in the following manner: Data from the National Bureau of Standards¹⁹ were available for the

mass absorption coefficient for the range 8×10^7 to $8 \times 10^{14} \text{ cm}^{-1}$. These data were extended by extrapolation to the K-edge location at $4.35 \times 10^6 \text{ cm}^{-1}$. This only assumes that the power n remains constant from the K-edge discontinuity to the slightly higher wave numbers stated.

The magnitude of the discontinuity was determined from Figures 3 and 4 of Engström's book.²⁰ Those figures indicate, respectively, the ratio of mass absorption coefficients and the difference between the coefficients on either side of the discontinuity. This fixed the bottom of the K-edge and left only the region between 2.1×10^5 and $4.3 \times 10^6 \text{ cm}^{-1}$ to be filled in. (Data were available up to approximately $2.1 \times 10^5 \text{ cm}^{-1}$ from the Heller, Hamm, Birkhoff, and Painter work.)

The data were joined between the points $2.1 \times 10^5 \text{ cm}^{-1}$ and the bottom of the K-edge by assuming a linear relationship on a plot of the log of the Lambert coefficient versus the log of the wave number. The slope of this line would then correspond to n in the power law relationship.

The data from the paper of Heller et al. could be adjusted within the experimental limits, and a new line would be calculated each time. This gave an efficient means of adjustment while maintaining self-consistency among all the data.

Data for frequencies above 10^{15} cm^{-1} were effectively ignored, that being the range in which absorption predominately involves non-atomic/molecular phenomena. Inclusion of these data would have made use of the electronic sum rule impossible as a measure of the accuracy of the absorption spectrum. Further, since optical properties were

calculated only up to 10^6 cm^{-1} , inclusion or exclusion of these data would have had negligible if any effect on the results. The means for evaluation of the sum rule in this region above 10^{15} cm^{-1} is described below.

Application of the Sum Rule

Once the new absorption spectrum was completed, the electronic sum rule was applied to test its accuracy. The sum rule, as derived in Chapter III, in SI units, is

$$Z = \left(\frac{4\pi c^2 \epsilon_0}{n_0 e^2} \right) \int_0^\infty \alpha(\nu) d\nu \quad (2.9)$$

where \underline{m} is the mass of an electron, \underline{c} is the speed of light in vacuum, $\underline{\epsilon}_0$ the permittivity constant, \underline{n}_0 the number of water molecules per cubic meter, and \underline{e} the electronic charge.

If numerical values of $\alpha(\nu)$ are available up to some appropriate ν_{max} , the integration from ν_{max} to infinity can be done analytically using the inverse power law relationship described above. The sum rule is written

$$Z = \left(\frac{4\pi c^2 \epsilon_0}{n_0 e^2} \right) \left[\int_0^{\nu_{\text{max}}} \alpha(\nu) d\nu + \int_{\nu_{\text{max}}}^\infty \alpha(\nu) d\nu \right] \quad (2.10)$$

Writing $\alpha(\nu) = A\nu^{-n}$ for $\nu \geq \nu_{\text{max}}$, so that $\alpha(\infty) = 0$, and integrating the second term, we obtain

$$Z = \left(\frac{4\pi c^2 \epsilon_0}{n_0 e^2} \right) \left[\int_0^{v_{\max}} \alpha(v) dv + \frac{A v_{\max}^{-n+1}}{(n-1)} \right] \quad (2.11)$$

Since $A v_{\max}^{-n} = \alpha(v_{\max})$, the result is

$$Z = \left(\frac{4\pi c^2 \epsilon_0}{n_0 e^2} \right) \int_0^{v_{\max}} \alpha(v) dv + \left[\frac{4\pi c^2 \epsilon_0 v_{\max}}{n_0 e^2 (n-1)} \right] \alpha(v_{\max}) \quad (2.12)$$

In the calculation of the sum rule integral, v_{\max} was $2 \times 10^7 \text{ cm}^{-1}$. The value of n was determined from the National Bureau of Standards data to be 2.6257. The numerical integration was done using Simpson's rule. As were all calculations for this research, the computation was done in a Fortran program with an AMDAHL 470 computer.

The first attempt yielded $Z = 8.99086$. Raising the experimental data of Heller et al. to their maximum within the stated error, except at the end points of the interval used, gave $Z = 10.26559$. A feature included in the data at $2.016 \times 10^5 \text{ cm}^{-1}$ had been easily smoothed over within the experimental error, and was therefore ignored for the above two calculations. The curve had been made to follow the power law relation from $1.667 \times 10^5 \text{ cm}^{-1}$ to the K-edge. For subsequent calculations, however, the power law relationship was applied only from $2.083 \times 10^5 \text{ cm}^{-1}$ to the K-edge, and the previously ignored feature was included. This had the effect of shifting the curve above its previous position for the entire region of the data calculated from the power law relation. It allowed the data below $2.083 \times 10^5 \text{ cm}^{-1}$ to be kept much closer to the

median experimental values. This is reasonable because the error stated by Heller et al. for the vicinity of $2.083 \times 10^5 \text{ cm}^{-1}$ is 20 percent, while it is 10 percent for the lower wave number regions.

After 16 adjustments, the spectrum yielded $Z = 10.00000$. Figures 1 and 2 illustrate the first and last curve in the region of adjustment. Figure 3 is a graph of the final absorption spectrum in full. For the above illustrations, $\log_{10} \alpha(\nu)$ is plotted against $\log_{10} \nu$. Further, a graph of the value of the sum rule integral, Z plotted against $\log_{10} \nu$, is included as Figure 4 to show where the significant contributions to the sum rule occur. It is clear that the region of the data of Heller et al. corresponds to the greatest slope of the curve, thereby indicating the most significant contribution to the sum.

With the completion of this compilation, the absorption spectrum was ready to be Fourier transformed to give $n(\nu)$.

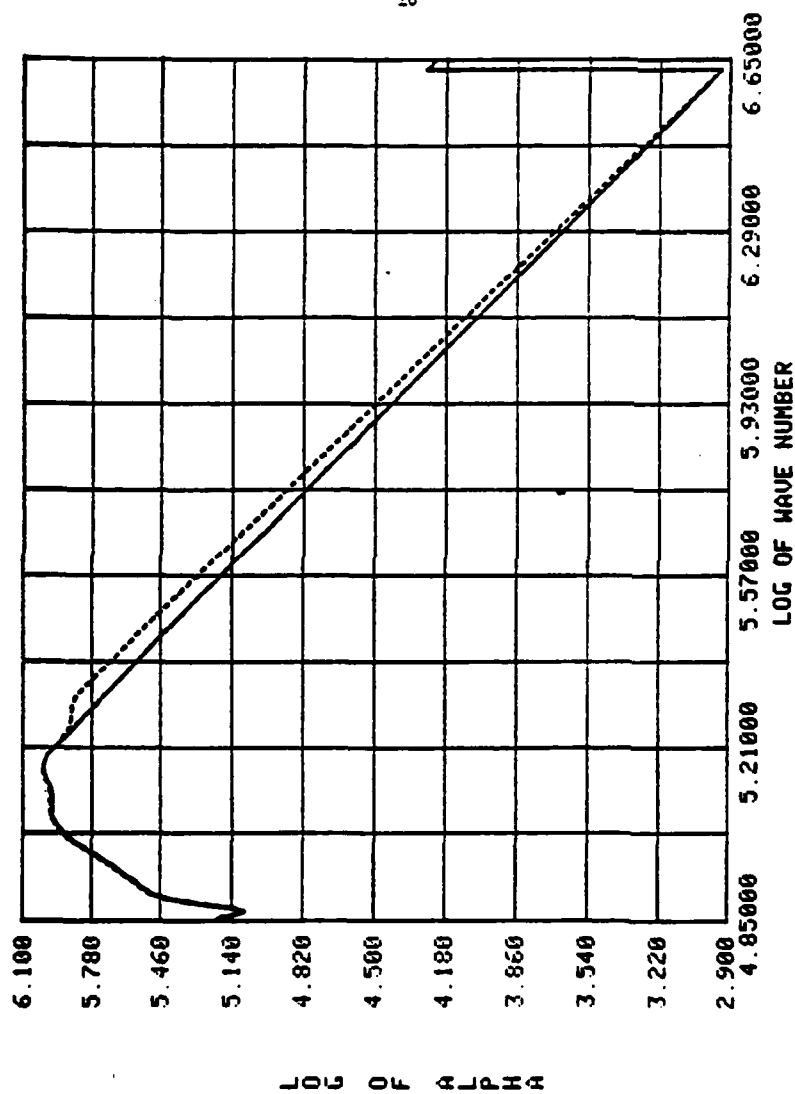


Fig. 1. The absorption spectrum in the region of adjustment. The log of the Lambert absorption coefficient, from 7.079×10^4 to $4.467 \times 10^6 \text{ cm}^{-1}$, is plotted against the log of the wave number. The dashed line is the final curve obtained, which caused the sum rule integral to yield 10.00000. The sharp feature on the right is the K-edge.

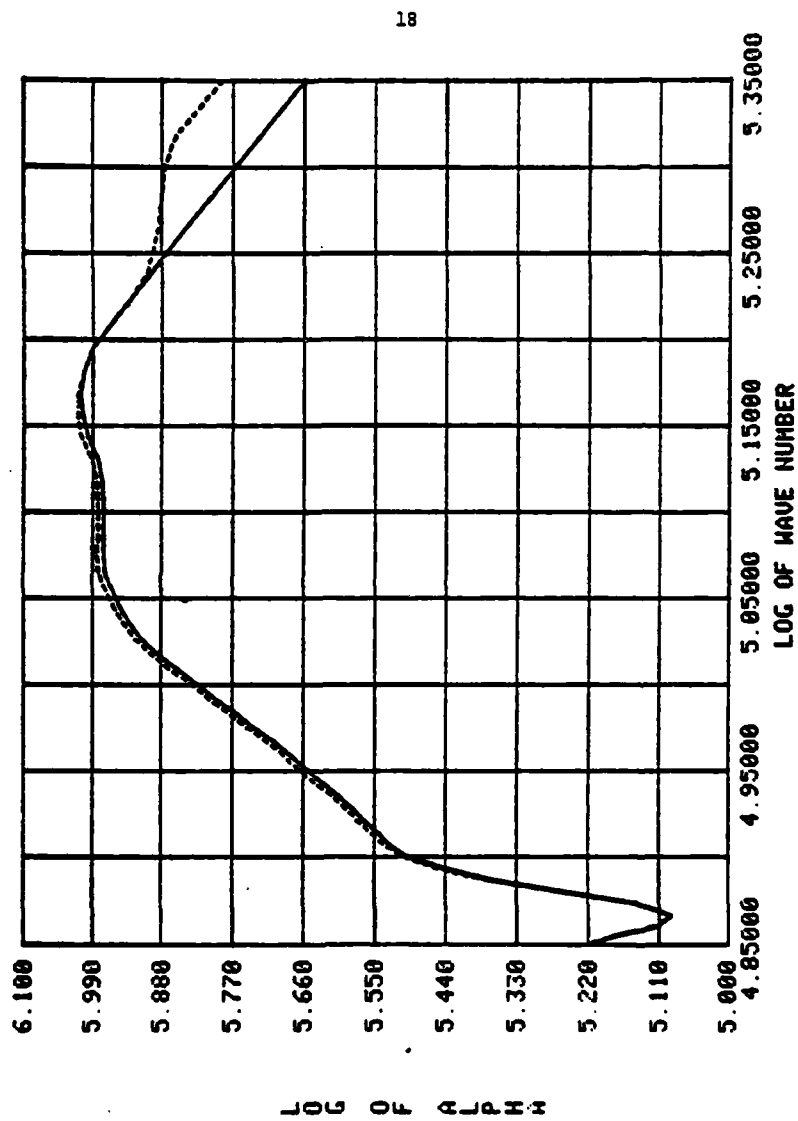


Fig. 2. Detail of Figure 1 in the region of the broad absorption peak.

The dashed line lies well within the experimental error quoted for the data represented by the solid line.

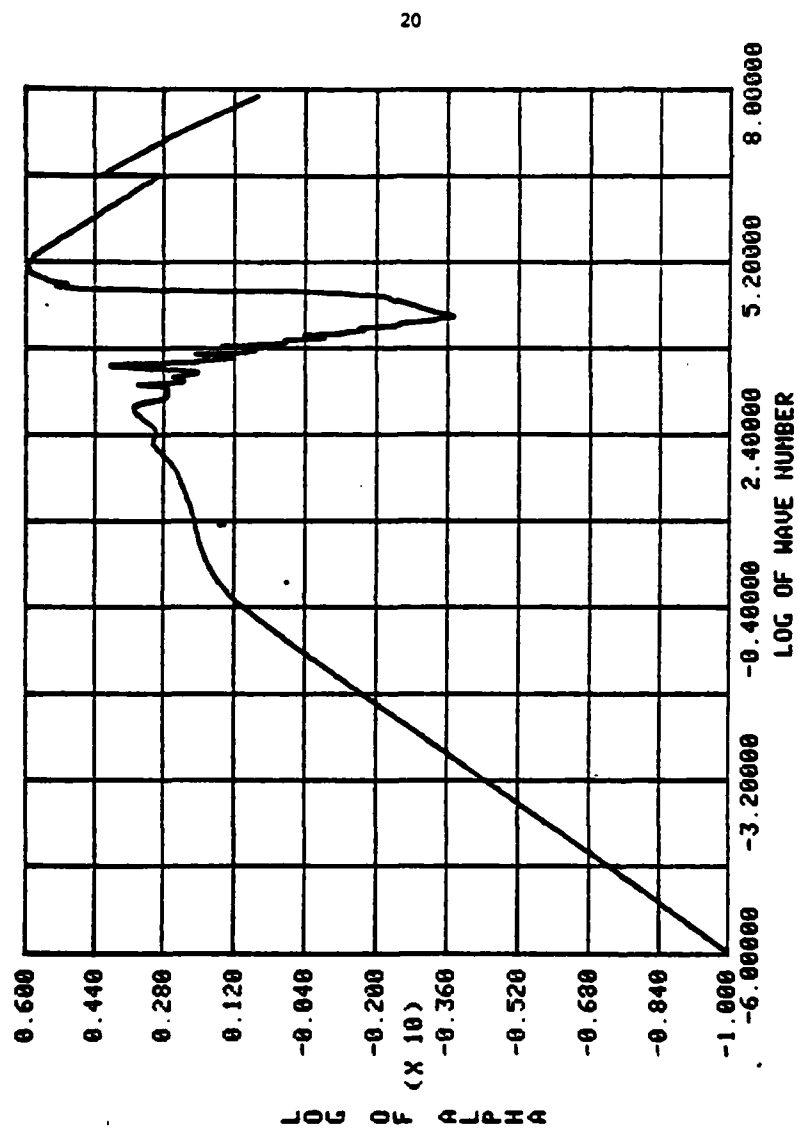


Fig. 3. The absorption spectrum in full as used in this work.

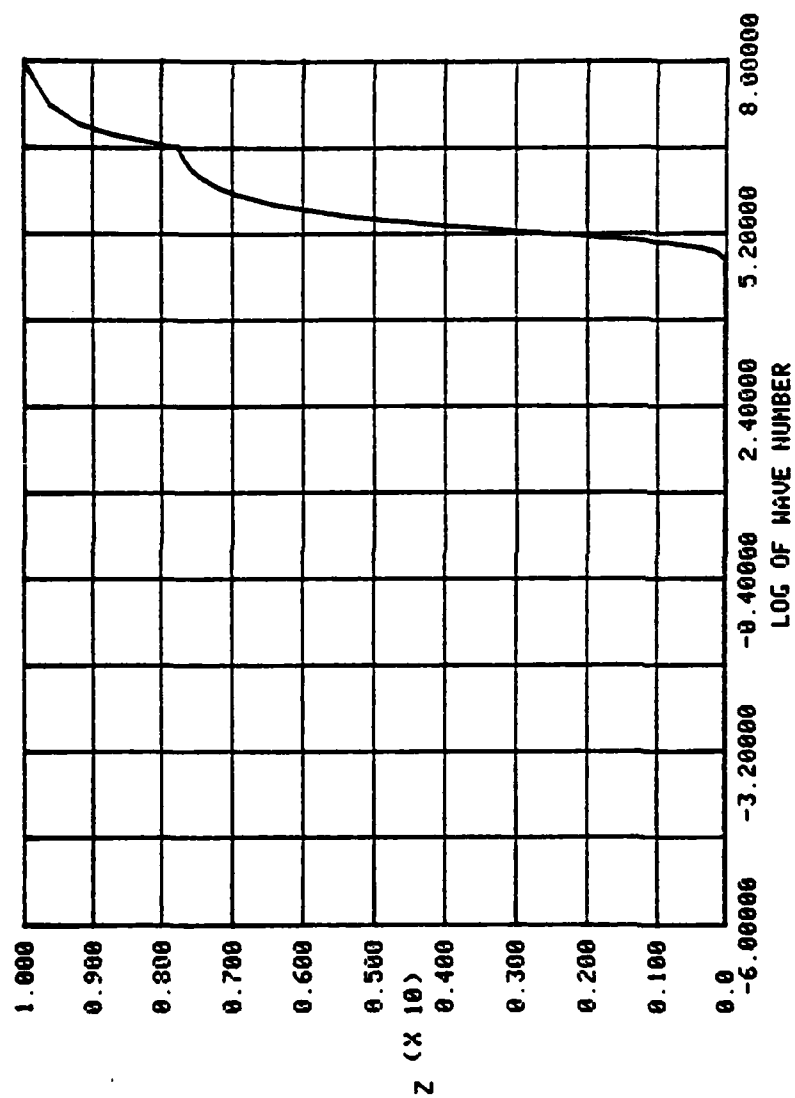


Fig. 4. The value of the sum rule integral plotted against the log of the value of the upper limit.

CHAPTER III

THEORETICAL METHODS

The Complex Refractive Index

The laws governing the propagation of electric and magnetic fields are Maxwell's equations. We can find an expression for the fields in a medium which will yield the relationship between absorption and phase velocity, the time response and dielectric functions, dispersion relationships, and sum rules.

Maxwell's equations, in cgs units, are²¹

$$\nabla \cdot \vec{D} = 4\pi\rho \quad (3.1)$$

$$\nabla \cdot \vec{B} = 0 \quad (3.2)$$

$$\nabla \times \vec{E} + \frac{1}{c} \frac{\partial \vec{B}}{\partial t} = \vec{0} \quad (3.3)$$

$$\nabla \times \vec{H} - \frac{1}{c} \frac{\partial \vec{D}}{\partial t} = \frac{4\pi}{c} \vec{J} \quad (3.4)$$

The quantities in the equations are defined as follows:

\vec{E} \equiv the electric field

\vec{D} \equiv the electric displacement

\vec{B} \equiv the magnetic induction

\vec{H} \equiv the magnetic field

\vec{J} \equiv the current density

ρ \equiv the charge density

The constitutive relations for \vec{D} , \vec{H} , and \vec{J} are

$$\vec{D} = \epsilon \vec{E} \quad (3.5)$$

$$\vec{B} = \mu \vec{H} \quad (3.6)$$

$$\vec{J} = \sigma \vec{E} \quad (3.7)$$

where ϵ is the dielectric function, μ is the magnetic permeability, and σ is the conductivity.

For an infinite medium which is charge free ($\rho=0$), homogeneous, isotropic, and linear (ϵ , μ , and σ do not depend on position or time), and conducting ($\sigma \neq 0$), the equations reduce to

$$\nabla \cdot \vec{E} = 0 \quad (3.8)$$

$$\nabla \cdot \vec{H} = 0 \quad (3.9)$$

$$\nabla \times \vec{E} + \frac{\mu}{c} \frac{\partial \vec{H}}{\partial t} = \vec{0} \quad (3.10)$$

$$\nabla \times \vec{H} - \frac{\epsilon}{c} \frac{\partial \vec{E}}{\partial t} = \frac{4\pi\sigma}{c} \vec{E} \quad (3.11)$$

Taking the curl of Equation (3.10),

$$\nabla \times (\nabla \times \vec{E} + \frac{\mu}{c} \frac{\partial \vec{H}}{\partial t}) = \nabla \times \vec{0} = \vec{0}$$

$$\nabla \times \nabla \times \vec{E} + \frac{\mu}{c} \nabla \times \frac{\partial \vec{H}}{\partial t} = \vec{0} \quad (3.12)$$

Interchanging the order of differentiation,

$$\nabla \times \nabla \times \vec{E} + \frac{\mu}{c} \frac{\partial}{\partial t} (\nabla \times \vec{H}) = \vec{0} \quad (3.13)$$

Using the identity $\nabla \times \nabla \times \vec{E} = \nabla(\nabla \cdot \vec{E}) - \nabla^2 \vec{E}$, and noting from Equation (3.8) that the divergence of \vec{E} vanishes, we may replace the first term of Equation (3.13) by $-\nabla^2 \vec{E}$:

$$-\nabla^2 \vec{E} + \frac{\mu}{c} \frac{\partial}{\partial t} (\nabla \times \vec{H}) = 0 \quad (3.14)$$

We obtain the curl of \vec{H} from Equation (3.11):

$$\begin{aligned} -\nabla^2 \vec{E} + \frac{\mu}{c} \frac{\partial}{\partial t} \left(\frac{\epsilon}{c} \frac{\partial \vec{E}}{\partial t} + \frac{4\pi\sigma}{c} \vec{E} \right) &= 0 \\ \nabla^2 \vec{E} - \frac{\mu\epsilon}{c^2} \frac{\partial^2 \vec{E}}{\partial t^2} - \frac{4\pi\sigma\mu}{c^2} \frac{\partial \vec{E}}{\partial t} &= 0 \end{aligned} \quad (3.15)$$

Similarly, taking the curl of Equation (3.11),

$$\begin{aligned} \nabla \times (\nabla \times \vec{H} - \frac{\epsilon}{c} \frac{\partial \vec{E}}{\partial t}) &= \nabla \times \left(\frac{4\pi\sigma}{c} \vec{E} \right) \\ \nabla \times \nabla \times \vec{H} - \frac{\epsilon}{c} \frac{\partial}{\partial t} (\nabla \times \vec{E}) &= \frac{4\pi\sigma}{c} (\nabla \times \vec{E}) \end{aligned} \quad (3.16)$$

Obtaining the curl of \vec{E} from Equation (3.10), and using the same identity for $\nabla \times \nabla \times \vec{H}$, with $\nabla \cdot \vec{H} = 0$ from Equation (3.9),

$$\begin{aligned} -\nabla^2 \vec{H} - \frac{\epsilon}{c} \frac{\partial}{\partial t} \left(-\frac{\mu}{c} \frac{\partial \vec{H}}{\partial t} \right) - \frac{4\pi\sigma}{c} \left(-\frac{\mu}{c} \frac{\partial \vec{H}}{\partial t} \right) &= 0 \\ \nabla^2 \vec{H} - \frac{\mu\epsilon}{c^2} \frac{\partial^2 \vec{H}}{\partial t^2} - \frac{4\pi\sigma\mu}{c^2} \frac{\partial \vec{H}}{\partial t} &= 0 \end{aligned} \quad (3.17)$$

Thus, \vec{E} and \vec{H} both satisfy the same wave equation:

$$\left\{ \nabla^2 - \frac{\mu\epsilon}{c^2} \frac{\partial^2}{\partial t^2} - \frac{4\pi\sigma\mu}{c^2} \frac{\partial}{\partial t} \right\} \begin{pmatrix} \vec{E} \\ \vec{H} \end{pmatrix} = 0 \quad (3.18)$$

We assume a solution of the form

$$\vec{E} = \vec{E}_0 e^{i(\vec{k} \cdot \vec{x} - \omega t)} \quad (3.19)$$

where \vec{E}_0 is a constant vector. With $\kappa \equiv |\vec{k}|$, we note the following:

$$\nabla^2 \vec{E} = \vec{E}_0 (i\vec{k}) \cdot (i\vec{k}) e^{i(\vec{k} \cdot \vec{x} - \omega t)} = -\kappa^2 \vec{E} \quad (3.20)$$

$$\frac{\partial \vec{E}}{\partial t} = -i\omega \vec{E} \quad (3.21)$$

$$\frac{\partial^2 \vec{E}}{\partial t^2} = (-i\omega)(-i\omega) \vec{E} = -\omega^2 \vec{E} \quad (3.22)$$

Then, substituting Equations (3.20), (3.21), and (3.22) into Equation (3.18),

$$\left\{ \nabla^2 - \frac{\mu\epsilon}{c^2} \frac{\partial^2}{\partial t^2} - \frac{4\pi\sigma\mu}{c^2} \frac{\partial}{\partial t} \right\} \vec{E} = \left[-\kappa^2 + \frac{\mu\epsilon}{c^2} \omega^2 + i \left(\frac{4\pi\sigma\mu}{c^2} \right) \omega \right] \vec{E} \quad (3.23)$$

The coefficient of \vec{E} must vanish. This requires that

$$\kappa^2 = \frac{\mu\epsilon\omega^2}{c^2} + i \left(\frac{4\pi\sigma\mu\omega}{c^2} \right) \quad (3.24)$$

Assuming κ is complex, we write $\kappa \equiv \alpha + i\beta$. Then,

$$\kappa^2 = (\alpha + i\beta)^2 = \alpha^2 - \beta^2 + 2i\alpha\beta \quad (3.25)$$

$$\text{Re}(\kappa^2) = \alpha^2 - \beta^2 \quad (3.26)$$

$$\text{Im}(\kappa^2) = 2\alpha\beta \quad (3.27)$$

To find the real and imaginary parts of κ^2 , we assume that ϵ , μ , and σ are complex:

$$\epsilon \equiv \epsilon_r + i\epsilon_i \quad (3.28)$$

$$\mu \equiv \mu_r + i\mu_i \quad (3.29)$$

$$\sigma \equiv \sigma_r + i\sigma_i \quad (3.30)$$

Then, substituting into Equation (3.24),

$$\begin{aligned} \kappa^2 = & (\epsilon_r + i\epsilon_i)(\mu_r + i\mu_i)\frac{\omega^2}{c^2} + \\ & i4\pi(\sigma_r + i\sigma_i)(\mu_r + i\mu_i)\frac{\omega}{c^2} \end{aligned} \quad (3.31)$$

$$\begin{aligned} \kappa^2 = & \left[(\epsilon_r\mu_r - \epsilon_i\mu_i)\frac{\omega^2}{c^2} - 4\pi(\sigma_i\mu_r + \sigma_r\mu_i)\frac{\omega}{c^2} \right] + \\ & i \left[(\epsilon_i\mu_r + \epsilon_r\mu_i)\frac{\omega^2}{c^2} + 4\pi(\sigma_r\mu_r - \sigma_i\mu_i)\frac{\omega}{c^2} \right] \end{aligned} \quad (3.32)$$

We then define

$$\gamma \equiv (\epsilon_r\mu_r - \epsilon_i\mu_i)\frac{\omega^2}{c^2} - 4\pi(\sigma_i\mu_r + \sigma_r\mu_i)\frac{\omega}{c^2} \quad (3.33)$$

$$\delta \equiv (\epsilon_i\mu_r + \epsilon_r\mu_i)\frac{\omega^2}{c^2} + 4\pi(\sigma_r\mu_r - \sigma_i\mu_i)\frac{\omega}{c^2} \quad (3.34)$$

Thus,

$$\kappa^2 = \gamma + i\delta \quad (3.35)$$

From Equations (3.26) and (3.27), we obtain

$$\gamma = \alpha^2 - \beta^2 \quad (3.36)$$

$$\delta = 2\alpha\beta \quad (3.37)$$

Using $\beta = \delta/2\alpha$ from Equation (3.37), the following quadratic results:

$$4\alpha^4 - \delta^2 = 4\gamma\alpha^2 \quad (3.38)$$

$$4(\alpha^2)^2 - 4\gamma(\alpha^2) - \delta^2 = 0 \quad (3.39)$$

The solutions are

$$\alpha^2 = \frac{1}{2}[\gamma \pm (\gamma^2 + \delta^2)^{\frac{1}{2}}] \quad (3.40)$$

Since α is real, α^2 must be greater than zero. We must choose the plus sign. Therefore,

$$\alpha = \left[\frac{\gamma + (\gamma^2 + \delta^2)^{\frac{1}{2}}}{2} \right]^{\frac{1}{2}} \quad (3.41)$$

Similarly, $\alpha = \delta/2\beta$ yields the quadratic

$$4(\beta^2)^2 + 4\gamma(\beta^2) - \delta^2 = 0 \quad (3.42)$$

with solutions

$$\beta^2 = \frac{1}{2}[-\gamma \pm (\gamma^2 + \delta^2)^{\frac{1}{2}}] \quad (3.43)$$

Again we must choose the plus sign:

$$\beta = \left[\frac{-\gamma + (\gamma^2 + \delta^2)^{\frac{1}{2}}}{2} \right]^{\frac{1}{2}} \quad (3.44)$$

With the result $\vec{k} = \kappa\hat{k} = (\alpha + i\beta)\hat{k}$, the complex phase velocity \hat{v}_p can be defined:

$$\vec{k} \cdot \vec{x} - \omega t = \text{constant} \quad (3.45)$$

$$d(\vec{k} \cdot \vec{x} - \omega t) = 0 \quad (3.46)$$

$$\vec{k} \cdot d\vec{x} - \omega dt = 0 \quad (3.47)$$

$$(\alpha + i\beta) \vec{k} \cdot d\vec{x} = \omega dt \quad (3.48)$$

$$\hat{k} \cdot d\vec{x} = \left(\frac{\omega}{\alpha + i\beta} \right) dt \quad (3.49)$$

Measuring \hat{v}_p in the direction of \hat{k} , $\hat{k} \cdot d\vec{x} = |\hat{k}| |d\vec{x}| = dx$, and

$$dx = \left(\frac{\omega}{\alpha + i\beta} \right) dt \quad (3.50)$$

$$\frac{dx}{dt} \equiv \hat{v}_p = \frac{\omega}{\alpha + i\beta} \quad (3.51)$$

If we define the complex refractive index \underline{N} as

$$\underline{N} \equiv \frac{c}{\hat{v}_p} \equiv n + ik \quad (3.52)$$

we finally obtain

$$\underline{N} = \frac{c}{\omega} (\alpha + i\beta) \quad (3.53)$$

Thus, with \underline{n} the real part of the refractive index, and \underline{k} the imaginary part, the result is

$$n = \frac{c}{\omega} \alpha \quad (3.54)$$

$$k = \frac{c}{\omega} \beta \quad (3.55)$$

As an example of the relationship between ϵ and \underline{N} , consider a

non-conducting ($\sigma=0$), non-magnetic ($\mu=1$) material such as water. With these conditions,

$$\gamma = \epsilon_r \frac{\omega^2}{c^2} \quad \text{and} \quad \delta = \epsilon_i \frac{\omega^2}{c^2} \quad (3.56)$$

Then,

$$\alpha = \left[\frac{\gamma + (\gamma^2 + \delta^2)^{1/2}}{2} \right]^{1/2} = \frac{\omega}{c} \left[\frac{\epsilon_r + (\epsilon_r^2 + \epsilon_i^2)^{1/2}}{2} \right]^{1/2} \quad (3.57)$$

$$\beta = \left[\frac{-\gamma + (\gamma^2 + \delta^2)^{1/2}}{2} \right]^{1/2} = \frac{\omega}{c} \left[\frac{-\epsilon_r + (\epsilon_r^2 + \epsilon_i^2)^{1/2}}{2} \right]^{1/2} \quad (3.58)$$

Using Equation (3.53),

$$N = \frac{c}{\omega} \left\{ \frac{\omega}{c} \left[\frac{\epsilon_r + (\epsilon_r^2 + \epsilon_i^2)^{1/2}}{2} \right]^{1/2} + i \frac{\omega}{c} \left[\frac{-\epsilon_r + (\epsilon_r^2 + \epsilon_i^2)^{1/2}}{2} \right]^{1/2} \right\} \quad (3.59)$$

$$N = [\tfrac{1}{2}(|\epsilon| + \epsilon_r)]^{1/2} + i [\tfrac{1}{2}(|\epsilon| - \epsilon_r)]^{1/2} \quad (3.60)$$

Squaring both sides,

$$N^2 = \tfrac{1}{2}(|\epsilon| + \epsilon_r) - \tfrac{1}{2}(|\epsilon| - \epsilon_r) + 2i [\tfrac{1}{2}(|\epsilon| + \epsilon_r)]^{1/2} [\tfrac{1}{2}(|\epsilon| - \epsilon_r)]^{1/2} \quad (3.61)$$

$$N^2 = \epsilon_r + i\epsilon_i = \epsilon \quad (3.62)$$

The result is that, for water, the complex refractive index is the square of the dielectric function.

In general,

$$\kappa = \alpha + i\beta = \frac{\omega}{c} (n + ik) \quad (3.63)$$

Substituting into Equation (3.19),

$$\vec{E} = \vec{E}_0 e^{\frac{i\omega}{c}(n+ik)\hat{k}\cdot\vec{x}} e^{-i\omega t} \quad (3.64)$$

$$\vec{E} = \vec{E}_0 e^{\frac{i\omega}{c}n(\hat{k}\cdot\vec{x})} e^{-\frac{\omega}{c}k(\hat{k}\cdot\vec{x})} e^{-i\omega t} \quad (3.65)$$

Clearly, k governs attenuation of the wave amplitude, and n governs the real phase velocity. Thus, the terms attenuation (or extinction) coefficient and real refractive index for k and n respectively.

The Lambert Absorption Coefficient

The Lambert absorption coefficient, α , is defined as the fractional decrease in intensity over distance:

$$\alpha \equiv -\frac{1}{I} \frac{dI}{dx} \quad (3.66)$$

We obtain an expression for the intensity by integrating:

$$-\alpha dx = \frac{dI}{I} \quad (3.67)$$

$$\int_0^x (-\alpha) dx' = \int_{I_0}^I \frac{dI'}{I'} \quad (3.68)$$

$$-\alpha x = \ln\left(\frac{I}{I_0}\right) \quad (3.69)$$

$$I = I_0 e^{-\alpha x} \quad (3.70)$$

The intensity is proportional to the square of the magnitude of the electric field vector:

$$I = |\vec{E}|^2 = |\vec{E}_0|^2 e^{-2\frac{\omega}{c}k(\hat{k} \cdot \vec{x})} \quad (3.71)$$

$$\frac{dI}{dx} = |\vec{E}_0|^2 \left(-\frac{2\omega k}{c}\right) |\hat{k}| e^{-2\frac{\omega}{c}k(\hat{k} \cdot \vec{x})} \quad (3.72)$$

$$-\frac{1}{I} \frac{dI}{dx} = \frac{2\omega k}{c} = \alpha \quad (3.73)$$

Writing $\omega = 2\pi f$ and $f = c/\lambda$, $\omega = 2\pi c/\lambda$. Then,

$$\alpha = \frac{2k}{c} \frac{2\pi c}{\lambda} = \frac{4\pi k}{\lambda} \quad (3.74)$$

With the definition of wave number, ν , as $1/\lambda$,

$$\alpha = 4\pi k\nu \quad (3.75)$$

Absorption can also be written in terms of the formula

$$I = I_0 e^{-\frac{\mu}{\rho} m} \quad (3.76)$$

where μ is defined as the linear absorption coefficient (cm^{-1}), ρ is the density of the absorber (gm/cm^3), and m is the mass per area of the absorber (gm/cm^2). Then, μ/ρ is the mass absorption coefficient (cm^2/gm).

It is easily shown that $\mu = \alpha$. From the definition of the Lambert coefficient, Equation (3.70), we require that

$$\alpha x = \frac{\mu}{\rho} m \quad (3.77)$$

Now, $x/m = \text{volume}/\text{mass} = 1/\rho$. Thus,

$$\alpha \frac{x}{m} = \alpha \frac{1}{\rho} = \mu \frac{1}{\rho} \quad (3.78)$$

The result is $\mu = \alpha$. The mass absorption coefficient, then, can be written as α/ρ .

The Kramers-Kronig Relations as Obtained

From the Response Function

The real and imaginary parts of the dielectric function are related by a dispersion relation. This is a result of the frequency dependence of the quantities involved and our insistence on causality. The method was outlined by Peterson and Knight.²² The relations will later be shown to apply also to the complex refractive index.

To be most general, the fields should be written as a Fourier superposition of the fields due to all frequencies. We begin by noting the definition of the electric displacement in cgs units:

$$\vec{D} = \vec{E} + 4\pi\vec{P} \quad (3.79)$$

With the assumption of linearity, the polarization can be written

$$\vec{P} = \chi_e(\omega) \vec{E} \quad (3.80)$$

$\chi_e(\omega)$ is the frequency-dependent electric susceptibility. Then,

$$\vec{D} = \vec{E} + 4\pi\chi_e(\omega) \vec{E} = [1 + 4\pi\chi_e(\omega)]\vec{E} \quad (3.81)$$

In general, the frequency-dependent dielectric function is defined by

$$\vec{D} = \epsilon(\omega) \vec{E} \quad (3.82)$$

The result is

$$\epsilon(\omega) = 1 + 4\pi\chi_e(\omega) \quad (3.83)$$

The frequency-dependent fields are written as

$$\vec{D}(\vec{x}, \omega) = \epsilon(\omega) \vec{E}(\vec{x}, \omega) \quad (3.84)$$

where $\vec{D}(\vec{x}, \omega)$ and $\vec{E}(\vec{x}, \omega)$ are members of the Fourier-transform pairs

$$\vec{D}(\vec{x}, t) = \frac{1}{\sqrt{2\pi}} \int_{-\infty}^{\infty} \vec{D}(\vec{x}, \omega) e^{-i\omega t} d\omega \quad (3.85)$$

$$\vec{D}(\vec{x}, \omega) = \frac{1}{\sqrt{2\pi}} \int_{-\infty}^{\infty} \vec{D}(\vec{x}, t) e^{+i\omega t} dt \quad (3.86)$$

and

$$\vec{E}(\vec{x}, t) = \frac{1}{\sqrt{2\pi}} \int_{-\infty}^{\infty} \vec{E}(\vec{x}, \omega) e^{-i\omega t} d\omega \quad (3.87)$$

$$\vec{E}(\vec{x}, \omega) = \frac{1}{\sqrt{2\pi}} \int_{-\infty}^{\infty} \vec{E}(\vec{x}, t) e^{+i\omega t} dt \quad (3.88)$$

We proceed from Equation (3.85) as follows:

$$\vec{D}(\vec{x}, t) = \frac{1}{\sqrt{2\pi}} \int_{-\infty}^{\infty} \epsilon(\omega) \vec{E}(\vec{x}, \omega) e^{-i\omega t} d\omega \quad (3.89)$$

$$\vec{D}(\vec{x}, t) = \frac{1}{\sqrt{2\pi}} \int_{-\infty}^{\infty} [1 + 4\pi\chi_e(\omega)] \vec{E}(\vec{x}, \omega) e^{-i\omega t} d\omega \quad (3.90)$$

$$\begin{aligned}\vec{D}(\vec{x}, t) &= \frac{1}{\sqrt{2\pi}} \int_{-\infty}^{\infty} \vec{E}(\vec{x}, \omega) e^{-i\omega t} d\omega + \\ &\quad \frac{1}{\sqrt{2\pi}} \int_{-\infty}^{\infty} 4\pi\chi_e(\omega) \vec{E}(\vec{x}, \omega) e^{-i\omega t} d\omega\end{aligned}\quad (3.91)$$

$$\vec{D}(\vec{x}, t) = \vec{E}(\vec{x}, t) + \frac{1}{\sqrt{2\pi}} \int_{-\infty}^{\infty} 4\pi\chi_e(\omega) \vec{E}(\vec{x}, \omega) e^{-i\omega t} d\omega \quad (3.92)$$

We define the function $G(\tau)$ as

$$G(\tau) = \frac{1}{\sqrt{2\pi}} \int_{-\infty}^{\infty} 4\pi\chi_e(\omega) e^{-i\omega\tau} d\omega \quad (3.93)$$

$G(\tau)$ is thus the Fourier transform of $4\pi\chi_e(\omega)$. Thus,

$$4\pi\chi_e(\omega) = \frac{1}{\sqrt{2\pi}} \int_{-\infty}^{\infty} G(\tau) e^{+i\omega\tau} d\tau \quad (3.94)$$

Substituting this into Equation (3.92) and interchanging the order of integration,

$$\vec{D}(\vec{x}, t) = \vec{E}(\vec{x}, t) + \frac{1}{\sqrt{2\pi}} \int_{-\infty}^{\infty} G(\tau) \left[\frac{1}{\sqrt{2\pi}} \int_{-\infty}^{\infty} \vec{E}(\vec{x}, \omega) e^{-i\omega(t-\tau)} d\omega \right] d\tau \quad (3.95)$$

$$\vec{D}(\vec{x}, t) = \vec{E}(\vec{x}, t) + \frac{1}{\sqrt{2\pi}} \int_{-\infty}^{\infty} G(\tau) \vec{E}(\vec{x}, t-\tau) d\tau \quad (3.96)$$

The fact that $\epsilon(\omega)$ is a function of ω leads directly to this form for $\vec{D}(\vec{x}, t)$, which has a non-local (temporally) contribution from

$\vec{E}(\vec{x}, t)$. $G(\tau)$ is, evidently, the response function. Causality requires that there be no contribution to $\vec{D}(\vec{x}, t)$ from $\vec{E}(\vec{x}, t-\tau)$ for $\tau < 0$ (no contribution from the future). Then, $G(\tau)$ must be zero for $\tau < 0$.

$\vec{D}(\vec{x}, t)$ and $\vec{E}(\vec{x}, t)$ must be real. Therefore, subtracting from Equation (3.96) its complex conjugate, we obtain the following:

$$\vec{D}(\vec{x}, t) - \vec{D}^*(\vec{x}, t) = \vec{E}(\vec{x}, t) - \vec{E}^*(\vec{x}, t) + \frac{1}{\sqrt{2\pi}} \int_{-\infty}^{\infty} [G(\tau) \vec{E}(\vec{x}, t-\tau) - G^*(\tau) \vec{E}^*(\vec{x}, t-\tau)] d\tau \quad (3.97)$$

$$0 = 0 + \frac{1}{\sqrt{2\pi}} \int_{-\infty}^{\infty} [G(\tau) - G^*(\tau)] \vec{E}(\vec{x}, t-\tau) d\tau \quad (3.98)$$

This implies that $G(\tau) = G^*(\tau)$, or that $G(\tau)$ is real. We can, from this, deduce some properties of $4\pi\chi_e(\omega)$, and thus of $\epsilon(\omega)$. Using the definition of $G(\tau)$ and Equation (3.83),

$$G(\tau) = \frac{1}{\sqrt{2\pi}} \int_{-\infty}^{\infty} [\epsilon(\omega) - 1] e^{-i\omega\tau} d\omega \quad (3.99)$$

The complex conjugate is

$$G^*(\tau) = \frac{1}{\sqrt{2\pi}} \int_{-\infty}^{\infty} [\epsilon^*(\omega) - 1] e^{+i\omega\tau} d\omega \quad (3.100)$$

In Equation (3.99) we substitute $-\omega$ for ω and obtain

$$G(\tau) = \frac{1}{\sqrt{2\pi}} \int_{-\infty}^{\infty} [\epsilon(-\omega) - 1] e^{+i\omega\tau} d\omega \quad (3.101)$$

Subtracting Equation (3.100) from Equation (3.101),

$$G(\tau) - G^*(\tau) = \frac{1}{\sqrt{2\pi}} \int_{-\infty}^{\infty} [\epsilon(-\omega) - 1] e^{i\omega\tau} d\omega - \frac{1}{\sqrt{2\pi}} \int_{-\infty}^{\infty} [\epsilon^*(\omega) - 1] e^{i\omega\tau} d\omega \quad (3.102)$$

$$0 = \frac{1}{\sqrt{2\pi}} \int_{-\infty}^{\infty} [\epsilon(-\omega) - \epsilon^*(\omega)] e^{i\omega\tau} d\omega \quad (3.103)$$

This implies that $\epsilon(-\omega) = \epsilon^*(\omega)$. Then

$$\text{Re}[\epsilon(-\omega)] + i\text{Im}[\epsilon(-\omega)] = \text{Re}[\epsilon(\omega)] - i\text{Im}[\epsilon(\omega)] \quad (3.104)$$

$$\text{Re}[\epsilon(-\omega)] = \text{Re}[\epsilon(\omega)] \quad (3.105)$$

Thus, $\text{Re}[\epsilon(\omega)]$ is an even function in ω ; further, the function $\text{Re}[\epsilon(\omega) - 1] = \text{Re}[4\pi\chi_e(\omega)]$ is even in ω .

$$\text{Im}[\epsilon(-\omega)] = -\text{Im}[\epsilon(\omega)] \quad (3.106)$$

Thus, $\text{Im}[\epsilon(\omega)]$ is an odd function in ω ; further, the function $\text{Im}[\epsilon(\omega) - 1] = \text{Im}[4\pi\chi_e(\omega)]$ is odd in ω .

Using the above results, we can separate $G(\tau)$ into a part symmetric in τ , and a part anti-symmetric in τ . Beginning with the definition of $G(\tau)$, separating the susceptibility and the exponential into real and imaginary parts, we find

$$G(\tau) = \frac{1}{\sqrt{2\pi}} \int_{-\infty}^{\infty} \left\{ \operatorname{Re}[4\pi\chi_e(\omega)] \cos(\omega\tau) + \operatorname{Im}[4\pi\chi_e(\omega)] \sin(\omega\tau) \right\} d\omega + \\ \frac{i}{\sqrt{2\pi}} \int_{-\infty}^{\infty} \left\{ \operatorname{Im}[4\pi\chi_e(\omega)] \cos(\omega\tau) + \operatorname{Re}[4\pi\chi_e(\omega)] \sin(\omega\tau) \right\} d\omega \quad (3.107)$$

The integrand of the second integral is odd in ω and, therefore, vanishes.

Thus,

$$G(\tau) = \frac{1}{\sqrt{2\pi}} \int_{-\infty}^{\infty} \operatorname{Re}[4\pi\chi_e(\omega)] \cos(\omega\tau) d\omega + \\ \frac{1}{\sqrt{2\pi}} \int_{-\infty}^{\infty} \operatorname{Im}[4\pi\chi_e(\omega)] \sin(\omega\tau) d\omega \quad (3.108)$$

The first integral is even in τ . We define it as $G_s(\tau)$ (where the subscript implies the symmetric property). Note that it can be written

$$G_s(\tau) = \frac{1}{\sqrt{2\pi}} \int_{-\infty}^{\infty} \operatorname{Re}[4\pi\chi_e(\omega)] e^{-i\omega\tau} d\omega \quad (3.109)$$

since the term containing the sine function is odd, causing that part of the integral to vanish. It is evident that $G_s(\tau)$ is the Fourier transform of $\operatorname{Re}[4\pi\chi_e(\omega)]$. Then,

$$\operatorname{Re}[4\pi\chi_e(\omega)] = \frac{1}{\sqrt{2\pi}} \int_{-\infty}^{\infty} G_s(\tau) e^{+i\omega\tau} d\tau \quad (3.110)$$

The second integral is odd in τ . We define it as $G_a(\tau)$ (where the subscript implies the anti-symmetric property). Note that it can be written

$$G_a(\tau) = \frac{i}{\sqrt{2\pi}} \int_{-\infty}^{\infty} \text{Im}[4\pi\chi_e(\omega)] e^{-i\omega\tau} d\omega \quad (3.111)$$

since the term containing the cosine function is odd, causing that part of the integral to vanish. It is evident that $G_a(\tau)$ is the Fourier transform of $i\text{Im}[4\pi\chi_e(\omega)]$. Then,

$$\text{Im}[4\pi\chi_e(\omega)] = -\frac{i}{\sqrt{2\pi}} \int_{-\infty}^{\infty} G_a(\tau) e^{+i\omega\tau} d\tau \quad (3.112)$$

We can relate the components of $G(\tau)$ by knowing that $G(\tau) = 0$ for $\tau < 0$, that $G_s(\tau)$ is even in τ , and that $G_a(\tau)$ is odd in τ . For $\tau < 0$,

$$G(\tau < 0) = G_s(\tau < 0) + G_a(\tau < 0) = 0 \quad (3.113)$$

$$G_s(\tau < 0) = -G_a(\tau < 0) \quad (3.114)$$

For $\tau > 0$ (and in general),

$$G_s(-\tau) = G_s(\tau) \quad (3.115)$$

$$G_a(-\tau) = -G_a(\tau) \quad (3.116)$$

Since $\tau > 0$ implies that $-\tau < 0$, Equations (3.114) and (3.116) give

$$G_s(-\tau) = -G_a(-\tau) = G_a(\tau) \quad (3.117)$$

Thus, for $\tau > 0$,

$$G_s(-\tau) = G_s(\tau) = G_a(\tau) \quad (3.118)$$

The first result is from the symmetry property, and the last result is from Equation (3.117). Therefore,

$$G_s(\tau > 0) = G_a(\tau > 0) \quad (3.119)$$

Now we can relate the real and imaginary parts of $4\pi\chi_e(\omega)$. Separating the integral into one over negative τ and another over positive τ ,

$$\text{Re}[4\pi\chi_e(\omega)] = \frac{1}{\sqrt{2\pi}} \int_{-\infty}^0 G_s(\tau) e^{i\omega\tau} d\tau + \frac{1}{\sqrt{2\pi}} \int_0^{\infty} G_s(\tau) e^{i\omega\tau} d\tau \quad (3.120)$$

Then, using Equations (3.114) and (3.119),

$$\text{Re}[4\pi\chi_e(\omega)] = \frac{1}{\sqrt{2\pi}} \int_{-\infty}^0 [-G_a(\tau)] e^{i\omega\tau} d\tau + \frac{1}{\sqrt{2\pi}} \int_0^{\infty} G_a(\tau) e^{i\omega\tau} d\tau \quad (3.121)$$

Substituting $-\tau$ for τ in the first integral, we can recombine the integrals into

$$\text{Re}[4\pi\chi_e(\omega)] = \frac{1}{\sqrt{2\pi}} \int_0^{\infty} G_a(\tau) (e^{-i\omega\tau} + e^{i\omega\tau}) d\tau \quad (3.122)$$

We now substitute for $G_a(\tau)$ from Equation (3.111):

$$\begin{aligned} \operatorname{Re}[4\pi\chi_e(\omega)] &= \frac{1}{\sqrt{2\pi}} \int_0^\infty \left\{ \frac{i}{\sqrt{2\pi}} \int_{-\infty}^\infty \operatorname{Im}[4\pi\chi_e(\omega')] e^{-i\omega'\tau} d\omega' \right\} \times \\ &\quad \times (e^{-i\omega\tau} + e^{i\omega\tau}) d\tau \end{aligned} \quad (3.123)$$

Interchanging the order of integration and performing the integral over τ ,

$$\operatorname{Re}[4\pi\chi_e(\omega)] = \frac{1}{2\pi} \int_{-\infty}^\infty \operatorname{Im}[4\pi\chi_e(\omega')] \left(\frac{1}{\omega' + \omega} + \frac{1}{\omega' - \omega} \right) d\omega' \quad (3.124)$$

$$\begin{aligned} \operatorname{Re}[4\pi\chi_e(\omega)] &= \frac{1}{2\pi} \int_{-\infty}^\infty \frac{\operatorname{Im}[4\pi\chi_e(\omega')] d\omega'}{(\omega' + \omega)} + \\ &\quad \frac{1}{2\pi} \int_{-\infty}^\infty \frac{\operatorname{Im}[4\pi\chi_e(\omega')] d\omega'}{(\omega' - \omega)} \end{aligned} \quad (3.125)$$

Substituting $-\omega'$ for ω' in the first integral, and using the fact that $\operatorname{Im}[4\pi\chi_e(\omega)]$ is odd in ω , we obtain

$$\operatorname{Re}[4\pi\chi_e(\omega)] = \frac{1}{\pi} \int_{-\infty}^\infty \frac{\operatorname{Im}[4\pi\chi_e(\omega')] d\omega'}{(\omega' - \omega)} \quad (3.126)$$

Now, using

$$\operatorname{Re}[4\pi\chi_e(\omega)] = \operatorname{Re}[\epsilon(\omega) - 1] = \operatorname{Re}[\epsilon(\omega)] - 1 \quad (3.127)$$

$$\operatorname{Im}[4\pi\chi_e(\omega)] = \operatorname{Im}[\epsilon(\omega) - 1] = \operatorname{Im}[\epsilon(\omega)] \quad (3.128)$$

the result is

$$\operatorname{Re}[\epsilon(\omega)] = 1 + \frac{1}{\pi} \int_{-\infty}^{\infty} \frac{\operatorname{Im}[\epsilon(\omega')]}{(\omega' - \omega)} d\omega' \quad (3.129)$$

Similarly, separating Equation (3.112) into two integrals and using Equations (3.114) and (3.119),

$$\operatorname{Im}[4\pi\chi_e(\omega)] = \frac{i}{\sqrt{2\pi}} \int_0^{\infty} G_s(\tau) (e^{-i\omega\tau} - e^{i\omega\tau}) d\tau \quad (3.130)$$

Substituting for $G_s(\tau)$ from Equation (3.109),

$$\begin{aligned} \operatorname{Im}[4\pi\chi_e(\omega)] &= \frac{i}{\sqrt{2\pi}} \int_0^{\infty} \left\{ \frac{1}{\sqrt{2\pi}} \int_{-\infty}^{\infty} \operatorname{Re}[4\pi\chi_e(\omega')] e^{-i\omega'\tau} d\omega' \right\} \times \\ &\quad \times (e^{-i\omega\tau} - e^{i\omega\tau}) d\tau \end{aligned} \quad (3.131)$$

Interchanging the order of integration and performing the integral over τ , we find

$$\operatorname{Im}[4\pi\chi_e(\omega)] = \frac{1}{2\pi} \int_{-\infty}^{\infty} \operatorname{Re}[4\pi\chi_e(\omega')] \left(\frac{1}{\omega' + \omega} - \frac{1}{\omega' - \omega} \right) d\omega' \quad (3.132)$$

$$\begin{aligned} \operatorname{Im}[4\pi\chi_e(\omega)] &= \frac{1}{2\pi} \int_{-\infty}^{\infty} \frac{\operatorname{Re}[4\pi\chi_e(\omega')]}{(\omega' + \omega)} d\omega' - \\ &\quad \frac{1}{2\pi} \int_{-\infty}^{\infty} \frac{\operatorname{Re}[4\pi\chi_e(\omega')]}{(\omega' - \omega)} d\omega' \end{aligned} \quad (3.133)$$

Substituting $-\omega'$ for ω' in the first integral and using the symmetry of $\operatorname{Re}[4\pi\chi_e(\omega)]$, these integrals become

$$\operatorname{Im}[4\pi\chi_e(\omega)] = -\frac{1}{\pi} \int_{-\infty}^{\infty} \frac{\operatorname{Re}[4\pi\chi_e(\omega')]}{(\omega' - \omega)} d\omega' \quad (3.134)$$

Thus, we obtain

$$\operatorname{Im}[\varepsilon(\omega)] = -\frac{1}{\pi} \int_{-\infty}^{\infty} \frac{\operatorname{Re}[\varepsilon(\omega')] - 1}{(\omega' - \omega)} d\omega' \quad (3.135)$$

These relations can be expressed slightly differently. Beginning with Equation (3.124), we combine the two terms in parentheses to form

$$\operatorname{Re}[4\pi\chi_e(\omega)] = \frac{1}{\pi} \int_{-\infty}^{\infty} \frac{\omega' \operatorname{Im}[4\pi\chi_e(\omega')]}{(\omega'^2 - \omega^2)} d\omega' \quad (3.136)$$

Relying on the evenness of the integrand,

$$\operatorname{Re}[4\pi\chi_e(\omega)] = \frac{2}{\pi} \int_0^{\infty} \frac{\omega' \operatorname{Im}[4\pi\chi_e(\omega')]}{(\omega'^2 - \omega^2)} d\omega' \quad (3.137)$$

$$\operatorname{Re}[\varepsilon(\omega)] = 1 + \frac{2}{\pi} \int_0^{\infty} \frac{\omega' \operatorname{Im}[\varepsilon(\omega')]}{(\omega'^2 - \omega^2)} d\omega' \quad (3.138)$$

Similarly, beginning with Equation (3.132),

$$\operatorname{Im}[4\pi\chi_e(\omega)] = -\frac{\omega}{\pi} \int_{-\infty}^{\infty} \frac{\operatorname{Re}[4\pi\chi_e(\omega')]}{(\omega'^2 - \omega^2)} d\omega' \quad (3.139)$$

$$\operatorname{Im}[4\pi\chi_e(\omega)] = -\frac{2\omega}{\pi} \int_0^{\infty} \frac{\operatorname{Re}[4\pi\chi_e(\omega')]}{(\omega'^2 - \omega^2)} d\omega' \quad (3.140)$$

$$\text{Im}[\epsilon(\omega)] = -\frac{2\omega}{\pi} \int_0^{\infty} \frac{\text{Re}[\epsilon(\omega')] - 1}{(\omega'^2 - \omega^2)} d\omega' \quad (3.141)$$

Equations (3.129) and (3.135), or alternatively (3.138) and (3.141), are the Kramers-Kronig relations.

The Lorentz Oscillator Model

Derivation of the dispersion relations for the complex refractive index requires some knowledge of the analytic properties of the function $N(\omega)$. Since, for water, $N^2(\omega) = \epsilon(\omega)$, it is clear that a knowledge of the properties of $\epsilon(\omega)$ will prove helpful in investigating the properties of $N(\omega)$. We begin with the Lorentz model of the dielectric function.

Consider the motion of an electron in an applied electric field. The electron is bound to the nucleus with a force constant k , and it experiences a damping force, proportional to its velocity, $-m\gamma v$. The equation of motion is

$$\vec{F} = m \frac{d^2 \vec{x}}{dt^2} = -k\vec{x} - m\gamma \vec{v} + (-e)\vec{E} \quad (3.142)$$

$$m \frac{d^2 \vec{x}}{dt^2} + m\gamma \frac{d\vec{x}}{dt} + k\vec{x} = -e\vec{E} \quad (3.143)$$

We assume an oscillating field vector with angular frequency ω :

$$\vec{E} = \vec{E}_0 e^{-i\omega t} \quad (3.144)$$

Then, substituting for \vec{E} in Equation (3.143),

$$m \frac{d^2 \vec{x}}{dt^2} + m\gamma \frac{d\vec{x}}{dt} + k\vec{x} = -e\vec{E}_0 e^{-i\omega t} \quad (3.145)$$

We assume a solution of the form

$$\vec{x} = \vec{x}_0 e^{-i\omega t} \quad (3.146)$$

Then, taking derivatives,

$$\frac{d\vec{x}}{dt} = -i\omega \vec{x}_0 e^{-i\omega t} \quad (3.147)$$

$$\frac{d^2 \vec{x}}{dt^2} = -\omega^2 \vec{x}_0 e^{-i\omega t} \quad (3.148)$$

The equation of motion becomes

$$-m\omega^2 \vec{x}_0 e^{-i\omega t} - i\gamma m\omega \vec{x}_0 e^{-i\omega t} + k\vec{x}_0 e^{-i\omega t} = -e\vec{E}_0 e^{-i\omega t} \quad (3.149)$$

Dividing by m and the exponential,

$$(-\omega^2 - i\gamma\omega + \frac{k}{m}) \vec{x}_0 = -\frac{e\vec{E}_0}{m} \quad (3.150)$$

Writing $\sqrt{k/m}$ as ω_0 , the natural oscillator frequency,

$$\vec{x}_0 = -\frac{e\vec{E}_0}{m(\omega_0^2 - \omega^2 - i\gamma\omega)} \quad (3.151)$$

Then, writing \vec{x}_0 as in Equation (3.146), we obtain

$$\vec{x} = - \frac{e\vec{E}_0 e^{-i\omega t}}{m(\omega_0^2 - \omega^2 - i\gamma\omega)} = - \frac{e\vec{E}}{m(\omega_0^2 - \omega^2 - i\gamma\omega)} \quad (3.152)$$

The dipole moment for this single oscillator is

$$\vec{p} = -e\vec{x} = \frac{e^2 \vec{E}}{m(\omega_0^2 - \omega^2 - i\gamma\omega)} \quad (3.153)$$

If there are N such oscillators per unit volume, the polarization, \vec{P} , is given by

$$\vec{P} = N\vec{p} = \frac{Ne^2 \vec{E}}{m(\omega_0^2 - \omega^2 - i\gamma\omega)} \quad (3.154)$$

Therefore, the electric susceptibility, χ_e , is given by

$$\vec{P} = \chi_e \vec{E} = \left[\frac{Ne^2}{m(\omega_0^2 - \omega^2 - i\gamma\omega)} \right] \vec{E} \quad (3.155)$$

The dielectric function is related to χ_e as follows:

$$\epsilon = 1 + 4\pi\chi_e = 1 + \frac{4\pi Ne^2}{m(\omega_0^2 - \omega^2 - i\gamma\omega)} \quad (3.156)$$

The term $4\pi Ne^2/m$ is frequently written ω_p^2 , where ω_p is called the plasma frequency.

$$\epsilon = 1 + \frac{\omega_p^2}{(\omega_0^2 - \omega^2 - i\gamma\omega)} \quad (3.157)$$

This single oscillator model can be extended to account for multiple oscillators. For N total electrons per unit volume, there are N_j with natural frequency ω_{oj} and damping constant γ_j . The obvious constraint is

$$\sum_j N_j = N \quad (3.158)$$

Then, adding up contributions from all types of electrons (oscillators),

$$\epsilon = 1 + \frac{4\pi e^2}{m} \sum_j \frac{N_j}{(\omega_{oj}^2 - \omega^2 - i\gamma_j \omega)} \quad (3.159)$$

This can be separated into real and imaginary parts:

$$\epsilon = 1 + \frac{4\pi e^2}{m} \sum_j \frac{N_j [(\omega_{oj}^2 - \omega^2) + i\gamma_j \omega]}{(\omega_{oj}^2 - \omega^2)^2 + \gamma_j^2 \omega^2} \quad (3.160)$$

$$= \left[1 + \frac{4\pi e^2}{m} \sum_j \frac{N_j (\omega_{oj}^2 - \omega^2)}{(\omega_{oj}^2 - \omega^2)^2 + \gamma_j^2 \omega^2} \right] +$$

$$i \left[\frac{4\pi e^2}{m} \sum_j \frac{N_j \gamma_j \omega}{(\omega_{oj}^2 - \omega^2)^2 + \gamma_j^2 \omega^2} \right] \quad (3.161)$$

AD-A133 530

OPTICAL PROPERTIES OF NATURAL MINERALS AND OTHER
MATERIALS IN THE 350-500. (U) MISSOURI UNIV-KANSAS CITY
DEPT OF PHYSICS M R QUERRY AUG 83 ARO-16512.2-65

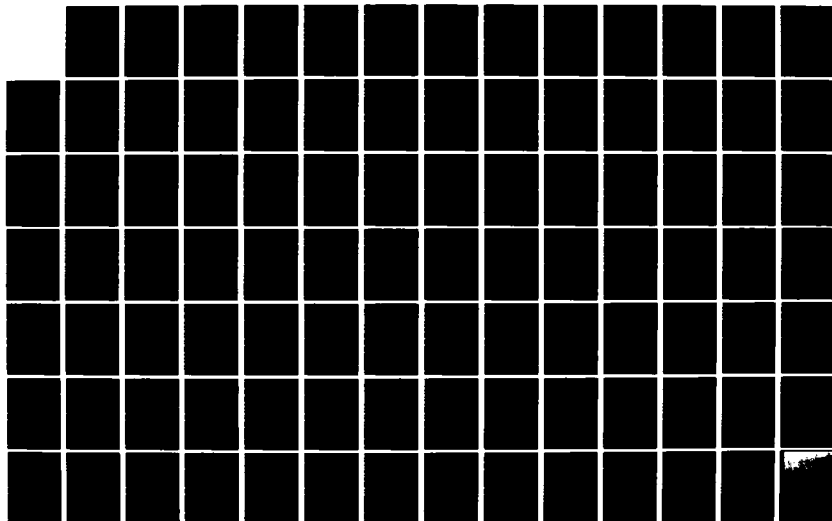
4/4

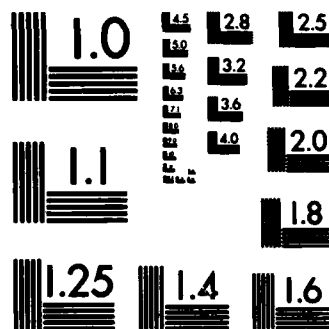
UNCLASSIFIED

DAAG29-79-C-0131

F/G 8/7

NL





MICROCOPY RESOLUTION TEST CHART
NATIONAL BUREAU OF STANDARDS-1963-A

Analytic Properties of $N(\omega)$

For water, $\epsilon(\omega) = N^2(\omega)$. Then, Equation (3.157) gives

$$N^2(\omega) = 1 + \frac{\omega_p^2}{\omega_o^2 - \omega^2 - i\gamma\omega} \quad (3.162)$$

The zeroes of $N^2(\omega)$ are $\underline{\omega_a}$ and $\underline{\omega_b}$, obtained as follows:

$$0 = 1 + \frac{\omega_p^2}{\omega_o^2 - \omega^2 - i\gamma\omega} \quad (3.163)$$

$$\omega_p^2 = -\omega_o^2 + \omega^2 + i\gamma\omega \quad (3.164)$$

$$\omega^2 + (i\gamma)\omega - (\omega_p^2 + \omega_o^2) = 0 \quad (3.165)$$

$$\omega = -i\left(\frac{\gamma}{2}\right) \pm \left(\omega_o^2 + \omega_p^2 - \frac{\gamma^2}{4}\right)^{1/2} \quad (3.166)$$

With the following definition

$$\omega_1^2 \equiv \omega_o^2 + \omega_p^2 - \frac{\gamma^2}{4} \quad (3.167)$$

(ω_1 is real), the zeroes are

$$\omega_a = \omega_1 - i\left(\frac{\gamma}{2}\right) \quad (3.168)$$

$$\omega_b = -\omega_1 - i\left(\frac{\gamma}{2}\right) \quad (3.169)$$

The poles of $N^2(\omega)$ are $\underline{\omega_c}$ and $\underline{\omega_d}$, obtained as follows:

$$\omega_o^2 - \omega^2 - i\gamma\omega = 0 \quad (3.170)$$

$$\omega = -i\left(\frac{\gamma}{2}\right) \pm \left(\omega_o^2 - \frac{\gamma^2}{4}\right)^{\frac{1}{2}} \quad (3.171)$$

With the following definition

$$\omega_2^2 \equiv \omega_o^2 - \frac{\gamma^2}{4} \quad (3.172)$$

(ω_2 is real), the poles are

$$\omega_c = \omega_2 - i\left(\frac{\gamma}{2}\right) \quad (3.173)$$

$$\omega_d = -\omega_2 - i\left(\frac{\gamma}{2}\right) \quad (3.174)$$

We can write²³

$$N^2(\omega) = \frac{(\omega - \omega_a)(\omega - \omega_b)}{(\omega - \omega_c)(\omega - \omega_d)} \quad (3.175)$$

This can be verified by direct substitution from Equations (3.168), (3.169), (3.173), and (3.174). The result is

$$N(\omega) = \left[\frac{(\omega - \omega_a)(\omega - \omega_b)}{(\omega - \omega_c)(\omega - \omega_d)} \right]^{\frac{1}{2}} \quad (3.176)$$

Since the function $N(\omega)$ is multi-valued, its branch line structure must be found in order to determine where it is analytic. The procedure was outlined by Churchill.²⁴

Consider the functions

$$f_a(\omega) = \omega - \omega_a \quad (3.177)$$

$$f_b(\omega) = \omega - \omega_b \quad (3.178)$$

both of which are entire in the complex plane. Using Equation (3.168),

$$f_a(\omega) = \omega - \omega_1 + i\left(\frac{\gamma}{2}\right) \quad (3.179)$$

ω_1 and γ are real. We define

$$z \equiv \omega + i\left(\frac{\gamma}{2}\right) \quad (3.180)$$

Then, redefining $f_a(\omega)$ as $f_1^2(z)$,

$$\omega - \omega_a = z - \omega_1 \quad (3.181)$$

$$f_1(z) = (z - \omega_1)^{1/2} = \sqrt{r_1} e^{i\left(\frac{\theta_1}{2}\right)} \quad (3.182)$$

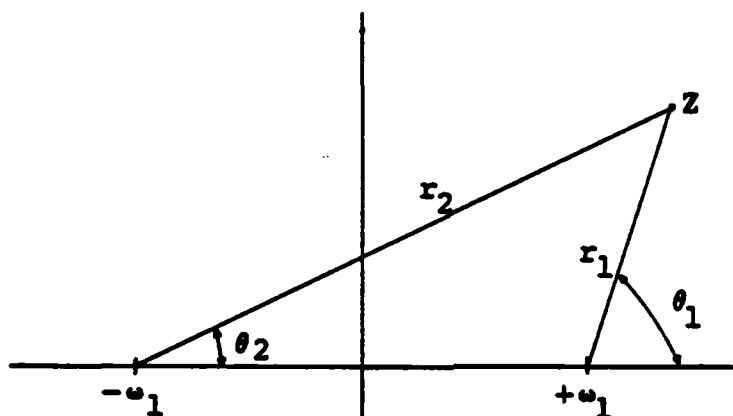
Similarly, using Equation (3.169),

$$f_b(\omega) = \omega + \omega_1 + i\left(\frac{\gamma}{2}\right) \quad (3.183)$$

With the corresponding definition of $f_b(\omega)$ as $f_2^2(z)$,

$$f_2(z) = (z + \omega_1)^{\frac{1}{2}} = \sqrt{r_2} e^{i\left(\frac{\theta_2}{2}\right)} \quad (3.184)$$

The polar coordinates for $f_1(z)$ and $f_2(z)$ are defined as in the following:



We define the function

$$f(z) \equiv [f_1(z)][f_2(z)] \quad (3.185)$$

$$f(z) = (z - \omega_1)^{\frac{1}{2}} (z + \omega_1)^{\frac{1}{2}} = \sqrt{r_1 r_2} e^{i\left[\frac{(\theta_1 + \theta_2)}{2}\right]} \quad (3.186)$$

We may define the domain of $f(z)$ as $\{0 \leq \theta_1 < 2\pi, 0 \leq \theta_2 < 2\pi, r_1 > 0, r_2 > 0, \text{ and } r_1 + r_2 > 2\omega_1\}$. The last condition is imposed so that $f(z)$ is analytic in its domain. This result is equivalent to the statement that $f(z)$ is analytic everywhere except on the closed line segment connecting $-\omega_1$ and $+\omega_1$. This is shown as follows:

The branch cuts for $f_1(z)$ and $f_2(z)$ are the rays $\theta_1=0$ and $\theta_2=0$ respectively. Thus, $f(z)$ is analytic whenever $z \neq \omega_1$ and $\theta_2 \neq 0$. The value of $f_1(z)$ is continuous (analytic) across $\theta_1=\pi$ ($f_1=i\sqrt{r_1}$), but the value of $f_2(z)$ jumps from $+\sqrt{r_2}$ to $-\sqrt{r_2}$ as z crosses from above to below this line segment connecting $-\omega_1$ and $+\omega_1$. Thus, $f(z)$ is not continuous (and not analytic) on that line segment.

Now, to investigate the behavior of $f(z)$ on the ray $\theta_1=0$, $r_1>0$, we define the function

$$F(z) \equiv \sqrt{r_1} e^{i\left(\frac{\phi_1}{2}\right)} \sqrt{r_2} e^{i\left(\frac{\phi_2}{2}\right)} \quad (3.187)$$

in the domain $\{-\pi<\phi_1<\pi, -\pi<\phi_2<\pi, r_1>0, r_2>0\}$. $F(z)$ is continuous across the ray $\phi_1=0$ and is thus analytic there. (This is the same region of the real line as $\theta_1=0$, $r_1>0$.) If we can show that $f(z)=F(z)$ on, above, and below the ray $\theta_1=\phi_1=0$, then we will have shown $f(z)$ to be analytic on that ray. On the ray $\theta_1=\phi_1=0$, as well as above it, $\theta_1=\phi_1$ and $\theta_2=\phi_2$. Thus, $f(z)=F(z)$ for z on or above the ray $\theta_1=\phi_1=0$. For z below this ray, $\phi_1=\theta_1-2\pi$ and $\phi_2=\theta_2-2\pi$. Then,

$$F(z) = \sqrt{r_1} e^{i\left(\frac{\phi_1}{2}\right)} \sqrt{r_2} e^{i\left(\frac{\phi_2}{2}\right)} \quad (3.188)$$

$$F(z) = \sqrt{r_1} e^{i\left[\frac{(\theta_1-2\pi)}{2}\right]} \sqrt{r_2} e^{i\left[\frac{(\theta_2-2\pi)}{2}\right]} \quad (3.189)$$

$$F(z) = \sqrt{r_1 r_2} e^{i\left[\frac{(\theta_1+\theta_2)}{2}\right]} e^{-i2\pi} = \sqrt{r_1 r_2} e^{i\left[\frac{(\theta_1+\theta_2)}{2}\right]} = f(z) \quad (3.190)$$

Therefore, $f(z)$ is analytic on the ray $\theta_1=0$, $r_1>0$.

The branch line for $f(z)$ is



In crossing from above to below the branch line, the function shifts from

$$f_+ = \sqrt{r_1} e^{i\left(\frac{\pi}{2}\right)} e^{-i\delta} \sqrt{r_2} e^{i(0)} e^{+i\delta} = i\sqrt{r_1 r_2} \quad (3.191)$$

($0 < \delta < 1$) to

$$f_- = \sqrt{r_1} e^{i\left(\frac{\pi}{2}\right)} e^{+i\delta} \sqrt{r_2} e^{i(\pi)} e^{-i\delta} = -i\sqrt{r_1 r_2} \quad (3.192)$$

Now consider the functions

$$f_c(w) \equiv (w - w_c) \quad (3.193)$$

$$f_d(w) \equiv (w - w_d) \quad (3.194)$$

both of which are entire in the complex plane. Using Equations (3.173), (3.174), and (3.180),

$$f_c(\omega) = \omega - \omega_2 + i\left(\frac{\gamma}{2}\right) = z - \omega_2 \quad (3.195)$$

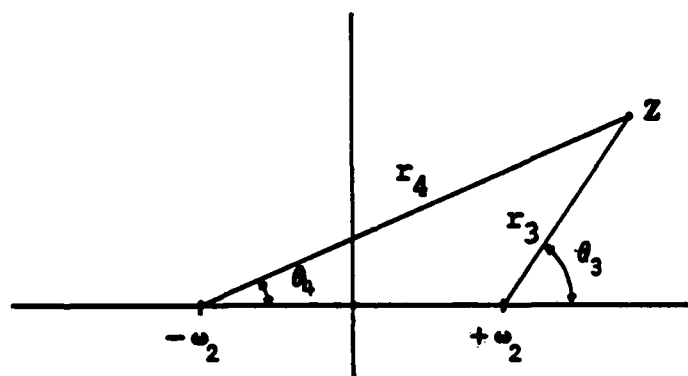
$$f_d(\omega) = \omega + \omega_2 + i\left(\frac{\gamma}{2}\right) = z + \omega_2 \quad (3.196)$$

We now define the following functions:

$$g_1(z) \equiv (z - \omega_2)^{\frac{1}{2}} = \sqrt{r_3} e^{i\left(\frac{\theta_3}{2}\right)} \quad (3.197)$$

$$g_2(z) \equiv (z + \omega_2)^{\frac{1}{2}} = \sqrt{r_4} e^{i\left(\frac{\theta_4}{2}\right)} \quad (3.198)$$

The polar coordinates for $g_1(z)$ and $g_2(z)$ are defined as in the following:



We may define

$$g(z) \equiv g_1(z) g_2(z) = \sqrt{r_3 r_4} e^{i\left[\frac{(\theta_3 + \theta_4)}{2}\right]} \quad (3.199)$$

in the domain $\{0 \leq \theta_3 < 2\pi, 0 \leq \theta_4 < 2\pi, r_3 > 0, r_4 > 0, r_3 + r_4 > 2\omega_2\}$. As in the treatment for $f(z)$, the branch line for $g(z)$ is the closed line segment

connecting $-\omega_2$ and $+\omega_2$. Note that

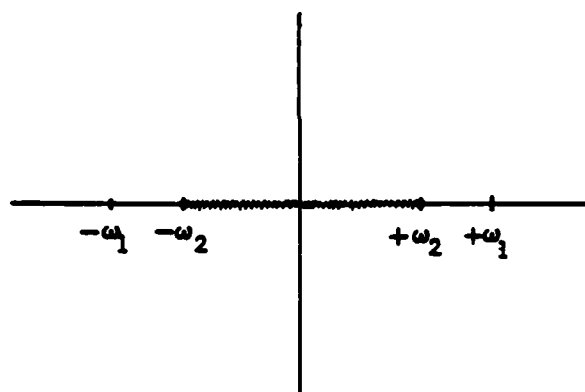
$$|\omega_1| = |\operatorname{Re}(\omega_a)| = |\operatorname{Re}(\omega_b)| = |(\omega_0^2 + \omega_p^2 - \frac{\gamma^2}{4})^{\frac{1}{2}}| \quad (3.200)$$

$$|\omega_2| = |\operatorname{Re}(\omega_c)| = |\operatorname{Re}(\omega_d)| = |(\omega_0^2 - \frac{\gamma^2}{4})^{\frac{1}{2}}| \quad (3.201)$$

Therefore,

$$|\omega_1| > |\omega_2| \quad (3.202)$$

The branch line for $g(z)$ is



In crossing from above to below the branch line, $g(z)$ shifts from $+i\sqrt{r_3 r_4}$ to $-i\sqrt{r_3 r_4}$. In crossing from above to below the ray $\theta_4 = \pi$, $g(z)$ varies continuously through $-\sqrt{r_3 r_4}$. In crossing from above to below the ray $\theta_3 = 0$, $g(z)$ varies continuously through $+\sqrt{r_3 r_4}$.

Now, given the composite function

$$h(z) \equiv \frac{f(z)}{g(z)} \quad (3.203)$$

$h(z)$ is clearly continuous and analytic except perhaps on the closed line segment connecting $-w_1$ and $+w_1$. (This segment contains the segment connecting $-w_2$ and $+w_2$.)

First, consider the segment $-w_1$ to $-w_2$. For z crossing from above to below, $h(z)$ goes from

$$h_+ = \frac{f_+}{g_+} = \frac{i\sqrt{r_1 r_2}}{-\sqrt{r_3 r_4}} = -i\sqrt{\frac{r_1 r_2}{r_3 r_4}} \quad (3.204)$$

to

$$h_- = \frac{f_-}{g_-} = \frac{-i\sqrt{r_1 r_2}}{-\sqrt{r_3 r_4}} = +i\sqrt{\frac{r_1 r_2}{r_3 r_4}} \quad (3.205)$$

The function is discontinuous, and thus not analytic, on that segment.

Second, consider the segment $-w_2$ to $+w_2$. For z crossing from above to below, $h(z)$ goes from

$$h_+ = \frac{f_+}{g_+} = \frac{i\sqrt{r_1 r_2}}{i\sqrt{r_3 r_4}} = \sqrt{\frac{r_1 r_2}{r_3 r_4}} \quad (3.206)$$

to

$$h_- = \frac{f_-}{g_-} = \frac{-i\sqrt{r_1 r_2}}{-i\sqrt{r_3 r_4}} = \sqrt{\frac{r_1 r_2}{r_3 r_4}} \quad (3.207)$$

The function is continuous and analytic on that segment.

Third, consider the segment $+w_2$ to $+w_1$. For z crossing from above to below, $h(z)$ goes from

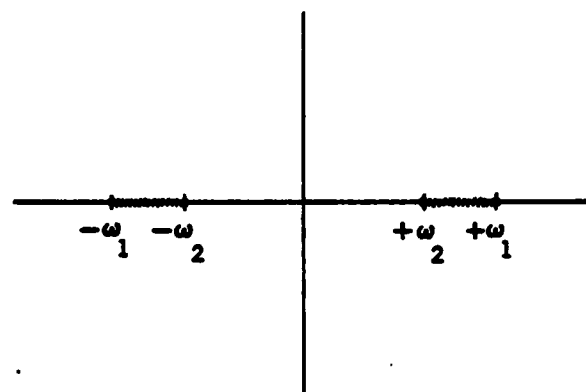
$$h_+ = \frac{f_+}{g_+} = \frac{i\sqrt{r_1 r_2}}{\sqrt{r_3 r_4}} = i\sqrt{\frac{r_1 r_2}{r_3 r_4}} \quad (3.208)$$

to

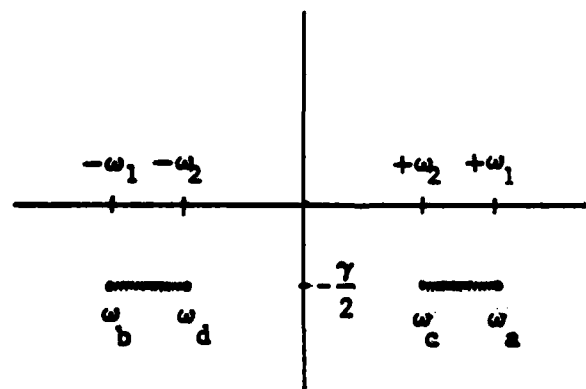
$$h_- = \frac{f_-}{g_-} = \frac{-i\sqrt{r_1 r_2}}{\sqrt{r_3 r_4}} = -i\sqrt{\frac{r_1 r_2}{r_3 r_4}} \quad (3.209)$$

The function is discontinuous, and thus not analytic, on that segment.

The branch line structure for $h(z)$, therefore, is



Substituting $z = \omega + i\left(\frac{\gamma}{2}\right)$, $\omega = z - i\left(\frac{\gamma}{2}\right)$, from Equation (3.180), we obtain $N(\omega)$ with branch lines as follows:



The result is that $N(\omega)$ is analytic on the real line and in the upper half plane.

We can find the high frequency limit for $N(\omega)$ as follows:

For $|\omega| \gg |\omega_0|$,

$$N^2(\omega) = 1 + \frac{\omega_p^2}{\omega_0^2 - \omega^2 - i\gamma\omega} + 1 - \frac{\omega_p^2}{\omega^2} \quad (3.210)$$

$$N(\omega) = \left(1 - \frac{\omega_p^2}{\omega^2}\right)^{1/2} = 1 - \frac{\omega_p^2}{2\omega^2} - \frac{\omega_p^4}{8\omega^4} - \dots = 1 - \frac{\omega_p^2}{2\omega^2} \quad (3.211)$$

As $\omega \rightarrow \infty$, $N(\omega) \rightarrow 1$.

This derivation is not invalidated by requiring a more complicated, or more realistic, model of $\epsilon(\omega)$. Any model can be written in the form

$$\epsilon(\omega) = \frac{\prod_{m=1}^M (\omega - Z_m)}{\prod_{n=1}^N (\omega - P_n)} \quad (3.212)$$

where Z_m are zeroes and P_n are poles of the function.²⁵ Causality implies that all the zeroes and poles lie below the real axis.²⁶ The result is the same analytical properties for $N(\omega)$.

The Kramers-Kronig Relations as Obtained

From the Cauchy Integral Formula

With the above examination of the analytical properties of $\epsilon(\omega)$ and $N(\omega)$, we can derive the dispersion relations for $N(\omega)$. We demonstrate the process first by obtaining the Kramers-Kronig relations for the dielectric function by contour integration.

We can show that the definition of $\epsilon(\omega)$ via the time response function is consistent with the derived analytic properties. The definition of $G(\tau)$ yields

$$4\pi\chi_e(\omega) = \epsilon(\omega) - 1 = \frac{1}{\sqrt{2\pi}} \int_{-\infty}^{\infty} G(\tau) e^{i\omega\tau} d\tau \quad (3.213)$$

Since $G(\tau)=0$ for $\tau<0$, we can write

$$\epsilon(\omega) - 1 = \frac{1}{\sqrt{2\pi}} \int_0^{\infty} G(\tau) e^{i\omega\tau} d\tau \quad (3.214)$$

Separating ω into its real and imaginary parts,

$$\epsilon(\omega) - 1 = \frac{1}{\sqrt{2\pi}} \int_0^{\infty} G(\tau) e^{i\omega_r\tau} e^{-\omega_i\tau} d\tau \quad (3.215)$$

It is clear that, for finite $G(\tau)$, the function $\epsilon(\omega)-1$ exists, as does its derivative, for all ω such that $\omega_i \geq 0$. Therefore, the function $\epsilon(\omega)-1$ is analytic on the real axis and in the upper half plane.

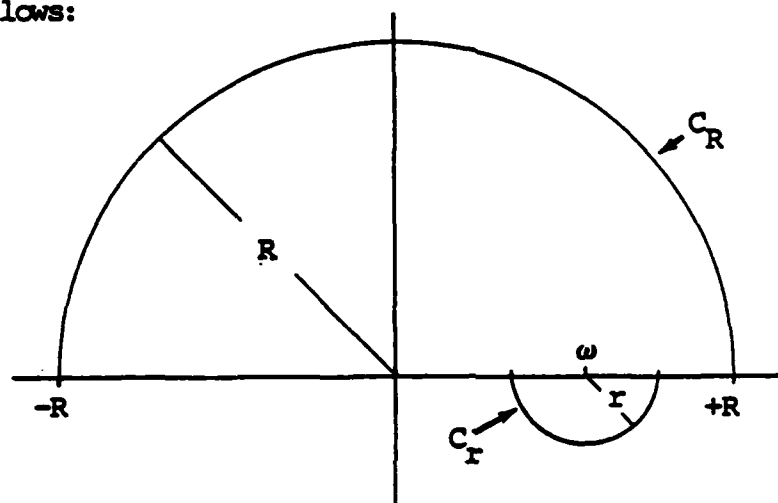
As a result, for any closed contour in the domain of analyticity of $\epsilon(\omega)-1$, the Cauchy integral formula allows us to write

$$\epsilon(\omega) - 1 = \frac{1}{2\pi i} \oint_C \frac{[\epsilon(\omega') - 1] d\omega'}{(\omega' - \omega)} \quad (3.216)$$

We will want to investigate the function for real, positive ω .

Therefore, placing ω on the positive real axis, we choose a contour

C as follows:



The integral around this contour can be written as the sum of four parts:

$$\begin{aligned} \oint_C \frac{[\epsilon(\omega') - 1] d\omega'}{(\omega' - \omega)} &= \int_{-R}^{\omega-r} \frac{[\epsilon(\omega') - 1] d\omega'}{(\omega' - \omega)} + \int_{C_r} \frac{[\epsilon(\omega') - 1] d\omega'}{(\omega' - \omega)} + \\ &\quad \int_{\omega+r}^R \frac{[\epsilon(\omega') - 1] d\omega'}{(\omega' - \omega)} + \int_{C_R} \frac{[\epsilon(\omega') - 1] d\omega'}{(\omega' - \omega)} \end{aligned} \quad (3.217)$$

Now, writing

$$\omega' = \omega + re^{i\theta} \quad (3.218)$$

$$d\omega' = ire^{i\theta} d\theta \quad (3.219)$$

we can write the second integral as

$$\int_{-\pi}^0 \frac{[\epsilon(\omega')-1]ire^{i\theta} d\theta}{(\omega+re^{i\theta}-\omega)} = \int_{-\pi}^0 [\epsilon(\omega')-1]id\theta \quad (3.220)$$

Writing

$$\omega' = Re^{i\phi} \quad (3.221)$$

$$d\omega' = ire^{i\phi} d\phi \quad (3.222)$$

we can write the last integral as

$$\int_0^{\pi} \frac{[\epsilon(\omega')-1]ire^{i\phi} d\phi}{(Re^{i\phi}-\omega)} \quad (3.223)$$

Then,

$$\begin{aligned} \oint_C \frac{[\epsilon(\omega')-1]d\omega'}{(\omega'-\omega)} &= \int_{-R}^{\omega-r} \frac{[\epsilon(\omega')-1]d\omega'}{(\omega'-\omega)} + \int_{-\pi}^0 [\epsilon(\omega')-1]id\theta + \\ &\quad \int_{\omega+r}^R \frac{[\epsilon(\omega')-1]d\omega'}{(\omega'-\omega)} + \int_0^{\pi} \frac{[\epsilon(\omega')-1]ire^{i\phi} d\phi}{(Re^{i\phi}-\omega)} \end{aligned} \quad (3.224)$$

Now we apply a limiting process, allowing R to approach ∞ and r to approach zero. Since this includes and excludes no new poles, the

integral on the left of Equation (3.224) remains the same. The first and third integrals on the right become the Cauchy principal value (denoted P.V.) of the integral along the real line. In the second integral on the right, ω' becomes ω and the function $\epsilon(\omega)-1$ can be moved outside the integral sign, the remainder yielding πi . The fourth integral on the right vanishes because $\epsilon(\omega')$ approaches one as the magnitude of ω' increases without bound. Thus,

$$\oint_C \frac{[\epsilon(\omega')-1]d\omega'}{(\omega'-\omega)} = \text{P.V.} \left\{ \int_{-\infty}^{\infty} \frac{[\epsilon(\omega')-1]d\omega'}{(\omega'-\omega)} \right\} + \pi i [\epsilon(\omega)-1] \quad (3.225)$$

Now, using this in Equation (3.216) and rearranging, we obtain

$$\epsilon(\omega) - 1 = \frac{1}{\pi i} \text{P.V.} \left\{ \int_{-\infty}^{\infty} \frac{[\epsilon(\omega')-1]d\omega'}{(\omega'-\omega)} \right\} \quad (3.226)$$

Separating the functions into real and imaginary parts yields the Kramers-Kronig relations.

One difficulty with the above derivation is the excursion into the lower half plane by the contour C_{τ} . This path is of infinitesimal length; and with $\omega_1 < \delta$ for all δ , the function given by Equation (3.215) remains regular even with $\tau \rightarrow \infty$. Further, the physical constraints on $G(\tau)$ require that $G(\tau) \rightarrow 0$ as $\tau \rightarrow \infty$. However, this difficulty can be avoided by distorting the contour above, instead of below, the pole at ω on the real axis. Then, since no poles are enclosed, the integral must yield zero:

$$\oint_{C'} \frac{[\varepsilon(\omega') - 1] d\omega'}{(\omega' - \omega)} = 0 \quad (3.227)$$

As before, the integral is divided into four parts. The limit is taken allowing $R \rightarrow \infty$ and $r \rightarrow 0$. The only difference is the integration around the small semi-circular contour around ω which is counter-clockwise and yields $-\pi i [\varepsilon(\omega) - 1]$, the negative of the prior result. This, however, conspires with the zero on the right of Equation (3.227) to give the same answer as before, namely Equation (3.226) and the Kramers-Kronig relations.

The only requirements for the derivation of the Kramers-Kronig relations above were the analyticity of the function $\varepsilon(\omega) - 1$ in the upper half plane and on the real line, and the vanishing of the function for $|\omega| \rightarrow \infty$. We can, thus, derive similar relations for the complex index of refraction. We must use $N(\omega) - 1$, however, since $N(\omega) \rightarrow 1$ as $|\omega| \rightarrow \infty$. We write

$$N(\omega) - 1 = \frac{1}{2\pi i} \oint_C \frac{[N(\omega') - 1] d\omega'}{(\omega' - \omega)} \quad (3.228)$$

using a contour enclosing the pole at ω (real). If we wish to use a contour excluding that pole, the integral on the right of Equation (3.228) yields zero. In either case, the result is

$$N(\omega) - 1 = \frac{1}{\pi i} \text{P.V.} \left\{ \int_{-\infty}^{\infty} \frac{[N(\omega') - 1] d\omega'}{(\omega' - \omega)} \right\} \quad (3.229)$$

Separating the functions into their real and imaginary parts,

$$n(\omega) = 1 + \frac{1}{\pi} \int_{-\infty}^{\infty} \frac{k(\omega') d\omega'}{(\omega' - \omega)} \quad (3.230)$$

$$k(\omega) = -\frac{1}{\pi} \int_{-\infty}^{\infty} \frac{[n(\omega') - 1] d\omega'}{(\omega' - \omega)} \quad (3.231)$$

These are the Kramers-Kronig relations for the complex refractive index.

The Real Part of $N(\omega)$ as a Fourier Transform

We can obtain $n(\omega)$ as a series of two Fourier transforms. This will be the basis for the calculation described in Chapter IV. Beginning with Equation (3.230), we divide the integral into two equal parts.

$$n(\omega) - 1 = \frac{1}{2\pi} \int_{-\infty}^{\infty} \frac{k(\omega') d\omega'}{(\omega' - \omega)} + \frac{1}{2\pi} \int_{-\infty}^{\infty} \frac{k(\omega') d\omega'}{(\omega' - \omega)} \quad (3.232)$$

Substituting $-\omega'$ for ω' in the first integral, using the fact that $k(\omega')$ is odd, and reversing the limits, we can recombine the integrals.

$$n(\omega) - 1 = \frac{1}{2\pi} \int_{-\infty}^{\infty} k(\omega') \left[\frac{1}{(\omega' + \omega)} + \frac{1}{(\omega' - \omega)} \right] d\omega' \quad (3.233)$$

Now we rely on the value of the integral

$$i \int_0^{\infty} \left[e^{-i(\omega' + \omega)\tau} + e^{-i(\omega' - \omega)\tau} \right] d\tau = \frac{1}{(\omega' + \omega)} + \frac{1}{(\omega' - \omega)} \quad (3.234)$$

Substituting this integral over τ into Equation (3.233), we obtain

$$n(\omega)-1 = \frac{1}{2\pi} \int_{-\infty}^{\infty} k(\omega') \left\{ i \int_0^{\infty} \left[e^{-i(\omega'+\omega)\tau} + e^{-i(\omega'-\omega)\tau} \right] d\tau \right\} d\omega' \quad (3.235)$$

Since $k(\omega')$ is continuous, we can reverse the order of integration.

$$n(\omega)-1 = \frac{1}{2\pi} \int_0^{\infty} \left[\int_{-\infty}^{\infty} k(\omega') e^{-i\omega'\tau} d\omega' \right] (e^{-i\omega\tau} + e^{i\omega\tau}) d\tau \quad (3.236)$$

$$n(\omega)-1 = \frac{1}{\sqrt{2\pi}} \int_0^{\infty} \left\{ \frac{1}{\sqrt{2\pi}} \int_{-\infty}^{\infty} [ik(\omega')] e^{-i\omega'\tau} d\omega' \right\} e^{-i\omega\tau} d\tau +$$

$$\frac{1}{\sqrt{2\pi}} \int_0^{\infty} \left\{ \frac{1}{\sqrt{2\pi}} \int_{-\infty}^{\infty} [ik(\omega')] e^{-i\omega'\tau} d\omega' \right\} e^{+i\omega\tau} d\tau \quad (3.237)$$

Substituting $-\tau$ for τ , the first integral in Equation (3.237) becomes

$$\frac{1}{\sqrt{2\pi}} \int_{-\infty}^0 \left\{ \frac{1}{\sqrt{2\pi}} \int_{-\infty}^{\infty} [ik(\omega')] e^{+i\omega'\tau} d\omega' \right\} e^{+i\omega\tau} d\tau \quad (3.238)$$

Now, substituting $-\omega'$ for ω' , using the oddness of $k(\omega')$, and reversing the limits, the integral (3.238) becomes

$$\frac{1}{\sqrt{2\pi}} \int_{-\infty}^0 \left\{ -\frac{1}{\sqrt{2\pi}} \int_{-\infty}^{\infty} [ik(\omega')] e^{-i\omega'\tau} d\omega' \right\} e^{+i\omega\tau} d\tau \quad (3.239)$$

The result is

$$n(\omega)-1 = \frac{1}{\sqrt{2\pi}} \int_{-\infty}^0 \left\{ -\frac{1}{\sqrt{2\pi}} \int_{-\infty}^{\infty} [ik(\omega')] e^{-i\omega'\tau} d\omega' \right\} e^{+i\omega\tau} d\tau +$$

$$+ \frac{1}{\sqrt{2\pi}} \int_0^{\infty} \left\{ \frac{1}{\sqrt{2\pi}} \int_{-\infty}^{\infty} [ik(\omega')] e^{-i\omega'\tau} d\omega' \right\} e^{i\omega\tau} d\tau \quad (3.240)$$

If we define $\underline{f(\tau)}$ as the Fourier transform of $\underline{ik(\omega')}$,

$$f(\tau) \equiv \frac{1}{\sqrt{2\pi}} \int_{-\infty}^{\infty} [ik(\omega')] e^{-i\omega'\tau} d\omega' \quad (3.241)$$

the function $\underline{n(\omega)-1}$ can be written

$$n(\omega)-1 = \frac{1}{\sqrt{2\pi}} \int_{-\infty}^0 [-f(\tau)] e^{i\omega\tau} d\tau + \frac{1}{\sqrt{2\pi}} \int_0^{\infty} [f(\tau)] e^{i\omega\tau} d\tau \quad (3.242)$$

Now we define $\underline{g(\tau)}$ as

$$g(\tau) \equiv \begin{cases} -f(\tau), & \tau \leq 0 \\ +f(\tau), & \tau > 0 \end{cases} \quad (3.243)$$

Then,

$$n(\omega)-1 = \frac{1}{\sqrt{2\pi}} \int_{-\infty}^{\infty} g(\tau) e^{i\omega\tau} d\tau \quad (3.244)$$

Thus, $\underline{n(\omega)-1}$ is the Fourier transform of the $\underline{g(\tau)}$ function.

The Electronic Sum Rule

We are now in a position to derive the electronic sum rule.

Beginning with the Kramers-Kronig relation for the real part of the refractive index, Equation (3.230), we express the integral over positive frequencies.

$$n(\omega) - 1 = \frac{2}{\pi} \int_0^{\infty} \frac{\omega' k(\omega') d\omega'}{(\omega'^2 - \omega^2)} \quad (3.245)$$

Now, we define ω_c as some cut-off frequency above which there is no absorption due to electronic oscillation. Then, that portion of the integral from ω_c to ∞ can be omitted.

$$n(\omega) = 1 + \frac{2}{\pi} \int_0^{\omega_c} \frac{\omega' k(\omega') d\omega'}{(\omega'^2 - \omega^2)} \quad (3.246)$$

Choosing some $\omega \gg \omega_c$, the ω^2 term dominates the ω'^2 in the denominator of the integrand. Ignoring ω'^2 by comparison,

$$n(\omega) = 1 + \frac{2}{\pi} \left(-\frac{1}{\omega^2} \right) \int_0^{\omega_c} \omega' k(\omega') d\omega' \quad (3.247)$$

This expression becomes more accurate as ω becomes larger. Also, for large ω , Equation (3.211) gives

$$n(\omega) = 1 - \frac{\omega_p^2}{2\omega^2} \quad (3.248)$$

This also becomes more accurate as ω becomes larger. We take the limiting case, $\omega \rightarrow \infty$. Then, equating the right sides of Equations (3.247) and (3.248),

$$1 - \frac{\omega_p^2}{2\omega^2} = 1 - \frac{2}{\pi\omega^2} \int_0^{\omega_c} \omega' k(\omega') d\omega' \quad (3.249)$$

$$\omega_p^2 = \frac{4}{\pi} \int_0^{\omega_c} \omega' k(\omega') d\omega' \quad (3.250)$$

We can extend the upper limit to ∞ since the integrand contributes nothing for $\omega > \omega_c$.

$$\omega_p^2 = \frac{4}{\pi} \int_0^{\infty} \omega' k(\omega') d\omega' \quad (3.251)$$

We substitute $4\pi n_o e^2/m$ for ω_p^2 and write N as $Z n_o$, where Z is the number of electrons in the molecule and n_o is the number of water molecules per unit volume.

$$\frac{4\pi n_o e^2}{m} = \frac{4}{\pi} \int_0^{\infty} \omega' k(\omega') d\omega' \quad (3.252)$$

$$Z = \frac{m}{2\pi n_o e^2} \int_0^{\infty} \omega' k(\omega') d\omega' \quad (3.253)$$

Now, we write the angular frequency in terms of wave number.

$$\omega' = 2\pi c\nu \quad (3.254)$$

$$d\omega' = 2\pi c d\nu \quad (3.255)$$

Substituting Equations (3.254) and (3.255) into Equation (3.253), we obtain

$$Z = \frac{4\pi c^2}{n_o e^2} \int_0^{\infty} \nu k(\nu) d\nu \quad (3.256)$$

We substitute $\alpha(\nu)/4\pi\nu$ for $k(\nu)$.

$$Z = \frac{mc^2}{m_0 e^2} \int_0^\infty \alpha(v) dv \quad (3.257)$$

Transforming to mks units, we obtain the sum rule used in the calculations described in Chapter IV.

$$Z = \frac{4\pi c^2 \epsilon_0}{n_0 e^2} \int_0^\infty \alpha(v) dv \quad (3.258)$$

CHAPTER IV

NUMERICAL METHODS

The Numerical Computation of $n(\omega)$ from $k(\omega)$

In Chapter III, we obtained Equation (3.230) expressing $n(\omega)$ in terms of an integral involving $k(\omega')$. For numerical calculation of $n(\omega)$, we must rely on numerical values of $k(\omega)$ known at discrete values of ω over a finite spectrum.

Assuming there is some ω_{\max} above which $k(\omega)$ yields a negligible contribution to the integral, we can restrict our attention to those values of $|\omega| \leq \omega_{\max}$. Since $k(\omega)$ is an odd function,

$$k(0) = 0 \quad (4.1)$$

Further, if we know $k(\omega)$ for $0 < \omega \leq \omega_{\max}$, we automatically know $k(\omega)$ for $-\omega_{\max} \leq \omega < 0$. We divide the interval $-\omega_{\max} \leq \omega \leq \omega_{\max}$ into N segments each of width $\Delta\omega$.

We begin by evaluating $f(\tau)$, the Fourier transform of $ik(\omega')$, as specified in Equation (3.241).

$$f(\tau) = \frac{1}{\sqrt{2\pi}} \int_{-\infty}^{\infty} ik(\omega') e^{-i\omega'\tau} d\omega' \quad (4.2)$$

This integral must be transformed into a discrete sum. For the N points

(including $j=0$) from $j=-N/2$ to $j=(N/2)-1$, with

$$\omega = j\Delta\omega \quad (4.3)$$

$$\tau = m\Delta\tau \quad (4.4)$$

(the index m to be summed over later), we find

$$f(\tau) = f(m) = \frac{i}{\sqrt{2\pi}} \sum_{j=-\frac{N}{2}}^{\frac{N}{2}-1} k(j) e^{-i(j\Delta\omega)(m\Delta\tau)} \Delta\omega \quad (4.5)$$

The summation is to $(N/2)-1$ since the function is presumed periodic (to be Fourier transformable) with period $N\Delta\omega$.²⁷ The value at $j=N/2$ is the first value of the next period of the function. ($N \rightarrow \infty$ in the Fourier integral.) We write ω and $\Delta\omega$ in terms of wave number.

$$\omega = 2\pi\nu \quad (4.6)$$

$$\Delta\omega = 2\pi\Delta\nu \quad (4.7)$$

$$f(m) = i\Delta\nu\sqrt{2\pi} \sum_{j=-\frac{N}{2}}^{\frac{N}{2}-1} k(j) e^{-i2\pi j m \Delta\nu \Delta\tau} \quad (4.8)$$

Now we impose the condition of periodicity by requiring that

$$f(m+qN) = f(m) \quad (4.9)$$

where q is any integer. Substituting $m+qN$ for m in Equation (4.8) and

applying Equation (4.9) yields

$$e^{-i2\pi j q N c \Delta v \Delta \tau} = 1 \quad (4.10)$$

Therefore, $j q N c \Delta v \Delta \tau$ must be an integer. With $j q$ integral, we can require $N c \Delta v \Delta \tau$ to be unity. Then,

$$\Delta \tau = \frac{1}{N c \Delta v} \quad (4.11)$$

$$f(m) = i c \Delta v \sqrt{2\pi} \sum_{j=-\frac{N}{2}}^{\frac{N}{2}-1} k(j) e^{-i2\pi \left(\frac{m}{N}\right) j} \quad (4.12)$$

The only values of $k(j)$ known from real data are those $N/2$ points for $0 < j \leq N/2$. Since $k(j)$ is odd about zero, the values of $k(j)$ in that part of the sum over negative integers must be replaced by $-k(-j)$.

$$f(m) = i c \Delta v \sqrt{2\pi} \left\{ \sum_{j=-\frac{N}{2}}^{-1} [-k(-j)] e^{-i2\pi \left(\frac{m}{N}\right) j} + \sum_{j=0}^{\frac{N}{2}-1} k(j) e^{-i2\pi \left(\frac{m}{N}\right) j} \right\} \quad (4.13)$$

This can be transformed into a sum over positive integers by defining a new index.

$$l \equiv N + j \quad (4.14)$$

We substitute l for j in the first sum in Equation (4.13), then change

the dummy index l back to j.

$$f(m) = ic\Delta v\sqrt{2\pi} \left\{ \sum_{j=\frac{N}{2}}^{N-1} [-k(N-j)] e^{-i2\pi\left(\frac{m}{N}\right)j} + \sum_{j=0}^{\frac{N}{2}-1} k(j) e^{-i2\pi\left(\frac{m}{N}\right)j} \right\} \quad (4.15)$$

We define the function k'(j) as follows:

$$k'(j) \equiv \begin{cases} -k(N-j), & \frac{N}{2} \leq j < N \\ k(j), & 0 \leq j < \frac{N}{2} \end{cases} \quad (4.16)$$

Then we can combine the sums in Equation (4.15).

$$f(m) = ic\Delta v\sqrt{2\pi} \sum_{j=0}^{N-1} k'(j) e^{-i2\pi\left(\frac{m}{N}\right)j} \quad (4.17)$$

We can calculate $n(\omega)-1$ with this function $f(m)$. The integral in Equation (3.242) can be transformed into a discrete sum. For a particular

ω_0 ,

$$\omega_0 = l_0 \Delta \omega \quad (4.18)$$

$$n(\omega_0)-1 = \frac{1}{\sqrt{2\pi}} \sum_{m=\frac{N}{2}}^{-1} [-f(m)] e^{i(l_0 \Delta \omega)(m\Delta \tau)} \Delta \tau +$$

$$+ \frac{1}{\sqrt{2\pi}} \sum_{m=0}^{\frac{N}{2}-1} f(m) e^{i(1_0 \Delta \omega)(m \Delta \tau)} \Delta \tau \quad (4.19)$$

Now, using Equations (4.7) and (4.11), we obtain

$$n(\omega_0) - 1 = \frac{1}{Nc\Delta v\sqrt{2\pi}} \left\{ \sum_{m=-\frac{N}{2}}^{-1} [-f(m)] e^{i2\pi\left(\frac{1_0}{N}\right)m} + \sum_{m=0}^{\frac{N}{2}-1} f(m) e^{i2\pi\left(\frac{1_0}{N}\right)m} \right\} \quad (4.20)$$

As before, this can be written as a sum over positive integers.

$$n(\omega_0) - 1 = \frac{1}{Nc\Delta v\sqrt{2\pi}} \left\{ \sum_{m=\frac{N}{2}}^{N-1} [-f(m-N)] e^{i2\pi\left(\frac{1_0}{N}\right)m} + \sum_{m=0}^{\frac{N}{2}-1} f(m) e^{i2\pi\left(\frac{1_0}{N}\right)m} \right\} \quad (4.21)$$

We obtain $-f(m-N)$ and $f(m)$ from Equation (4.17) and substitute into Equation (4.21).

$$n(\omega_0) - 1 = \left(\frac{1}{N}\right) \left\{ \sum_{m=\frac{N}{2}}^{N-1} \left[-\sum_{j=0}^{N-1} k'(j) e^{-i2\pi\left(\frac{m}{N}\right)j} \right] e^{i2\pi\left(\frac{1_0}{N}\right)m} + \sum_{m=0}^{\frac{N}{2}-1} \left[\sum_{j=0}^{N-1} k'(j) e^{-i2\pi\left(\frac{m}{N}\right)j} \right] e^{i2\pi\left(\frac{1_0}{N}\right)m} \right\} \quad (4.22)$$

Now we define the following function:

$$A(m) \equiv \begin{cases} -\sum_{j=0}^{N-1} k'(j) e^{-i2\pi\left(\frac{m}{N}\right)j}, & \frac{N}{2} \leq m \leq N-1 \\ +\sum_{j=0}^{N-1} k'(j) e^{-i2\pi\left(\frac{m}{N}\right)j}, & 0 \leq m \leq \frac{N}{2}-1 \end{cases} \quad (4.23)$$

The result is

$$n(\omega_0) = 1 + \left(\frac{i}{N}\right) \sum_{m=0}^{N-1} A(m) e^{i2\pi\left(\frac{1_0}{N}\right)m} \quad (4.24)$$

As one can see by tracing back from $A(m)$ in Equation (4.23) through $k'(j)$ in Equation (4.16), this enables the numerical calculation of $n(\omega)$ directly from the $k(\omega)$ spectrum.

Calculations

Each of these sums was computed by arranging appropriate arrays and using the FAST FOURIER TRANSFORM algorithm on the AMDAHL 470 computer. The wave number spectrum was divided into $2^{17} = 131,072$ equal intervals. Since, for most $k(j)$'s, $j\Delta v$ fell between values of v for which $k(v)$ data were available, the program interpolated to obtain the appropriate $k(j)$. Then, the program calculated the $n(v)$ spectrum, yielding a value of $n(v)$ for each v for which a $k(v)$ value had been input. Again, the program interpolated between the values of $n(m\Delta v)$, obtained for integral m , to arrive at $n(v)$ for the appropriate wave numbers.

The calculation was first done over the range 0 to $5 \times 10^6 \text{ cm}^{-1}$. As is evident from the Kramers-Kronig integral, the greatest contribution

is obtained from those values of $k(v)$ for v closest to the wave number for which $n(v)$ is being calculated. Thus, as long as the wave number being investigated is not near an end point of the range of calculation, it should yield a reasonable result. The result should be less reliable as one approaches an endpoint. This was found to be true.

The density of the data points input was much greater at low wave numbers than at high wave numbers. As a result, even with 2^{17} intervals, those intervals at the low end included, and glossed over, many data points. The resolution was, in effect, reduced at the low end. The phenomenon is illustrated by Figure 5, which shows the region 0 to 50 cm^{-1} . The jagged line was calculated by dividing the region of 0 to $5 \times 10^5 \text{ cm}^{-1}$ into 2^{17} intervals. The data, then, had influence every 3.8 cm^{-1} . The smooth line was calculated by dividing the region of 0 to $5 \times 10^4 \text{ cm}^{-1}$ into 2^{17} intervals, resulting in effective data every 0.38 cm^{-1} , and increased resolution.

In order to overcome the problem of resolution, it was necessary to choose a smaller range for the calculation. Division of the larger range into more and smaller intervals would have required more computer memory than was available. So long as the region of interest was kept some distance from the endpoints of the range, the results were good. With the intention of combining the results into a composite spectrum, calculations were made over the following regions, illustrated by the indicated figures: 0 to $5 \times 10^6 \text{ cm}^{-1}$, Figure 6; 0 to $5 \times 10^5 \text{ cm}^{-1}$, Figure 7; 0 to $5 \times 10^4 \text{ cm}^{-1}$, Figure 8; 0 to $5 \times 10^3 \text{ cm}^{-1}$, Figure 9; 0 to $5 \times 10^2 \text{ cm}^{-1}$, Figure 10; 0 to $5 \times 10^1 \text{ cm}^{-1}$, Figure 11; 0 to $5 \times 10^0 \text{ cm}^{-1}$, Figure 12; 0 to $5 \times 10^{-1} \text{ cm}^{-1}$, Figure 13.

The phenomenon of deviation from good results as an endpoint is approached is illustrated by Figure 14. There, the values obtained from calculations over the two ranges 0 to 5×10^6 and 0 to $5 \times 10^5 \text{ cm}^{-1}$ are superimposed. It is apparent that, as the vicinity of $1 \times 10^5 \text{ cm}^{-1}$ is passed, the calculation over the smaller range gives values which begin to differ from the other values, the latter being presumably more accurate since they are farther from an endpoint. This is characteristic of most of the calculations. The results seem accurate up to approximately $1 \times 10^n \text{ cm}^{-1}$ for a calculation over the range of 0 to $5 \times 10^n \text{ cm}^{-1}$. It seems reasonable, then, to use that part of each spectrum not limited by poor resolution or by proximity to an endpoint.

Since the Fourier transform technique is most accurate in defining the shape of the curve, but less accurate in defining its absolute position, it was deemed desirable to fix the height of the curve at an appropriate point. This was done by calculating the difference between the number obtained at a particular point by the program and a reasonably certain number for the same point obtained from experimental or other data. This difference was then added to (or subtracted from) the values obtained for the entire spectrum. The point used to fix the first calculated spectrum, from 0 to $5 \times 10^6 \text{ cm}^{-1}$, was $\nu = 1.5802781 \times 10^4 \text{ cm}^{-1}$, for which the value assigned was $n = 1.33146$.

This same point was similarly fixed in the calculations over the ranges 0 to 5×10^5 and 0 to $5 \times 10^4 \text{ cm}^{-1}$. For calculations over the ranges 0 to 5×10^n for $n < 4$, a point was chosen in the graph of the calculated spectrum for 0 to $5 \times 10^{n+1} \text{ cm}^{-1}$ which seemed most likely to be

stable; that is, a point was chosen as far to the left (low wave number) as was reasonable, provided it was a region not undergoing violent oscillations, and hopefully provided it had a slope approximately zero.

Accordingly, the following points were fixed for the ranges specified: for 0 to $5 \times 10^3 \text{ cm}^{-1}$, $\nu = 2.103778 \times 10^3 \text{ cm}^{-1}$ was fixed at $n = 1.311148$; for 0 to $5 \times 10^2 \text{ cm}^{-1}$, $\nu = 1.064143 \times 10^2 \text{ cm}^{-1}$ was fixed at $n = 1.886343$; for 0 to $5 \times 10^1 \text{ cm}^{-1}$, $\nu = 8.332974 \text{ cm}^{-1}$ was fixed at $n = 2.481153$; for 0 to $5 \times 10^0 \text{ cm}^{-1}$, $\nu = 9.090965 \times 10^{-1} \text{ cm}^{-1}$ was fixed at $n = 6.094436$; for 0 to $5 \times 10^{-1} \text{ cm}^{-1}$, $\nu = 1.204759 \times 10^{-1} \text{ cm}^{-1}$ was fixed at $n = 8.676634$.

The process of joining the parts into one complete spectrum was accomplished by matching slopes and applying a weighted average. The goal was to obtain a smooth transition from one curve to the next in the region where the greater accuracy was presumed to shift from the first to the second curve.

No adjustment was necessary in several cases. The curve calculated for the range 0 to $5 \times 10^1 \text{ cm}^{-1}$ was joined to the curve for the range 0 to $5 \times 10^2 \text{ cm}^{-1}$ at the point fixed as described above, at $\nu = 8.332974 \text{ cm}^{-1}$. This is illustrated in Figure 18. The curve for the range 0 to $5 \times 10^2 \text{ cm}^{-1}$ was joined to that for 0 to $5 \times 10^3 \text{ cm}^{-1}$ at the point $\nu = 1.064143 \times 10^2 \text{ cm}^{-1}$, as illustrated in Figure 19. The curve for the range 0 to $5 \times 10^3 \text{ cm}^{-1}$ was joined to that for the range 0 to $5 \times 10^4 \text{ cm}^{-1}$ at $\nu = 2.103778 \times 10^3 \text{ cm}^{-1}$, as illustrated in Figure 20. The curve for the range 0 to $5 \times 10^5 \text{ cm}^{-1}$ was joined to that for 0 to $5 \times 10^6 \text{ cm}^{-1}$ at $\nu = 3.076097 \times 10^4 \text{ cm}^{-1}$, as shown in Figure 22.

Adjustments were necessary in four cases. For the low end, the

value for $n(\nu)$ calculated from the Cole-Cole equation was used to fix the single point $\nu=1 \times 10^{-3} \text{ cm}^{-1}$. The curve there was assumed to have nearly zero slope. Then, a smooth transition was created up to the slope at $\nu=7.144963 \times 10^{-2} \text{ cm}^{-1}$ as calculated from the curve for 0 to $5 \times 10^{-1} \text{ cm}^{-1}$. A weighted average was applied to assure that the values of $n(\nu)$ were as required at the endpoints, $n=8.8486$ at $1 \times 10^{-3} \text{ cm}^{-1}$ (from the Cole-Cole equation) and $n=8.7978$ at $7.144963 \times 10^{-2} \text{ cm}^{-1}$ (from the calculation over the range 0 to $5 \times 10^{-1} \text{ cm}^{-1}$). The result is illustrated by Figure 15. The curves for the ranges 0 to 5×10^{-1} and 0 to $5 \times 10^0 \text{ cm}^{-1}$ were connected by a similar procedure, the difference being that the slope at the lower end was calculated from the data just as was the slope at the higher end. The transition is illustrated by Figure 16. The curves for the ranges 0 to 5×10^0 and 0 to $5 \times 10^1 \text{ cm}^{-1}$ were connected by the same process, as shown in Figure 17. The curves for the ranges 0 to 5×10^4 and 0 to $5 \times 10^5 \text{ cm}^{-1}$ were connected by applying only a weighted average since this resulted in a smooth transition and left the fixed point, $\nu=1.580278 \times 10^4 \text{ cm}^{-1}$, intact. This is illustrated by Figure 21.

The final $n(\nu)$ spectrum is presented in Chapter V in both graphical and tabular form.

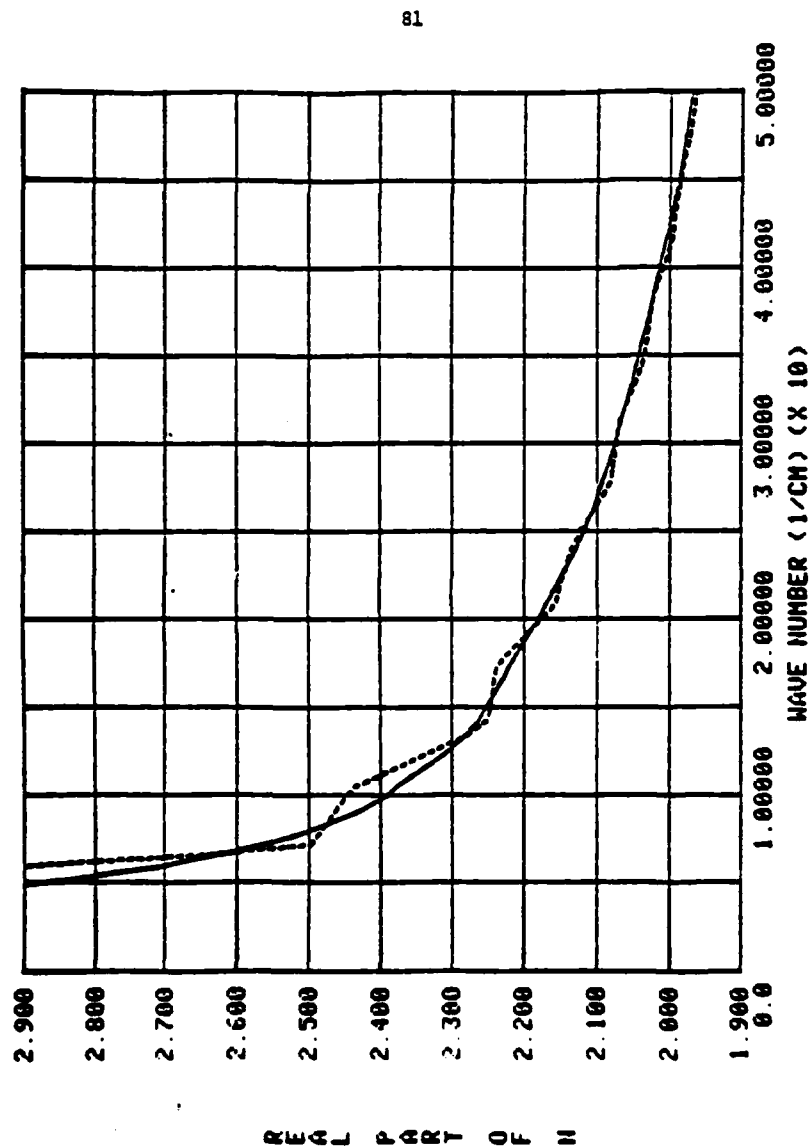


Fig. 5. An illustration of the increased resolution obtained by reducing the range of calculation. The solid line is the curve for $n(\nu)$ obtained by calculation over the range 0 to $5 \times 10^4 \text{ cm}^{-1}$. The dashed line is the curve obtained by calculation over the range 0 to $5 \times 10^5 \text{ cm}^{-1}$. The latter curve shows decreased resolution.

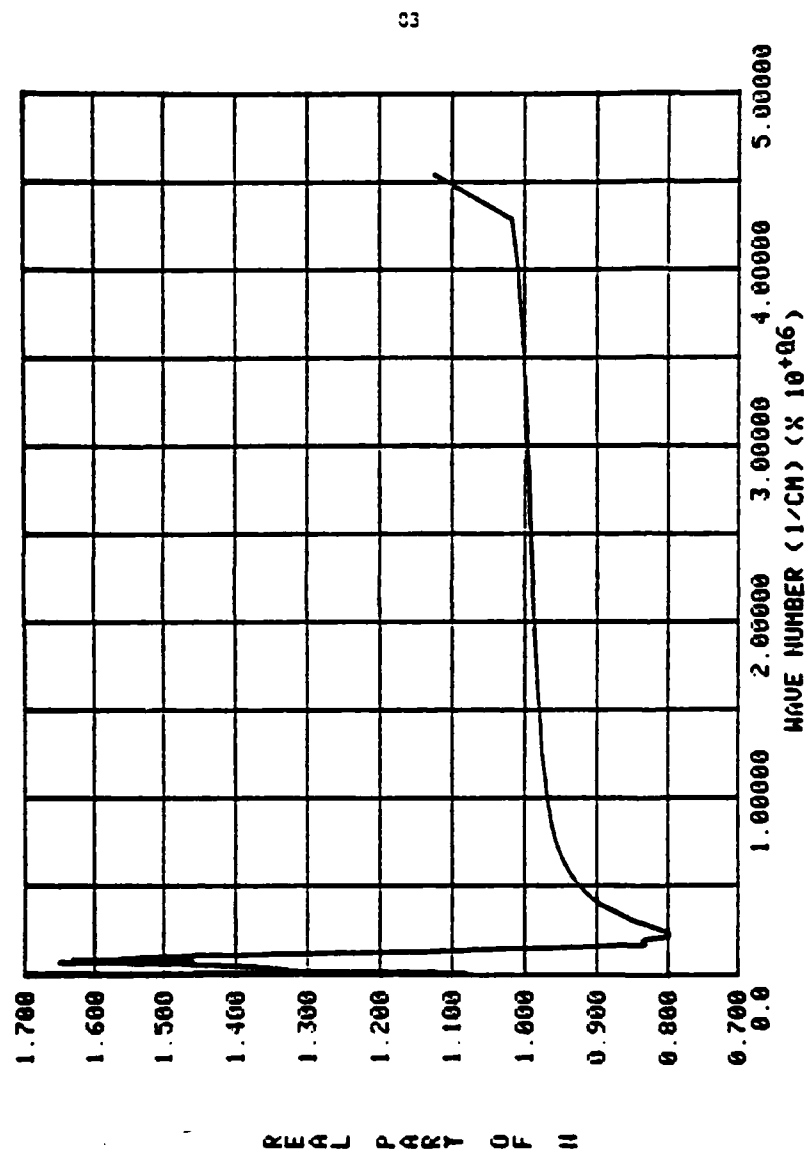


Fig. 6. The spectrum calculated for the range 0 to $5 \times 10^6 \text{ cm}^{-1}$. The inaccuracy at the right end of the curve (primarily due to the last datum point) is a result of proximity to the endpoint of the range of calculation. This is characteristic of the results illustrated in Figures 7 through 13 also. The phenomenon is discussed in the text.

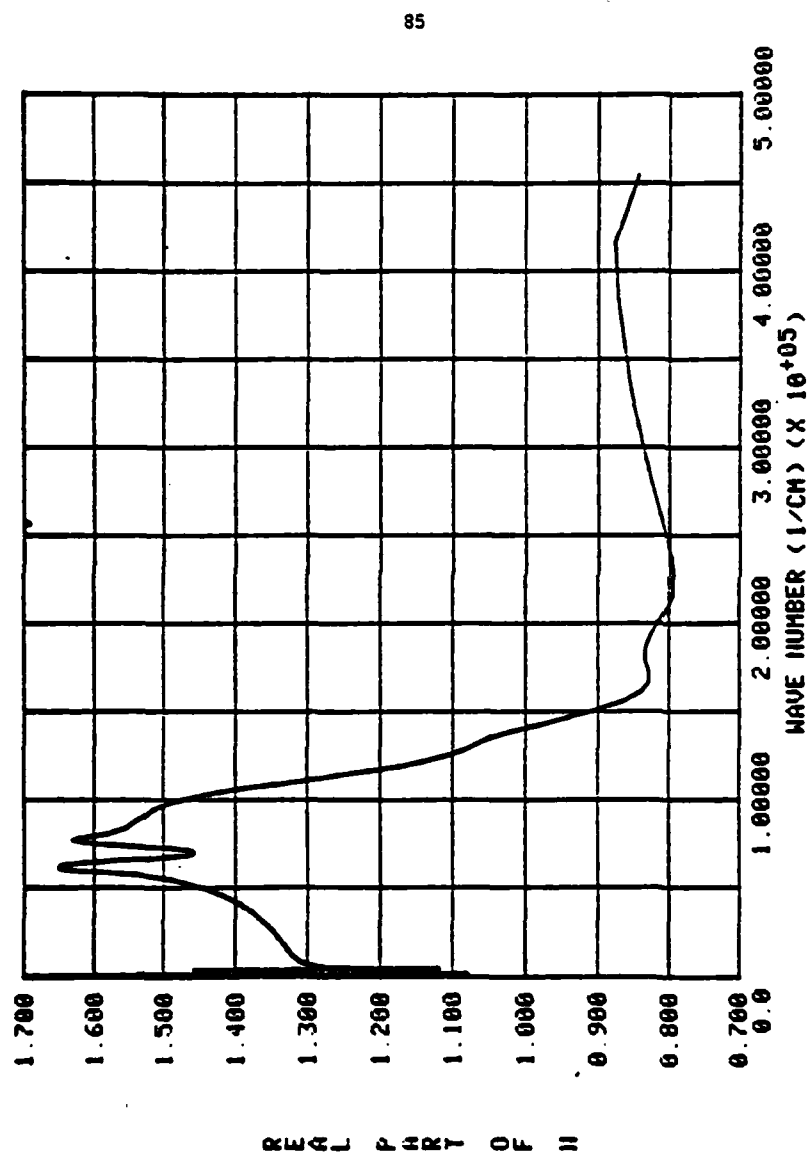


Fig. 7. The spectrum calculated for the range 0 to $5 \times 10^5 \text{ cm}^{-1}$.

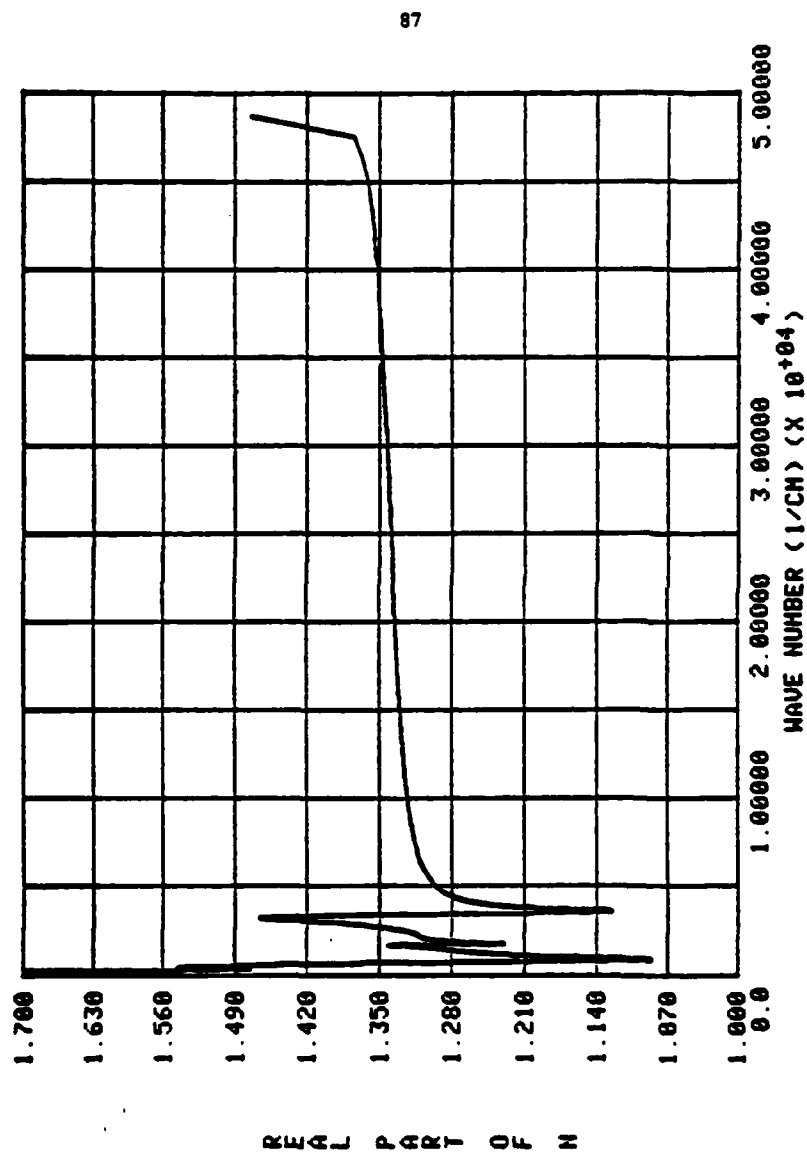


Fig. 8. The spectrum calculated for the range 0 to $5 \times 10^4 \text{ cm}^{-1}$.

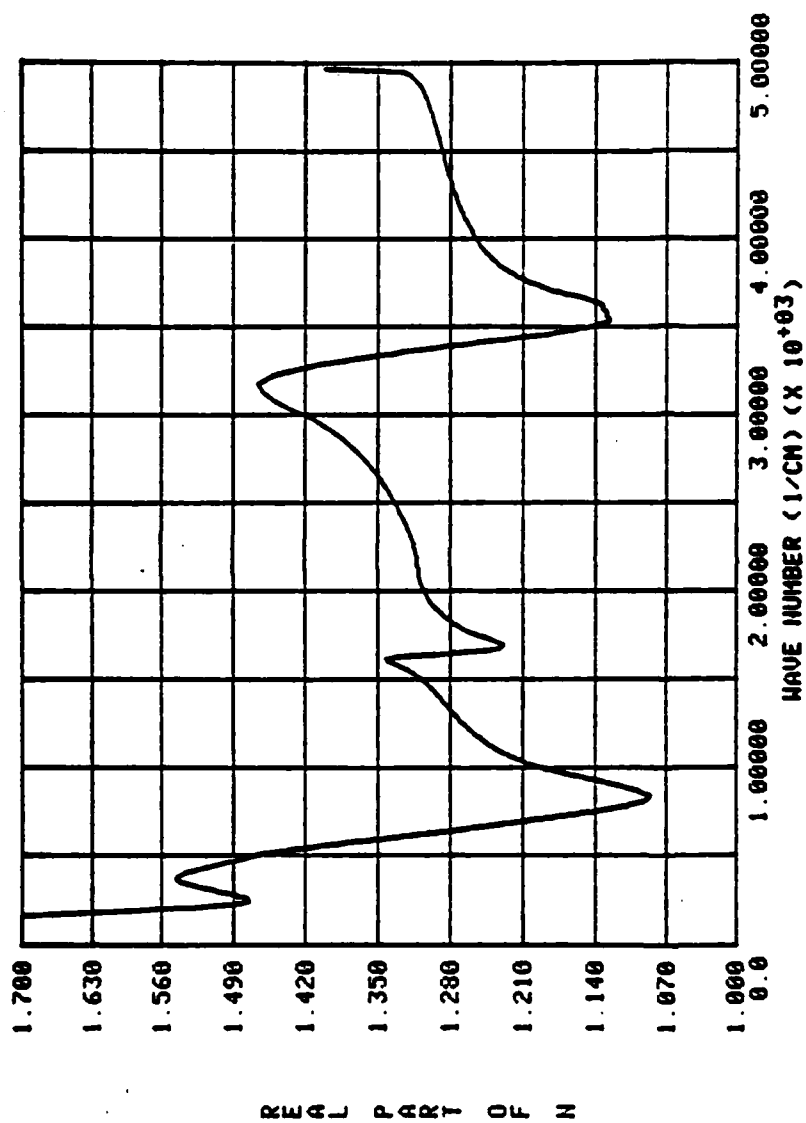


Fig. 9. The spectrum calculated for the range 0 to $5 \times 10^3 \text{ cm}^{-1}$.

91

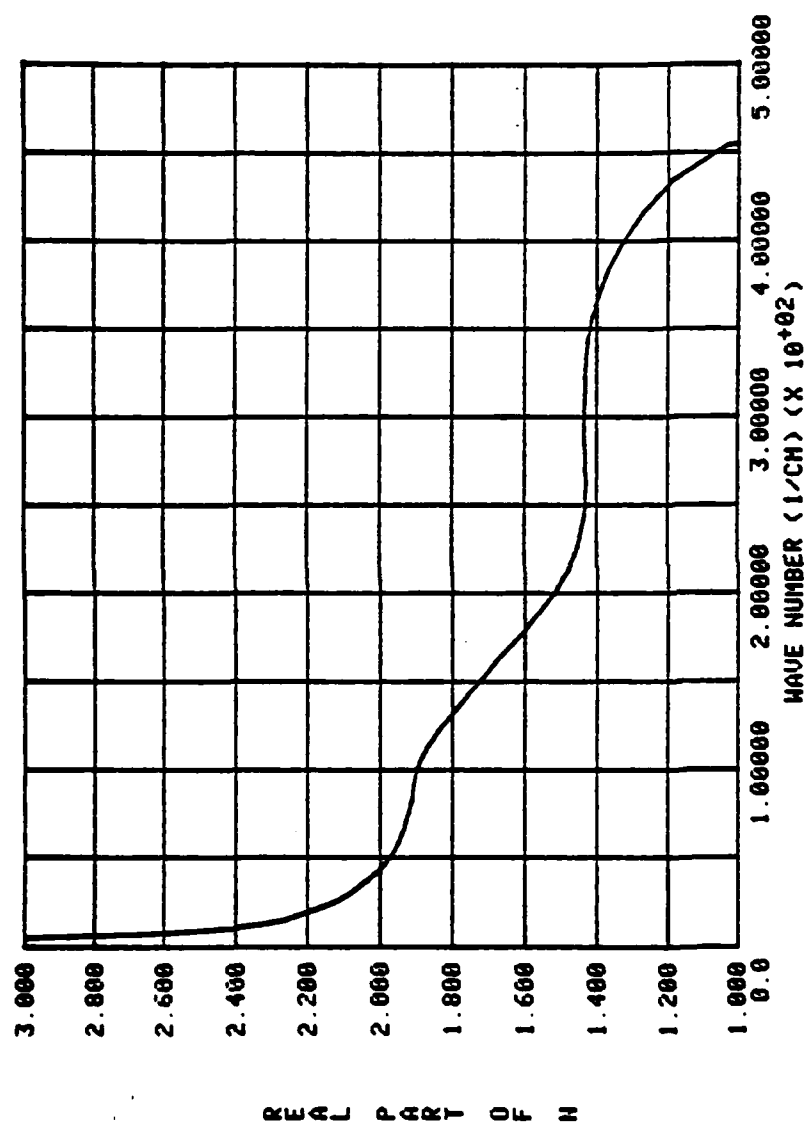


Fig. 10. The spectrum calculated for the range 0 to $5 \times 10^2 \text{ cm}^{-1}$.

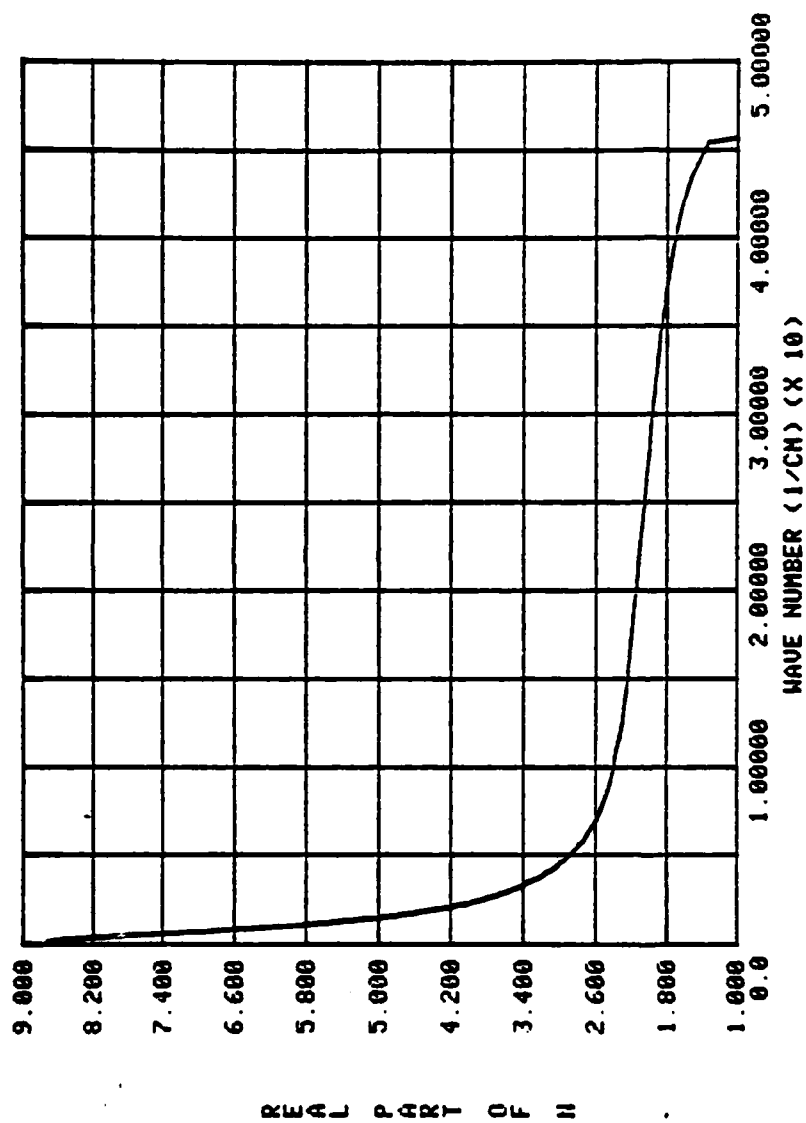


Fig. 11. The spectrum calculated for the range 0 to $5 \times 10^1 \text{ cm}^{-1}$.

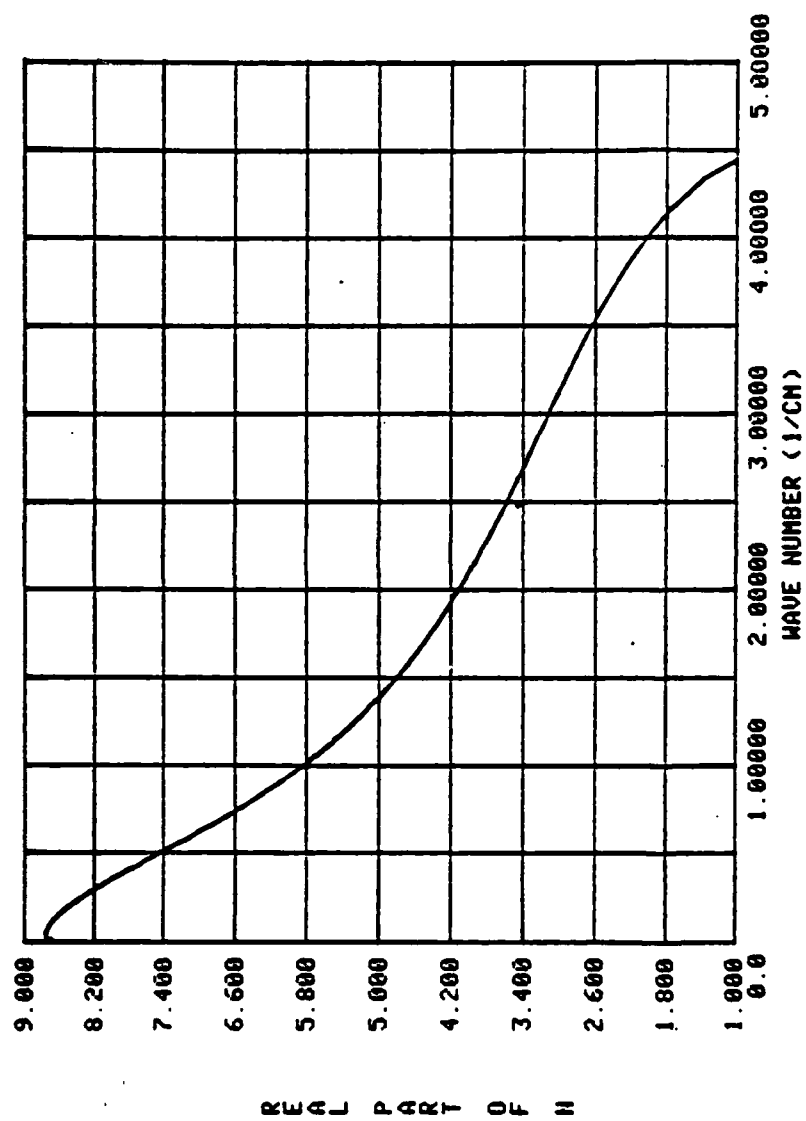


Fig. 12. The spectrum calculated for the range 0 to 5 cm^{-1} .

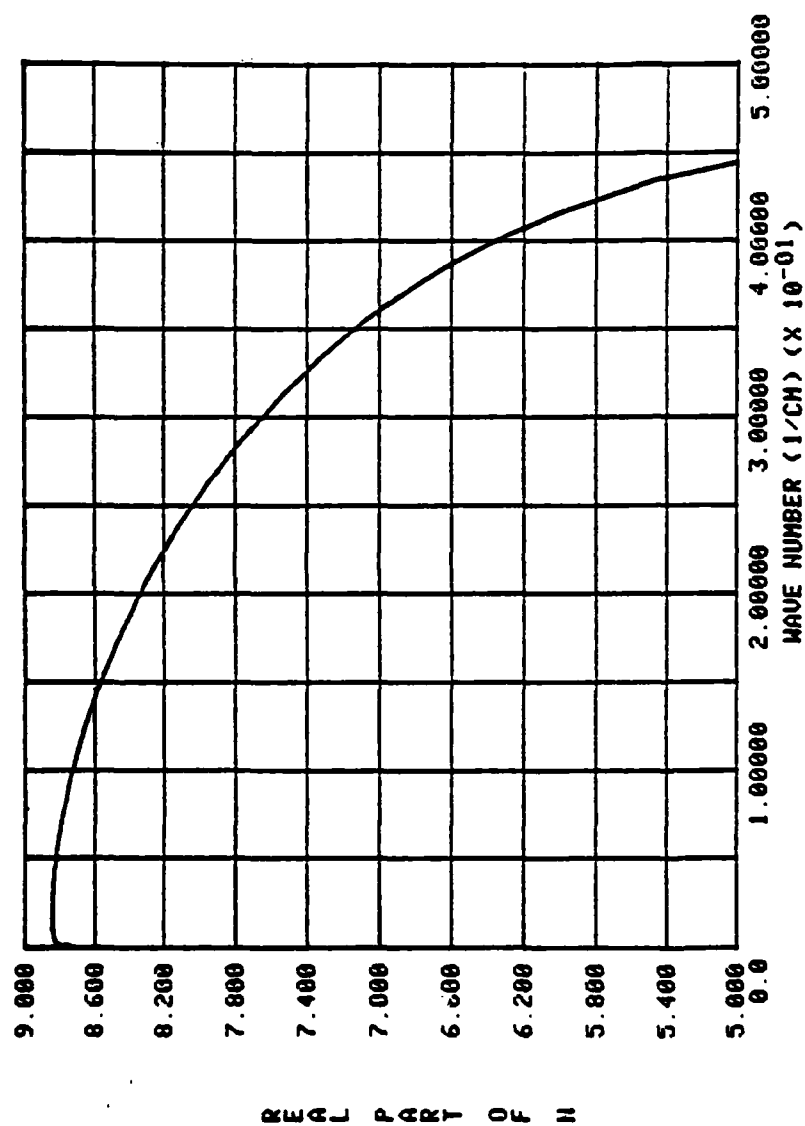


Fig. 13. The spectrum calculated for the range 0 to $5 \times 10^{-1} \text{ cm}^{-1}$.

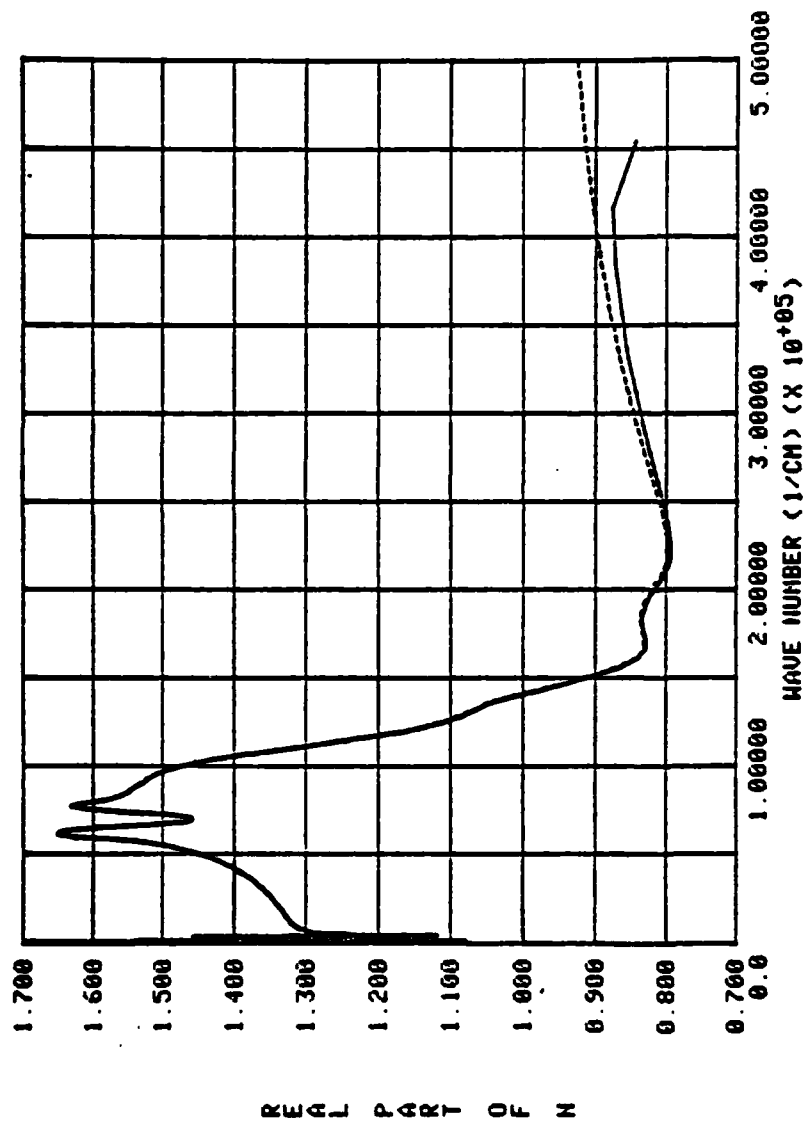


Fig. 14. An illustration of inaccuracy as an endpoint is approached.

The dashed line is $n(v)$ as obtained by calculation over the range 0 to $5 \times 10^6 \text{ cm}^{-1}$. The solid line was obtained by calculation over the smaller range 0 to $5 \times 10^5 \text{ cm}^{-1}$. The latter deviates from the dashed line as it approaches the right endpoint of the range of calculation.

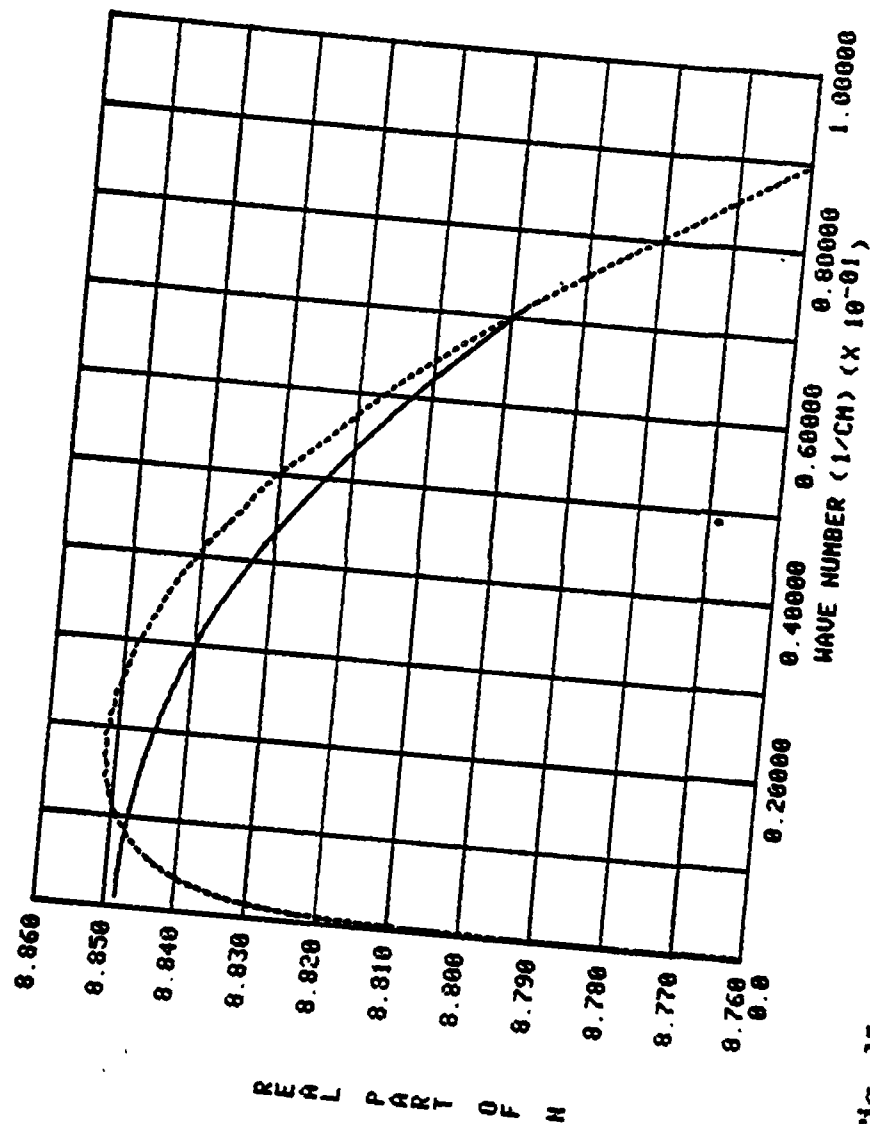


Fig. 15. Fitting low frequency results. The dashed line is $n(\nu)$ as obtained by calculation over the range 0 to $5 \times 10^{-1} \text{ cm}^{-1}$. The solid line is that calculated to connect the value of $n(\nu)$ at $1 \times 10^{-3} \text{ cm}^{-1}$ (as obtained from the Cole-Cole equation) with the dashed curve in a smooth manner. The procedure is described in the text.

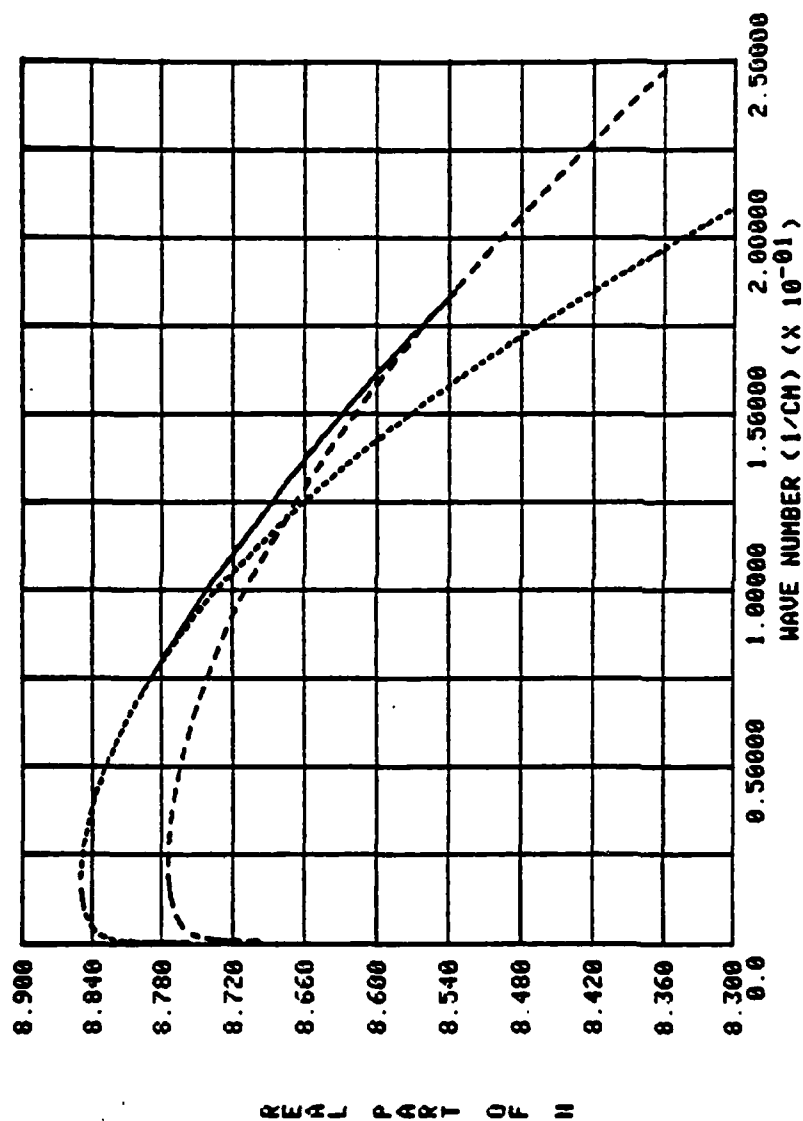


Fig. 16. The transition in the region of 10^{-1} cm^{-1} . The short dashes are $n(v)$ as obtained by calculation over the range 0 to $5 \times 10^{-1} \text{ cm}^{-1}$. The long dashes are $n(v)$ as calculated over the range 0 to 5 cm^{-1} . The solid curve is the calculated transition between the two.

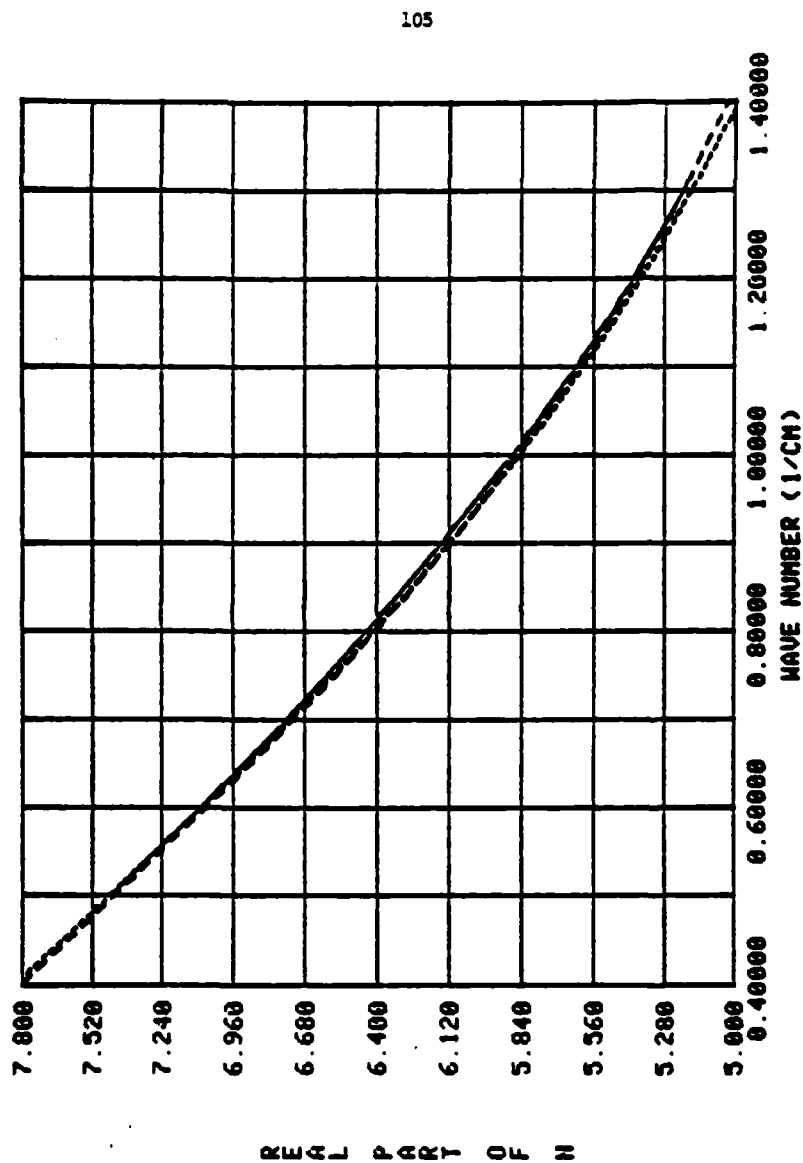


Fig. 17. The transition in the region of 1 cm^{-1} . The short dashes are $n(\nu)$ as obtained by calculation over the range 0 to 5 cm^{-1} . The long dashes are $n(\nu)$ as calculated over the range 0 to $5 \times 10^1 \text{ cm}^{-1}$. The solid curve is the calculated transition between the two.

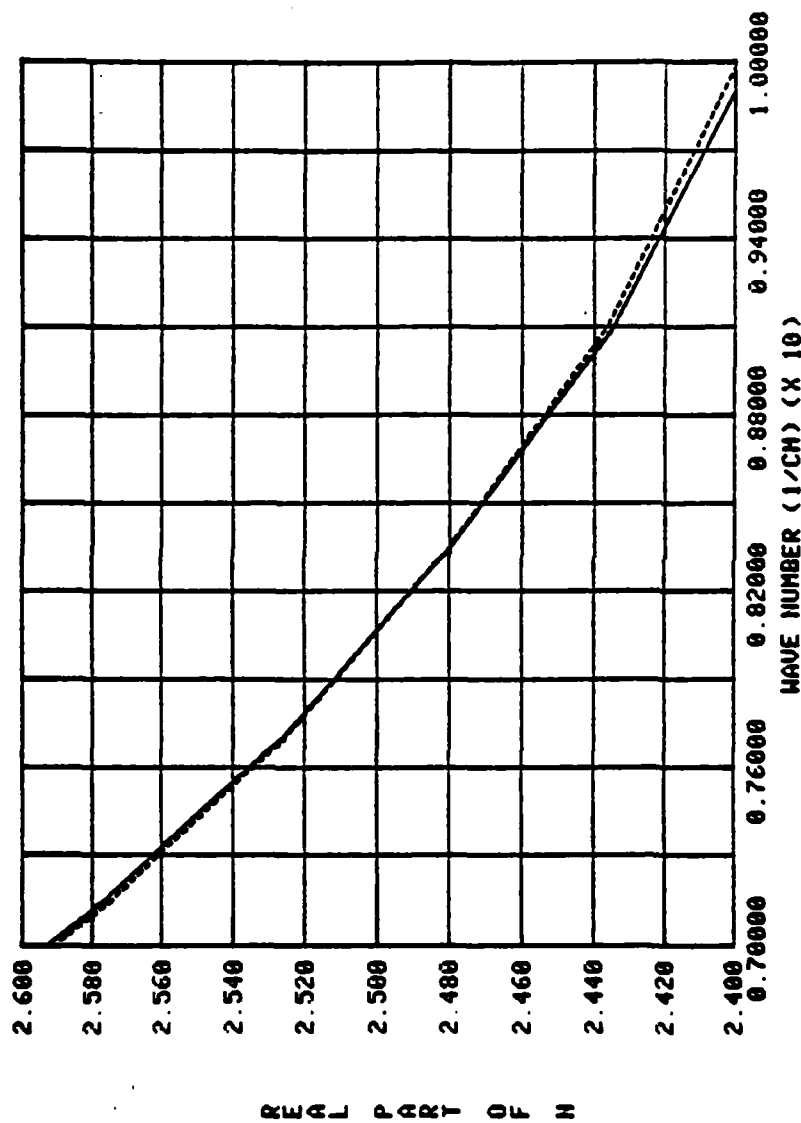


Fig. 18. The transition in the region of 10 cm^{-1} . The solid line is $n(\nu)$ as obtained by calculation over the range 0 to $5 \times 10^1 \text{ cm}^{-1}$. The dashed line is $n(\nu)$ as calculated over the range 0 to $5 \times 10^2 \text{ cm}^{-1}$. The two curves were connected at their point of intersection.

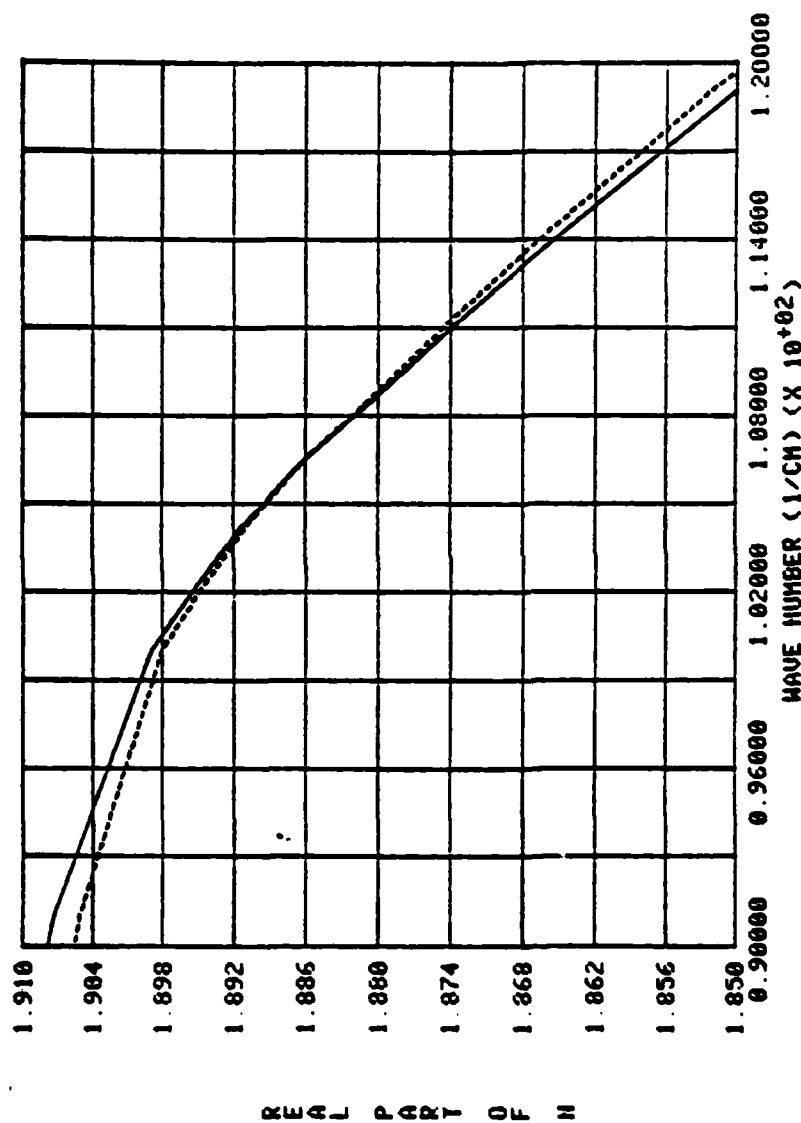


Fig. 19. The transition in the region of 10^2 cm^{-1} . The solid line is $n(\nu)$ as obtained by calculation over the range 0 to $5 \times 10^2 \text{ cm}^{-1}$. The dashed line is $n(\nu)$ as calculated over the range 0 to $5 \times 10^3 \text{ cm}^{-1}$. The two curves were connected at their point of intersection

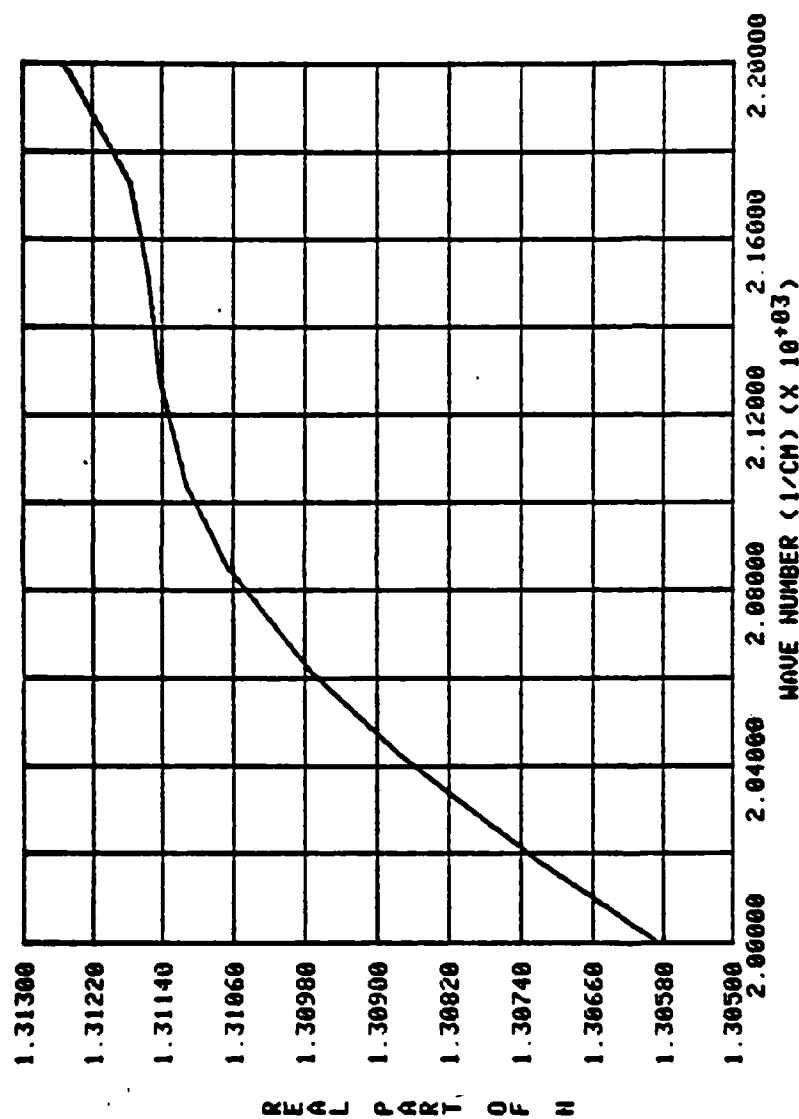


Fig. 20. The transition in the region of 10^3 cm^{-1} . The solid line is $n(\nu)$ as obtained by calculation over the range 0 to $5 \times 10^3 \text{ cm}^{-1}$. The dashed line is $n(\nu)$ as calculated over the range 0 to $5 \times 10^4 \text{ cm}^{-1}$. The two curves were connected at their point of intersection. The curves are so close together in this region that they are difficult to distinguish.

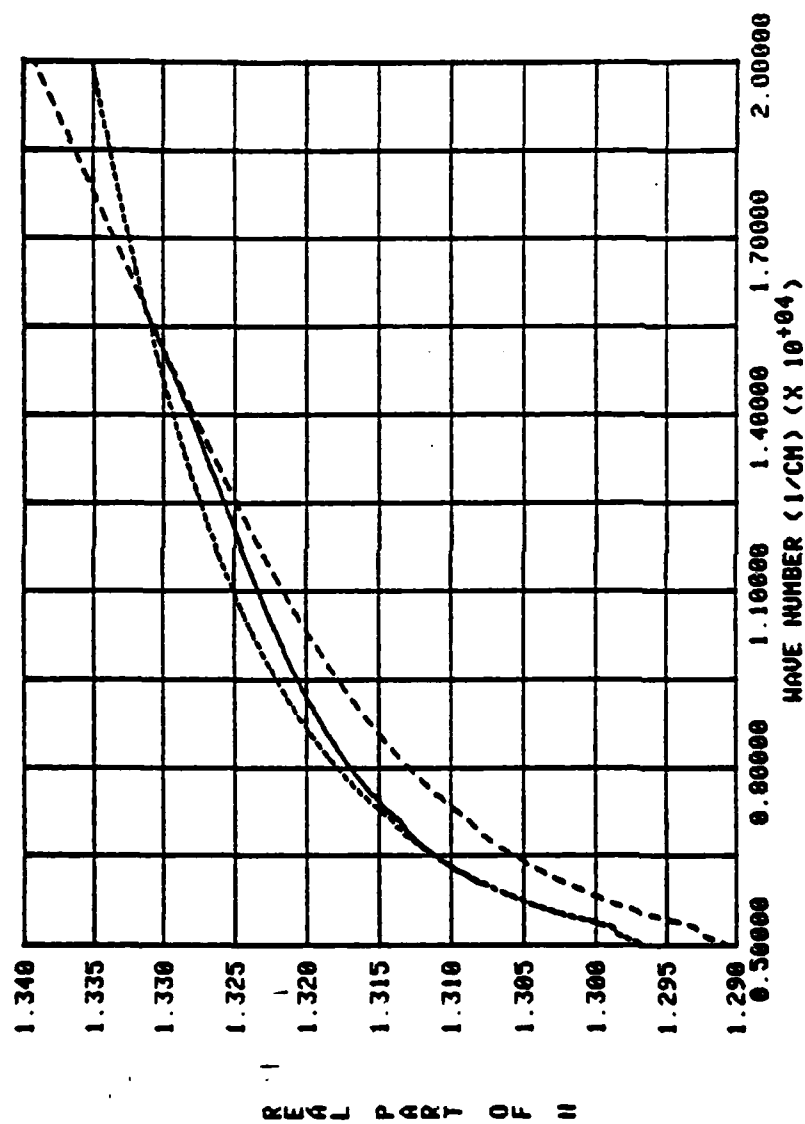


Fig. 21. The transition in the region of 10^4 cm^{-1} . The short dashes are $n(\nu)$ as obtained by calculation over the range 0 to $5 \times 10^4 \text{ cm}^{-1}$. The long dashes are $n(\nu)$ as calculated over the range 0 to $5 \times 10^5 \text{ cm}^{-1}$. The solid line is the calculated transition between the two.

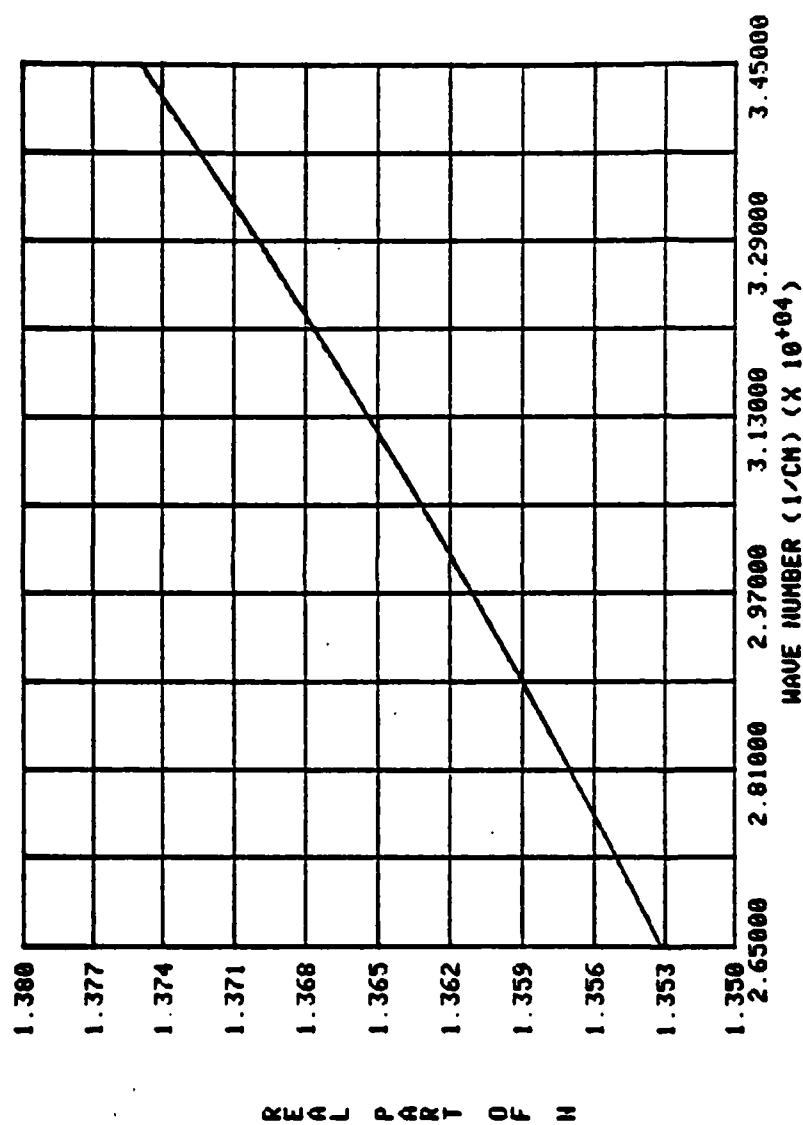


Fig. 22. The transition in the region of 10^5 cm^{-1} . The solid line is $n(\nu)$ as obtained by calculation over the range 0 to $5 \times 10^5 \text{ cm}^{-1}$. The dashed line is $n(\nu)$ as calculated over the range 0 to $5 \times 10^6 \text{ cm}^{-1}$. The curves are so close together in this region that they are difficult to distinguish.

CHAPTER V

RESULTS

The final spectrum was obtained by combination of the several calculated curves as described in Chapter IV. To present only data of reasonably certain accuracy, values are not reported for the extreme endpoint regions of less than $1 \times 10^{-3} \text{ cm}^{-1}$ and greater than $1 \times 10^6 \text{ cm}^{-1}$. The $n(\nu)$ spectrum is shown in Figures 23 through 30. The values of both the real and imaginary parts of $N(\nu)$ (n and k) are presented in Table 1, immediately below. These results are discussed in Chapter VI.

TABLE 1*

THE COMPLEX REFRACTIVE INDEX OF WATER

Wave Number (cm^{-1})	n	k
1.0000000D-03	8.848600	6.9309081D-03
1.0092529D-03	8.848600	7.0111643D-03
1.0209395D-03	8.848600	7.0597634D-03
1.0303861D-03	8.848600	7.1415116D-03
1.0423174D-03	8.848600	7.2075912D-03
1.0519619D-03	8.848600	7.2910511D-03
1.0641430D-03	8.848600	7.3585144D-03
1.0764652D-03	8.848599	7.4437220D-03
1.0864256D-03	8.848599	7.5299162D-03
1.0990058D-03	8.848599	7.5995897D-03
1.1117317D-03	8.848599	7.6875888D-03
1.1246050D-03	8.848599	7.7587211D-03
1.1376273D-03	8.848599	7.8485629D-03
1.1481536D-03	8.848599	7.9577473D-03
1.1641260D-03	8.848599	8.0313794D-03

TABLE 1-Continued

Wave Number (cm^{-1})	n	k
1.1776060D-03	8.848598	8.1243784D-03
1.1912420D-03	8.848598	8.2184543D-03
1.2050359D-03	8.848598	8.3327844D-03
1.2189896D-03	8.848598	8.4292735D-03
1.2359474D-03	8.848598	8.5268798D-03
1.2502590D-03	8.848598	8.6256165D-03
1.2647363D-03	8.848598	8.7456107D-03
1.2823306D-03	8.848597	8.8468801D-03
1.3001696D-03	8.848597	8.9493222D-03
1.3152248D-03	8.848597	9.0947370D-03
1.3335214D-03	8.848597	9.2000491D-03
1.3520726D-03	8.848596	9.3280345D-03
1.3708818D-03	8.848596	9.4578004D-03
1.3899526D-03	8.848596	9.5673165D-03
1.4092888D-03	8.848596	9.7004112D-03
1.4288940D-03	8.848595	9.8580302D-03
1.4487719D-03	8.848595	9.9951690D-03
1.4689263D-03	8.848595	1.0157577D-02
1.4927944D-03	8.848594	1.0298883D-02
1.5135612D-03	8.848594	1.0442155D-02
1.5381546D-03	8.848594	1.0611827D-02
1.5631476D-03	8.848593	1.0759452D-02
1.5885467D-03	8.848593	1.0909131D-02
1.6143586D-03	8.848592	1.1111947D-02
1.6405898D-03	8.848592	1.1292501D-02
1.6672472D-03	8.848591	1.1475990D-02
1.6943378D-03	8.848591	1.1662459D-02
1.7258379D-03	8.848590	1.1851959D-02
1.7538805D-03	8.848589	1.2072303D-02
1.7864876D-03	8.848589	1.2268463D-02
1.8197009D-03	8.848588	1.2496550D-02
1.8535316D-03	8.848587	1.2728879D-02
1.8879913D-03	8.848586	1.2965526D-02
1.9230917D-03	8.848585	1.3206573D-02
1.9588447D-03	8.848585	1.3483112D-02
1.9998619D-03	8.848584	1.3733782D-02
2.0417379D-03	8.848582	1.3989112D-02
2.0844909D-03	8.848581	1.4282037D-02
2.1281390D-03	8.848580	1.4581095D-02
2.1727012D-03	8.848579	1.4920732D-02
2.2233099D-03	8.848577	1.5233165D-02
2.2750974D-03	8.848576	1.5587991D-02
2.3280913D-03	8.848574	1.5914395D-02
2.3823195D-03	8.848572	1.6322630D-02

TABLE 1-Continued

Wave Number (cm^{-1})	n	k
2.4378108D-03	8.848570	1.6702833D-02
2.5003454D-03	8.848568	1.7131293D-02
2.5644840D-03	8.848566	1.7570744D-02
2.6302680D-03	8.848563	1.8021467D-02
2.7039584D-03	8.848560	1.8483752D-02
2.7797133D-03	8.848557	1.9001599D-02
2.8575905D-03	8.848554	1.9533953D-02
2.9444216D-03	8.848550	2.0081222D-02
3.0269134D-03	8.848546	2.0739111D-02
3.1260794D-03	8.848541	2.1320144D-02
3.2284941D-03	8.848536	2.2018622D-02
3.3342641D-03	8.848531	2.2739983D-02
3.4514374D-03	8.848524	2.3484977D-02
3.5727284D-03	8.848518	2.4366331D-02
3.7068072D-03	8.848510	2.5222617D-02
3.8459178D-03	8.848501	2.6229508D-02
3.9994475D-03	8.848491	2.7213860D-02
4.1686938D-03	8.848480	2.8365480D-02
4.3451022D-03	8.848467	2.9565835D-02
4.5498806D-03	8.848452	3.0888025D-02
4.7643099D-03	8.848435	3.2343733D-02
5.0003453D-03	8.848415	3.3946120D-02
5.2601727D-03	8.848392	3.5710024D-02
5.5590426D-03	8.848364	3.7652181D-02
5.8884366D-03	8.848330	3.9791485D-02
6.2517269D-03	8.848291	4.2343831D-02
6.6680677D-03	8.848243	4.5059892D-02
7.1449633D-03	8.848183	4.8282544D-02
7.6913044D-03	8.848109	5.1974479D-02
8.3368118D-03	8.848013	5.6206966D-02
9.0991327D-03	8.847889	6.1205457D-02
1.0000000D-02	8.847727	6.7265154D-02
1.0092529D-02	8.847710	6.8044048D-02
1.0209395D-02	8.847688	6.8515707D-02
1.0303861D-02	8.847671	6.9309081D-02
1.0423174D-02	8.847648	6.9950391D-02
1.0519619D-02	8.847630	7.0760378D-02
1.0641430D-02	8.847606	7.1415116D-02
1.0764652D-02	8.847582	7.2242064D-02
1.0864256D-02	8.847563	7.3078587D-02
1.0990058D-02	8.847537	7.3754775D-02
1.1117317D-02	8.847512	7.4608815D-02
1.1246050D-02	8.847485	7.5472745D-02
1.1376273D-02	8.847459	7.6171085D-02

TABLE 1-Continued

Wave Number (cm^{-1})	n	k
1.1481536D-02	8.847437	7.7230731D-02
1.1641260D-02	8.847403	7.7945338D-02
1.1776060D-02	8.847374	7.8847902D-02
1.1912420D-02	8.847344	7.9760918D-02
1.2050359D-02	8.847314	8.0870503D-02
1.2189896D-02	8.847283	8.1806939D-02
1.2359474D-02	8.847244	8.2754219D-02
1.2502590D-02	8.847212	8.3905445D-02
1.2647363D-02	8.847178	8.4877024D-02
1.2823306D-02	8.847137	8.5859854D-02
1.3001696D-02	8.847094	8.7054283D-02
1.3152248D-02	8.847058	8.8265329D-02
1.3335214D-02	8.847013	8.9287393D-02
1.3520726D-02	8.846967	9.0529505D-02
1.3708818D-02	8.846920	9.1788895D-02
1.3899526D-02	8.846871	9.2851761D-02
1.4092888D-02	8.846821	9.4360480D-02
1.4288940D-02	8.846769	9.5673165D-02
1.4487719D-02	8.846716	9.7004112D-02
1.4689263D-02	8.846662	9.8580302D-02
1.4927944D-02	8.846596	9.9951690D-02
1.5135612D-02	8.846538	1.0134216D-01
1.5381546D-02	8.846468	1.0298883D-01
1.5631476D-02	8.846396	1.0442155D-01
1.5885467D-02	8.846321	1.0611827D-01
1.6143586D-02	8.846244	1.0759452D-01
1.6405898D-02	8.846164	1.0934279D-01
1.6672472D-02	8.846082	1.1137562D-01
1.6943378D-02	8.845997	1.1318533D-01
1.7258379D-02	8.845896	1.1502444D-01
1.7538805D-02	8.845804	1.1716291D-01
1.7864876D-02	8.845696	1.1906665D-01
1.8197009D-02	8.845583	1.2128027D-01
1.8535316D-02	8.845467	1.2325091D-01
1.8879913D-02	8.845345	1.2583172D-01
1.9230917D-02	8.845220	1.2817111D-01
1.9588447D-02	8.845089	1.3085495D-01
1.9998619D-02	8.844936	1.3328772D-01
2.0417379D-02	8.844776	1.3576573D-01
2.0844909D-02	8.844609	1.3860859D-01
2.1281390D-02	8.844436	1.4151098D-01
2.1727012D-02	8.844254	1.4480720D-01
2.2233099D-02	8.844044	1.4783938D-01
2.2750974D-02	8.843823	1.5093506D-01

TABLE 1-Continued

Wave Number (cm ⁻¹)	n	k
2.3280913D-02	8.843591	1.5445079D-01
2.3823195D-02	8.843349	1.5804841D-01
2.4378108D-02	8.843095	1.6210266D-01
2.5003454D-02	8.842801	1.6587852D-01
2.5644840D-02	8.842491	1.7013362D-01
2.6302680D-02	8.842166	1.7449788D-01
2.7039584D-02	8.841790	1.7897408D-01
2.7797133D-02	8.841394	1.8398827D-01
2.8575905D-02	8.840974	1.8914294D-01
2.9444216D-02	8.840491	1.9444203D-01
3.0269134D-02	8.840020	2.0081222D-01
3.1260794D-02	8.839434	2.0643824D-01
3.2284941D-02	8.838809	2.1320144D-01
3.3342641D-02	8.838141	2.2018622D-01
3.4514374D-02	8.837375	2.2739983D-01
3.5727284D-02	8.836475	2.3560806D-01
3.7068072D-02	8.835449	2.4411257D-01
3.8459178D-02	8.834348	2.5350711D-01
3.9994475D-02	8.833091	2.6344511D-01
4.1686938D-02	8.831656	2.7408808D-01
4.3451022D-02	8.830103	2.8595003D-01
4.5498806D-02	8.828230	2.9832534D-01
4.7643099D-02	8.826184	3.1231306D-01
5.0003453D-02	8.823834	3.2771034D-01
5.2601727D-02	8.821129	3.4481817D-01
5.5590426D-02	8.817867	3.6298622D-01
5.8884366D-02	8.814082	3.8369854D-01
6.2517269D-02	8.809677	4.0727724D-01
6.6680677D-02	8.804337	4.3370072D-01
7.1449633D-02	8.797836	4.6364987D-01
7.6913044D-02	8.788091	4.9829915D-01
8.3368118D-02	8.776133	5.3800975D-01
9.0991327D-02	8.761392	5.8450757D-01
1.0000000D-01	8.743107	6.4089981D-01
1.0101829D-01	8.741029	6.4705343D-01
1.0204694D-01	8.738919	6.5335639D-01
1.0308607D-01	8.736776	6.5984229D-01
1.0415977D-01	8.734549	6.6634653D-01
1.0526888D-01	8.732236	6.7296138D-01
1.0638930D-01	8.729884	6.7975145D-01
1.0752266D-01	8.727494	6.8672071D-01
1.0869261D-01	8.725011	6.9382532D-01
1.0990058D-01	8.722432	7.0093887D-01
1.1112199D-01	8.719808	7.0833083D-01

TABLE 1-Continued

Wave Number (cm ⁻¹)	n	k
1.1235697D-01	8.717139	7.1591612D-01
1.1363183D-01	8.714366	7.2363597D-01
1.1494762D-01	8.711486	7.3137505D-01
1.1627866D-01	8.708553	7.3940119D-01
1.1765219D-01	8.705507	7.4756704D-01
1.1904194D-01	8.702404	7.5603194D-01
1.2047585D-01	8.699181	7.6453988D-01
1.2195511D-01	8.695941	7.7326819D-01
1.2345253D-01	8.692637	7.8222221D-01
1.2499712D-01	8.689204	7.9142569D-01
1.2659017D-01	8.685638	8.0073746D-01
1.2820353D-01	8.681999	8.1038267D-01
1.2986736D-01	8.678217	8.2014406D-01
1.3158307D-01	8.674287	8.3021417D-01
1.3332144D-01	8.670273	8.4060147D-01
1.3514501D-01	8.666029	8.5092277D-01
1.3699351D-01	8.661691	8.6176756D-01
1.3889928D-01	8.657181	8.7275057D-01
1.4083156D-01	8.652568	8.8448433D-01
1.4285650D-01	8.647693	8.9596314D-01
1.4494392D-01	8.642623	9.0779993D-01
1.4706184D-01	8.637431	9.2021677D-01
1.4924507D-01	8.632030	9.3280345D-01
1.5153048D-01	8.626323	9.4556229D-01
1.5385089D-01	8.620473	9.5893715D-01
1.5624280D-01	8.614382	9.7272515D-01
1.5874498D-01	8.607948	9.8671139D-01
1.6128724D-01	8.601342	1.0011292D+00
1.6394569D-01	8.594362	1.0159917D+00
1.6664796D-01	8.587191	1.0310747D+00
1.6947280D-01	8.579613	1.0471048D+00
1.7242491D-01	8.571605	1.0628945D+00
1.7542844D-01	8.563363	1.0801651D+00
1.7856651D-01	8.554652	1.0969584D+00
1.8180256D-01	8.545560	1.1150392D+00
1.8518252D-01	8.535947	1.1328963D+00
1.8866876D-01	8.526995	1.1520999D+00
1.9230917D-01	8.517490	1.1710897D+00
1.9606497D-01	8.507814	1.1912150D+00
1.9998619D-01	8.497290	1.2119652D+00
2.0407979D-01	8.486470	1.2330768D+00
2.0835312D-01	8.474673	1.2560015D+00
2.1276491D-01	8.462521	1.2778802D+00
2.1737020D-01	8.449912	1.3022373D+00

TABLE 1-Continued

Wave Number (cm ⁻¹)	n	k
2.2222863D-01	8.435660	1.3270587D+00
2.2724796D-01	8.420858	1.3520419D+00
2.3254125D-01	8.405156	1.3781299D+00
2.3812226D-01	8.389151	1.4047212D+00
2.4389337D-01	8.371979	1.4341354D+00
2.4997697D-01	8.352700	1.4631544D+00
2.5638936D-01	8.332788	1.4931043D+00
2.6314796D-01	8.311297	1.5250713D+00
2.7027134D-01	8.288448	1.5570055D+00
2.7777938D-01	8.264599	1.5910731D+00
2.8569326D-01	8.238281	1.6270097D+00
2.9410337D-01	8.209818	1.6629919D+00
3.0304003D-01	8.179843	1.7009445D+00
3.1253596D-01	8.147128	1.7409654D+00
3.2255219D-01	8.112180	1.7811075D+00
3.3334965D-01	8.074469	1.8238543D+00
3.4482600D-01	8.033791	1.8680571D+00
3.5710835D-01	7.989355	1.9142125D+00
3.7033947D-01	7.941322	1.9610567D+00
3.8459178D-01	7.889643	2.0108985D+00
4.0003685D-01	7.831158	2.0639071D+00
4.1667745D-01	7.768902	2.1134411D+00
4.3481048D-01	7.701126	2.1701519D+00
4.5456919D-01	7.625553	2.2242835D+00
4.7621163D-01	7.544423	2.2802903D+00
5.0003453D-01	7.455943	2.3377074D+00
5.2625956D-01	7.358822	2.3965701D+00
5.5552038D-01	7.252419	2.4608783D+00
5.8830156D-01	7.135674	2.5187795D+00
6.2502876D-01	7.007965	2.5756695D+00
6.6665325D-01	6.867192	2.6296027D+00
7.1433183D-01	6.711149	2.6846653D+00
7.6930756D-01	6.538143	2.7333179D+00
8.3333572D-01	6.346035	2.7731295D+00
9.0909653D-01	6.131865	2.8065976D+00
1.0000000D+00	5.879378	2.8300242D+00
1.0101015D+00	5.853423	2.8276467D+00
1.0204083D+00	5.827179	2.8314972D+00
1.0309320D+00	5.800631	2.8350462D+00
1.0416696D+00	5.773802	2.8317841D+00
1.0526403D+00	5.746661	2.8347198D+00
1.0638245D+00	5.719272	2.8308714D+00
1.0752761D+00	5.691521	2.8331537D+00
1.0869511D+00	5.663535	2.8351768D+00

TABLE 1-Continued

Wave Number (cm ⁻¹)	n	k
1.0989046D+00	5.635201	2.8302848D+00
1.1111175D+00	5.606586	2.8315885D+00
1.1235955D+00	5.577699	2.8325667D+00
1.1363706D+00	5.548489	2.8331537D+00
1.1494233D+00	5.519027	2.8268980D+00
1.1627866D+00	5.489262	2.8267679D+00
1.1764677D+00	5.459203	2.8262472D+00
1.1904742D+00	5.428878	2.8253363D+00
1.2048140D+00	5.398286	2.8240354D+00
1.2195230D+00	5.367389	2.8157892D+00
1.2345537D+00	5.336323	2.8137152D+00
1.2500000D+00	5.304929	2.8111249D+00
1.2659017D+00	5.273172	2.8079550D+00
1.2820353D+00	5.241539	2.8047241D+00
1.2986736D+00	5.209531	2.8008519D+00
1.3158307D+00	5.177179	2.7963411D+00
1.3332144D+00	5.146161	2.7918375D+00
1.3514501D+00	5.116001	2.7860579D+00
1.3699351D+00	5.083439	2.7866995D+00
1.3889928D+00	5.047771	2.7802903D+00
1.4083156D+00	5.013994	2.7738952D+00
1.4285650D+00	4.979800	2.7662418D+00
1.4494392D+00	4.946351	2.7579738D+00
1.4706184D+00	4.915201	2.7497306D+00
1.4924507D+00	4.881015	2.7471991D+00
1.5153048D+00	4.844068	2.7370967D+00
1.5385089D+00	4.811400	2.7270314D+00
1.5624280D+00	4.776470	2.7226395D+00
1.5874498D+00	4.740422	2.7107542D+00
1.6128724D+00	4.704528	2.7051425D+00
1.6394569D+00	4.667698	2.6920935D+00
1.6664796D+00	4.631138	2.6852835D+00
1.6947280D+00	4.593558	2.6711000D+00
1.7242491D+00	4.555811	2.6618902D+00
1.7542844D+00	4.518750	2.6466112D+00
1.7856651D+00	4.482558	2.6362716D+00
1.8180256D+00	4.442443	2.6253677D+00
1.8518252D+00	4.403706	2.6072948D+00
1.8866876D+00	4.367201	2.5947179D+00
1.9230917D+00	4.328263	2.5810127D+00
1.9606497D+00	4.288766	2.5667883D+00
1.9998619D+00	4.248425	2.5514681D+00
2.0407979D+00	4.207585	2.5350711D+00
2.0835312D+00	4.166540	2.5176198D+00

TABLE 1-Continued

Wave Number (cm ⁻¹)	n	k
2.1276491D+00	4.125763	2.4997130D+00
2.1737020D+00	4.084851	2.4807908D+00
2.2222863D+00	4.045111	2.4603118D+00
2.2724796D+00	4.003601	2.4450635D+00
2.3254125D+00	3.960586	2.4226470D+00
2.3812226D+00	3.917021	2.4043082D+00
2.4389337D+00	3.873564	2.3800723D+00
2.4997697D+00	3.829496	2.3598812D+00
2.5638936D+00	3.785136	2.3328679D+00
2.6314796D+00	3.741930	2.3098839D+00
2.7027134D+00	3.695213	2.2855469D+00
2.7777938D+00	3.650102	2.2547072D+00
2.8569326D+00	3.607096	2.2278715D+00
2.9410337D+00	3.563346	2.1993287D+00
3.0304003D+00	3.516889	2.1741532D+00
3.1253596D+00	3.468221	2.1423486D+00
3.2255219D+00	3.422465	2.1095516D+00
3.3334965D+00	3.374610	2.0791707D+00
3.4482600D+00	3.326631	2.0426321D+00
3.5710835D+00	3.279470	2.0090472D+00
3.7033947D+00	3.228984	1.9732865D+00
3.8459178D+00	3.179887	1.9310350D+00
4.0003685D+00	3.133464	1.8909940D+00
4.1667745D+00	3.084049	1.8534896D+00
4.3481048D+00	3.032401	1.8092148D+00
4.5456919D+00	2.983258	1.7627476D+00
4.7621163D+00	2.933900	1.7178694D+00
5.0003453D+00	2.881863	1.6702833D+00
5.2625956D+00	2.831974	1.6165537D+00
5.5552038D+00	2.781861	1.5670763D+00
5.8830156D+00	2.729264	1.5107414D+00
6.2502876D+00	2.679108	1.4517443D+00
6.6665325D+00	2.629097	1.3928044D+00
7.1433183D+00	2.577344	1.3301179D+00
7.6930756D+00	2.527536	1.2609276D+00
8.3329735D+00	2.461153	1.1912150D+00
9.0907560D+00	2.436760	1.1199281D+00
1.0000000D+01	2.399111	1.0418139D+00
1.0519619D+01	2.385313	1.0110908D+00
1.1117317D+01	2.363856	9.8353573D-01
1.1776060D+01	2.337241	9.5014556D-01
1.2502590D+01	2.312599	9.1157025D-01
1.3335214D+01	2.290196	8.7254964D-01
1.4288940D+01	2.270109	8.3136195D-01

TABLE 1-Continued

Wave Number (cm ⁻¹)	n	k
1.5381546D+01	2.254575	7.9211848D-01
1.6672472D+01	2.236685	7.6171085D-01
1.7258379D+01	2.228339	7.4780806D-01
1.7864876D+01	2.220374	7.3585144D-01
1.8535316D+01	2.210869	7.2408599D-01
1.9230917D+01	2.200349	7.1250865D-01
1.9998619D+01	2.188736	6.9950391D-01
2.0844909D+01	2.177335	6.8515707D-01
2.1727012D+01	2.166254	6.7265154D-01
2.2750974D+01	2.153213	6.5885545D-01
2.3823195D+01	2.139507	6.4534232D-01
2.5003454D+01	2.125742	6.2920207D-01
2.6302680D+01	2.112811	6.1346550D-01
2.7797133D+01	2.099543	5.9674686D-01
2.9444216D+01	2.086956	5.8048385D-01
3.1260794D+01	2.073976	5.6596574D-01
3.3342641D+01	2.059773	5.5054160D-01
3.4514374D+01	2.052476	5.4298789D-01
3.5727284D+01	2.045135	5.3553782D-01
3.7068072D+01	2.037243	5.2818996D-01
3.8459178D+01	2.029224	5.2094292D-01
3.9994475D+01	2.020318	5.1379532D-01
4.1686938D+01	2.010446	5.0558030D-01
4.3451022D+01	2.001418	4.9635242D-01
4.5498806D+01	1.992287	4.8729297D-01
4.7643099D+01	1.983438	4.7839887D-01
5.0003453D+01	1.974559	4.6966710D-01
5.2601727D+01	1.965156	4.6109471D-01
5.5590426D+01	1.955736	4.5059892D-01
5.8884366D+01	1.948419	4.4034203D-01
6.2517269D+01	1.941655	4.3330145D-01
6.6680677D+01	1.934154	4.2637344D-01
7.1449633D+01	1.927412	4.2052338D-01
7.6913044D+01	1.919973	4.1859125D-01
8.3368118D+01	1.911671	4.1666800D-01
9.0991327D+01	1.907505	4.1762851D-01
1.0000000D+02	1.899131	4.3831885D-01
1.0209395D+02	1.895435	4.4339434D-01
1.0423174D+02	1.891384	4.4852860D-01
1.0641430D+02	1.886330	4.5476826D-01
1.0864256D+02	1.880545	4.6003423D-01
1.1117317D+02	1.874242	4.6536117D-01
1.1376273D+02	1.867327	4.7183499D-01
1.1641260D+02	1.859854	4.7729858D-01

TABLE 1-Continued

Wave Number (cm ⁻¹)	n	k
1.1912420D+02	1.851943	4.8393847D-01
1.2189896D+02	1.842330	4.9067072D-01
1.2502590D+02	1.830882	4.9635242D-01
1.2823306D+02	1.819110	5.0209991D-01
1.3152248D+02	1.805539	5.0791395D-01
1.3520726D+02	1.790800	5.1025838D-01
1.3899526D+02	1.777162	5.1379532D-01
1.4288940D+02	1.762824	5.1735678D-01
1.4689263D+02	1.747333	5.2094292D-01
1.5135612D+02	1.729441	5.2334749D-01
1.5631476D+02	1.709762	5.2455393D-01
1.6143586D+02	1.690223	5.2455393D-01
1.6672472D+02	1.669053	5.2576315D-01
1.7258379D+02	1.643739	5.2334749D-01
1.7864876D+02	1.619157	5.1616689D-01
1.8535316D+02	1.594131	5.0791395D-01
1.9230917D+02	1.567492	4.9749663D-01
1.9998619D+02	1.542270	4.7729858D-01
2.0417379D+02	1.531473	4.6750918D-01
2.0844909D+02	1.520272	4.5792056D-01
2.1281390D+02	1.508821	4.4646780D-01
2.1727012D+02	1.499424	4.3230489D-01
2.2233099D+02	1.491543	4.1762851D-01
2.2750974D+02	1.485266	4.0252248D-01
2.3280913D+02	1.480747	3.8796285D-01
2.3823195D+02	1.477194	3.7392986D-01
2.4378108D+02	1.475642	3.5874854D-01
2.5003454D+02	1.476571	3.4418358D-01
2.5644840D+02	1.478232	3.3173412D-01
2.6302680D+02	1.481006	3.1899960D-01
2.7039584D+02	1.486740	3.0675394D-01
2.7797133D+02	1.492960	2.9908191D-01
2.8575905D+02	1.498932	2.9160176D-01
2.9444216D+02	1.505906	2.8627943D-01
3.0269134D+02	1.511879	2.8300242D-01
3.1260794D+02	1.519076	2.7976291D-01
3.2284941D+02	1.527225	2.7911948D-01
3.3342641D+02	1.535500	2.8170214D-01
3.4514374D+02	1.542658	2.8892834D-01
3.5727284D+02	1.546272	2.9908191D-01
3.7068072D+02	1.546670	3.1030598D-01
3.8459178D+02	1.544080	3.2269344D-01
3.9994475D+02	1.537967	3.3557542D-01
4.1686938D+02	1.529309	3.4816903D-01

TABLE 1-Continued

Wave Number (cm ⁻¹)	n	k
4.3451022D+02	1.516402	3.6290265D-01
4.5498806D+02	1.499422	3.7221181D-01
4.7643099D+02	1.483693	3.8175976D-01
5.0003453D+02	1.467642	3.9335995D-01
5.0118723D+02	1.467249	3.9426674D-01
5.0234259D+02	1.467000	3.9517562D-01
5.0350061D+02	1.466543	3.9699967D-01
5.0466130D+02	1.465400	3.9883214D-01
5.0582466D+02	1.463349	4.0067306D-01
5.0815944D+02	1.460391	4.0067306D-01
5.0933087D+02	1.459690	4.0159671D-01
5.1050500D+02	1.458719	4.0252248D-01
5.1168184D+02	1.457713	4.0345039D-01
5.1286138D+02	1.456898	4.0438044D-01
5.1404365D+02	1.455604	4.0624698D-01
5.1522864D+02	1.453825	4.0718347D-01
5.1641637D+02	1.452188	4.0812213D-01
5.1760683D+02	1.450255	4.0906295D-01
5.1999600D+02	1.447502	4.0906295D-01
5.2119471D+02	1.446666	4.1000594D-01
5.2239619D+02	1.445486	4.1095110D-01
5.2360044D+02	1.444197	4.1189844D-01
5.2480746D+02	1.442846	4.1284796D-01
5.2601727D+02	1.441618	4.1379967D-01
5.2722986D+02	1.439563	4.1570969D-01
5.2966344D+02	1.435881	4.1570969D-01
5.3088444D+02	1.434643	4.1666800D-01
5.3210826D+02	1.432797	4.1762851D-01
5.3333490D+02	1.431240	4.1762851D-01
5.3456436D+02	1.429982	4.1859125D-01
5.3579666D+02	1.428308	4.1955620D-01
5.3703180D+02	1.426178	4.2052338D-01
5.3951062D+02	1.422820	4.2052338D-01
5.4075432D+02	1.421557	4.2149278D-01
5.4200089D+02	1.419809	4.2246442D-01
5.4325033D+02	1.417548	4.2343831D-01
5.4450265D+02	1.415276	4.2343831D-01
5.4701596D+02	1.412092	4.2343831D-01
5.4827696D+02	1.410419	4.2441443D-01
5.4954087D+02	1.408657	4.2441443D-01
5.5080770D+02	1.406786	4.2539281D-01
5.5207744D+02	1.404604	4.2539281D-01
5.5462571D+02	1.401123	4.2539281D-01
5.5590426D+02	1.399826	4.2539281D-01

TABLE 1-Continued

Wave Number (cm ⁻¹)	n	k
5.5718575D+02	1.398169	4.2637344D-01
5.5847019D+02	1.396377	4.2637344D-01
5.5975760D+02	1.394313	4.2735633D-01
5.6234133D+02	1.390838	4.2637344D-01
5.6363766D+02	1.389417	4.2735633D-01
5.6493697D+02	1.387734	4.2735633D-01
5.6623929D+02	1.385875	4.2834149D-01
5.6754461D+02	1.383660	4.2834149D-01
5.7016427D+02	1.380029	4.2834149D-01
5.7147864D+02	1.378598	4.2834149D-01
5.7279603D+02	1.376758	4.2932892D-01
5.7411646D+02	1.374519	4.2932892D-01
5.7676646D+02	1.370751	4.2932892D-01
5.7809605D+02	1.369211	4.2932892D-01
5.7942870D+02	1.367219	4.3031862D-01
5.8076442D+02	1.364655	4.3031862D-01
5.8344510D+02	1.361083	4.2932892D-01
5.8479008D+02	1.359301	4.3031862D-01
5.8613816D+02	1.356772	4.3031862D-01
5.8884366D+02	1.352834	4.2932892D-01
5.9020108D+02	1.351233	4.2932892D-01
5.9156163D+02	1.349696	4.2932892D-01
5.9292532D+02	1.347481	4.3031862D-01
5.9566214D+02	1.342949	4.2932892D-01
5.9703529D+02	1.341074	4.2932892D-01
5.9841160D+02	1.338869	4.2932892D-01
6.0117374D+02	1.334869	4.2834149D-01
6.0255959D+02	1.333056	4.2834149D-01
6.0394863D+02	1.330870	4.2834149D-01
6.0673633D+02	1.326773	4.2735633D-01
6.0813500D+02	1.324631	4.2735633D-01
6.0953690D+02	1.322675	4.2637344D-01
6.1094202D+02	1.320901	4.2637344D-01
6.1376201D+02	1.317122	4.2539281D-01
6.1517687D+02	1.315327	4.2539281D-01
6.1659500D+02	1.313112	4.2539281D-01
6.1944108D+02	1.308540	4.2441443D-01
6.2086903D+02	1.306556	4.2343831D-01
6.2373484D+02	1.303145	4.2246442D-01
6.2517269D+02	1.301310	4.2246442D-01
6.2661386D+02	1.298872	4.2246442D-01
6.2950618D+02	1.294706	4.2052338D-01
6.3095734D+02	1.292723	4.2052338D-01
6.3241185D+02	1.290576	4.1955620D-01

TABLE 1-Continued

Wave Number (cm ⁻¹)	n	k
6.3533093D+02	1.286576	4.1859125D-01
6.3679552D+02	1.284709	4.1762851D-01
6.3826349D+02	1.282639	4.1762851D-01
6.4120958D+02	1.278233	4.1570969D-01
6.4268772D+02	1.276473	4.1475358D-01
6.4565423D+02	1.272559	4.1379967D-01
6.4714262D+02	1.270391	4.1284796D-01
6.4863443D+02	1.268440	4.1189844D-01
6.5162839D+02	1.265082	4.1000594D-01
6.5313055D+02	1.263173	4.1000594D-01
6.5614527D+02	1.258880	4.0812213D-01
6.5765784D+02	1.256977	4.0718347D-01
6.6069345D+02	1.253631	4.0531264D-01
6.6221650D+02	1.251704	4.0531264D-01
6.6374307D+02	1.249380	4.0438044D-01
6.6680677D+02	1.245318	4.0252248D-01
6.6834392D+02	1.243348	4.0159671D-01
6.7142885D+02	1.239445	3.9975154D-01
6.7297666D+02	1.237500	3.9883214D-01
6.7608298D+02	1.233597	3.9699967D-01
6.7764151D+02	1.231631	3.9608659D-01
6.8076936D+02	1.227627	3.9426674D-01
6.8233869D+02	1.225566	3.9335995D-01
6.8548823D+02	1.220973	3.9155263D-01
6.8706844D+02	1.218762	3.8975361D-01
6.9023980D+02	1.215328	3.8707056D-01
6.9183097D+02	1.213645	3.8618032D-01
6.9502432D+02	1.209428	3.8440599D-01
6.9662651D+02	1.207465	3.8263980D-01
6.9984200D+02	1.203552	3.8088173D-01
7.0145530D+02	1.201594	3.7913174D-01
7.0469307D+02	1.197623	3.7738979D-01
7.0631755D+02	1.195603	3.7565584D-01
7.0957777D+02	1.191399	3.7392986D-01
7.1121351D+02	1.189086	3.7221181D-01
7.1449633D+02	1.184740	3.6964952D-01
7.1614341D+02	1.182458	3.6795113D-01
7.1944898D+02	1.178513	3.6457774D-01
7.2276980D+02	1.174089	3.6206800D-01
7.2443596D+02	1.172049	3.5957554D-01
7.2777980D+02	1.167947	3.5710024D-01
7.2945751D+02	1.165763	3.5464198D-01
7.3282453D+02	1.161869	3.5139060D-01
7.3451387D+02	1.160150	3.4897165D-01

TABLE 1-Continued

Wave Number (cm ⁻¹)	n	k
7.3790423D+02	1.156338	3.4656934D-01
7.4131024D+02	1.151643	3.4260220D-01
7.4301914D+02	1.149628	3.4024374D-01
7.4644876D+02	1.145850	3.3634900D-01
7.4989421D+02	1.141428	3.3249885D-01
7.5162289D+02	1.139515	3.2945048D-01
7.5509223D+02	1.135773	3.2567929D-01
7.5683290D+02	1.133825	3.2269344D-01
7.6032628D+02	1.130583	3.1826592D-01
7.6383578D+02	1.126485	3.1389915D-01
7.6559661D+02	1.124841	3.1030598D-01
7.6913044D+02	1.122067	3.0604842D-01
7.7268059D+02	1.118262	3.0115505D-01
7.7446180D+02	1.116753	2.9770775D-01
7.7803655D+02	1.114243	2.9294773D-01
7.8162780D+02	1.110319	2.8826382D-01
7.8342964D+02	1.108999	2.8365480D-01
7.8704579D+02	1.107403	2.7911948D-01
7.9067863D+02	1.104624	2.7402497D-01
7.9432823D+02	1.100816	2.6902345D-01
7.9615935D+02	1.099603	2.6411322D-01
7.9983426D+02	1.098011	2.5929261D-01
8.0352612D+02	1.095643	2.5280761D-01
8.0723503D+02	1.092375	2.4762252D-01
8.0909590D+02	1.091270	2.4198595D-01
8.1283052D+02	1.090913	2.3593379D-01
8.1658237D+02	1.089721	2.2950394D-01
8.2035154D+02	1.087212	2.2376396D-01
8.2224265D+02	1.086723	2.1766577D-01
8.2603795D+02	1.087993	2.1124680D-01
8.2985077D+02	1.087926	2.0548974D-01
8.3368118D+02	1.087480	1.9897117D-01
8.3752928D+02	1.086163	1.9265937D-01
8.3945999D+02	1.086474	1.8654781D-01
8.4333476D+02	1.089062	1.8021467D-01
8.4722741D+02	1.090622	1.7409654D-01
8.5113804D+02	1.092339	1.6779930D-01
8.5506671D+02	1.094339	1.6210266D-01
8.5901332D+02	1.096068	1.5696042D-01
8.6297855D+02	1.096584	1.5198130D-01
8.6496792D+02	1.097503	1.4716012D-01
8.6896043D+02	1.100705	1.4216417D-01
8.7297137D+02	1.103057	1.3702195D-01
8.7700082D+02	1.105361	1.3206573D-01

TABLE 1-Continued

Wave Number (cm ⁻¹)	n	k
8.8104887D+02	1.107674	1.2699603D-01
8.8511561D+02	1.110334	1.2184007D-01
8.8920112D+02	1.113289	1.1716291D-01
8.9330548D+02	1.116059	1.1292501D-01
8.9742879D+02	1.118841	1.0834033D-01
9.0157114D+02	1.122010	1.0394178D-01
9.0573260D+02	1.125466	9.9951690D-02
9.0991327D+02	1.128640	9.6781009D-02
9.1411324D+02	1.131445	9.3280345D-02
9.1833260D+02	1.134419	8.9699525D-02
9.2257143D+02	1.137372	8.6455006D-02
9.2682982D+02	1.140345	8.2944987D-02
9.3110788D+02	1.143601	7.9577473D-02
9.3540567D+02	1.146959	7.6522675D-02
9.3972331D+02	1.150368	7.3585144D-02
9.4406088D+02	1.153843	7.0923497D-02
9.4841846D+02	1.157248	6.8515707D-02
9.5279616D+02	1.160584	6.6189659D-02
9.5719407D+02	1.163960	6.3942578D-02
9.6161228D+02	1.167354	6.1914183D-02
9.6605088D+02	1.170827	5.9950132D-02
9.7050997D+02	1.174182	5.8450757D-02
9.7498964D+02	1.178360	5.6336536D-02
9.7948999D+02	1.180893	5.8048385D-02
9.8627949D+02	1.183900	5.3800975D-02
9.9083194D+02	1.187365	5.2697516D-02
9.9540542D+02	1.190334	5.1735678D-02
1.0000000D+03	1.193164	5.0791395D-02
1.0046158D+03	1.195932	4.9979297D-02
1.0092529D+03	1.198600	4.9293555D-02
1.0162487D+03	1.202228	4.8505406D-02
1.0209395D+03	1.204471	4.7839887D-02
1.0256519D+03	1.206729	4.7183499D-02
1.0303861D+03	1.208909	4.6643394D-02
1.0351422D+03	1.211068	4.6003423D-02
1.0423174D+03	1.214136	4.5372232D-02
1.0471285D+03	1.216115	4.4749702D-02
1.0519619D+03	1.218113	4.4339434D-02
1.0592537D+03	1.220909	4.3731074D-02
1.0641430D+03	1.222699	4.3330145D-02
1.0690549D+03	1.224439	4.2932892D-02
1.0764652D+03	1.226967	4.2343831D-02
1.0814340D+03	1.228589	4.1955620D-02
1.0864256D+03	1.230259	4.1475358D-02

TABLE 1-Continued

Wave Number (cm ⁻¹)	n	k
1.0939564D+03	1.232659	4.1095110D-02
1.0990058D+03	1.234142	4.0718347D-02
1.1040786D+03	1.235657	4.0345039D-02
1.1117317D+03	1.237862	3.9883214D-02
1.1168632D+03	1.239322	3.9517562D-02
1.1246050D+03	1.241424	3.9155263D-02
1.1297959D+03	1.242789	3.8796285D-02
1.1376273D+03	1.244791	3.8440599D-02
1.1428783D+03	1.246095	3.8088173D-02
1.1481536D+03	1.247433	3.7825976D-02
1.1561122D+03	1.249353	3.7479185D-02
1.1641260D+03	1.251193	3.7135574D-02
1.1694994D+03	1.252405	3.6879935D-02
1.1776060D+03	1.254220	3.6541817D-02
1.1830416D+03	1.255384	3.6373923D-02
1.1912420D+03	1.257072	3.6040445D-02
1.1967405D+03	1.258240	3.5792344D-02
1.2050359D+03	1.259903	3.5627893D-02
1.2133889D+03	1.261488	3.5301255D-02
1.2189896D+03	1.262564	3.5139060D-02
1.2274392D+03	1.264125	3.4897165D-02
1.2359474D+03	1.265652	3.4656934D-02
1.2416523D+03	1.266657	3.4497700D-02
1.2502590D+03	1.268163	3.4260220D-02
1.2589254D+03	1.269613	3.4102808D-02
1.2647363D+03	1.270543	3.3946120D-02
1.2735031D+03	1.271952	3.3712437D-02
1.2823306D+03	1.273363	3.3480362D-02
1.2912193D+03	1.274794	3.3249885D-02
1.3001696D+03	1.276220	3.3097115D-02
1.3061709D+03	1.277123	3.3020994D-02
1.3152248D+03	1.278508	3.2793679D-02
1.3243415D+03	1.279895	3.2718256D-02
1.3335214D+03	1.281248	3.2567929D-02
1.3427650D+03	1.282606	3.2493025D-02
1.3520726D+03	1.283912	3.2418293D-02
1.3614447D+03	1.285242	3.2269344D-02
1.3708818D+03	1.286624	3.2195127D-02
1.3803843D+03	1.287944	3.2195127D-02
1.3899526D+03	1.289296	3.2047204D-02
1.3995873D+03	1.290696	3.2047204D-02
1.4092888D+03	1.292093	3.1973497D-02
1.4190575D+03	1.293609	3.1899960D-02
1.4288940D+03	1.295193	3.1973497D-02

TABLE 1-Continued

Wave Number (cm ⁻¹)	n	k
1.4387986D+03	1.296751	3.2121080D-02
1.4487719D+03	1.298382	3.2195127D-02
1.4588143D+03	1.300125	3.2418293D-02
1.4689263D+03	1.301901	3.2718256D-02
1.4825181D+03	1.304521	3.3097115D-02
1.4927944D+03	1.306716	3.3712437D-02
1.5031420D+03	1.309021	3.4497700D-02
1.5135612D+03	1.311404	3.5627893D-02
1.5275661D+03	1.314837	3.7306984D-02
1.5381546D+03	1.317726	3.9245525D-02
1.5488166D+03	1.320468	4.1762851D-02
1.5631476D+03	1.325038	4.4852860D-02
1.5739829D+03	1.329242	4.9521084D-02
1.5885467D+03	1.335754	5.6988883D-02
1.5995580D+03	1.339863	6.9468855D-02
1.6143586D+03	1.341605	8.7859786D-02
1.6255488D+03	1.330121	1.1716291D-01
1.6405898D+03	1.295314	1.3085495D-01
1.6519618D+03	1.268459	1.2496550D-01
1.6672472D+03	1.242862	1.0685384D-01
1.6788040D+03	1.231892	8.6455006D-02
1.6943378D+03	1.229239	6.2199965D-02
1.7100153D+03	1.234896	4.3230489D-02
1.7258379D+03	1.242239	3.2945048D-02
1.7378008D+03	1.248370	2.4819335D-02
1.7538805D+03	1.256584	2.0313752D-02
1.7701090D+03	1.262994	1.6587852D-02
1.7864876D+03	1.268802	1.4183720D-02
1.8030177D+03	1.273883	1.2583172D-02
1.8197009D+03	1.278291	1.1582176D-02
1.8365383D+03	1.282194	1.0784255D-02
1.8535316D+03	1.285729	1.0298883D-02
1.8706821D+03	1.289015	9.8807553D-03
1.8879913D+03	1.292117	9.7901680D-03
1.9054607D+03	1.294933	9.9035328D-03
1.9230917D+03	1.297550	1.0110908D-02
1.9408859D+03	1.299910	1.0611827D-02
1.9588447D+03	1.301965	1.1111947D-02
1.9815270D+03	1.304258	1.1797504D-02
1.9998619D+03	1.305885	1.2410525D-02
2.0183664D+03	1.307228	1.3115660D-02
2.0417379D+03	1.308720	1.3702195D-02
2.0606299D+03	1.309721	1.4414187D-02
2.0844909D+03	1.310657	1.4989603D-02

TABLE 1-Continued

Wave Number (cm ⁻¹)	n	k
2.1037784D+03	1.311148	1.5516371D-02
2.1281390D+03	1.311451	1.5696042D-02
2.1527817D+03	1.311588	1.5480684D-02
2.1727012D+03	1.311785	1.4716012D-02
2.1978599D+03	1.312483	1.3607870D-02
2.2233099D+03	1.313587	1.2381981D-02
2.2490546D+03	1.314920	1.1396989D-02
2.2750974D+03	1.316398	1.0298883D-02
2.3014418D+03	1.318113	9.3065806D-03
2.3280913D+03	1.319948	8.4487049D-03
2.3550493D+03	1.321906	7.5995897D-03
2.3823195D+03	1.323997	6.8831961D-03
2.4099054D+03	1.326183	6.2199965D-03
2.4378108D+03	1.328504	5.6206966D-03
2.4717241D+03	1.331403	5.0674578D-03
2.5003454D+03	1.333929	4.6003423D-03
2.5292980D+03	1.336658	4.1570969D-03
2.5644840D+03	1.340174	3.8000573D-03
2.6001596D+03	1.343958	3.5301255D-03
2.6302680D+03	1.347393	3.4024374D-03
2.6668587D+03	1.351891	3.4024374D-03
2.7039584D+03	1.356937	3.5957554D-03
2.7415742D+03	1.362546	4.2343831D-03
2.7797133D+03	1.368863	5.1497974D-03
2.8183829D+03	1.376092	6.7887551D-03
2.8575905D+03	1.384213	9.3926933D-03
2.8973436D+03	1.393260	1.3206573D-02
2.9444216D+03	1.404875	1.9489026D-02
2.9853826D+03	1.417064	2.6108994D-02
3.0269134D+03	1.432585	3.6879935D-02
3.0760968D+03	1.449409	6.1064688D-02
3.1260794D+03	1.461522	9.2425146D-02
3.1768741D+03	1.466753	1.3483112D-01
3.2284941D+03	1.452013	1.9177418D-01
3.2809529D+03	1.411876	2.3976741D-01
3.3342641D+03	1.352917	2.7213860D-01
3.3496544D+03	1.334533	2.7213860D-01
3.3573761D+03	1.326310	2.7592442D-01
3.3728731D+03	1.307891	2.7847752D-01
3.3806484D+03	1.297762	2.8170214D-01
3.3884416D+03	1.285942	2.8235153D-01
3.4040819D+03	1.263935	2.8040783D-01
3.4119291D+03	1.252073	2.7976291D-01
3.4197944D+03	1.240033	2.7592442D-01

TABLE 1-Continued

Wave Number (cm ⁻¹)	n	k
3.4276779D+03	1.229654	2.7151270D-01
3.4434993D+03	1.208002	2.6472207D-01
3.4514374D+03	1.195889	2.5810127D-01
3.4593938D+03	1.185419	2.4933896D-01
3.4673685D+03	1.178446	2.3921596D-01
3.4833732D+03	1.162372	2.2897609D-01
3.4914032D+03	1.152284	2.1816754D-01
3.4994517D+03	1.145545	2.0596344D-01
3.5075187D+03	1.142386	1.9399482D-01
3.5237087D+03	1.133346	1.7980019D-01
3.5318317D+03	1.127523	1.6702833D-01
3.5399734D+03	1.125351	1.5409557D-01
3.5481339D+03	1.125532	1.4216417D-01
3.5563132D+03	1.128413	1.3115660D-01
3.5727284D+03	1.129478	1.2100133D-01
3.5809644D+03	1.127558	1.1188971D-01
3.5892193D+03	1.127959	1.0204463D-01
3.5974934D+03	1.130913	9.2851761D-02
3.6140986D+03	1.132778	8.3519934D-02
3.6224300D+03	1.131711	7.4437220D-02
3.6307805D+03	1.132860	6.4832108D-02
3.6391504D+03	1.136183	5.4801209D-02
3.6475395D+03	1.142068	4.6215765D-02
3.6643757D+03	1.149520	3.8000573D-02
3.6728230D+03	1.152876	2.8170214D-02
3.6812897D+03	1.160993	2.0501713D-02
3.6897760D+03	1.168874	1.8611876D-02
3.6982818D+03	1.174582	1.6397972D-02
3.7068072D+03	1.179962	1.4514101D-02
3.7239171D+03	1.188087	1.2699603D-02
3.7325016D+03	1.191390	1.0490354D-02
3.7411059D+03	1.195340	8.5465363D-03
3.7497300D+03	1.199289	7.3247051D-03
3.7583740D+03	1.202951	6.2775495D-03
3.7670380D+03	1.206519	5.3677236D-03
3.7757219D+03	1.209954	4.8282544D-03
3.7931498D+03	1.215699	4.3630495D-03
3.8018940D+03	1.218078	4.0159671D-03
3.8106582D+03	1.220535	3.3020994D-03
3.8194427D+03	1.223082	2.9770775D-03
3.8282474D+03	1.225483	2.7026521D-03
3.8370725D+03	1.227769	2.5750765D-03
3.8547836D+03	1.231834	2.4762252D-03
3.8636698D+03	1.233679	2.4254378D-03

TABLE 1-Continued

Wave Number (cm ⁻¹)	n	k
3.8725764D+03	1.235426	2.3866577D-03
3.8815037D+03	1.237089	2.3377074D-03
3.8904514D+03	1.238670	2.3109478D-03
3.8994199D+03	1.240167	2.2687683D-03
3.9174188D+03	1.243014	2.1418554D-03
3.9355008D+03	1.245672	2.0691413D-03
3.9536662D+03	1.248127	2.0173913D-03
3.9719155D+03	1.250383	1.9897117D-03
3.9810717D+03	1.251445	1.9533953D-03
3.9994475D+03	1.253465	1.9001599D-03
4.0179081D+03	1.255347	1.8104650D-03
4.0364539D+03	1.257102	1.7091892D-03
4.0457589D+03	1.257969	1.5804841D-03
4.0644333D+03	1.259683	1.4716012D-03
4.0831939D+03	1.261297	1.3483112D-03
4.1020410D+03	1.262824	1.2496550D-03
4.1114972D+03	1.263577	1.1502444D-03
4.1304750D+03	1.265059	1.0710017D-03
4.1495404D+03	1.266450	9.9035328D-04
4.1686938D+03	1.267787	9.0947370D-04
4.1879357D+03	1.269059	8.4877024D-04
4.1975898D+03	1.269682	7.9211848D-04
4.2169650D+03	1.270902	7.4266019D-04
4.2364297D+03	1.272062	6.8515707D-04
4.2559841D+03	1.273184	6.3648789D-04
4.2756289D+03	1.274257	5.9950132D-04
4.2953643D+03	1.275295	5.4298789D-04
4.3151908D+03	1.276305	5.1143464D-04
4.3251383D+03	1.276797	4.9180183D-04
4.3451022D+03	1.277755	4.6858690D-04
4.3651583D+03	1.278675	4.5059892D-04
4.3853070D+03	1.279561	4.2932892D-04
4.4055486D+03	1.280421	4.0812213D-04
4.4258837D+03	1.281256	3.8975361D-04
4.4463127D+03	1.282064	3.7392986D-04
4.4668359D+03	1.282852	3.5710024D-04
4.4874539D+03	1.283619	3.4577226D-04
4.5081670D+03	1.284365	3.4102808D-04
4.5289758D+03	1.285087	3.3868046D-04
4.5498806D+03	1.285790	3.3790152D-04
4.5708819D+03	1.286474	3.3946120D-04
4.5919801D+03	1.287139	3.4339198D-04
4.6131757D+03	1.287787	3.5058243D-04
4.6344692D+03	1.288418	3.5874854D-04

TABLE 1-Continued

Wave Number (cm ⁻¹)	n	k
4.6558609D+03	1.289033	3.7050165D-04
4.6773514D+03	1.289634	3.8263980D-04
4.6989411D+03	1.290221	3.9699967D-04
4.7206304D+03	1.290795	4.1762851D-04
4.7424199D+03	1.291353	4.4034203D-04
4.7643099D+03	1.291899	4.6429087D-04
4.7863009D+03	1.292438	4.8841629D-04
4.8083935D+03	1.292966	5.2940757D-04
4.8305880D+03	1.293476	5.7251932D-04
4.8528850D+03	1.293973	6.2056909D-04
4.8752849D+03	1.294457	6.7420217D-04
4.8977882D+03	1.294919	7.3924797D-04
4.9317380D+03	1.295606	8.0498937D-04
4.9545019D+03	1.296066	8.8877155D-04
4.9773708D+03	1.296499	9.9035328D-04
5.0003453D+03	1.296913	1.1010072D-03
5.0234259D+03	1.297292	1.2496550D-03
5.0466130D+03	1.297607	1.4021360D-03
5.0815944D+03	1.298051	1.5480684D-03
5.1050500D+03	1.298308	1.7170785D-03
5.1286138D+03	1.298472	1.8483752D-03
5.1522864D+03	1.298590	1.9089306D-03
5.1760683D+03	1.298681	1.9221627D-03
5.2119471D+03	1.298793	1.8272171D-03
5.2360044D+03	1.298791	1.6779930D-03
5.2601727D+03	1.298998	1.1608875D-03
5.2966344D+03	1.299545	9.2212574D-04
5.3210826D+03	1.299860	7.2242064D-04
5.3456436D+03	1.300214	5.2094292D-04
5.3703180D+03	1.300633	3.2047204D-04
5.4075432D+03	1.301291	1.8611876D-04
5.4325033D+03	1.301709	1.5516371D-04
5.4701596D+03	1.302269	1.4183720D-04
5.4954087D+03	1.302616	1.3797174D-04
5.5207744D+03	1.302947	1.3711663D-04
5.5590426D+03	1.303418	1.3592212D-04
5.5847019D+03	1.303718	1.3304242D-04
5.6234133D+03	1.304155	1.2186813D-04
5.6493697D+03	1.304442	1.1201860D-04
5.6754461D+03	1.304727	1.0512116D-04
5.7147864D+03	1.305142	9.9997730D-05
5.7411646D+03	1.305413	9.5102108D-05
5.7809605D+03	1.305809	8.9000028D-05
5.8076442D+03	1.306070	8.4098867D-05

TABLE 1-Continued

Wave Number (cm ⁻¹)	n	k
5.8479008D+03	1.306453	8.0498937D-05
5.8884366D+03	1.306829	7.7426592D-05
5.9156163D+03	1.307073	7.6013397D-05
5.9566214D+03	1.307435	7.4953194D-05
5.9841160D+03	1.307672	7.4044046D-05
6.0255959D+03	1.308021	7.3975881D-05
6.0673633D+03	1.308341	7.5908453D-05
6.0953690D+03	1.308548	7.9029665D-05
6.1376201D+03	1.308855	8.0963662D-05
6.1659500D+03	1.309055	8.3097918D-05
6.2086903D+03	1.309352	8.8042049D-05
6.2517269D+03	1.309642	9.3473853D-05
6.2950618D+03	1.309928	9.9400860D-05
6.3241185D+03	1.310114	1.0707551D-04
6.3679552D+03	1.310387	1.1402239D-04
6.4120958D+03	1.310659	1.2396245D-04
6.4565423D+03	1.310923	1.3483112D-04
6.4863443D+03	1.311097	1.4414187D-04
6.5313055D+03	1.311352	1.6024709D-04
6.5765784D+03	1.311604	1.7409654D-04
6.6221650D+03	1.311852	1.9578984D-04
6.6680677D+03	1.312093	2.2479681D-04
6.7142885D+03	1.312318	2.6594397D-04
6.7608298D+03	1.312525	3.0184928D-04
6.8076936D+03	1.312715	3.3868046D-04
6.8548823D+03	1.312888	3.6040445D-04
6.9023980D+03	1.313055	3.6373923D-04
6.9502432D+03	1.313220	3.6290265D-04
6.9984200D+03	1.313373	3.5382633D-04
7.0469307D+03	1.313518	3.1973497D-04
7.0957777D+03	1.313671	2.5397452D-04
7.1449633D+03	1.313871	1.5303478D-04
7.1944898D+03	1.314104	1.0599616D-04
7.2443596D+03	1.314329	7.8017161D-05
7.2945751D+03	1.314547	5.8035021D-05
7.3451387D+03	1.314760	4.5049517D-05
7.4131024D+03	1.315031	4.0465988D-05
7.4644876D+03	1.315228	2.8489849D-05
7.5162289D+03	1.315425	2.2505577D-05
7.5683290D+03	1.315618	1.9120099D-05
7.6383578D+03	1.315868	1.6390422D-05
7.6913044D+03	1.316052	1.4002002D-05
7.7446180D+03	1.316233	1.2211532D-05
7.8162780D+03	1.316470	1.1394365D-05

TABLE 1-Continued

Wave Number (cm ⁻¹)	n	k
7.8704579D+03	1.316645	1.0904861D-05
7.9432823D+03	1.316873	1.0790713D-05
7.9983426D+03	1.317042	1.1002215D-05
8.0723503D+03	1.317263	1.1388857D-05
8.1283052D+03	1.317427	1.1602462D-05
8.2035154D+03	1.317641	1.1790172D-05
8.2603795D+03	1.317799	1.1905843D-05
8.3368118D+03	1.318008	1.1994997D-05
8.3945999D+03	1.318162	1.1812182D-05
8.4722741D+03	1.318366	1.1603263D-05
8.5506671D+03	1.318566	1.1195156D-05
8.6297855D+03	1.318763	1.0688829D-05
8.6896043D+03	1.318909	9.3064735D-06
8.7700082D+03	1.319103	5.9510026D-06
8.8511561D+03	1.319296	3.8689235D-06
8.9330548D+03	1.319488	2.6283920D-06
9.0157114D+03	1.319678	2.0384034D-06
9.0991327D+03	1.319865	1.7084023D-06
9.1833260D+03	1.320051	1.4986152D-06
9.2682982D+03	1.320233	1.3285874D-06
9.3540567D+03	1.320416	1.2588968D-06
9.4406088D+03	1.320596	1.2989431D-06
9.5279616D+03	1.320775	1.4193521D-06
9.6161228D+03	1.320952	1.6900134D-06
9.7050997D+03	1.321128	2.0007376D-06
9.7948999D+03	1.321303	2.3522861D-06
9.9083194D+03	1.321521	2.6877579D-06
1.0000000D+04	1.321695	2.9997851D-06
1.0046158D+04	1.321780	3.1310510D-06
1.0092529D+04	1.321866	3.2530455D-06
1.0162487D+04	1.321994	3.3364924D-06
1.0209395D+04	1.322080	3.4181423D-06
1.0256519D+04	1.322165	3.4800873D-06
1.0303861D+04	1.322249	3.5017904D-06
1.0351422D+04	1.322333	3.4640978D-06
1.0423174D+04	1.322462	3.3580731D-06
1.0471285D+04	1.322546	3.1899960D-06
1.0519619D+04	1.322630	2.9321767D-06
1.0592537D+04	1.322757	2.5573498D-06
1.0641430D+04	1.322842	2.1691528D-06
1.0690549D+04	1.322926	1.7708841D-06
1.0764652D+04	1.323054	1.3683278D-06
1.0814340D+04	1.323138	1.0597176D-06
1.0864256D+04	1.323222	8.3040536D-07

TABLE 1-Continued

Wave Number (cm ⁻¹)	n	k
1.0939564D+04	1.323351	6.6956099D-07
1.0990058D+04	1.323434	5.6988883D-07
1.1040786D+04	1.323520	5.1497974D-07
1.1117317D+04	1.323648	4.8617222D-07
1.1168632D+04	1.323732	4.6215765D-07
1.1246050D+04	1.323859	4.4034203D-07
1.1297959D+04	1.323946	4.2343831D-07
1.1376273D+04	1.324074	4.0531264D-07
1.1428783D+04	1.324159	3.9065208D-07
1.1481536D+04	1.324244	3.7479185D-07
1.1561122D+04	1.324373	3.5464198D-07
1.1641260D+04	1.324502	3.3480362D-07
1.1694994D+04	1.324590	3.1534805D-07
1.1776060D+04	1.324718	2.9294773D-07
1.1830416D+04	1.324805	2.6902345D-07
1.1912420D+04	1.324937	2.4591790D-07
1.1967405D+04	1.325025	2.2427979D-07
1.2050359D+04	1.325157	2.0407516D-07
1.2133889D+04	1.325290	1.8188218D-07
1.2189896D+04	1.325379	1.6210266D-07
1.2274392D+04	1.325512	1.4480720D-07
1.2359474D+04	1.325648	1.3298117D-07
1.2416523D+04	1.325739	1.2699603D-07
1.2502590D+04	1.325874	1.2496550D-07
1.2589254D+04	1.326012	1.2583172D-07
1.2647363D+04	1.326104	1.2817111D-07
1.2735031D+04	1.326244	1.3390295D-07
1.2823306D+04	1.326382	1.4086080D-07
1.2912193D+04	1.326524	1.4783938D-07
1.3001696D+04	1.326667	1.5268281D-07
1.3061709D+04	1.326764	1.5696042D-07
1.3152248D+04	1.326909	1.5804841D-07
1.3243415D+04	1.327055	1.5804841D-07
1.3335214D+04	1.327201	1.5587991D-07
1.3427650D+04	1.327350	1.5303478D-07
1.3520726D+04	1.327502	1.4581095D-07
1.3614447D+04	1.327652	1.3483112D-07
1.3708818D+04	1.327808	1.1502444D-07
1.3803843D+04	1.327963	9.1367164D-08
1.3899526D+04	1.328120	7.2910511D-08
1.3995873D+04	1.328279	5.9950132D-08
1.4092888D+04	1.328440	4.9979297D-08
1.4190575D+04	1.328603	4.1000594D-08
1.4288940D+04	1.328769	3.3480362D-08

TABLE 1-Continued

Wave Number (cm^{-1})	n	k
1.4387986D+04	1.328938	2.9633991D-08
1.4487719D+04	1.329106	2.6533231D-08
1.4588143D+04	1.329278	2.4705301D-08
1.4689263D+04	1.329452	2.3003300D-08
1.4825181D+04	1.329690	2.1766577D-08
1.4927944D+04	1.329869	2.0979259D-08
1.5031420D+04	1.330052	2.0313752D-08
1.5135612D+04	1.330238	1.9399482D-08
1.5275661D+04	1.330490	1.7774203D-08
1.5381546D+04	1.330683	1.6741337D-08
1.5488166D+04	1.330877	1.6061649D-08
1.5631476D+04	1.331144	1.5696042D-08
1.5739829D+04	1.331345	1.5516371D-08
1.5885467D+04	1.331619	1.5024158D-08
1.5995580D+04	1.331826	1.4716012D-08
1.6143586D+04	1.332106	1.3989112D-08
1.6255488D+04	1.332317	1.3298117D-08
1.6405898D+04	1.332598	1.2381981D-08
1.6519618D+04	1.332813	1.1318533D-08
1.6672472D+04	1.333100	9.6336340D-09
1.6788040D+04	1.333316	7.7230731D-09
1.6943378D+04	1.333609	6.3648789D-09
1.7100153D+04	1.333902	5.2214382D-09
1.7258379D+04	1.334200	4.4339434D-09
1.7378008D+04	1.334425	3.8440599D-09
1.7538805D+04	1.334729	3.4339198D-09
1.7701090D+04	1.335035	3.1317720D-09
1.7864876D+04	1.335344	2.8693937D-09
1.8030177D+04	1.335656	2.6594397D-09
1.8197009D+04	1.335972	2.4422501D-09
1.8365383D+04	1.336292	2.2687683D-09
1.8535316D+04	1.336615	2.0979259D-09
1.8706821D+04	1.336943	1.8870793D-09
1.8879913D+04	1.337273	1.7570744D-09
1.9054607D+04	1.337607	1.6397972D-09
1.9230917D+04	1.337944	1.5696042D-09
1.9408859D+04	1.338288	1.4614708D-09
1.9588447D+04	1.338635	1.2670395D-09
1.9815270D+04	1.339073	1.0784255D-09
1.9998619D+04	1.339430	9.2425146D-10
2.0183664D+04	1.339791	7.8485629D-10
2.0417379D+04	1.340248	7.3415903D-10
2.0606299D+04	1.340620	7.1579744D-10
2.0844909D+04	1.341093	7.0923497D-10

TABLE 1-Continued

Wave Number (cm ⁻¹)	n	k
2.1037784D+04	1.341475	7.0111643D-10
2.1281390D+04	1.341961	7.2910511D-10
2.1527817D+04	1.342455	7.4953194D-10
2.1727012D+04	1.342858	7.5995897D-10
2.1978599D+04	1.343368	7.7945338D-10
2.2233099D+04	1.343889	8.0870503D-10
2.2490546D+04	1.344418	8.6854064D-10
2.2750974D+04	1.344956	9.3926933D-10
2.3014418D+04	1.345505	1.0180993D-09
2.3280913D+04	1.346066	1.0884040D-09
2.3550493D+04	1.346636	1.1689344D-09
2.3823195D+04	1.347219	1.2583172D-09
2.4099054D+04	1.347811	1.3390295D-09
2.4378108D+04	1.348417	1.4216417D-09
2.4717241D+04	1.349159	1.4886416D-09
2.5003454D+04	1.349793	1.5804841D-09
2.5292980D+04	1.350438	1.6626091D-09
2.5644840D+04	1.351231	1.7611248D-09
2.6001596D+04	1.352046	1.8398827D-09
2.6302680D+04	1.352740	1.9399482D-09
2.6668587D+04	1.353594	2.0313752D-09
2.7039584D+04	1.354470	2.1173378D-09
2.7415742D+04	1.355370	2.2171248D-09
2.7797133D+04	1.356295	2.3162751D-09
2.8183829D+04	1.357247	2.4198595D-09
2.8575905D+04	1.358224	2.5280761D-09
2.8973436D+04	1.359231	2.6533231D-09
2.9444216D+04	1.360441	2.7656049D-09
2.9853826D+04	1.361513	2.8826382D-09
3.0269134D+04	1.362616	2.9839404D-09
3.0760968D+04	1.363990	3.0816985D-09
3.1260794D+04	1.365376	3.1899960D-09
3.1768741D+04	1.366812	3.3249885D-09
3.2284941D+04	1.368287	3.5464198D-09
3.2809529D+04	1.369839	3.8263980D-09
3.3342641D+04	1.371437	4.1475358D-09
3.3884416D+04	1.373098	4.4034203D-09
3.4514374D+04	1.375086	4.7950169D-09
3.5075187D+04	1.376902	5.4049309D-09
3.5727284D+04	1.379072	5.7914878D-09
3.6391504D+04	1.381341	6.2920207D-09
3.7068072D+04	1.383726	6.8515707D-09
3.7757219D+04	1.386239	7.4437220D-09
3.8459178D+04	1.388881	7.9944786D-09

143

TABLE 1-Continued

Wave Number (cm ⁻¹)	n	k
3.9174188D+04	1.391674	8.6057781D-09
3.9994475D+04	1.394993	9.3065806D-09
4.0831939D+04	1.398535	9.9035328D-09
4.1686938D+04	1.402321	1.0490354D-08
4.2559841D+04	1.406358	1.0710017D-08
4.3451022D+04	1.410702	1.1010072D-08
4.4463127D+04	1.415921	1.1582176D-08
4.5498806D+04	1.421603	1.2699603D-08
4.6558609D+04	1.427828	1.9988957D-08
4.7643099D+04	1.434685	3.8440599D-08
4.8752849D+04	1.442296	6.7110449D-08
5.0003453D+04	1.451724	1.1010072D-07
5.1286138D+04	1.462543	1.8496525D-07
5.2601727D+04	1.475183	3.6223478D-07
5.4075432D+04	1.491881	1.2495112D-06
5.5590426D+04	1.513343	5.9950132D-05
5.7147864D+04	1.543062	8.3905445D-04
5.7411646D+04	1.549412	1.1824700D-03
5.8076442D+04	1.568183	2.0035037D-03
5.8884366D+04	1.605555	3.9975154D-03
5.9566214D+04	1.635062	3.9975154D-02
6.0255959D+04	1.647245	7.2408599D-02
6.0953690D+04	1.653100	1.0394178D-01
6.1659500D+04	1.652917	1.3514194D-01
6.2517269D+04	1.650184	1.6702833D-01
6.3241185D+04	1.641473	2.0220419D-01
6.4120958D+04	1.620422	2.3377074D-01
6.4863443D+04	1.596861	2.5810127D-01
6.5765784D+04	1.559942	2.7719803D-01
6.6680677D+04	1.521276	2.7719803D-01
6.7608298D+04	1.489551	2.6411322D-01
6.8548823D+04	1.469275	2.4087412D-01
6.9502432D+04	1.460977	2.1666569D-01
7.0469307D+04	1.461485	1.9265937D-01
7.1449633D+04	1.471129	1.6779930D-01
7.2443596D+04	1.496271	1.4216417D-01
7.3451387D+04	1.536403	1.3328772D-01
7.4644876D+04	1.586268	1.4886416D-01
7.5683290D+04	1.619420	1.8697784D-01
7.6913044D+04	1.633849	2.3921596D-01
7.8162780D+04	1.626822	2.8760084D-01
7.9432823D+04	1.606068	3.2195127D-01
8.0723503D+04	1.584638	3.3868046D-01
8.2035154D+04	1.570304	3.4897165D-01

TABLE 1-Continued

Wave Number (cm ⁻¹)	n	k
8.3368118D+04	1.560870	3.5957554D-01
8.4722741D+04	1.553435	3.7050165D-01
8.6297855D+04	1.548070	3.8263980D-01
8.7700082D+04	1.543211	3.9883214D-01
8.9330548D+04	1.535363	4.1475358D-01
9.0991327D+04	1.528933	4.3031862D-01
9.2682982D+04	1.523589	4.4852860D-01
9.4406088D+04	1.516305	4.7074980D-01
9.6161228D+04	1.506677	4.9293555D-01
9.7948999D+04	1.493473	5.1854941D-01
1.0000000D+05	1.476628	5.4298789D-01
1.0209395D+05	1.455868	5.7516194D-01
1.0423174D+05	1.425425	6.0504844D-01
1.0641430D+05	1.387639	6.2920207D-01
1.0864256D+05	1.346760	6.4385807D-01
1.1117317D+05	1.302663	6.5281503D-01
1.1376273D+05	1.259495	6.5734013D-01
1.1641260D+05	1.214969	6.5734013D-01
1.1912420D+05	1.173382	6.4534232D-01
1.2189896D+05	1.140628	6.2920207D-01
1.2502590D+05	1.111682	6.1346550D-01
1.2823306D+05	1.087685	5.9812250D-01
1.3152248D+05	1.068724	5.8585500D-01
1.3520726D+05	1.049744	5.8048385D-01
1.3899526D+05	1.020921	5.8585500D-01
1.4288940D+05	0.981692	5.7914878D-01
1.4689263D+05	0.941801	5.6336536D-01
1.5135612D+05	0.903527	5.3553782D-01
1.5631476D+05	0.866994	5.0325737D-01
1.6143586D+05	0.840575	4.5581661D-01
1.6672472D+05	0.830901	4.1189844D-01
1.7258379D+05	0.831628	3.7392986D-01
1.7864876D+05	0.835295	3.4977611D-01
1.8535316D+05	0.835240	3.3097115D-01
1.9230917D+05	0.830957	3.1534805D-01
1.9998619D+05	0.820742	2.9977136D-01
2.0844909D+05	0.805579	2.7656049D-01
2.1727012D+05	0.797007	2.4142939D-01
2.2750974D+05	0.797737	2.0882868D-01
2.3823195D+05	0.802291	1.7980019D-01
2.5003454D+05	0.809997	1.5338756D-01
2.6302680D+05	0.819753	1.3025372D-01
2.7797133D+05	0.830720	1.0934279D-01
2.9444216D+05	0.842171	9.0738197D-02

TABLE 1-Continued

Wave Number (cm ⁻¹)	n	k
3.1260794D+05	0.854141	7.4608815D-02
3.3342641D+05	0.866493	6.0644322D-02
3.5727284D+05	0.878766	4.8505406D-02
3.8459178D+05	0.890837	3.8175976D-02
4.1686938D+05	0.902694	2.9497835D-02
4.5498806D+05	0.913973	2.2273586D-02
5.0003453D+05	0.924583	1.6360258D-02
5.5590426D+05	0.934744	1.1635636D-02
6.2517269D+05	0.944124	7.9577473D-03
7.1449633D+05	0.952792	5.1735678D-03
7.6913044D+05	0.956954	4.0718347D-03
8.3368118D+05	0.960953	3.1462276D-03
9.0991327D+05	0.964778	2.3702281D-03
1.0000000D+06	0.968416	1.7449788D-03

* The data in the first and third columns are in Fortran, double precision, exponential notation. For example, 5.0D-04 means 5.0×10^{-4} .

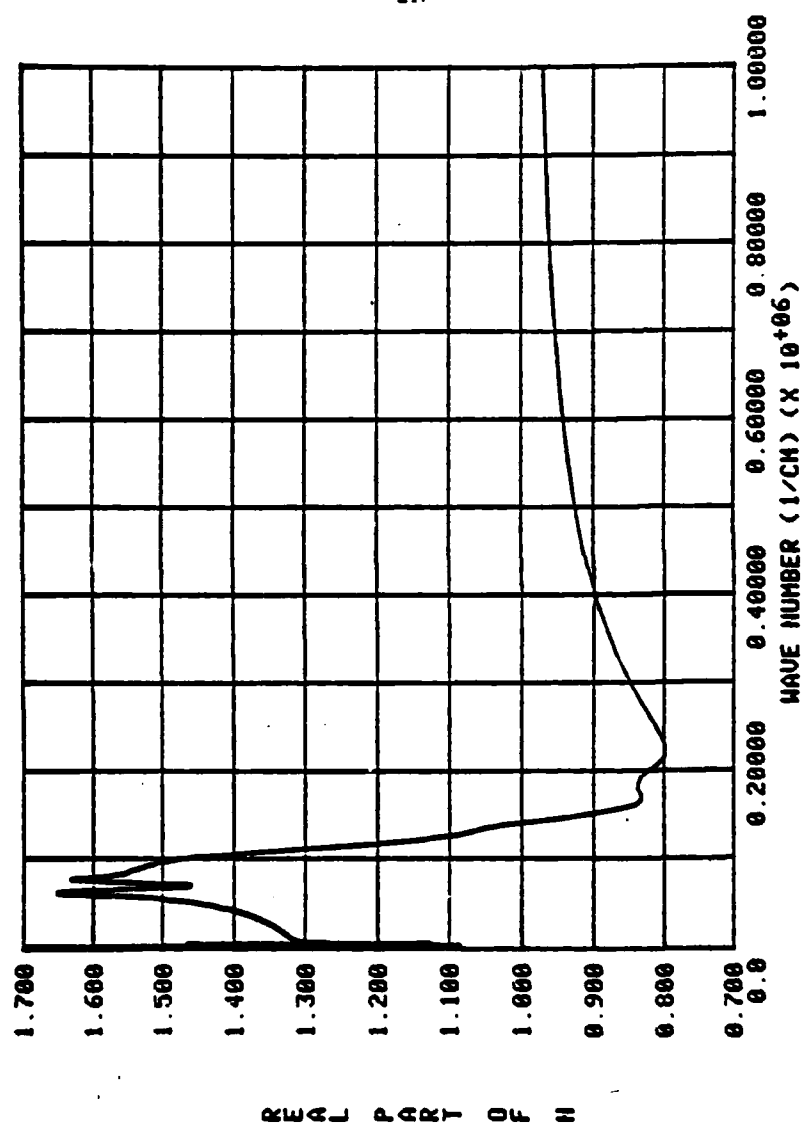


Fig. 23. The final spectrum of $n(\nu)$ from 0 to 10^6 cm^{-1} .

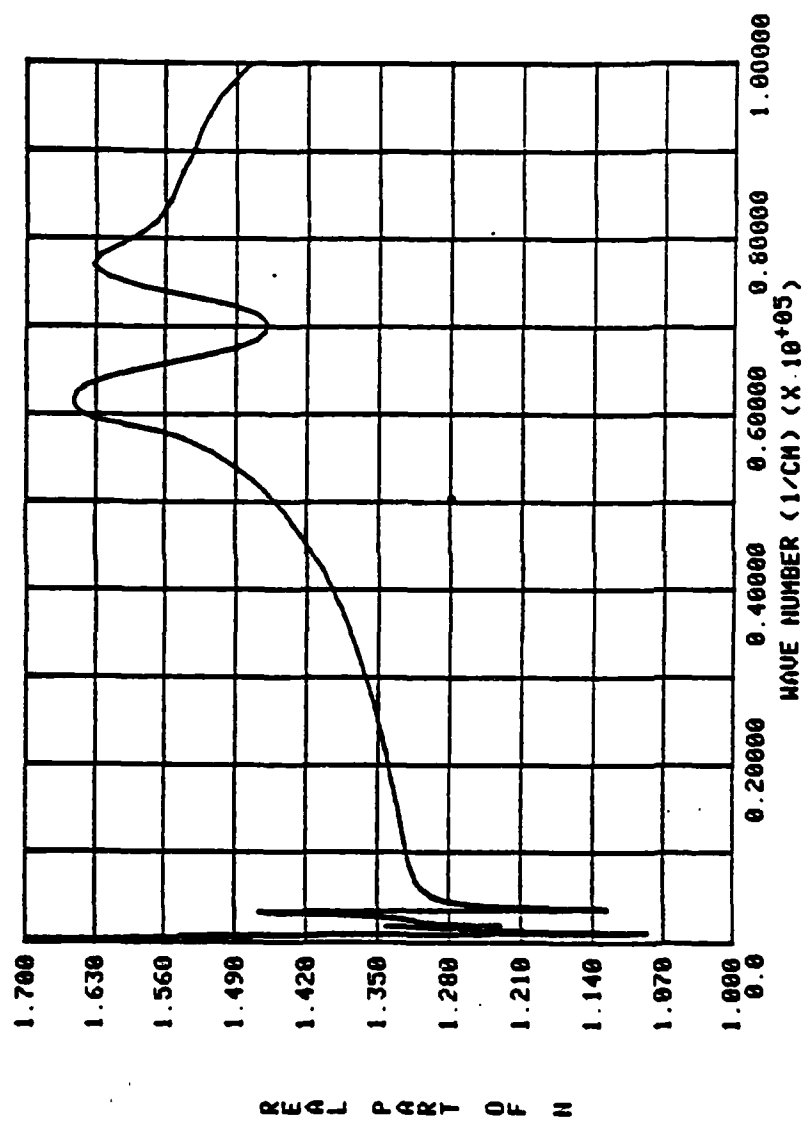


Fig. 24. The final spectrum of $n(\nu)$ from 0 to 10^5 cm^{-1} .

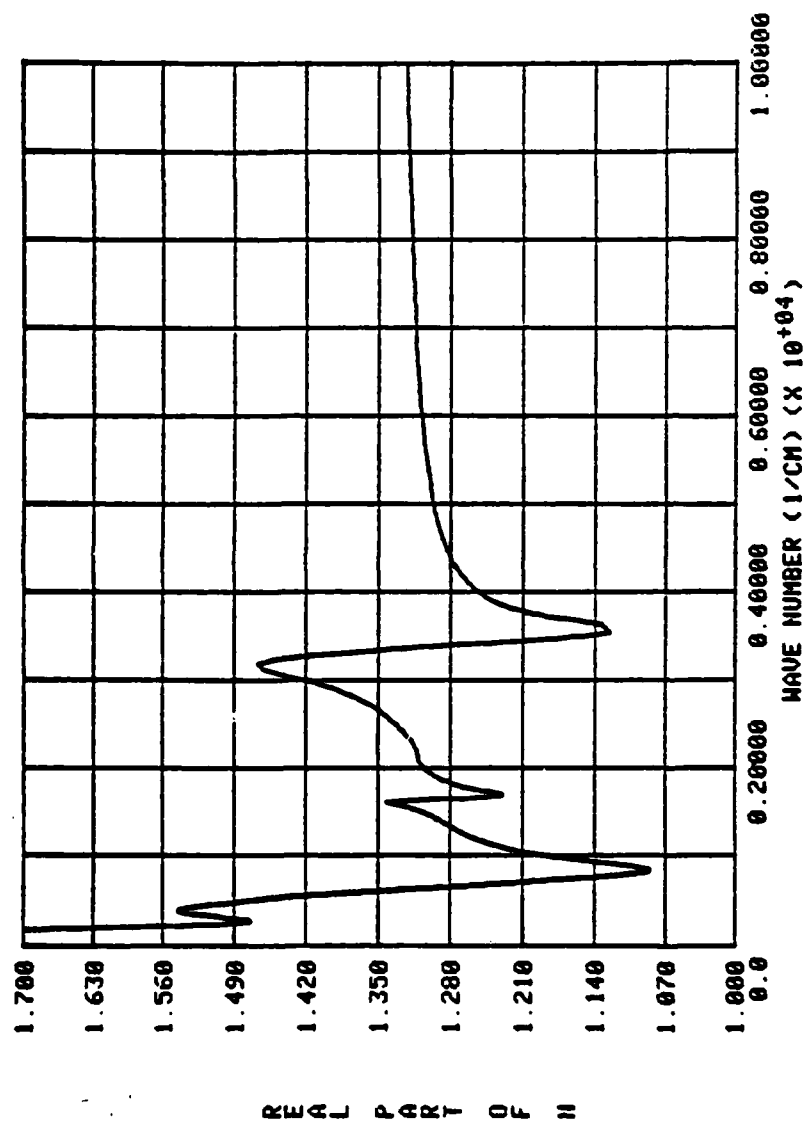


Fig. 25. The final spectrum of $n(\nu)$ from 0 to 10^4 cm^{-1} .

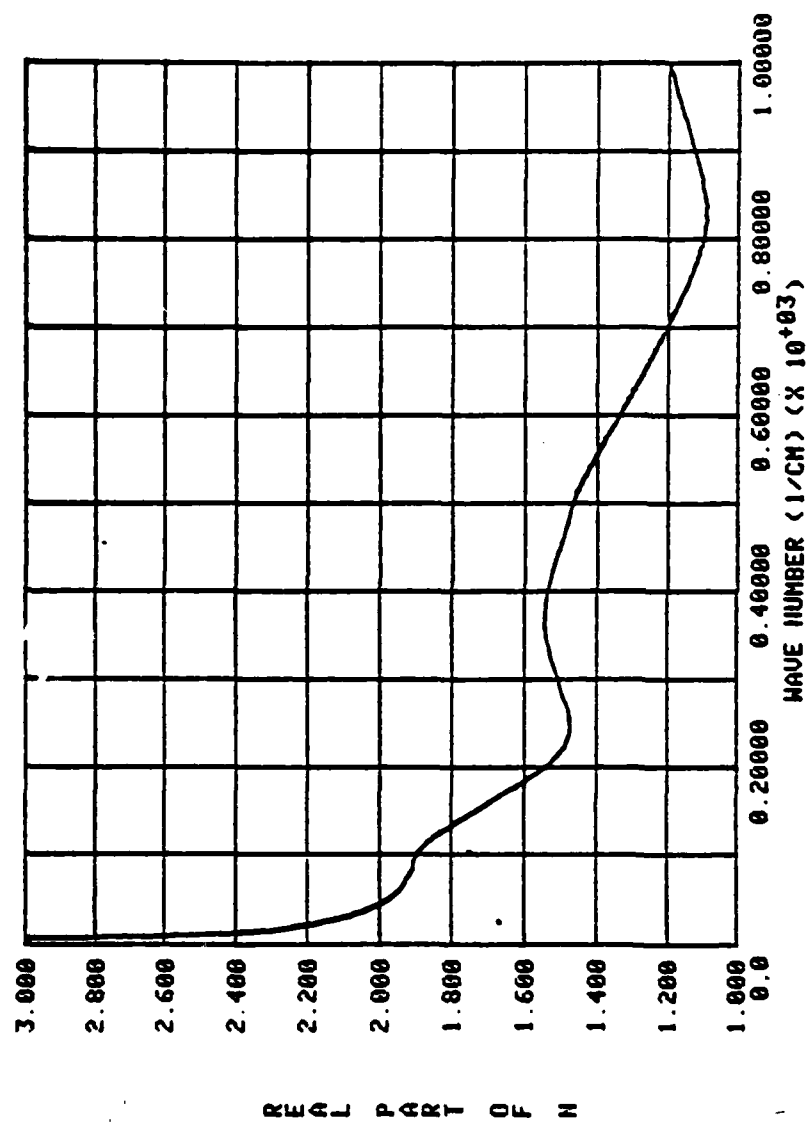


Fig. 26. The final spectrum of $n(\nu)$ from 0 to 10^3 cm^{-1} .

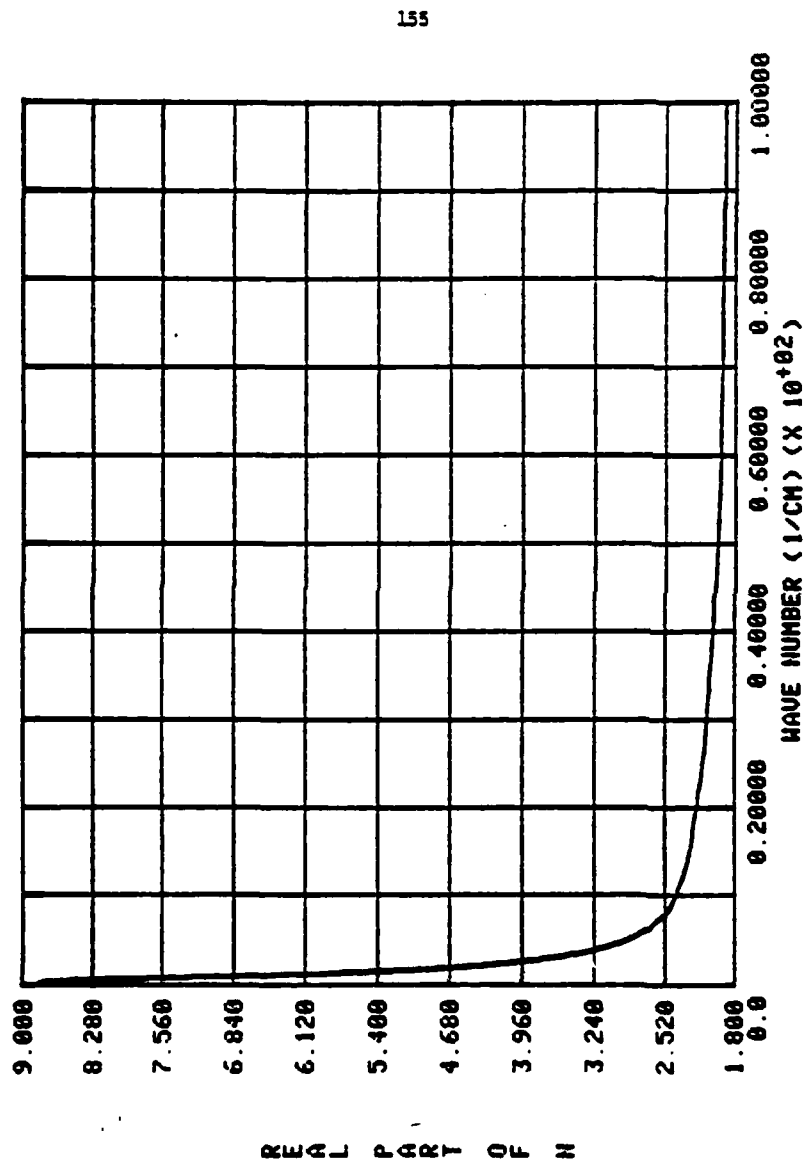


Fig. 27. The final spectrum of $n(\nu)$ from 0 to 10^2 cm^{-1} .

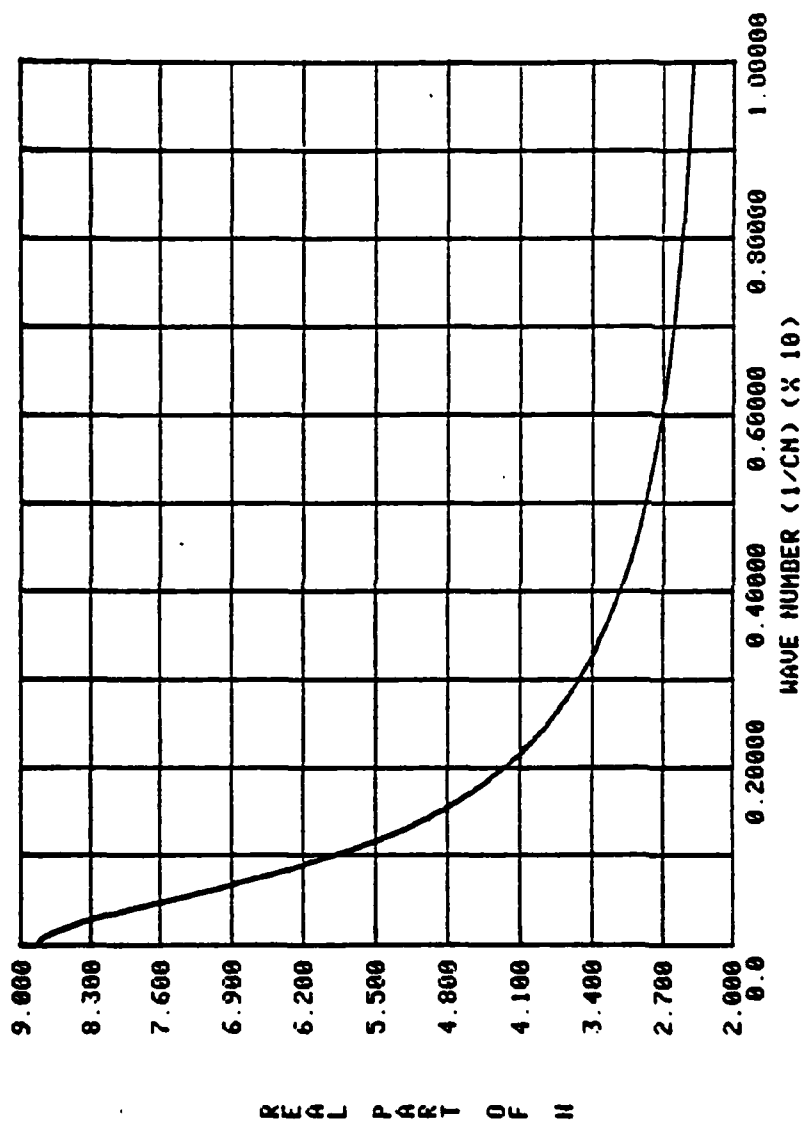


Fig. 28. The final spectrum of $n(\nu)$ from 0 to 10 cm^{-1} .

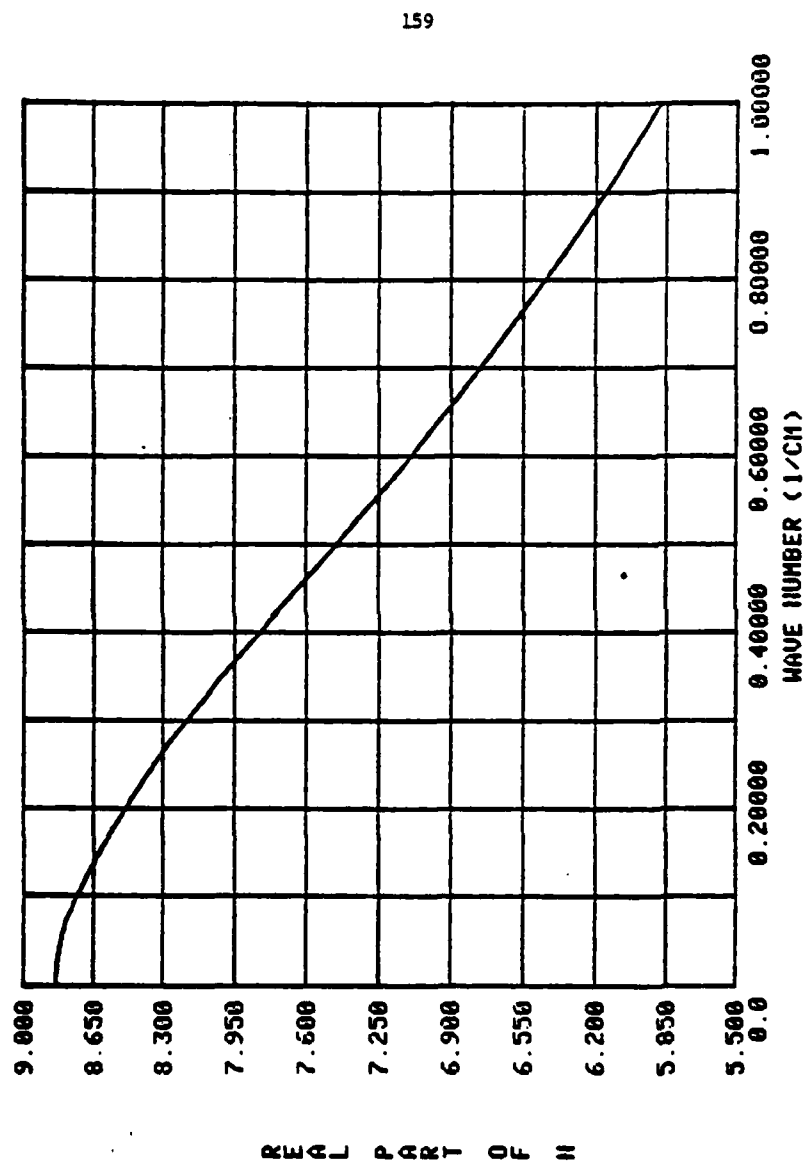


Fig. 29. The final spectrum of $n(\nu)$ from 0 to 1 cm^{-1} .

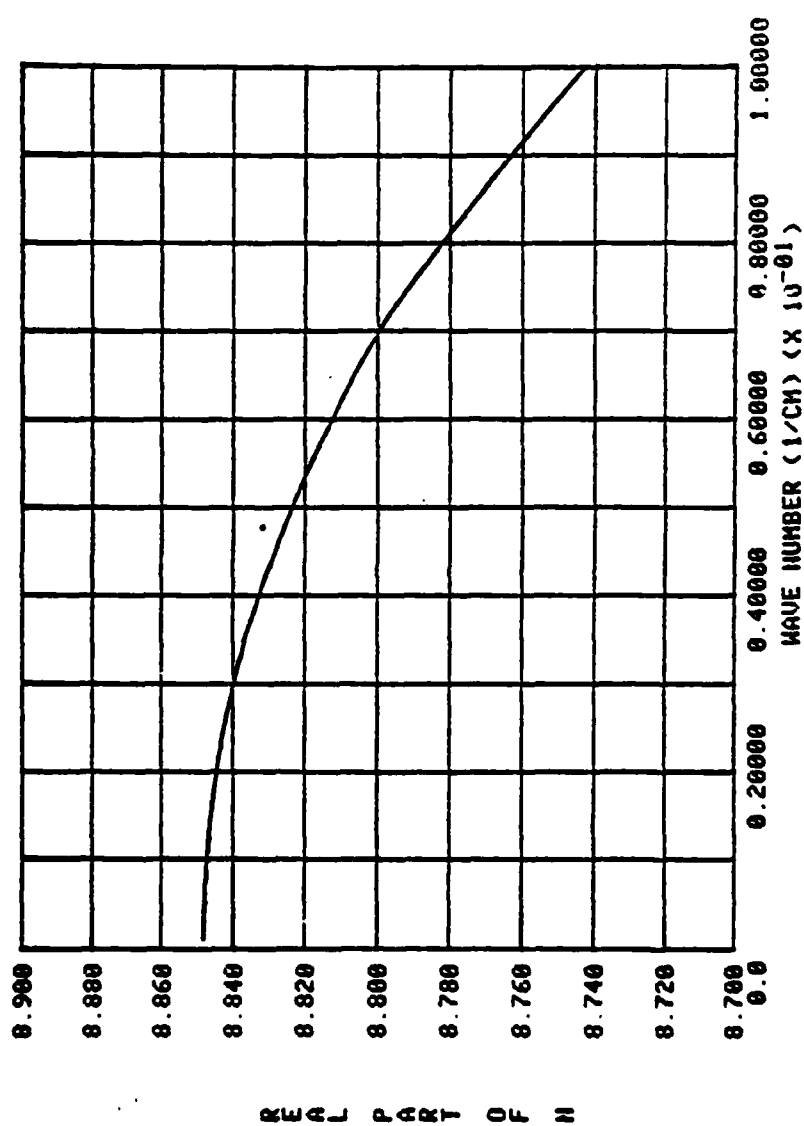


Fig. 30. The final spectrum of $n(\nu)$ from 0 to 10^{-1} cm^{-1} .

CHAPTER VI

CONCLUSION

The process of obtaining the complex refractive index of water began with the acquisition of an absorption spectrum that spanned approximately 14 decades, from 10^{-6} to 10^8 cm^{-1} . This spectrum comprised smoothly joined data from various sources, and was adjusted within experimental error until an electronic sum rule yielded proper results. This spectrum was appropriately Fourier transformed to give the real part of the complex refractive index. Calculations over several regions were joined to create a smooth spectrum over the range 10^{-3} to 10^6 cm^{-1} . The result was a complete and self-consistent spectrum of both real and imaginary parts of the complex refractive index over 9 decades.

To address the question of error in the calculation of $n(\nu)$, the literature was again consulted to find sufficient data for comparison. The following four spectral locations were chosen: 10 cm^{-1} , 5×10^2 cm^{-1} , 2×10^3 cm^{-1} , and 1×10^4 cm^{-1} . The procedure was to average the data, then find the percent difference between the mean and the results obtained in this research.

At 10 cm^{-1} , the data of Downing and Williams, Afsar and Hasted, and Zolotarev et al.²⁸ yielded a mean value of 2.588.

The value obtained in this research was 2.399, a difference of 7.6 percent. In the paper by Downing and Williams, 10 cm^{-1} was the lowest frequency point of their calculations. Their paper stated that the data become "coarse at the lowest frequencies."²⁹ Further, they obtained optical constants for their calculations from Ray,³⁰ whose data were presented graphically and not in tabular form, thereby allowing for considerable inaccuracy. The work by Afsar and Hasted used a Fourier transform spectrophotometer. As a result, their calculations for the low endpoint of the range, which is near 10 cm^{-1} , are subject to the same problems as are outlined in Chapter IV above. The data of Zolotarev et al. are a result of Kramers-Kronig calculations, equivalent to the Fourier transform method. The data used are sparse in the region of 10 cm^{-1} , thus raising the objection that resolution in that range was not good. Considering all the above factors, one might well conclude that the results of the present study are more accurate at 10 cm^{-1} than the values used for comparison.

At $5 \times 10^2\text{ cm}^{-1}$, values by Hale and Querry, Downing and Williams, Pontier and Dechambenoy,³¹ Rusk et al.,³² and Zolotarev et al. gave a mean of 1.473. The present work gives 1.468, a difference of 0.4 percent. The same authors reported data at $2 \times 10^3\text{ cm}^{-1}$ which gave a mean of 1.323. The present work gives 1.306, a difference of 1.3 percent. At $1 \times 10^4\text{ cm}^{-1}$, data of Hale and Querry, Pontier and Dechambenoy, and Zolotarev et al. gave a mean of 1.325. The present study gives 1.322, a 0.2 percent difference. These values are much closer

to those of the comparison works than at lower wave number regions. To the extent that they differ, it is believed that the use of such a broad ranged and self-consistent absorption spectrum as is illustrated in Figure 3 gives more reliable results. Considering the uncertainty, however, it is probably reasonable to say that the values of $n(\nu)$ are accurate only to three significant figures.

One might hope that the future will bring more efficient algorithms for the computation of a spectrum over a broad range. The ideal would be a single calculation over a very large range with very fine divisions among the data. This would give a spectrum accurate near the endpoints and high in resolution, one which is entirely self-consistent. Hopefully, the present work is a small step in that direction.

REFERENCES

1. George M. Hale and Marvin R. Querry, *Appl. Opt.* 12, 555 (1973).
2. J. M. Heller, Jr., R. N. Hamm, R. D. Birkhoff, and L. R. Painter, *J. Chem. Phys.* 60, 3483 (1974).
3. Harry D. Downing and Dudley Williams, *J. Geophys. Res.* 80, 1656 (1975).
4. O. V. Kopelevich, *Opt. Spektrosk.* 41, 666 (1976) [*Opt. Spectrosc.* 41, 391 (1976)].
5. M. N. Afsar and J. B. Hasted, *J. Opt. Soc. Am.* 67, 902 (1977).
6. Marvin R. Querry, Phillip G. Cary, and Richard C. Waring, *Appl. Opt.* 17, 3587 (1978).
7. A. C. Tam and C. K. N. Patel, *Appl. Opt.* 18, 3348 (1979).
8. Kenneth S. Cole and Robert H. Cole, *J. Chem. Phys.* 9, 341 (1941).
9. Arne Engstrom, X-ray Microanalysis in Biology and Medicine (Elsevier, Amsterdam, 1962), p. 9.
10. Reference 9, pp. 10-11.
11. J. Lenoble and B. Saint-Guilly, *Compt. Rend.* 240, 954 (1955).
12. L. R. Painter, R. D. Birkhoff, and E. T. Arakawa, *J. Chem. Phys.* 51, 243 (1969).
13. Charles W. Robertson and Dudley Williams, *J. Opt. Soc. Am.* 61, 1316 (1971).
14. P. Debye, Polar Molecules (Chemical Catalogue, New York, 1929).

15. Reference 14, p. 94.
16. Reference 14, p. 85.
17. Reference 8, p. 346.
18. J. B. Hasted, in Water, a Comprehensive Treatise, edited by Felix Franks (Plenum, New York, 1972), pp. 276-289.
19. J. H. Hubbell, Nat. Stand. Ref. Data Ser., Nat. Bur. Stand. 29 (1969).
20. Reference 9, pp. 10-11.
21. J. D. Jackson, Classical Electrodynamics (Wiley, New York, 1975), p. 218.
22. C. W. Peterson and Bruce W. Knight, J. Opt. Soc. Am. 63, 1238 (1973).
23. Reference 21, pp. 284-5 and 314-15.
24. R. V. Churchill, J. W. Brown, and R. F. Verhey, Complex Variables and Applications (McGraw-Hill, New York, 1974), pp. 88-93.
25. D. W. Berreman and F. C. Unterwald, Phys. Rev. 174, 791 (1968).
26. Reference 25, p. 792.
27. E. O. Brigham, The Fast Fourier Transform (Prentice-Hall, Englewood Cliffs, 1974), pp. 94-97.
28. V. M. Zolotarev, B. A. Mikhailov, L. I. Aperovich, and S. I. Popov, Opt. Spektrosk. 27, 790 (1969) [Opt. Spectrosc. 27, 430 (1969)].
29. Reference 3, p. 1657.
30. Peter S. Ray, Appl. Opt. 11, 1836 (1972).
31. L. Pontier and C. Dechambenoy, Ann. Geophys. 22, 633 (1966).
32. A. N. Rusk, D. Williams, and M. R. Querry, J. Opt. Soc. Am. 61, 895 (1971).

VITA

David Jay Segelstein was born on December 21, 1949, in New York City. After moving to Kansas City, Missouri, in 1952, he was educated in local public schools and graduated from Southwest High School in 1967. In 1971, he graduated from Columbia University with a Bachelor of Arts degree in Sociology.

Mr. Segelstein attended the University of Missouri-Kansas City Law School, receiving the Juris Doctor degree in 1975. Thereafter, he practiced law until 1978, when he returned to the University of Missouri-Kansas City to study Physics. Upon completion of his degree requirements, Mr. Segelstein plans to continue his education in a doctoral program at Princeton University beginning in September, 1981.

VI. References

H.E. Bennett and J.O. Porteus, "Relation between surface roughness and specular reflectance at normal incidence," J. Opt. Soc. Am. 51, 123-129 (1961).

G.M. Hale and M.R. Querry, "Optical constants of water in the 200-nm to 200- μ m wavelength region," Appl. Opt. 12, 555-563 (1973).

O.B. Toon, J.B. Pollack, and B.N. Khare, "The optical constants of several atmospheric aerosol species: ammonium sulfate aluminum oxide, and sodium chloride," J. Geophys. Res. 81, 5733-5748 (1976).

O.B. Toon, J.B. Pollack, and C. Sagan, "Physical properties of the particles composing the martian dust storm of 1971-1972." Icarus 30, 663-696 (1977).

F.E. Volz, "Infrared optical constants of ammonium sulfate, sahara dust, volcanic pumice, and fly ash," Appl. Opt. 12, 564-568 (1973).

END

FILMED

10-83

DTIC